Standard Model and Exotic Diboson Production with the ATLAS Detector

A thesis submitted to

The University of Manchester

for the degree of

Doctor of Philosophy

in the Faculty of

Engineering and Physical Sciences

Marilyn D. Marx

Particle Physics Group

School of Physics and Astronomy

2013

Standard Model and Exotic Diboson Production with the ATLAS Detector

Marilyn D. Marx

Abstract

This thesis discusses phenomenological and experimental aspects of diboson production at the Large Hadron Collider. An implementation of anomalous triple gauge boson couplings for massive vector boson pair production at leading and next-to-leading order in α_s using the POWHEG method into the Monte Carlo event generator Herwig++ is outlined and studied. A measurement of the $W^{\pm}Z$ production cross section is presented using 4.6 fb^{-1} of luminosity from proton-proton collisions produced at a centre of mass energy of $\sqrt{s} = 7$ TeV and collected by the ATLAS detector. Final states with three leptons and missing transverse momentum are used. Differential cross section measurements are unfolded as a function of the Z boson transverse momentum and the diboson invariant mass for the first time using LHC data. Limits on anomalous triple gauge boson couplings are set using the Z boson transverse momentum distribution and currently give the most stringent limits using this channel only. Lastly, a search for heavy graviton resonances decaying to Z boson pairs is performed. One boson is allowed to decay leptonically and the other boson hadronically, either into a pair of jets or, in the highly boosted case, into one merged jet. The analysis uses 7.2 fb^{-1} of $\sqrt{s} = 8$ TeV data and sets the most stringent limits on the considered benchmark model to date. All presented measurements are in good agreement with Standard Model predictions.

Contents

List of Figures

List of Tables

Declaration

No portion of the work referred to in this thesis has been submitted in support of an application for another degree or qualification of this or any other university or other institute of learning.

Copyright

The author of this thesis (including any appendices and/or schedules to this thesis) owns certain copyright or related rights in it (the "Copyright") and she has given The University of Manchester certain rights to use such Copyright, including for administrative purposes.

Copies of this thesis, either in full or in extracts and whether in hard or electronic copy, may be made **only** in accordance with the Copyright, Designs and Patents Act 1988 (as amended) and regulations issued under it or, where appropriate, in accordance with licensing agreements which the University has from time to time. This page must form part of any such copies made.

The ownership of certain Copyright, patents, designs, trade marks and other intellectual property (the "Intellectual Property") and any reproductions of copyright works in the thesis, for example graphs and tables ("Reproductions"), which may be described in this thesis, may not be owned by the author and may be owned by third parties. Such Intellectual Property and Reproductions cannot and must not be made available for use without the prior written permission of the owner(s) of the relevant Intellectual Property and/or Reproductions.

Further information on the conditions under which disclosure, publication and commercialisation of this thesis, the Copyright and any Intellectual Property and/or Reproductions described in it may take place is available in the University IP Policy, in any relevant Thesis restriction declarations deposited in the University Library, The University Librarys regulations and in The University's policy on Presentation of Theses.

Acknowledgments

First of all I would like to thank my supervisors Mike Seymour and Alex Oh for giving me the opportunity to learn about what a theorist does and what an experimentalist does and how it is important that they do things together. I am deeply grateful for all the knowledge they were so relentlessly willing to share and for all their help, patience and guidance throughout the past three and a half years.

Thank you:

To Keith Hamilton, Peter Richardson and David Grellscheid for teaching me about Herwig++.

To all the wonderful people, too numerous to list, that I had the pleasure of being on an analysis team with, for their experience, ideas and help and for motivating me to try harder.

To everybody in the Manchester Particle Physics Group both at Manchester and at CERN. For many interesting discussions, serious and not, and for repeatedly forcing me to leave my desk and do something fun in the real world instead. Special thanks go to Fred Loebinger for letting me be an undergraduate and a graduate student and for making it that much easier. Thank you also to Sabah Salih for always being available when the computers decided to not do what they should and for generally helping wherever possible.

To all the proofreaders who have taken the time to read any part of this thesis.

To Mary K. Gaillard, for kindling my interest to start this particle physics endeavour in the first place and for being a true inspiration.

To John, for many long discussions about code, muons and dancing penguins.

To Anna, for initially teaching me about tag and probe and the ATLAS framework and, through our shared love of nail polish, red wine, vampires, exploding chestnuts and bickering about work, becoming one of the people most dearest to me.

To Michael, for always being there for me with an open ear and an open heart and for filling every single day with exactly the right amount of light.

Finally, the biggest thank you of all goes to my parents, for endlessly giving and never asking for anything in return. I would not be where I am today without your unconditional love and support. Kuckt, ech hun erem en Expiiriment erleine getahen!

– Ce qui embellit le désert, dit le petit prince,

c'est qu'il cache un puits quelque part...

Antoine de Saint-Exupéry, Le Petit Prince

Chapter 1

Introduction

Diboson production is a versatile and important mechanism for many reasons. It is a crucial background for Higgs boson studies and numerous other processes, it can probe vector boson scattering and give hints as to how such processes are regularised at the TeV scale, it offers a way to test the predictions of the Standard Model to high precision and it is sensitive to the production and decay of new particles.

This thesis documents a phenomenological study of anomalous triple gauge boson couplings in massive vector boson pair production and two analyses using datasets collected with the ATLAS detector at the Large Hadron Collider at centre of mass energies of 7 TeV and 8 TeV, respectively. The first analysis is a measurement of the inclusive and differential $W^{\pm}Z$ production cross sections using fully leptonic final states and sets limits on anomalous coupling parameters accessible through the $W^{+}W^{-}Z$ vertex. The second analysis exploits boosted topologies and searches for heavy resonances decaying into two Z bosons, one of which, in turn, decays leptonically and the other hadronically.

The remainder of this thesis is organised as follows. A historical review and an introductory description of the Standard Model of particle physics is given in chapter 2. An overview of Quantum Chromodynamics, the theory of the strong force, is presented and then special emphasis is placed on the mechanism of electroweak symmetry breaking. Diboson production and its particular features, such as gauge boson self-interactions, are discussed in chapter 3. The current theoretical and experimental status of $W^{\pm}Z$ production is also reviewed in light of the results presented here. The implementation of anomalous triple gauge couplings for diboson production into the Herwig++ Monte Carlo event generator is described in chapter 4. Calculations of virtual corrections are included as well as leading and next-to-leading order results of the implementation. Chapter 5 gives an overview of the setup and performance of the Large Hadron Collider while chapter 6 provides a detailed description of the ATLAS detector. Chapter 7 explains some of the experimental techniques used to convert detector signals into reconstructed physics objects needed for data analysis. In chapter 8, the full $W^{\pm}Z \to \ell^{\pm}\nu\ell^{+}\ell^{-}$ analysis is documented. Measurements of the fiducial and total production cross section, differential cross section distributions as well as limits on anomalous triple gauge boson couplings are presented. Chapter 9 describes the $G^{*} \to ZZ \to \ell^{+}\ell^{-}q\bar{q}$ heavy resonance search and sets limits on the bulk Randall-Sundrum graviton model. Lastly, chapter 10 summarises the conclusions drawn from the work presented in this thesis.

Chapter 2

The Standard Model

2.1 History and Overview

The Standard Model (SM) is the current theoretical framework of particle physics that describes the interactions of fundamental particles, so-called *quarks* and *leptons*, through force mediators, so-called *gauge bosons*. Table 2.1 lists the four known fundamental forces in the universe – the strong, weak, electromagnetic and gravitational forces – together with their approximate range of interaction. The electromagnetic and gravitational forces have an infinite range and obey an inverse square law. The range of the strong and weak forces can be estimated through Heisenberg's uncertainty principle and the masses of the force-carrying particles, which are the pions for the strong nuclear force and the W and Z bosons for the weak force. One of the shortcomings of the SM is that it does not accommodate gravity as there is no experimentally confirmed understanding of this force at the quantum level yet. Much effort has gone into trying to combine gravity with the SM to form a Theory of Everything, for example through theories of extended objects like strings or branes, but so far such attempts have only seen limited success.

Force	Range
electromagnetic	∞
weak	10^{-17} m
strong	10^{-15} m
gravity	∞

Table 2.1: The four fundamental forces and their range.

Experimentally, the SM predictions, down to very subtle effects, have withstood many precise tests and continue to do so as new data is acquired. The recent discovery of a Higgs boson [1, 2] together with a few other highlights will be discussed in more detail in the following sections. Theoretically, one of the biggest successes was the unification of the electromagnetic and weak forces to the so-called electroweak force and the generation of mass through spontaneous symmetry breaking (SSB).

Figure 2.1 shows all the building blocks of the SM as it is pictured today. Matter is

made up of fundamental spin $\frac{1}{2}$ particles which are divided into two types, *leptons* and *quarks*. Collectively, these are classified as *fermions*[1]. There are six leptons and six quarks, organised into three generations, plus anti-matter versions of each of these particles. In addition, there are four spin 1 force-mediating bosons and the spin 0 Higgs boson, whose field provides a mechanism to generate mass.

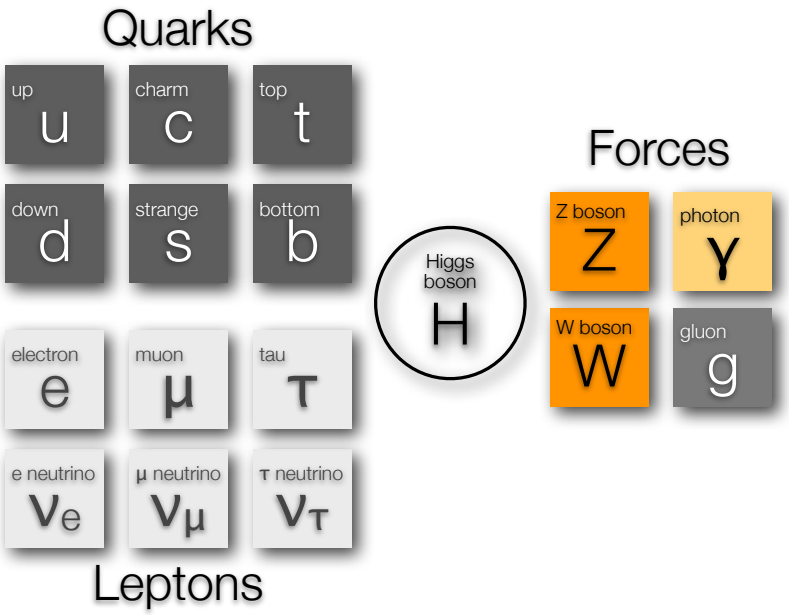

Figure 2.1: The building blocks of the Standard Model of particle physics.

The picture of the SM has not always been this clear and the model had to undergo numerous modifications and additions before being formulated in the way it is understood today. It is interesting to go back in time and follow the path of particle physics discoveries as more and more pieces of the puzzle were put together [3].

The ancient Greeks already had a notion of fundamental particles and first proposed the concept of an atom, from $\alpha\tau o\mu o\varsigma$ meaning indivisible, but the field of modern particle physics saw its beginning in 1897 when J.J. Thomson discovered the *electron*. The discovery (and the name) of the *proton* is usually credited to Ernest Rutherford who performed his famous gold foil scattering and "splitting of the atom" experiments in 1911 and 1917 respectively, the latter at the University of Manchester. Rutherford also proposed the idea of the *neutron* which his research assistant James Chadwick then discovered experimentally [4] in 1932.

Both Max Planck, in 1900 in the context of black-body radiation, and Albert Einstein, in 1905 to explain the photoelectric effect, proposed the idea that electromagnetic radiation

[1] Although it should be noted that the name fermion really refers to any particle with half-integer spin, be it fundamental or composite.

is quantised. In 1923, Arthur Compton discovered the so-called Compton scattering [5] which provides experimental evidence that light behaves as a particle, the *photon*.

In 1934, Hideki Yukawa predicted the existence of a *meson* to explain why protons in a nuclei do not just electromagnetically repel each other. In 1947, Cecil Powell and his group analysed cosmic ray data and found two different particles that qualify mass-wise as the meson hypothesised by Yukawa. One of them is the *pion* [6], indeed a meson, and the other one is the *muon*, a lepton, which Carl Anderson and his student had already observed in 1936.

In 1927, Dirac wrote down his famous equation for spin $\frac{1}{2}$ particles which unfortunately had the tricky problem of allowing negative energy solutions. After an unconvincing attempt by Dirac to explain these solutions as "holes in a sea of electrons" [7, 8], Carl Anderson discovered the *positron* in a cloud chamber in 1932 [9]. In the early 1940s Richard Feynman and Ernst Stückelberg reformulated and solved the problem by stating that negative energy solutions are positive solutions of a different particle, namely the *antiparticle*, of the same mass but opposite charge as the original particle. Experimental confirmation followed shortly after when the first antiproton and antineutron were observed at the Berkeley Bevatron in 1955 and 1956, respectively [10, 11].

Wolfgang Pauli suggested the existence of a new particle involved in radioactive nuclei decays in 1930 and four years later Enrico Fermi published a model of nuclear beta decay involving *neutrinos*. Their existence was first experimentally confirmed in 1956 in the Cowan-Reines neutrino experiment [12].

In 1947, a new neutral particle, now known as the kaon [13], was seen to decay into a pair of charged pions. This discovery was followed by over a decade of discoveries of a whole plethora of strongly interacting heavy particles. Nobody had really foreseen these particles which showed the interesting feature that they were produced at a much higher rate than they decayed. In 1961, to bring some structure into these observations, Murray Gell-Mann proposed the Eightfold Way arranging all these baryons and mesons, collectively called hadrons, according to their charge and their *strangeness*.

Three years later, in an attempt to understand why all these particles fit into patterns, Gell-Mann and George Zweig independently proposed that these hadrons are composite objects made up of more fundamental particles, the *quarks*. The model states that the quarks come in three flavours – up, down and strange – and that baryons are made of three quarks whereas mesons are made of a quark and an antiquark. Experimentally, the quark model was reinforced in the late 60s when deep inelastic scattering experiments at SLAC indicated the presence of three lumps inside a proton rather than only one [14]. The quark model, however, seemed to violate the Pauli principle. An idea by Oscar Greenberg came to the rescue in 1964 when he suggested that quarks not only exist in three flavours but also in three *colours* – red, green and blue [15]. Direct experimental evidence for colour is threefold [14, 16]. Firstly, in 1951 Fermi and his Chicago group discovered the Δ^{++} particle, which was seen as a $\pi^+ p$ resonance. This baryon is composed of three up quarks which would violate the Pauli exclusion principle if it were not for an additional colour quantum number. Secondly, measurements of the pion decay rate to photons, $\Gamma(\pi^0 \to \gamma\gamma)$ and, thirdly, measurements of the ratio of $e^+e^- \to$ hadrons and $e^+e^- \to \mu^+\mu^-$ cross sections is sensitive[2] to the number of colours N_c. To complete

[2]The former and the latter are $\propto N_c^2 \left[(\frac{2}{3})^2 - (\frac{1}{3})^2\right]$ and $\propto N_c \sum_f Q_f^2$, respectively. Q_f is the charge of the

the picture, Frank Wilczek, David Gross and David Politzer in 1973 theorised the concept of asymptotic freedom of the strong force which will be explained in more detail in section 2.2.

In the summer of 1974 Samuel Ting discovered the J/ψ meson at BNL [17] and the discovery was confirmed shortly after by Burton Richter's group at SLAC [18]. This unexpected find is often referred to as the "November Revolution" as the particle exhibits an extraordinarily long lifetime of $\sim 10^{-20}$ s, which is roughly 1000 times longer than expected. This is explained by the fact that this particle is a bound state, $c\bar{c}$, of a new quark, the *charm* quark. This result nicely completed a parallel between quarks and leptons, as there were now four of each. The idea of a fourth flavour was however already introduced ten years earlier by James Bjørken and Sheldon Glashow [19] and again in 1970 by Glashow, John Iliopoulos and Luciano Maiani through the GIM mechanism [20]. The latter actually required the existence of a fourth quark, rather than just suggesting it.

In 1975, evidence for a third generation of particles was found with the discovery of a new lepton, now known as the τ lepton [21]. In 1977, the counterpart in the quark sector was nicely reconciled when Leon Lederman's group at Fermilab discovered the Υ, a bound state of *bottom* quarks [22]. Finally, the last, very much expected piece in the quark puzzle, the *top* quark, was discovered in 1995 by the CDF and DØ collaborations at the Tevatron [23, 24].

In a rather adequate, as indicated by the latest LHC data, attempt to explain why particles have mass, Peter Higgs submitted his paper to Physical Review Letters [25] in 1964. The same year Englert and Brout [26] and Guralnik, Hagen and Kibble [27] published their related papers. Higgs suggested the existence of one, or more, new massive scalar bosons whose field could generate mass through spontaneous breaking of the local gauge symmetry. By 1967, Sheldon Glashow, Stephen Weinberg and Abdus Salam had brought together their ideas of combining the electromagnetic and weak forces into one electroweak force and incorporating the Higgs boson into their model [28–30]. Only a few years later, Martinus Veltman and Gerardus 't Hooft proved that this was a renormalizable theory and more details will be given in section 2.3. Highly anticipated experimental proof came in 1983 when the massive electroweak W and Z gauge bosons were found at CERN [31]. On July 4$^{\text{th}}$ 2012, the most sought-after discovery, that of a Higgs-like boson, was announced by the ATLAS and CMS experiments at the Large Hadron Collider[3] (LHC) [1, 2].

To summarise all the above, the SM is a quantum field theory which is gauge invariant under the SU(3)×SU(2)×U(1) group. The SU(3) component describes Quantum Chromodynamics (QCD), the theory of the strong force whose gauge boson is the gluon and more details are given section 2.2. The SU(2)×U(1) component describes the electroweak force, where the W, Z and γ gauge bosons are the mediators of the group. More details can be found in section 2.3. Gauge boson properties, like their charge and mass, are listed in table 2.2 [32]. While the photon and gluon are stable, the $W^{\pm}$ and Z bosons decay very quickly and their lifetime can be estimated using

$$\tau = \frac{\hbar}{\Gamma} \tag{2.1}$$

different quark flavours.

[3]There appears to be an asymmetry between the "material-oriented" US and the "interaction-oriented" Europe. The US has discovered most quarks and leptons, Europe the gauge bosons (and a Higgs boson).

Particle	Mass	Charge	Force
γ	$< 10^{-18}$ eV	0	electromagnetic
$W^{\pm}$	80.385 ± 0.015 GeV	± 1	weak
Z	91.1876 ± 0.0021 GeV	0	weak
g	0	0	strong

Table 2.2: The gauge bosons of the Standard Model with spin 1 [32].

where $\hbar$ is the reduced Planck constant and Γ is the total decay width. The measured total decay widths of the $W^{\pm}$ and Z bosons are 2.085 ± 0.042 GeV and 2.4952 ± 0.0023 GeV [32] respectively, giving a lifetime of the order of 10^{-25} s.

The same properties are summarised in tables 2.3 and 2.4 for the SM quarks and leptons, respectively. Quarks can undergo all three types of interactions – strong, electromagnetic and weak. The charged leptons can interact electromagnetically and weakly whereas the neutrinos interact purely through the weak interaction. For these 12 particles, there exist corresponding antiparticles with the same mass but opposite charge.

Particle	Generation	Mass	Charge
u	1	$2.3^{+0.7}_{-0.5}$ MeV	$+\frac{2}{3}$
d	1	$4.8^{+0.7}_{-0.3}$ MeV	$-\frac{1}{3}$
c	2	1.275 ± 0.025 GeV	$+\frac{2}{3}$
s	2	95 ± 5 MeV	$-\frac{1}{3}$
t	3	173.2 ± 0.9 GeV	$+\frac{2}{3}$
b	3	4.18 ± 0.03 GeV	$-\frac{1}{3}$

Table 2.3: The quarks of the Standard Model with spin $\frac{1}{2}$. The u, d and s quark masses are "current-quark masses" in the $\overline{MS}$ scheme at a scale $\mu \approx 2$ GeV while b and c are "running" masses, also in the $\overline{MS}$ scheme [32], and the top quark mass is taken from direct measurements of the pole mass [33].

The main interaction vertices for the strong, weak and electromagnetic forces are shown in figure 2.2. Additionally, there are gauge boson self-interaction vertices for the weak and strong forces, since these are non-Abelian. They will be discussed in more detail in the following two sections.

2.2 Quantum Chromodynamics

QCD is the theory of the strong nuclear force and it describes the interactions between quarks and gluons. The underlying structure of QCD is the non-Abelian SU(3) gauge group with a colour degree of freedom N_c which can occur in three types – red, green and blue

Particle	Generation	Mass	Charge	Mean Lifetime
e^-	1	511.0 keV	-1	$> 4.6 \times 10^{26}$ years
ν_e	1	< 2 eV	0	
μ^-	2	105.7 MeV	-1	2.197×10^{-6} s
ν_μ	2	< 2 eV	0	
τ^-	3	1.777 GeV	-1	290.6×10^{-15} s
ν_τ	3	< 2 eV	0	

Table 2.4: The leptons of the Standard Model with spin $\frac{1}{2}$ [32]. The neutrino mass limits are derived from tritium β-decay experiments [34].

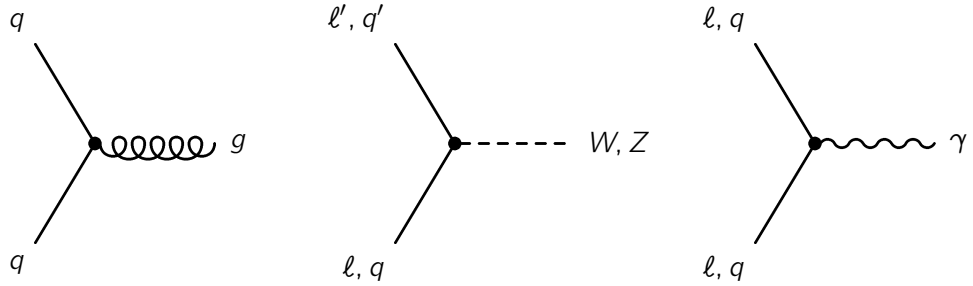

Figure 2.2: The fundamental strong, weak and electromagnetic interaction vertices.

commonly referred to as r, g and b. Colour is a quantum number that is conserved in all physical processes. The QCD Lagrangian, which is invariant under local gauge transformations, can be expressed as[4]

$$\mathcal{L}_{\mathrm{QCD}} = -\frac{1}{4} F^A_{\mu\nu} F^{\mu\nu}_A + \sum_q \bar{\psi}_q (i \not{D} - m_q) \psi_q. \tag{2.2}$$

The field strength tensor

$$F^A_{\mu\nu} = \left[\partial_\mu \mathcal{A}^A_\nu - \partial_\nu \mathcal{A}^A_\mu - g_s f^{ABC} \mathcal{A}^B_\mu \mathcal{A}^C_\nu \right] \tag{2.3}$$

is derived from the gluon field $\mathcal{A}^A_\mu$ and the indices A, B, C run over the eight ($= N_c^2 - 1$) gluon colour degrees of freedom also known as a colour octet. As with any non-Abelian gauge group, self-interactions of the force mediator, in this case the gluon, are allowed and can be derived from the field strength tensor. The triple and quartic gluon self-coupling vertices, shown in figure 2.3, form together with the quark-gluon interaction vertex in figure 2.2 the main QCD interaction vertices. The Feynman rules for the latter can be found in many places [16, 35]. The f^{ABC} are the *structure constants* of the SU(3) group which relate the generator matrices in the fundamental (and similarly in the adjoint) representation of SU(3) by

$$[t^A, t^B] = i f^{ABC} t^C. \tag{2.4}$$

[4]The slashed notation in equation 2.2 is short for $\not{D} = \gamma^\mu D_\mu$, where γ^μ are the Dirac matrices.

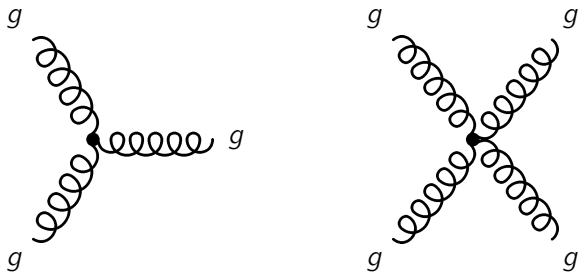

Figure 2.3: The triple and quartic gluon self-coupling vertices.

The *generators* t^A are equal to a half of the 3×3 hermitian, traceless Gell-Mann matrices λ^A. The normalisation of these matrices is by convention defined as

$$\text{Tr } t^A t^B = T_R \, \delta^{AB} \tag{2.5}$$

where $T_R = \frac{1}{2}$ is the colour-factor for a gluon to split into a $q\bar{q}$ pair. The generators obey two further relations

$$\sum_A t^A_{ab} t^A_{bc} = C_F \, \delta_{ac} \tag{2.6}$$

and

$$\text{Tr } T^C T^D = \sum_{A,B} f^{ABC} f^{ABD} = C_A \, \delta^{CD} \tag{2.7}$$

where $C_F = \frac{N_c^2 - 1}{2N_c} = \frac{4}{3}$ and $C_A = N_c = 3$ are the fundamental and adjoint colour-factors that associate gluon emission to a quark and a gluon, respectively [16, 32]. The quark fields are denoted by ψ_q where q runs over the six quark flavours. The covariant derivate D_μ can be written as

$$(D_\mu)_{AB} = \partial_\mu \delta_{AB} + i g_s (t^C \mathcal{A}^C_\mu)_{AB}. \tag{2.8}$$

In analogy with the Quantum Electrodynamics (QED) fine structure constant, the strong coupling constant α_s is defined as

$$\alpha_s = \frac{g_s^2}{4\pi}. \tag{2.9}$$

One can imagine some dimensionless observable R which only depends on the energy scale Q. To calculate R as a perturbation series in α_s, the ultraviolet (UV) divergences that appear must be removed and this is done by renormalizing the coupling constant. This introduces an arbitrary mass scale μ, the renormalization scale, at which the removal of the UV divergences is performed. It can be shown [16] that any Q scale dependence of an observable only enters through the *running* of the coupling constant $\alpha_s(Q^2)$. To lowest order, the QCD running coupling constant α_S is

$$\alpha_s(Q^2) = \frac{12\pi}{(11N_c - 4n_f T_R) \log \frac{Q^2}{\Lambda^2_{QCD}}}, \tag{2.10}$$

where n_f the number of flavours. From this equation, it can be seen that α_s decreases with increasing Q^2 and becomes small for short distances or high energies and large for large distances or low energies. This effect is called *asymptotic freedom* and ensures that perturbation

theory works at high energy[5]. Λ_{QCD} is the scale at which the effective coupling becomes large and perturbation theory is unreliable. For values of Q^2 much larger than Λ^2_{QCD}, the effective coupling is small and perturbative QCD gives a good description. Λ_{QCD} is determined experimentally and is of the order of an average hadronic mass ($\sim$ 200 MeV) [14]. The world average value measured for α_s is [32]

$$\alpha_s(m_Z^2) = 0.1184 \pm 0.0007. \tag{2.11}$$

Another concept, somewhat related to asymptotic freedom, is *confinement* which states that quarks and gluons cannot exist as free, isolated particles over macroscopic distances. However, since perturbation theory breaks down at low enough energies, there is no rigorous, direct proof that confinement always holds. Rather, it is assumed, since partons are only ever observed confined in colour singlet states of the form $\frac{1}{\sqrt{3}}(r\bar{r} + g\bar{g} + b\bar{b})$ for mesons and $\frac{1}{\sqrt{6}}(rgb - rbg + gbr - grb + brg - bgr)$ for baryons. Similarly, there are no free gluons, which are realised as a colour octet.

At hadron colliders, composite objects interact with each other whereas the matrix element calculation of a hard process assumes an interaction between quarks and gluons. To relate the parton cross section to the proton cross section, the *factorisation theorem* is therefore invoked as

$$\sigma(s) = \int dx_1 dx_2 f_1^{(P_1)}(x_1, \mu_F^2) f_2^{(P_2)}(x_2, \mu_F^2) \hat{\sigma}(x_1 x_2 s, \mu_F^2) \tag{2.12}$$

where x_1 and x_2 are the momentum fractions carried away by each parton from the original proton momentum and f_1 and f_2 are the corresponding parton distribution functions (PDFs). This theorem essentially states that the hard (perturbative) and soft (non-perturbative) parts of a proton-proton collision can be split up. The full proton-proton cross section can be calculated from an integration over x_1 and x_2 of the parton cross section $\hat{\sigma}$ convolved with f_1 and f_2, which all depend on the factorisation scale μ_F. The dependence on μ_F becomes weaker as higher orders are included in the calculation. This theorem is universal in the sense that the PDFs are not process dependent. They contain all the non-perturbative information on the probability of finding a parton with a given momentum and flavour inside a proton. The PDFs can and have been computed using different experimental data sets. Figure 2.4 shows PDFs for the gluon and all different quark flavours from the MSTW collaboration at next-to-leading order (NLO) in α_s at the 68% C.L [36]. At low energy, the three valence quarks in the proton, one d and two u quarks, carry essentially all of the momentum. At larger energies, the sea quarks and gluons can be resolved. It should be noted that at LHC energies the fraction carried by gluons is very significant which makes the gluon fusion contribution to Higgs production (and other processes) so important. It can further be noted that, as one moves to higher Q^2 values, the probability of finding low x values increases rapidly.

2.3 Electroweak Sector

The concept of the electromagnetic and weak interactions as a unified gauge structure was first proposed by Glashow, Weinberg and Salam (GWS) [28–30]. The theory in-

[5] At very high energies, the theory becomes effectively free, hence the name.

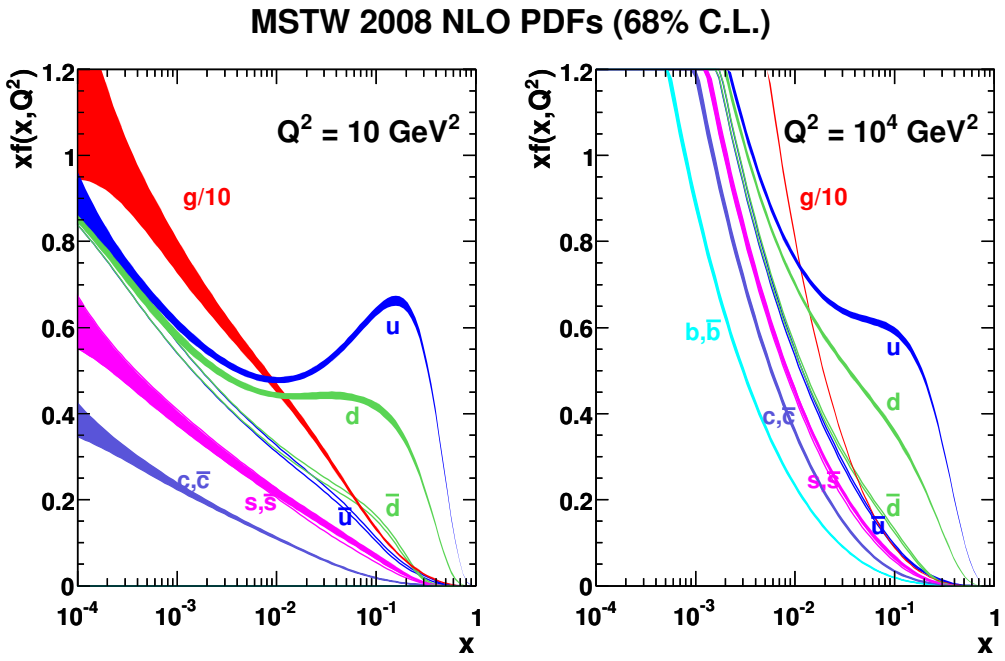

Figure 2.4: MSTW 2008 NLO PDFs at $Q^2 = 10$ GeV^2 and $Q^2 = 10^4$ GeV^2. The widths of the bands indicate the uncertainties on the PDFs [36].

cludes local gauge invariance and SSB. The electroweak (EW) Lagrangian derived from the SU(2)×U(1) symmetry group can be written down as

$$\mathcal{L}_{\text{EW}} = \mathcal{L}_{\text{bosons}} + \mathcal{L}_{\text{Higgs}} + \mathcal{L}_{\text{fermions}} + \mathcal{L}_{\text{Yukawa}} \tag{2.13}$$

where the different components correspond to the gauge boson kinetic and self-interaction terms, the Higgs field kinetic and potential terms which generate the gauge boson masses and gauge couplings to the Higgs boson, the fermion kinetic term which is responsible for the fermion interactions with the gauge bosons and lastly the Yukawa term which generates the fermion masses and their coupling to the Higgs boson. In the following [35], the exact form of these four terms will be described in detail in the same order as above.

In the original proposal by GWS, the EW Lagrangian contains four massless gauge bosons, W^i ($i = 1, 2, 3$) and B associated with the gauge groups SU(2) and U(1), respectively. Their kinetic term is given by

$$\mathcal{L}_{\text{bosons}} = -\frac{1}{4} W^i_{\mu\nu} W^{i\mu\nu} - \frac{1}{4} B_{\mu\nu} B^{\mu\nu} \tag{2.14}$$

where the gauge field strength can generally be written as

$$X^i_{\mu\nu} = \partial_\mu X^i_\nu - \partial_\nu X^i_\mu - g f^{ijk} X^j_\mu X^k_\nu \tag{2.15}$$

with g being the gauge coupling constant and f^{ijk} the structure constants of the considered group. The third term in equation 2.15 generates gauge boson self-interactions and it is

therefore present for all non-Abelian groups, here SU(2), but vanishes for Abelian groups, here U(1). The exact form of g, the SU(2) coupling constant, will be defined a little later on and the SU(2) *structure constants* f^{ijk} are simply equal to ϵ^{ijk}, the fully antisymmetric tensor. The commutation relations of the SU(2) *generators*, the weak isospin matrices T^i, are

$$[T^i, T^j] = i\epsilon^{ijk}T^k. \tag{2.16}$$

It is important to define the concept of a particle's *handedness*, as only left-handed fermions transform under the SU(2) symmetry. Helicity is defined as the projection of the spin onto the direction of the momentum

$$h \equiv \hat{p} \cdot \mathbf{S} = \frac{1}{2}\hat{p}_i \begin{pmatrix} \sigma^i & 0 \\ 0 & \sigma^i \end{pmatrix} \tag{2.17}$$

where $h = +1/2$ is right-handed and $h = -1/2$ is left-handed. Helicity is only an intrinsic property for massless particles because for a massive particle the helicity can always be swapped by changing into another frame of reference. The more general concept of *chirality* is therefore adopted since it is also valid for massive particles and completely equivalent to helicity for massless particles. To project out the left- or right-handed components of a particle spinor, one can apply the following operators, respectively

$$\begin{aligned} \gamma_L &= \frac{1}{2}(1 - \gamma^5) \\ \gamma_R &= \frac{1}{2}(1 + \gamma^5). \end{aligned} \tag{2.18}$$

The sign needs to be swapped for antiparticles. Furthermore, two important properties in EW theory are hypercharge Y and isospin[6] T_3, which is the third component of the SU(2) generator. They are related via the electromagnetic charge Q by

$$Y = 2(Q - T_3). \tag{2.19}$$

Left-handed fermions have $T_3 = \pm\frac{1}{2}$, the sign depends on Q, and right-handed fermions have $T_3 = 0$.

SSB and the Higgs field provide the transition from these four massless gauge bosons to the four gauge bosons mentioned earlier that are actually observed experimentally. The Higgs field is defined as a doublet of complex scalar fields invariant under SU(2) transformations with hypercharge $Y = 1$ and weak isospin $T_3 = \frac{1}{2}$

$$\phi = \begin{pmatrix} \phi^+ \\ \phi^0 \end{pmatrix}, \ \phi^\dagger = \begin{pmatrix} \phi^- & \overline{\phi^0} \end{pmatrix}. \tag{2.20}$$

The corresponding Lagrangian can be written as

$$\mathcal{L}_{\text{Higgs}} = (D_\mu\phi)^\dagger(D^\mu\phi) - V(\phi^\dagger\phi) \tag{2.21}$$

[6] This refers to weak isospin. There is also strong isospin I_3 which is $+\frac{1}{2}/-\frac{1}{2}/0$ for the $u/d/$all other quarks.

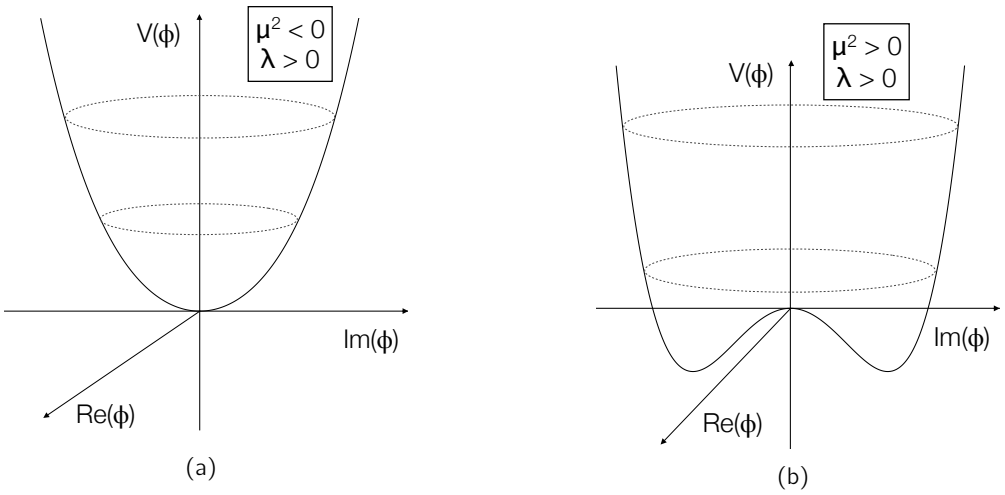

Figure 2.5: The Higgs potential for (a) $\mu^2 < 0$ and (b) $\mu^2 > 0$ values.

where the covariant derivative needed to make the system invariant under local gauge transformations is

$$D_\mu = \partial_\mu - igW_\mu^i T^i - i\frac{Y}{2}g'B_\mu. \tag{2.22}$$

The SU(2) generators are $T^i = \tau^i/2$, where $\tau^i = \sigma^i$ are the Pauli matrices. The Higgs potential, shown in figure 2.5, can be written as

$$V(\phi^\dagger\phi) = \lambda(\phi^\dagger\phi)^2 - \mu^2\phi^\dagger\phi \tag{2.23}$$

which is defined by the choice of the λ and μ parameters. If $\mu^2 < 0$ then the potential is purely positive with only a minimum at the origin, but if $\mu^2 > 0$ then $\phi = 0$ is an unstable maximum. In the latter case, the degenerate minima of the potential energy are described by a circle of radius

$$v = \sqrt{\frac{\mu^2}{\lambda}}. \tag{2.24}$$

Choosing a specific minimum, for example at

$$\phi_{\text{min}} = \frac{1}{\sqrt{2}}\begin{pmatrix}0\\ v\end{pmatrix}, \tag{2.25}$$

gives the vacuum a preferred direction in weak isospin space – this is known as the SSB mechanism. By inserting equation 2.25 into equation 2.21 and remembering that $\partial_\mu\phi_{\text{min}} = 0$, then $\mathcal{L}_{\text{Higgs}}$ gives

$$\begin{aligned}\left|-i(\frac{g}{2}W_\mu^i\tau^i + \frac{g'}{2}B_\mu)\phi\right|^2 &= \frac{1}{8}\left|\begin{pmatrix} gW_\mu^3 + g'B_\mu & g(W_\mu^1 - iW_\mu^2)\\ g(W_\mu^1 + iW_\mu^2) & -gW_\mu^3 + g'B_\mu\end{pmatrix}\begin{pmatrix}0\\ v\end{pmatrix}\right|^2 \\ &= m_W^2 W_\mu^+ W^{-\mu} + \frac{1}{2}m_Z^2 Z_\mu Z^\mu \end{aligned} \tag{2.26}$$

where the last equality is given if the following relations are adopted

$$W_\mu^\pm = \frac{1}{\sqrt{2}}\left(W_\mu^1 \mp iW_\mu^2\right) \tag{2.27}$$

$$Z_\mu^0 = \frac{1}{\sqrt{g^2+g'^2}}\left(gW_\mu^3 - g'B_\mu\right) \tag{2.28}$$

$$A_\mu = \frac{1}{\sqrt{g^2+g'^2}}\left(g'W_\mu^3 + gB_\mu\right). \tag{2.29}$$

The symmetry of this group is now spontaneously broken by the Higgs mechanism and the original four massless bosons W^i $(i = 1, 2, 3)$ and B associated to the SU(2) and U(1) gauge groups respectively recombine to give the four well known gauge bosons of electroweak theory. The three weak gauge bosons that have now acquired mass through SSB are the W^+, W^- and Z bosons while the photon γ remains massless. The photon vector field A_μ is orthogonal to Z_μ^0. This can be seen when expressing the new fields after SSB as a rotation of the old fields before SSB by a certain angle, in this case the weak mixing angle θ_w, which acts as a change of basis

$$\begin{pmatrix} Z^0 \\ A \end{pmatrix} = \begin{pmatrix} \cos\theta_w & -\sin\theta_w \\ \sin\theta_w & \cos\theta_w \end{pmatrix} \begin{pmatrix} W^3 \\ B \end{pmatrix}. \tag{2.30}$$

The coupling constants are

$$g = \frac{e}{\sin\theta_w} \text{ and } g' = \frac{e}{\cos\theta_w} \tag{2.31}$$

and the masses are

$$m_W = \frac{1}{2}gv \text{ and } m_Z = \frac{1}{2}v\sqrt{g^2+g'^2}. \tag{2.32}$$

By combining the last two equations, the relation between the weak gauge boson masses can be expressed as

$$\frac{m_W}{m_Z} = \cos\theta_w, \tag{2.33}$$

which holds at tree level. Information about loop corrections is given in reference [16].

Experimental data indicates that W bosons only couple to left-handed fermions. This implies that right-handed fermions must occur in singlets even if left-handed fermions occur in doublets[7] in the SU(2) group. The lepton and quark fields can therefore be defined as

$$\psi_L = \gamma_L \begin{pmatrix} \nu_\ell \\ \ell^- \end{pmatrix}, \gamma_L \begin{pmatrix} u \\ d' \end{pmatrix}, \gamma_L \begin{pmatrix} c \\ s' \end{pmatrix}, \gamma_L \begin{pmatrix} t \\ b' \end{pmatrix} \text{ and } \psi_R = \gamma_R\ \ell^-, \gamma_R\ q \tag{2.34}$$

where the γ_L and γ_R operators were already defined in equation 2.18, ℓ stands for the charged leptons e, μ and τ, and the prime on the quark doublets is related to the CKM matrix explained

[7] The right-handed neutrino is not explicitly forbidden but it would not interact with any of the other particles, except the Higgs boson if ν_R is a Dirac spinor.

below. The Lagrangian that describes the fermion interactions with the gauge bosons can then be written as

$$\mathcal{L}_{\text{fermions}} = \overline{\psi}_L i \not{D} \psi_L + \overline{\psi}_R i \not{D} \psi_R \tag{2.35}$$

with the correct use of hypercharge, either Y_L or Y_R, in the covariant derivative. The middle term in equation 2.22 vanishes for right-handed fields as their isospin is 0. The boson-fermion coupling strengths are

$$g_{\gamma ff} = eQ \tag{2.36}$$

$$g_{Wff} = \frac{g}{2\sqrt{2}}(1 - \gamma^5) \tag{2.37}$$

$$g_{Zff} = \frac{g}{2\cos\theta_w}(c_V - c_A\gamma^5) \tag{2.38}$$

where $c_V = T_3 - 2Q\sin^2\theta_w$ and $c_A = T_3$. Following this, the weak interaction does not conserve parity as there are vector-like terms ($\propto \gamma^\mu$) added to axial-like terms ($\propto \gamma^\mu\gamma^5$).

Lastly, the Yukawa term generates the fermion masses after the Higgs acquires a vacuum expectation value. Ordinary mass terms cannot simply be introduced into the Lagrangian because the left- and right-handed components of the fermion fields have different quantum numbers and would violate gauge invariance. However, the hypercharge difference between the left- and right-handed fermions of a certain flavour will always be ± 1, which is, as mentioned earlier, the hypercharge of the Higgs field. The following gauge invariant Lagrangian can be written down

$$\mathcal{L}_{\text{Yukawa}} = -g_e \bar{E}_L \phi g_R - g_d \bar{Q}_L \phi d_R - g_u \bar{Q}_L \phi^c u_R + h.c. \tag{2.39}$$

where the g_f's ($g_e, \ldots$) are the Yukawa couplings listed in table 2.5 [16], $\phi^c = i\sigma_2\phi^\dagger$ and the Q_L are the quark doublets defined in equation 2.34. To generalise, a Yukawa interaction of the form $g_f\bar{\psi}_f\phi\psi_f$ generates a fermion mass through SSB equal to

$$m_f = g_f v/\sqrt{2}. \tag{2.40}$$

y_e	3×10^{-6}	y_μ	6×10^{-4}	y_τ	1×10^{-2}
y_u	2×10^{-5}	y_c	9×10^{-3}	y_t	1
y_d	4×10^{-5}	y_s	8×10^{-4}	y_b	3×10^{-2}

Table 2.5: Yukawa couplings.

In equation 2.34, the down-type quarks were denoted with a prime in the quark doublets. This is related to the fact that there is more than one quark generation and therefore there can be extra coupling terms that mix generations. Hence, it does not make sense to discuss the probability of an u type quark coupling to a single d type quark but rather of the physical eigenstates that are linear superposition of d, s and b quarks with coefficients determined by the 3×3 Cabibbo-Kobayashi-Maskawa (CKM) mixing matrix defined as

$$\begin{pmatrix} d' \\ s' \\ b' \end{pmatrix} = \begin{pmatrix} V_{ud} & V_{us} & V_{ub} \\ V_{cd} & V_{cs} & V_{cb} \\ V_{td} & V_{ts} & V_{tb} \end{pmatrix} \begin{pmatrix} d \\ s \\ b \end{pmatrix}. \tag{2.41}$$

The most precise values of the CKM matrix components [32] currently available from flavour physics measurements are

$$V_{\mathrm{CKM}} = \begin{pmatrix} 0.97427 \pm 0.00015 & 0.22534 \pm 0.00065 & 0.00351^{+0.00015}_{-0.00014} \\ 0.22520 \pm 0.00065 & 0.97344 \pm 0.00016 & 0.0412^{+0.0011}_{-0.0005} \\ 0.00867^{+0.00029}_{-0.00031} & 0.0404^{+0.0011}_{-0.0005} & 0.999146^{+0.000021}_{-0.000046} \end{pmatrix}. \tag{2.42}$$

Chapter 3

Diboson Production

Diboson production allows a direct and precise measurement of gauge boson couplings, which is crucial for verifying the SU(2)×U(1) electroweak gauge structure. Additionally, a thorough understanding of diboson production is indispensable as it is an irreducible background for many Higgs and New Physics (NP) searches [37]. The discovery of a Higgs-like boson was announced in July 2012 with a mass of approximately 126 GeV. This implies that a significant fraction of Higgs events will decay to W^+W^- and ZZ pairs [38]. Furthermore, if a charged Higgs exists, many models predict its decay to $W^\pm Z$ pairs [39, 40] and the latter were shown to be an important background for W^+W^- scattering [41, 42]. In general, final states with three or more leptons and missing energy are common in many NP models that aim to reproduce SM predictions at lower energies, such as supersymmetry (SUSY) [43], technicolor [44], extra vector bosons [45] or extra dimensions [46].

This chapter first explains the origin, and further gives a detailed description, of electroweak gauge boson self-coupling vertices, then defines the concept of anomalous gauge boson couplings in an effective Lagrangian framework and lastly presents an overview of the available theoretical calculations, Monte Carlo (MC) implementations and experimental measurements of $W^\pm Z$ production, in light of the analysis described in chapter 8 of this thesis.

3.1 Gauge Boson Couplings

The non-Abelian nature of the SU(2)×U(1) electroweak gauge group requires the existence of triple (TGC) and quartic gauge couplings (QGC), which are vertices in which three or four electroweak gauge bosons couple to each other as shown in figure 3.1, just like the gluon self-coupling vertices in QCD. The exact form of the TGC and QGC specific terms in the Lagrangian are completely defined by the gauge structure and can be derived from equation 2.14. As established in the previous section, one massless and three massive electroweak gauge bosons remain after spontaneous symmetry breaking. However, due to certain symmetries and conservation laws not every combination of these bosons is allowed.

Focusing on TGCs, charge has to be conserved at a vertex which rules out four of the ten combinations. Photons cannot couple to each other because the U(1) group is Abelian, hence $\gamma\gamma\gamma$ and $Z\gamma\gamma$ vertices are ruled out. The reason why ZZZ and $ZZ\gamma$ vertices are not allowed in the SM can be explained by inspecting equation 2.15. The fully antisymmetric

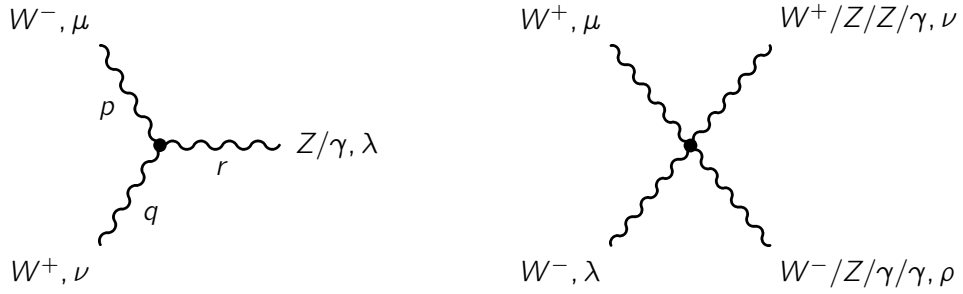

Figure 3.1: Triple (left) and quartic (right) electroweak gauge boson coupling vertices allowed in the Standard Model.

tensor ϵ^{ijk} will only allow a TGC vertex of the form $W^1W^2W^3$. Equations 2.27 – 2.29 showed that W^1 and W^2 make up the $W^\pm$ bosons and W^3 contributes to forming the Z or γ bosons. Therefore, the only possible TGC components are W^+W^-Z and $W^+W^-\gamma$. Similarly, the only allowed QGC vertex components are $W^iW^jW^iW^j$, where $i, j = 1, 2, 3$ and $i \neq j$, which explicitly means that only the combinations $W^+W^-W^+W^-$, W^+W^-ZZ, $W^+W^-Z\gamma$ and $W^+W^-\gamma\gamma$ are allowed. Picking out the terms that give an interaction of three fields from the expansion of equation 2.14 and reordering the fields so that they are expressed as a function of fields after SSB, meaning as a function of W^+, W^-, Z and A fields, the TGC Lagrangian corresponds to

$$\begin{aligned}\mathcal{L}_{TGC} = & ig_{WW\gamma}\left[A_\mu(W^-_\nu W^{+\mu\nu} - W^+_\nu W^{-\mu\nu}) + W^-_\mu W^+_\nu A^{\mu\nu}\right] \\ & + ig_{WWZ}\left[Z_\mu(W^-_\nu W^{+\mu\nu} - W^+_\nu W^{-\mu\nu}) + W^-_\mu W^+_\nu Z^{\mu\nu}\right]\end{aligned} \tag{3.1}$$

where the field tensor is now just $X_{\mu\nu} = \partial_\mu X_\nu - \partial_\nu X_\mu$ and the coupling strengths are

$$\begin{aligned}g_{WW\gamma} &= g\sin\theta_w = e \\ g_{WWZ} &= g\cos\theta_w = e\cot\theta_w.\end{aligned} \tag{3.2}$$

The Feynman rule for such vertices is given by

$$ig_{WWV}[(p-q)_\lambda g_{\mu\nu} + (q-r)_\mu g_{\nu\lambda} + (r-p)_\nu g_{\lambda\mu}] \tag{3.3}$$

where $V = Z$ or γ and all the momenta in figure 3.1 are assumed to be incoming [16]. In proton-proton collisions, these TGCs can appear in the so-called s-channel diagrams, which at leading order (LO) give the process $q\bar{q} \to V^* \to VV$. Experimentally, the measurement of W^+W^-, $W^\pm Z$ and $W^\pm\gamma$ production will probe the allowed W^+W^-Z and $W^+W^-\gamma$ TGC vertices mentioned earlier, whereas ZZ and $Z\gamma$ production will probe TGCs that are forbidden in the SM and which will not be discussed here further[1].

[1]Theoretical and experimental information about the SM forbidden TGCs can be found in references [47,48]. Even out of the allowed TGC vertices, the focus here will be on the WWZ vertex involved in $W^\pm Z$ production. A further motivation for this choice is that the $WW\gamma$ vertex has the only form it could have if QED is assumed to be correct and the W boson is assumed to be a point like vector boson.

The QGC Lagrangian can be derived in a similar manner and be written as

$$\begin{aligned}\mathcal{L}_{QGC} = &\frac{g_{WWWW}}{2}\left[W^{-\mu}W^{+\nu}W^{-}_{\mu}W^{+}_{\nu} - \left(W^{-\mu}W^{+}_{\mu}\right)^2\right] \\ &+ g_{WWZZ}\left[Z^{\mu}Z^{\nu}W^{-}_{\mu}W^{+}_{\nu} - Z^{\mu}Z_{\mu}W^{-\nu}W^{+}_{\nu}\right] \\ &+ g_{WWZ\gamma}\left[A^{\mu}Z^{\nu}(W^{-}_{\mu}W^{+}_{\nu} + W^{+}_{\mu}W^{-}_{\nu}) - 2A^{\mu}Z_{\mu}W^{-\nu}W^{+}_{\nu}\right] \\ &+ g_{WW\gamma\gamma}\left[A^{\mu}A^{\nu}W^{-}_{\mu}W^{+}_{\nu} - A^{\mu}A_{\mu}W^{-\nu}W^{+}_{\nu}\right] \end{aligned} \tag{3.4}$$

where the coupling strengths for the four different allowed combinations are

$$\begin{aligned} g_{WWWW} &= g^2 \\ g_{WWZZ} &= g^2\cos^2\theta_w \\ g_{WWZ\gamma} &= g^2\sin\theta_w\cos\theta_w \\ g_{WW\gamma\gamma} &= g^2\sin^2\theta_w = e^2. \end{aligned} \tag{3.5}$$

The Feynman rule for QGCs is given by

$$\pm i g_{WWVV}\left[2g_{\mu\nu}g_{\lambda\rho} - g_{\mu\lambda}g_{\nu\rho} - g_{\mu\rho}g_{\nu\lambda}\right] \tag{3.6}$$

where the + sign only applies for the $W^+W^-W^+W^-$ vertex and the − sign for the other three possibilities. It should be noted that the TGC Feynman rule has a gauge boson momentum dependence, which will be scrutinised more in the following section, whereas the QGC does not[2].

3.2 Anomalous Gauge Boson Couplings

The SM has been proven to be extremely successful but, despite its outstanding performance, there are a number of important questions left unanswered. To only briefly touch on a few, there is the large discrepancy between the scale of the Higgs field and the Planck scale, the difficulties of unifying gravity with the SM, the baryon asymmetry observed in the universe, the questions of why there are three fermion generations, why neutrinos have a very small mass and lastly what is dark matter [52].

It is therefore believed that the SM is only a low-energy limit of a more fundamental theory. As no unexpected observations have been made at the LHC yet, it is possible that NP exist at a higher scale but reproduce the SM predictions at currently available energies to within experimental precision.

The question is then how to look for something new while avoiding the needle in a haystack approach. This is where effective theories prove to be useful as, in absence of a specific new model, they allow one to probe for NP at a higher energy scale Λ and parametrize their low-energy effects in a generic, model-independent way by building less restrictive theories than the SM [47]. To quote Weinberg [53], "when you use quantum field theory to study low-energy phenomena, ... then you're not really making any assumption that could be wrong,

[2]QGCs will not be discussed here further but more information can be found in the literature [49–51].

unless of course Lorentz invariance or quantum mechanics . . . is wrong, provided you don't say specifically what the Lagrangian is. As long as you let it be the most general possible Lagrangian consistent with the symmetries of the theory, you're simply writing down the most general theory you could possibly write down".

An effective Lagrangian can be written in the form of an expansion of operators $\mathcal{O}_i^{(n)}$ of dimension mass^{n+4}

$$\mathcal{L}_{\text{eff}} = \sum_n \frac{1}{\Lambda^n} \sum_i \alpha_i^{(n)} \mathcal{O}_i^{(n)}. \tag{3.7}$$

This series has an infinite number of terms but they go as inverse powers of Λ. The necessary, general assumption for an effective Lagrangian to be valid is that the physics responsible for deviations is not directly observed experimentally and can only be seen through virtual effects. If this assumption does not hold, then the effective approach is not valid as the considered energies will be too close to Λ so that the terms in the expansion will all become equally important [47].

In a scenario where SU(2)×U(1) symmetry and the presence of one Higgs doublet field as the low energy degrees of freedom are assumed, the most general effective Lagrangian for a TGC vertex with two charged and one neutral vector boson, keeping only up to dimension 6 operators (which is a reasonable approximation for a large Λ), can be written as

$$\begin{aligned}\mathcal{L}_{WWV} = -g_{WWV}\Bigg[& ig_1^V \left(W_{\mu\nu}^\dagger W^\mu V^\nu - W_\mu^\dagger V_\nu W^{\mu\nu}\right) + i\kappa^V W_\mu^\dagger W_\nu V^{\mu\nu} + i\frac{\lambda^V}{m_W^2} W_{\rho\mu}^\dagger W^\mu{}_\nu V^{\nu\rho} \\ & - g_4^V W_\mu^\dagger W_\nu \left(\partial^\mu V^\nu + \partial^\nu V^\mu\right) + g_5^V \epsilon^{\mu\nu\rho\lambda} \left[W_\mu^\dagger \partial_\rho W_\nu - \partial_\rho W_\mu^\dagger W_\nu\right] V_\lambda \\ & + \frac{i}{2}\tilde{\kappa}^V W_\mu^\dagger W_\nu \epsilon^{\mu\nu\alpha\beta} V_{\alpha\beta} + \frac{i}{2}\frac{\tilde{\lambda}^V}{m_W^2} W_{\rho\mu}^\dagger W^\mu{}_\nu \epsilon^{\nu\rho\alpha\beta} V_{\alpha\beta}\Bigg]. \end{aligned} \tag{3.8}$$

The 14 different coupling parameters are listed in table 3.1 together with their SM value and their charge C, parity P and CP conserving or violating properties [47, 54].

Coupling	SM value	C	P	CP
g_1^V	1	+	+	+
κ^V	1	+	+	+
λ^V	0	+	+	+
g_4^V	0	−	+	−
g_5^V	0	−	−	+
$\tilde{\kappa}^V$	0	+	−	−
$\tilde{\lambda}^V$	0	+	−	−

Table 3.1: Properties of the 14 TGC parameters.

It can be seen that at tree level in the SM, only the terms in $g_1^Z = g_1^\gamma = 1$ and $\kappa^Z = \kappa^\gamma = 1$ will survive, with all other couplings vanishing. Together, these parameters offer various ways to search for C, P and/or CP violation. Assuming no CP violation, g_1^V, κ^V and λ^V also conserve C and P separately while g_5^V does not. CP violation in gauge-boson

interactions can be probed by the g_4^V, $\tilde{\kappa}^V$ and $\tilde{\lambda}^V$ parameters[3]. It should be noted that a low energy approximation is realised by neglecting higher order (dim > 6) operators [55].

For the results presented here, only terms that separately conserve C and P are kept. This eliminates the second and third line of equation 3.8 and the Lagrangian reduces to[4] [57]

$$\mathcal{L}_{WWV} = -ig_{WWV}\left[g_1^V(W^\dagger_{\mu\nu}W^\mu - W^{\dagger\mu}W_{\mu\nu})V^\nu + \kappa^V W^\dagger_\mu W_\nu V^{\mu\nu} + \frac{\lambda^V}{m_W^2}W^\dagger_{\rho\mu}W^\mu_\nu V^{\nu\rho}\right]. \tag{3.9}$$

The anomalous triple gauge coupling (aTGC) parameters of interest in this analysis can be defined as the deviation from their SM values as

$$\Delta g_1^V = g_1^V - 1 \tag{3.10}$$

$$\Delta\kappa^V = \kappa^V - 1 \tag{3.11}$$

$$\lambda^V. \tag{3.12}$$

From dimensional analysis, it can seen that to balance the dim $= 4$ Lagrangian on the LHS of equation 3.9, the aTGC parameters on the RHS must be dimensionless coefficients that multiply dim $= 4, 4$ and 6 operators for g_1^V, κ^V and λ^V, respectively. If further EM invariance and SU(2)×U(1) symmetry are required, the following conditions have to hold [58, 59]

$$g_1^\gamma = 1 \tag{3.13}$$

$$\Delta\kappa^Z = -\Delta\kappa^\gamma \tan^2\theta_w + \Delta g_1^Z \tag{3.14}$$

$$\lambda^Z = \lambda^\gamma = \lambda. \tag{3.15}$$

This reduces the problem down to three free parameters for the WWZ vertex, g_1^Z, κ^Z and λ^Z. The κ^γ and λ^γ parameters for the $WW\gamma$ vertex can be deduced from equations 3.14–3.15.

It is interesting to note that the $\hat{s}$, which is equivalent to the invariant diboson mass squared, dependence of the terms of the Lagrangian in equation 3.9 is process dependent. The exact proportionality is shown in table 3.2 [60]. This explains why the experimental limits on $\Delta\kappa^Z$ from a measurement of $W^\pm Z$ production will be less stringent than those on Δg_1^Z or λ^Z. To get a rough feeling for the size of these anomalous couplings and the existing constraints from "low-energy" measurements, the limits from different experiments will be presented in section 3.3.

aTGCs give rise to deviations from the SM prediction that grow with energy and will therefore eventually lead to unitarity violation. Limits on partial-wave amplitudes allow one to set stringent unitarity bounds for $W^\pm Z$ production

$$\gamma^2|g_1^Z - 1| < 29 \tag{3.16}$$

$$\gamma|\kappa^Z - 1| < 58 \tag{3.17}$$

$$\gamma^2|\lambda^Z| < 29 \tag{3.18}$$

[3] Sensitivity to CP violation and ways to test for it are discussed in references [55, 56].

[4] For the $V = \gamma$ case, there is a directly graspable physical meaning attached to the terms in equation 3.9. They correspond to the lowest order terms of W bosons coupling to a photon, they are the charge $Q_W = eg_1^\gamma$, the magnetic dipole moment $\mu_W = \frac{e}{2m_W}(g_1^\gamma + \kappa_\gamma + \lambda_\gamma)$ and the electric quadrupole moment $q_W = -\frac{e}{m_W^2}(\kappa_\gamma - \lambda_\gamma)$ of the W boson [55].

Coupling	W^+W^-	$W^\pm Z$
Δg_1^Z	$\sqrt{\hat{s}}$	$\hat{s}$
$\Delta\kappa^Z$	$\hat{s}$	$\sqrt{\hat{s}}$
λ^Z	$\hat{s}$	$\hat{s}$

Table 3.2: Dependence of terms in anomalous coupling parameters on $\hat{s}$ for the W^+W^- and $W^\pm Z$ processes.

where $\gamma^2 \approx \hat{s}/4m_W^2 \approx \hat{s}/4m_Z^2$ [61]. These bounds assume that there is only one aTGC and all others take their SM values. If more than one coupling deviates, then cancellations between the different aTGCs can occur and the unitarity bounds are weakened [62]. To avoid this tree-level unitarity violation, that is to avoid amplitudes for diboson production that grow with increasing energy, either the NP spectrum at high energies needs to be known to define a new Lagrangian or the anomalous couplings must be forced to vanish as $\sqrt{\hat{s}} \to \infty$. To achieve such a cutoff, an arbitrary form factor is often introduced according to

$$\alpha(\hat{s}) = \frac{\alpha_0}{(1 + \hat{s}/\Lambda^2)^n} \tag{3.19}$$

where α stands for Δg_1^Z, $\Delta\kappa^Z$ or λ^Z and α_0 is the value of the anomalous coupling at low energy. It should be noted that the analytical form of this cutoff is not unique and one could have made a different choice, for example a simple step function. Further discussion on form factors can be found in reference [47]. For the form chosen in equation 3.19, the smallest value of n that is compatible with unitarity is typically chosen, so that the denominator has at least the same $\hat{s}$ dependence as the numerator [61]. A frequent convention is to choose $n = 2$ to get a dipole form factor and Λ equal or close to 2 TeV [47, 58–60, 63–65]. This new effective Lagrangian is only a consistent theory if the radiative corrections are smaller than the tree-level contributions. The failure to satisfy this condition means that the fields involved in this new model do not have corresponding degrees of freedom in the low-energy limit [47, 66]. To avoid unitarity violation at high centre of mass energies, the unitarization method described above can be used in experimental measurements. However, one has to be careful with introducing form factors. Not introducing them can lead to unphysically large cross sections which in turn lead to an overestimation of the experimental sensitivity. However, if NP happen to be present at or around a chosen cutoff scale Λ, the form factor will dampen out aTGC contributions at this point. Much discussion within the LHC Electroweak Working Group has gone into this but without a clear consensus [67, 68]. For this reason, the measurement presented here will quote aTGC limits with and without a form factor.

Naturally the question arises what effect these aTGCs will have on measured physical quantities and how their presence can be detected or ruled out. The $\hat{s}$ dependence of aTGCs mentioned earlier translates into a modification of any observable that depends on $\hat{s}$ [64]. Examples are the production rate, i.e. the cross section, the diboson invariant or transverse mass or the leading lepton transverse momentum p_T, in case of leptonic boson decays. The general trend is that the presence of aTGCs will increase the number of events observed in the high energy tails, though it can also decrease it. More specifically, the cross section will

have a quadratic dependence on aTGCs since the amplitudes in the matrix element calculation have a linear aTGC dependence. This will be explained in more detail in section 8.12.3. In particular for $W^{\pm}Z$ production, the cross section depends very little on the sign of λ^Z and $\Delta\kappa^Z$, but significantly on the sign of Δg_1^Z [64]. Additionally, the terms in the Lagrangian in equation 3.9 containing a derivative will depend on the gauge boson momenta. The p_{T} of the Z boson is a particularly interesting distribution as it is ideal not only phenomenologically but also experimentally. It shows a sizeable yield increase in the high tail and a shape difference in the low tail depending on the sign of the aTGC, which is not given for all observables, and it is reasonably easy to measure experimentally. Angular distributions are more challenging to measure but also exhibit features that help discriminate between aTGC parameters. Most notably, distributions include boson or lepton rapidities and lepton decay angles, the latter being sensitive to spin information. aTGCs will enhance the distributions at large scattering angles of the outgoing bosons [69]. A compelling feature of $W^{\pm}Z$ production is the so-called approximate radiation zero for tree-level $q\bar{q}$ production at $\cos\theta \approx \pm 0.1$, where θ is the scattering angle of the Z boson with respect to the quark direction in the partonic centre of mass frame [64, 70]. In the SM, this dip, which leads to an observable dip in the Z boson centre of mass rapidity distribution, is caused by gauge cancellations. However, the presence of aTGCs spoils these cancellations and the dip is obscured. Actual distributions for different aTGC parameters will be shown in the following chapter and in chapter 8.

At current LHC centre of mass energies of $\sqrt{s} = 7$ or 8 TeV, NLO QCD corrections can be significant due to the increased gluon flux compared to for example the Tevatron. For the $W^{\pm}Z$ process, they are around 75%, with W^-Z, whose cross section is about 30% smaller than W^+Z at a p-p collider, experiencing a slightly larger increase than W^+Z due to PDFs [71]. However, for non-SM couplings these corrections are more modest. This can be seen particularly well in the shape of the Z boson p_{T} distribution, which is very strongly affected by $\mathcal{O}(\alpha_s)$ corrections. They can be up to a factor of five for $\sqrt{s} = 14$ TeV in the SM but less so for aTGCs, where they are only between 20%-40%. The quoted numbers apply for the inclusive cross section, a separate inspection needs to be performed for exclusive cross sections [64].

The influence of higher order EW corrections on diboson production has been studied widely [69, 72]. References show that these $\mathcal{O}(\alpha)$ corrections affect the same phase space region as aTGCs, namely large partonic centre of mass energies and large boson scattering angles. $\mathcal{O}(\alpha)$ corrections can decrease the LO differential cross section by up to 10%, 15% and 20% for $W^{\pm}Z$, W^+W^- and ZZ production, respectively [73].

3.3 $W^{\pm}Z$ Production

3.3.1 Theory

The LO $W^{\pm}Z$ production cross section at hadron colliders was first calculated in 1979 [74]. However, with the important gluon PDF contribution at the LHC, it is crucial to have a NLO QCD calculation. Boson pair production in association with jets was first considered in 1989 [75] and the first full $\mathcal{O}(\alpha_s)$ analytical calculation of production was published in the early 90s by two different groups [76, 77]. In 1999, the results were improved by $\mathcal{O}(\alpha_s)$

calculation using helicity amplitudes including leptonic decays of the massive bosons with conservation of spin correlation information [58, 78]. The same year followed the implementation into the parton-level Monte Carlo program `MCFM` [79]. This work includes a beyond zero-width approximation for the boson masses, singly resonant diagrams and interference effects between Z^* and γ^* propagators. The result was updated recently to include aTGCs [71]. The release of the event generator MC@NLO 4.0 [80] in 2010 allowed the incorporation of NLO matrix elements into a parton shower framework. Boson widths, full spin correlations and event-by-event reweighting for any aTGC parameters are included, however the γ^* contribution is not. Also in 2010, a NLO implementation into the Herwig++ event generator using the POWHEG method [81], an alternative parton shower matching generator to MC@NLO, was published [82, 83]. However, aTGCs and γ^* interference were not included. Finally, at the end of 2011, an accumulation of all things good was released. Diboson production is available in the `POWHEG BOX`, a general computer program for implementing NLO calculations in shower MC programs using the POWHEG method, which has all the same features as MCFM but in a parton showering framework [84].

3.3.2 Experiment

$W^{\pm}Z$ production was first observed at the Tevatron. CDF and DØ have both made measurements of its production cross section and have set limits on anomalous triple gauge boson couplings using fully- and semi-leptonic $W^{\pm}Z$ final states. Whilst the cross section results cannot be directly compared to the ones presented here as the Tevatron was a p-$\bar{p}$ collider running at $\sqrt{s} = 1.96$ TeV, it is still instructive to quote the results to get an idea of the precision of the measurements. The latest CDF measurement [85] for $W^{\pm}Z \to \ell^{\pm}\nu\ell^{+}\ell^{-}$ production used 7.1 fb^{-1} of data. They found 63 candidates with an expected background of 8 ± 1 events. The measured total production cross section is $\sigma = 3.93^{+0.60}_{-0.53}(\text{stat})^{+0.59}_{-0.46}(\text{syst})$ pb, in agreement with the SM NLO prediction of 3.50 ± 0.21 pb. The aTGC limits were derived using the p_{T} spectrum of the Z boson, a dipole form factor and $\Lambda = 1.5$ and 2 TeV cut-off values. DØ measured the $W^{\pm}Z$ production cross section in the fully leptonic final state using 4.1 fb^{-1} of data [86]. They found 34 candidates with 6.0 ± 0.6 expected background events which leads to a measured total cross section of $\sigma = 3.90^{+1.06}_{-0.90}$ pb. This is again in good agreement with the SM NLO prediction which DØ quotes as 3.25 ± 0.19 pb. They also used the Z boson p_{T} distribution to set aTGC limits. The limits from both of these measurements are summarised in table 3.3 and will be quoted again later to compare against the limits derived in the analysis presented in this thesis. DØ has since released a new result using 8.6 fb^{-1} of data and combining different final states [87]. Overall, these are the best limits available, whereas the ATLAS limits presented here are the most stringent using only $W^{\pm}Z \to \ell^{\pm}\nu\ell^{+}\ell^{-}$ production.

There is no direct $W^{\pm}Z$ measurement from LEP since it, as an $e^{+}e^{-}$ collider, could only produce neutral final states. There are hence only indirect limits on the WWZ vertex from WW production [88].

Finally, quoting some results from the LHC era, CMS [89] has released a $W^{\pm}Z$ cross section measurement using 1.09 fb^{-1} of $\sqrt{s} = 7$ TeV data with 75 observed candidate events[5].

[5] The total number of expected background events is not explicitly given.

The total measured cross section is stated to be $\sigma = 17.0 \pm 2.4(\text{stat}) \pm 1.1(\text{syst}) \pm 1.0(\text{lumi})$ pb, in agreement with the "theoretical NLO prediction of 19.790 ± 0.088" . CMS has only published indirect aTGC limits on the WWZ vertex, firstly using the leading lepton p_{T} distribution in WW production with 36 pb^{-1} of data [90] and more recently using the dijet p_{T} distribution in $WW/WZ \to \ell\nu jj$ production with 5 fb^{-1} of data [91]. ATLAS [92] has also produced a cross section measurement using 1.02 fb^{-1} of data and set aTGC limits. 71 candidates were observed with $12.1 \pm 1.4(\text{stat})^{+4.1}_{-2.0}(\text{syst})$ expected background events. The total measured cross section derived from this data is $\sigma = 20.5^{+3.1}_{-2.8}(\text{stat})^{+1.4}_{-1.3}(\text{syst})^{+0.9}_{-0.8}(\text{lumi})$ pb. aTGC limits derived using the number of events observed in each channel are quoted in table 3.3. This measurement is superseded by the one discussed in this thesis.

Experiment	Δg_1^Z	$\Delta\kappa^Z$	λ^Z
CDF [85]	[-0.08, 0.20]	[-0.39, 0.90]	[-0.08, 0.10]
DØ [86]	[-0.053, 0.156]	[-0.376, 0.686]	[-0.075, 0.093]
ATLAS [92]	[-0.16, 0.24]	[-0.8, 1.0]	[-0.14, 0.14]

Table 3.3: Observed aTGC limits from direct $W^{\pm}Z \to \ell^{\pm}\nu\ell^{+}\ell^{-}$ production at the 95% C.L.. The Tevatron limits use $\Lambda = 2$ TeV, LHC limits use $\Lambda = \infty$. Only a single parameter is varied at a time with the other parameters fixed to their SM value.

Chapter 4

Monte Carlo Implementation

This chapter will present the phenomenology work carried out during the first year of the Ph.D. It will cover the implementation of aTGC vertices for heavy diboson production into the Herwig++ event generator, which will first be described. The project is organised into two main parts, the LO implementation through the addition of anomalous Feynman rules into the generator and the NLO implementation using the POWHEG method, which will also be explained in detail. Finally, the results are presented in distributions of relevant observables for different aTGC parameters.

4.1 Herwig++

The event simulation is done with Herwig++ [93], a general-purpose Monte Carlo event generator for **H**adron **E**mission **R**eactions **W**ith **I**nterfering **G**luons that builds on ThePEG [94], a **T**oolkit for **H**igh **E**nergy **P**hysics **E**vent **G**eneration. The simulation of a process can be visualized best by breaking the generation up into several "bottom-up" stages.

1. *Hard process*: Partons (quarks or gluons) from the colliding hadrons (protons in this case) interact to produce the main outgoing particles. Parton level cross sections at LO or NLO are calculated using perturbative QCD and, combined with PDFs, give the total cross section.

2. *Initial and Final State QCD radiation* (ISR, FSR): Initial state refers to radiation from partons on their way into the hard collision, final state to radiation from partons produced in the collision. ISR and FSR are simulated via an angular ordered parton shower. The colour flow of the hard process is carefully traced so that coherent emission from soft gluons produced in the parton shower is ensured.

3. *Underlying event*: Even though the partons involved in the hard process have been taken care of, there are still remnants of the incoming hadrons left. The underlying event encompasses everything except the hard process and its associated parton shower. It is analysed using the eikonal scattering model [95] to treat multiple partonic scatterings. The important argument here is that the probability of partons interacting at a certain point is assumed to be independent of the rest of the distribution. For soft radiation,

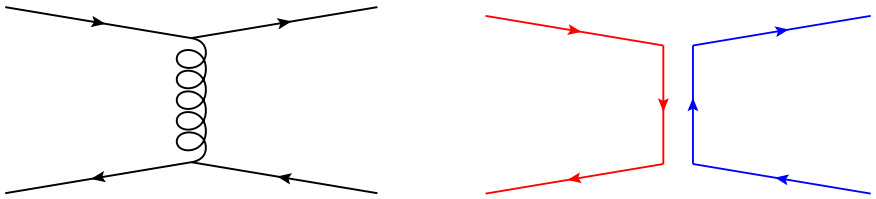

Figure 4.1: Colour flow.

even though the parton itself is only deviated by a small angle, the colour connection is "deviated" by almost 180° which induces gluon radiation all over the underlying event as accelerated charges radiate. Figure 4.1 tries to illustrate this colour connection flow of two partons crossing in the lab frame and exchanging a gluon. After this eikonal approximation the problem can be treated perturbatively and the scattering cross sections are calculated using standard PDFs.

4. *Hadronization*: All the final state coloured partons produced in the parton shower have colour partners, meaning another particle with whom they share their colour index. The cluster hadronization model [96] is used to combine these colour-anticolour pairs into colour singlets. These clusters are then decayed to hadrons[1].

5. *Hadron and heavy object decays*: Hadrons formed during the hadronization stage are decayed using matrix elements of their possible decays and spin correlation treatment between these decays. Other massive objects that might have been produced in the process usually have lifetimes shorter than the timescale of the parton shower and so they can produce additional parton showers at any point in the event generation. Herwig++ accurately accounts for this.

There are several `Handlers`[2] that go with these generation stages and they act in the following order:

1. `SubProcessHandler` generates the hard process.

2. `CascadeHandler` generates the parton shower.

3. `MultipleInteractionHandler` is technically a part of the previous `Handler`, it simulates the underlying event by generating additional hard scatters.

4. `HadronizationHandler` combines the coloured particles generated in the parton shower to form hadrons.

5. `DecayHandler` decays the hadrons produced in the previous step (and any other unstable particle for that matter).

[1] Very heavy or very light (meaning too light to make the decay into two hadrons kinematically possible) clusters are treated in a different way.

[2] Use of this specific font signals the reference to actual class names in ThePEG or Herwig++.

These `Handlers` can be switched on and off to the leisure and need of the user. For example, setting the `HadronizationHandler` to `NULL` in the input file turns off the hadronization step, which might not be needed for some analyses and which considerably minimises run time.

Herwig++ is particularly convenient for the task at hand because new models can be added by simply encoding new Feynman rules. It also allows correct treatment of spin correlations, which is important for the analysis of leptons produced from boson decays. The output of the generated events can be generated as a HepMC file [97] which stores particle data in either GenEvent or Ascii format, the latter can then be easily interfaced with analysis programs like ROOT [98]. The LO matrix elements are already present (`MEPP2VV`) and do not have to be recalculated, in fact they do not have to be touched at all as will be described in the next section. Finally, it should be noted that this analysis was done using the developer version and is not present in a released version of Herwig++.

4.2 Leading Order Implementation

The LO diagrams that are relevant for diboson production are shown in figure 4.2. The only diagram that can exhibit anomalous coupling behaviour is the s-channel diagram where three electroweak gauge bosons couple at the vertex point.

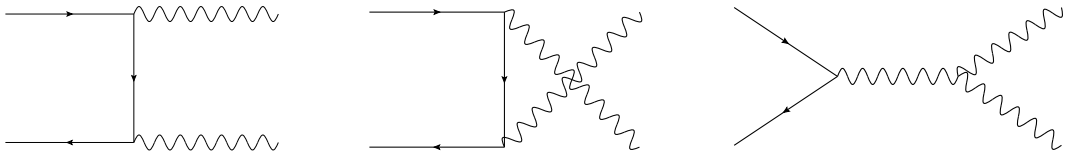

(a) t-channel (b) u-channel (c) s-channel

Figure 4.2: Leading order diagrams contributing to $q\bar{q} \to VV$ production.

The easiest way to implement this into Herwig++ is to create a new class, called `AnomalousWWWVertex` class, that replaces both the existing `VVVVertex` class in ThePEG and the `SMWWWVertex` class in Herwig++. The `VVVVertex` class is the base class that implements triple vector coupling vertices and it inherits from the underlying `AbstractVVVVertex` class which stores the allowed particles.

Before any implementation can be done, it is first necessary to compute the anomalous vertex function and relate its structure to the SM vertex function used in Herwig++. From the Lagrangian in equation 3.9 the corresponding vertex function [58] for $W_\mu^-(p)W_\nu^+(q)V_\lambda(r)$ shown in figure 3.1 can be derived

$$\begin{aligned}\frac{\Gamma^{\mu\nu\lambda}_{(p,q,r)}}{g_{WWV}} &= (g_1^V + \kappa^V + \lambda^V \frac{p^2}{m_W^2}) q^\mu g^{\nu\lambda} - (g_1^V + \kappa^V + \lambda^V \frac{q^2}{m_W^2}) p^\nu g^{\mu\lambda} \\ &\quad + \frac{\lambda^V}{m_W^2} r^\mu r^\nu (q-p)^\lambda - (g_1^V + \lambda^V \frac{r^2}{2m_W^2})(q-p)^\lambda g^{\mu\nu}. \end{aligned} \tag{4.1}$$

To recover the SM result, the SM values listed in table 3.1 need to be inserted and the vertex

function reduces to

$$\frac{\Gamma^{\mu\nu\lambda}_{(p,q,r)}}{g_{WWV}} = 2q^\mu g^{\nu\lambda} - 2p^\nu g^{\mu\lambda} - (q-p)^\lambda g^{\mu\nu}. \tag{4.2}$$

It can be seen that the third term here is exactly the first term in equation 3.3. To show that the remaining two terms are also equivalent to those in equation 3.3, the use of the momentum conservation condition $p + q + r = 0$ at the vertex and the Ward-Takahashi identity $p^\mu \epsilon_{p\mu} = p.\epsilon_p = 0$ are necessary. Applying the polarization vector to the first term in equation 4.2 gives

$$\begin{aligned} 2q^\mu \epsilon_{p\mu} g^{\nu\lambda} &= (q-p-r)^\mu \epsilon_{p\mu} g^{\nu\lambda} = (q-r)^\mu \epsilon_{p\mu} g^{\nu\lambda} \\ \Rightarrow 2q^\mu g^{\nu\lambda} &= (q-r)^\mu g^{\nu\lambda} \end{aligned}$$

and similarly for the second term in equation 3.3. This proves the complete equality of the aTGC vertex function in equation 4.1 to the SM form.

Applying the full set of polarisation vectors to equation 3.3 gives

$$\left[(p-q)^\lambda g^{\mu\nu} + (q-r)^\mu g^{\nu\lambda} + (r-p)^\nu g^{\mu\lambda}\right] \epsilon_{p\mu}\epsilon_{q\nu}\epsilon_{r\nu} \tag{4.3}$$

which is exactly the form that Herwig++ uses in the `VVVVertex` class for its standard TGC vertex calculation. This is the expression that needs to be modified so as to use the anomalous form of equation 4.1. More specifically, the vertex computation is done by introducing three `VectorWaveFunctions` that store the wavefunction and the momentum of a gauge boson so that it can be used to calculate helicity amplitudes of the matrix elements[3].

The `SMWWWVertex` class inherits from the `VVVVertex` class and, since it is designed to cover all SM allowed TGC vertices, namely WWZ and $WW\gamma$, all possible permutations in the boson order have to be included. This class also sets the correct coupling factor, e or $e\cot\theta_w$ respectively for the corresponding vertices.

These two classes are combined into a new `AnomalousWWWVertex` class that implements the aTGC vertex in equation 4.1 and contains 5 aTGC parameters, g_1^Z, g_1^γ, κ^Z, κ^γ and λ, that can be adjusted by the user in the input file by adding the following lines

```
create Herwig::AnomalousWWWVertex /Herwig/Vertices/AnomalousWWWVertex
HwAnomalousCouplings.so
set /Herwig/Model:Vertex/WWW /Herwig/Vertices/AnomalousWWWVertex
set /Herwig/Vertices/AnomalousWWWVertex:X 1
```

where `X` can be `gZ, kappaZ, lambda, gGamma or kappaGamma` and take any values from $[-10, 10]$. This new vertex class gives the same cross sections when run at SM values as the standard vertex class to a precision of 10^{-10}.

4.3 The POWHEG Method

Besides the tree-level calculation, it is important to consider contributions from higher order terms, which can become quite substantial at high energies and ignoring them would

[3] This is based on a reimplementation in C++ of the FORTRAN HELAS code [99].

give inaccurate theoretical predictions to model the LHC data. These NLO QCD corrections to the hardest emission are implemented in this analysis via the POWHEG method [81, 100], which will now be described.

Perturbative QCD (pQCD) allows one to calculate the matrix elements of all the Feynman diagrams that come into play at NLO, namely the virtual one-loop and real correction diagrams for diboson production shown in figures 4.4 and 4.5, respectively. However, to be able to make any exclusive predictions, Shower Monte Carlo (SMC) are used to perform a resummation of an infinite class of Feynman diagrams in a finite logarithmic order approximation to cancel all collinear (small angle) and soft (low energy) divergences. This is exactly what the POWHEG method does, it allows one to combine the advantages of NLO QCD calculations of the hard emission with leading logarithmic (LL) accuracy of SMC algorithms to give exclusive final states with NLO precision. To briefly explain the acronym, POWHEG, a **Po**sitive **W**eight **H**ardest **E**mission **G**enerator, has several convenient features that will be listed here and subsequently discussed.

1. It only generates events with *positive* weights,
2. it is *independent* of the SMC used subsequently,
3. it generates the hardest (with the largest p_{T}) emission *first*,
4. it uses the concept of *vetoed* and *truncated* showers to correctly treat soft coherent radiation. The latter is only needed if an angular ordered shower, like HERWIG or Herwig++ is used.

In general the NLO differential cross section can be written as

$$d\sigma_{NLO} = [B(v) + V(v)]d\Phi_v + [R(r,v) - C(v,r)\mathrm{P}]d\Phi_v d\Phi_r \tag{4.4}$$

where B are Born, V virtual, R real and C counterterm contributions. A Born final state has variables $v_1 ... v_l$ and a real emission final state has $v_1 ... v_l$ and r_1, r_2, r_3 variables, where the latter describe the additional radiated parton. P is an infrared (IR) and collinear insensitive projection operator whose action can essentially be summarised by $\mathrm{P}\{v_1 ... v_l, r_1, r_2, r_3\} \rightarrow \{v_1 ... v_l\}$. In other words, in the case of one soft parton, the projected configuration can be recovered from the full configuration through the removal of the former whereas, in the case of two collinear partons, the projected configuration is obtained by merging the latter two. The term $d\Phi_v d\Phi_r$ represents the Born and radiation phase space. Equation 4.4 can be rewritten in a more convenient way as

$$d\sigma_{NLO} = [V(v) + (R(v,r) - C(v,r))d\Phi_r \mathrm{P}]d\Phi_v + B(v)d\Phi_v \left[1 + \frac{R(v,r)}{B(v)}(1 - \mathrm{P})d\Phi_r\right] \tag{4.5}$$

where the last term in the square brackets is obtained by expanding up to $\mathcal{O}(\alpha_s)$ the sum of modified Sudakov form factors and using the projector properties described above

$$\Delta_R^{NLO}(0) + \Delta_R^{NLO}(p_{\mathrm{T}})\frac{R(v,r)}{B(v)}d\Phi_r. \tag{4.6}$$

The Sudakov form factor, at next-to-leading logarithmic (NLL) accuracy, is more specifically written as

$$\Delta_R^{NLO}(p_T) = \exp[-\int d\Phi_r \frac{R(v,r)}{B(v)}\theta(k_T(v,r) - p_T)] \tag{4.7}$$

where k_T is the transverse momentum of the radiated parton and θ is the step function. Collecting results from equations 4.5 – 4.7, the NLO cross section of the hardest emission can be expressed as

$$d\sigma_{NLO} = \bar{B}(v)d\Phi_v[\Delta_R^{NLO}(0) + \Delta_R^{NLO}(p_T)\frac{R(v,r)}{B(v)}d\Phi_r]. \tag{4.8}$$

The new function $\bar{B}$ introduced here is an important quantity in a POWHEG implementation because it ensures the generation of purely positively weighted events. It is defined as

$$\bar{B}(v) = B(v) + V(v) + \int (R(v,r) - C(v,r))d\Phi_r > 0. \tag{4.9}$$

$\bar{B}$ can only be negative if NLO terms are bigger than LO terms but in such a case perturbation theory no longer holds. It should be noted that the virtual and real terms are separately infinite (divergent) but their sum is finite. Technically, this is not the whole truth yet, because as it stands, the integral on the RHS of equation 4.9 is three-dimensional and one integration for every Born variable v is needed. There is a clever way to circumvent this problem by rewriting $\bar{B}$ as follows

$$\tilde{B}(v,r) = N[B(v) + V(v)] + R(v,r) - C(v,r) \tag{4.10}$$

where $N = \frac{1}{\int d\Phi_r}$ and consequently $\bar{B}(v) = \int \tilde{B}(v,r)d\Phi_r$. In this way it is possible to generate unweighted Born v and radiation r variables (using for example [101]) and then discard the radiation values, which is essentially the same as actually performing the $d\Phi_r$ integration.

It will now be explained how the hardest emission is generated first. In an angular-ordered shower[4] (AOS) the emission with the largest p_T is along the "hardest line", which is the one with the largest fraction z of the original incoming energy E. This is what is called the hardest emission and the aim is now to generate this emission first (which is not naturally given). Once the hardest emission is generated all subsequent emissions with a p_T greater than the p_T of the hardest emission are vetoed and the partons that are closest to each other in terms of p_T are paired up. To ensure that large angle, soft coherent radiation is introduced correctly, a so-called truncated shower is needed that stops at the angle of the hardest emission. In figure 4.3, this angle is represented as θ and partons 3 and 4 form the aforementioned "nearest in p_T"-pair. These partons are now showered from their separation angle θ to the cutoff, which is a lower bound to avoid collinear divergences, whereas parton 1 is showered from the biggest possible angle to the cutoff. Hence the truncated shower reintroduces soft radiation from partons 3 and 4 at angles larger than θ. The cutoff is needed because soft, collinear emission is infinitely likely and indistinguishable from non-emission. Several variables could be used for the cutoff but one in p_T is especially convenient for two

[4] It is beyond the scope of this thesis to completely review angular ordered shower Monte Carlos but details can be found for example in [81] or [93].

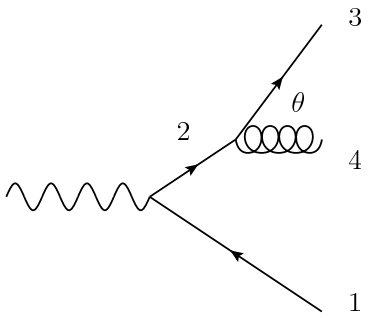

Figure 4.3: Diagram illustrating the truncated shower.

reasons: it cuts off both soft and collinear limits and $\alpha_s(p_T)$ is prevented from diverging. The cutoff is introduced at $p_T = \sqrt{t_0}/4$, where t_0 is the smallest $t = E^2\theta^2$ for which a branching can happen, E is the energy of the initial particle. The probability of a certain branching or split to happen is given by

$$dP = \frac{\alpha_s(p_T)}{2\pi}\hat{P}_{ij}(z)\frac{dt}{t}dz \tag{4.11}$$

where $\hat{P}$ is the unregularized Altarelli-Parisi splitting function. So by introducing a cutoff in p_T the argument of α_s is ensured to not be too small.

Finally, it should be noted that the POWHEG method generally agrees better with the next-to-next-to-leading order calculation than exact NLO calculations, like MC@NLO, because from the $\frac{R(v,r)}{B(v)}$ term in equation 4.8 it can seen that the differential cross section can be approximated as follows

$$\lim_{p_T\to\infty} d\sigma_{NLO} \approx \frac{\bar{B}(v)}{B(v)}R(v,r)d\Phi_v d\Phi_r = \{1 + f(\alpha_s)\}R(\Phi_{m+1})d\Phi_{m+1}. \tag{4.12}$$

assuming that the Born and virtual terms generate m body events and $f(\alpha_s)$ is the higher order k-factor.

4.4 Next-to-leading Order Implementation

Before explaining the NLO POWHEG implementation in more detail, the focus will first be on visualising all the relevant Feynman diagrams that will contribute to massive diboson production besides the tree-level graphs. Figure 4.4 shows all types of one-loop corrections that need to be considered; there are nine diagrams in total. There are four t-channel diagrams: one propagator correction, one box diagram and two triangle diagrams as the gluon can either attach to the q or $\bar{q}$ line; the same four diagrams for the u-channel which are obtained by swapping the attachment of the bosons to the quarks; and one s-channel diagram. Diagrams with loop corrections on external incoming legs are not shown as their contributions vanish in dimensional regularization. Figure 4.5 shows a selection of the 24 diagrams that contribute to the real corrections, these have an additional gluon either in the initial or in the final state. Considering all possible combinations of ordering the gluon and the two bosons, diagrams

(a) and (b) give all eight possibilities for $q\bar{q}$ processes, diagrams (c), (d) and (g) plus their three crossed diagrams and diagrams (e) and (f) give the eight contributions to qg processes. Another eight diagrams are obtained when swapping the incoming quark for an antiquark, corresponding to initial-state $g\bar{q}$ processes. Summing all these diagrams gives $3+9+24=36$ diagrams in total that contribute to a full NLO calculation.

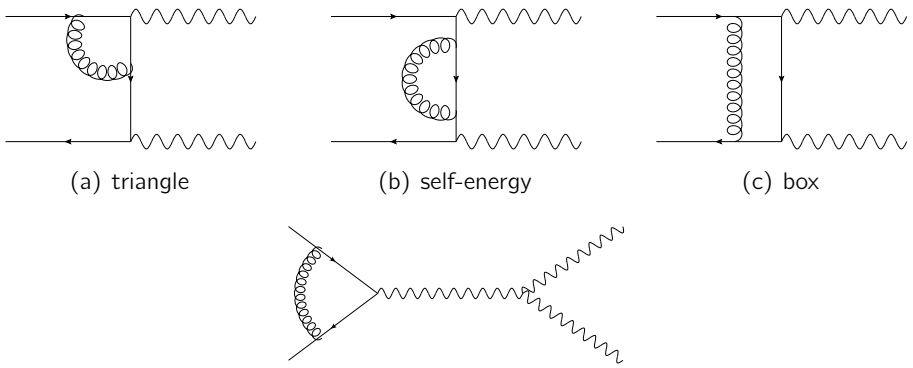

Figure 4.4: Virtual one-loop corrections.

The NLO aTGC analysis is built on the existing diboson POWHEG implementation in Herwig++ [82, 83]. The relevant class is `VVKinematics`, which encodes the two- and three-body kinematics needed for the NLO implementation and uses the same notation as references [77, 100, 102, 103] for simplicity and comparison reasons. The matrix elements are encoded in the `MEPP2VVPowheg` class which has several features that can be varied by the user. Just like for the TGC vertex class, one can choose to generate $W^{\pm}Z$, $W^{+}W^{-}$ or ZZ processes. It is possible to run at LO or NLO and one can either include all channels or choose specific channels from $q\bar{q}$, qg and $g\bar{q}$. The strong coupling constant α_s can be fixed or "running" and the same is true for electroweak and QCD factorization and renormalization scales. It is also possible to turn off the truncated shower, if need be.

An outline of the parts of the code relevant to an implementation of anomalous couplings is as follows. The modifications are relatively straightforward for LO terms and real corrections because, as well as using analytic results from aforementioned papers for testing purposes, the LO and real contributions have been independently implemented as helicity amplitudes so that spin density matrices for the decays of the boson can be calculated. The internal structure of Herwig++ then allows one to just use the new `AnomalousWWWVertex` class instead of the already present SM TGC vertex when evaluating the helicity amplitudes. It should be noted that there is a full spin correlation treatment. The main part of the code was written for $W^{\pm}Z$ production, which was then modified to calculate ZZ and $W^{+}W^{-}$ cross sections. The output from these transformations for ZZ and $W^{+}W^{-}$ production was cross checked with results from references [102] and [103], respectively. However, virtual corrections do not inherit from vertex classes as they were encoded by directly using the

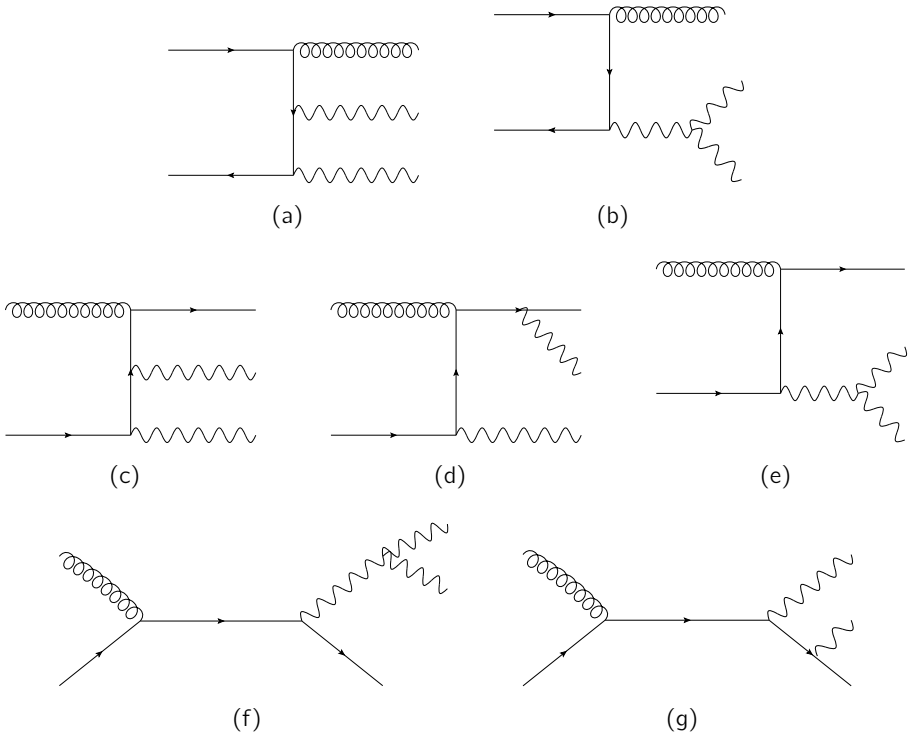

Figure 4.5: Real corrections for $q\bar{q}$, qg and $g\bar{q}$.

analytic functions[5] of reference [77]. To include anomalous couplings, the virtual corrections have to be recalculated [104].

As already mentioned and shown in figure 4.4, there are nine diagrams at the one-loop order. In general, the virtual corrections to the cross section are proportional to

$$\mathcal{M}^1 = \frac{1}{2s}\frac{1}{4N_C^2}\sum_{\text{Spin,Colour}}[\mathcal{A}^0\mathcal{A}^{1*} + \mathcal{A}^1\mathcal{A}^{0*}] \tag{4.13}$$

where the superscript 0 denotes Born amplitudes and the superscript 1 denotes one-loop amplitudes. For an anomalous coupling analysis, only interferences that contain either a tree-level or a one-loop s-channel are of interest. All the other purely t- or u-channel interferences remain unchanged. The one-loop corrections to the cross section involving either LO or one-loop s-channel diagrams can be split up into three terms:

- a term with one-loop s-channel and LO s-channel interferences,
- a term with one-loop s-channel and LO t-channel interferences and
- unfortunately a third term that has the one-loop t-channel interfering with the LO s-channel, which has a much more complicated structure.

These contributions are called $\mathcal{M}^1_S$, $\mathcal{M}^1_{TS}$ and $\mathcal{M}^1_{ST}$ respectively.

Calculation of $\mathcal{M}^1_S$

The aim is to show that the contribution to the cross section due to the one-loop s-channel vertex correction is proportional to the leading order s-channel amplitude squared. As already mentioned in the previous section, corrections due to gluon loops on either incoming legs, so called self-energy corrections, vanish identically in dimensional regularization. The one-loop vertex correction is shown in figure 4.6 and the Feynman rules for the relevant vertex points and propagators are annotated. The gluon propagator has a term that is proportional to $(1-\xi)\frac{k^\rho k^\sigma}{k^2}$, where $\xi = 0$ can be chosen in the Landau gauge. As is already expected from gauge invariance, it is possible to show that this part vanishes because it reduces to a term that is proportional to $\int \frac{d^D k}{(2\pi)^D}\frac{1}{k^4}$, which in turn vanishes in dimensional regularization. However the first term in the gluon propagator proportional to $g^{\rho\sigma}$ gives

$$\mathcal{A}^1_S = g_S^2\lambda_V\mu^{2\epsilon}t^a_{jk}t^b_{ki}\delta_{ab}\mathcal{A}^\mu_D\mathcal{I}_\mu \tag{4.14}$$

where $\mathcal{A}^\mu_D$ is the amplitude term that will finally attach the virtual boson to the missing LO electroweak TGC vertex and

$$\mathcal{I}_\mu = \int \frac{d^D k}{(2\pi)^D}\frac{\bar{v}_j(p_{\bar{q}})\gamma_\rho(\not{p}_{\bar{q}} - \not{k})\omega_\mu(c_R, c_L)(\not{p} + \not{k})\gamma^\rho u_i(p_q)}{k^2(p_q+k)^2(p_{\bar{q}}-k)^2}. \tag{4.15}$$

where $\omega_\mu(c_R, c_L) = \gamma_\mu(c_R\omega_+ + c_L\omega_-)$ and $c_L = c_R = 1$ for a photon, $c_L = 1$, $c_R = 0$ for a W boson and $c_L = I_3 - Q_q\sin^2\theta_w$, $c_R = Q_q\sin^2\theta_w$ for a Z boson. Feynman parameters are

[5] More specifically, functions (B.4)-(B.10) in appendix B of the FNR paper.

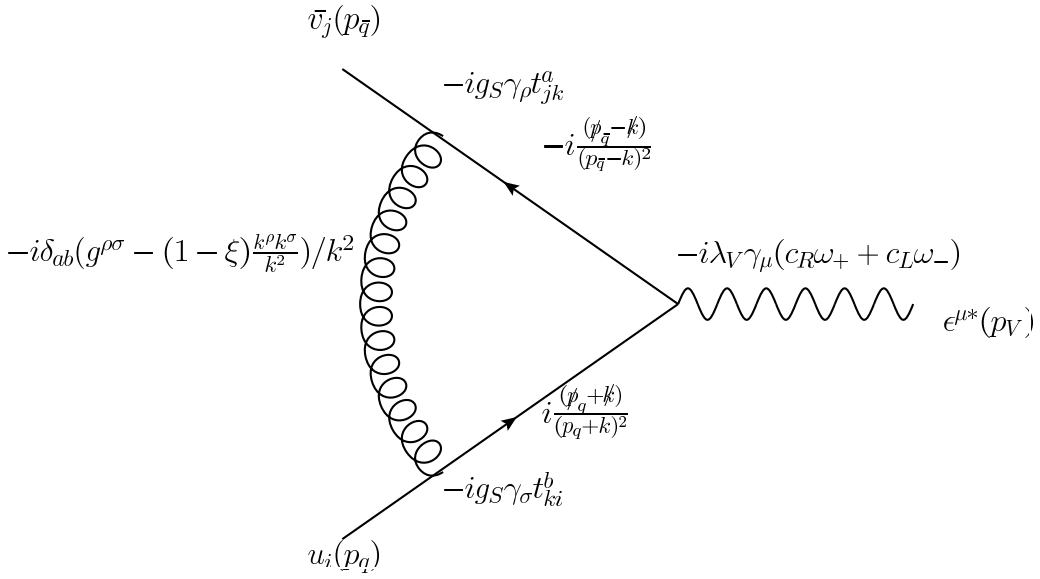

Figure 4.6: One loop s-channel.

used to solve this integral and, as there are three terms in the denominator in equation 4.15, this means, in general, applying

$$\frac{1}{ABC} = \int_0^1 dxdydz\delta(x+y+z-1)\frac{2!}{(xC+yB+zA)^3}. \tag{4.16}$$

After having done this parametrization and rearranging terms more conveniently, one finds

$$\mathcal{I}_\mu = 2\int_0^1 dx \int_0^{1-x} dy \int \frac{d^Dk}{(2\pi)^D}\left[\frac{-\bar{v}_j(p_{\bar{q}})\gamma_\rho(\not{k}-(1-x)\not{p}_{\bar{q}}-y\not{p}_q)\gamma_\mu(\not{k}+x\not{p}_{\bar{q}}+(1-y)\not{p}_q)\omega^\rho(c_R,c_L)u_i(p_q)}{(k^2+xys)^3}\right].$$

As the denominator is proportional to k^6, and so symmetric in k, any term with odd powers of k in the numerator will vanish (as an odd function integrates to zero over an even range). Hence the numerator $\mathcal{N}$ of the term in square brackets reduces to

$$\mathcal{N} = \bar{v}_j(p_{\bar{q}})\gamma_\rho\left[\not{k}\gamma_\mu\not{k} - \left((1-x)\not{p}_{\bar{q}} + y\not{p}_q\right)\gamma_\mu\left(x\not{p}_{\bar{q}} + (1-y)\not{p}_q\right)\right]\omega^\rho(c_R,c_L)u_i(p_q).$$

As the loop integral is symmetric, $k_\mu k_\alpha$ can be substituted with $\frac{g_{\mu\alpha}k^2}{D}$ and further, using $\gamma_\rho\gamma_\mu\gamma^\rho = (2-D)\gamma_\mu$ and $\{\gamma^\mu,\gamma^\nu\} = 2g^{\mu\nu}$ so that the Dirac equation $\bar{u}_i(p_1)\not{p}_1 = \not{p}_2 v_j(p_2) = 0$ can be applied. This then simplifies the numerator to

$$\mathcal{N} = -\left[-\tfrac{1}{D}(D-2)^2k^2 + 2(1-x)(1-y)s + xy(D-4)s\right]\bar{v}_j(p_{\bar{q}})\omega_\mu(c_R,c_L)u_i(p_q).$$

Using equation 4.14, summing over colour indices a, b, k and replacing $D = 4-2\epsilon$ gives

$$\mathcal{A}^1_S = ig_S^2\mu^{2\epsilon}C_F\mathcal{A}^0_S\mathcal{I} \tag{4.17}$$

where

$$\mathcal{I} = 4\int_0^1 dx \int_0^{1-x} dy \int \frac{d^D k}{(2\pi)^D} \frac{\left[(1-x-y+(1-\epsilon)xy)s - (1-\epsilon)^2(2-\epsilon)^{-1}k^2\right]}{(k^2+xys)^3}. \quad (4.18)$$

This integral can be tackled using standard loop integrals for the $\int \frac{d^D k}{(2\pi)^D}$ term [35] which gives

$$\mathcal{I} = \frac{i}{8\pi^2}\left(\frac{4\pi}{-s}\right)^{\epsilon}\Gamma(1+\epsilon)\int_0^1 dx\int_0^{1-x} dy \frac{1}{(xy)^{\epsilon}}\left[\frac{1-x-y+(1-\epsilon)xy}{xy} - \frac{(1-\epsilon)^2}{\epsilon}\right]. \quad (4.19)$$

Mathematica [105] can solve this integral as

$$\mathcal{I} = iN(-s)^{-\epsilon}\frac{(\Gamma(1-\epsilon))^2}{\Gamma(1-2\epsilon)}\left[\frac{2}{\epsilon^2}+\frac{3}{\epsilon}+\frac{8}{(1-2\epsilon)}\right] \quad (4.20)$$

where $N = (4\pi)^{\epsilon-2}\Gamma(1+\epsilon)$ and expanding $\frac{(\Gamma(1-\epsilon))^2}{\Gamma(1-2\epsilon)}$ gives $1 - i\pi\epsilon - \frac{2\pi^2\epsilon^2}{3} + \mathcal{O}(\epsilon^3)$. Equations 4.17 and 4.20 show that the one-loop vertex correction amplitude $\mathcal{A}_S^1$ is proportional to the leading order s-channel amplitude $\mathcal{A}_S^0$. The pure one-loop s-channel cross section at $\mathcal{O}(\alpha_s)$ is, up to the phase space integration, given by

$$\begin{aligned}
\mathcal{M}_S^1 &= \frac{1}{2s}\frac{1}{4N_C^2}\sum_{\text{Spin,Colour}}\left(\mathcal{A}_S^{0*}\mathcal{A}_S^1 + \mathcal{A}_S^0\mathcal{A}_S^{1*}\right) \\
&= -8\pi\alpha_s C_F\ \text{Im}\left[\mu^{2\epsilon}\mathcal{I}\right]\mathcal{M}_S^0 \\
&= -4\pi\alpha_s C_F N\left(\frac{s}{\mu^2}\right)^{-\epsilon}\left[\frac{4}{\epsilon^2}+\frac{6}{\epsilon}\right]\mathcal{M}_S^0 \\
&+ \frac{2\pi\alpha_s\left|F_{ij}\right|^2 C_F N}{sN_C}\left[16-\frac{8}{3}\pi^2\right]\frac{-1}{4\left|F_{ij}\right|^2 N_C}\sum_{\text{Spin,Colour}}\left|\mathcal{A}_s^0\right|^2
\end{aligned} \quad (4.21)$$

where F_{ij} are the couplings of the W to the quarks, more precisely

$$F_{ij} = \frac{g}{2\sqrt{2}}K_{ij} \quad (4.22)$$

where the K_{ij} are the corresponding CKM matrix elements with equation 4.17 and

$$\text{Im}\left[\mu^{2\epsilon}\mathcal{I}\right] = N\left(\frac{s}{\mu^2}\right)^{-\epsilon}\left[\frac{2}{\epsilon^2}+\frac{3}{\epsilon}\right] + N\left[8-\frac{4}{3}\pi^2\right] + \mathcal{O}(\alpha_s). \quad (4.23)$$

Hence the one-loop cross section due only to s-channel interference, $\mathcal{M}_S^1$, is directly proportional to the LO s-channel amplitude squared, $\left|\mathcal{A}_s^0\right|^2$. For the implementation into code this means that the analytic function from [77] can be replaced with the expression found here that uses LO helicity amplitudes which, as was explained earlier, include anomalous couplings by referring to the `AnomalousWWWVertex` class instead of the SM vertex class.

Calculation of $\mathcal{M}^1_{TS}$

The cross section from the interference of the one-loop s-channel with the LO t-channel can be calculated in a very similar way. Using equation 4.17 and its complex conjugate, the amplitude squared gives

$$\begin{aligned}\mathcal{M}^1_{TS} &= \frac{1}{2s}\frac{1}{4N_C^2}\sum_{\text{Spin,Colour}}\left(\mathcal{A}^{0*}_T\mathcal{A}^1_S + \mathcal{A}^0_T\mathcal{A}^{1*}_S\right)\\ &= -8\pi\alpha_s C_F\ \text{Re}\left[\mu^{2\epsilon}\mathcal{I}\right]\frac{1}{2s}\frac{1}{4N_C^2}\sum_{\text{Spin,Colour}}\text{Im}\left[\mathcal{A}^{0*}_T\mathcal{A}^0_S\right]\\ &\quad -4\pi\alpha_s C_F\ \text{Im}\left[\mu^{2\epsilon}\mathcal{I}\right]\mathcal{M}^0_{TS}\end{aligned}$$

which, assuming the term in $\text{Im}\left[\mathcal{A}^{0*}_T\mathcal{A}^0_S\right]$ does not contribute here[6], is again exactly proportional to the LO cross section of tree-level s- and t-channel interferences, $\mathcal{M}^0_{TS}$, and the same argument as for $\mathcal{M}^1_S$ applies.

Calculation of $\mathcal{M}^1_{ST}$

What is left are the terms that have interference of the LO s-channel, which can have anomalous coupling contributions, with all one-loop t-channel correction diagrams. There are four of these: one box diagram, two triangle diagrams and one with a gluon loop on the quark propagator.

$$\mathcal{M}^1_{ST} = \frac{1}{2s}\frac{1}{4N_C^2}\sum_{\text{Spin,Colour}}\left(\mathcal{A}^{0*}_S\mathcal{A}^1_T + \mathcal{A}^0_S\mathcal{A}^{1*}_T\right) \tag{4.24}$$

The calculation of these is non-trivial but, as an approximation, it is possible to write

$$\mathcal{M}^1_{ST}(AC) = \mathcal{M}^1_{ST}(SM)\times\frac{\mathcal{M}^0_{ST}(AC)}{\mathcal{M}^0_{ST}(SM)} \tag{4.25}$$

where (AC) denotes anomalous coupling and (SM) the SM contribution. This will of course not give the exactly correct NLO result but from a physics point of view this approximation is "self-consistent" as it does not neglect or create any divergences, since the one-loop cross section is proportional to the tree level by a factor of $\left(\frac{1}{\epsilon^2}+\frac{1}{\epsilon}\right)$ in both cases. Recalling the NLO POWHEG cross section as the result of integrating equation 4.8, it is possible to use this same argument to justify the approximation $\sigma_V \approx \frac{\langle\sigma_V\rangle}{\langle\sigma_B\rangle}\sigma_B$, where σ_i $(i = B, V)$ is the cross section for a given Born kinematic point with a particular phase point for the decays and $\langle\sigma_i\rangle$ is the same cross section averaged over decay phase spaces as both the stable one loop virtual correction have a factor of $\left(\frac{1}{\epsilon^2}+\frac{1}{\epsilon}\right)$ in the proportionality to the tree-level diagram.

[6] It is reasonable to assume that this term is small since the only contribution could come from the width term in the W^* propagator in the s-channel, which is tiny above the $W^\pm Z$ threshold.

4.5 Results

The results shown in this section are for $W^+Z \to e^+\nu_e e^+e^-$ production[7], the full implementation can deal with W^+W^-, $W^\pm Z$ and ZZ production. WZ distributions are chosen here for relevance with the experimental results presented in chapter 8. No form factor cutoff is applied for the results shown in this section. The event generation and analysis is done within Herwig++ and kinematic distributions are plotted using topdrawer [106]. The following colour scheme applies for kinematic distributions, unless stated otherwise:

black	SM
blue	$g_1^Z = 1.1$
cyan	$g_1^Z = 1.2$
yellow	$g_1^Z = 1.3$
green	$\kappa^Z = 1.2$
red	$\lambda = 0.1$

Figure 4.7 shows how the LO cross section varies as a function of the anomalous coupling parameter $\Delta\kappa^Z$. The same parabolic behaviour is obtained for Δg_1^Z and λ. A parabolic distribution is expected from the matrix element formula

$$|\mathcal{M}_0 + a\mathcal{M}_1 + b\mathcal{M}_2 + c\mathcal{M}_3|^2 \tag{4.26}$$

where $\mathcal{M}_0$ are the SM matrix elements, a, b, c are anomalous coupling coefficients and $\mathcal{M}_i$ are the corresponding anomalous matrix elements. If only one anomalous coupling parameter is considered at a time, then event weighting[8] can be done according to $w = \frac{\sigma(\alpha)}{\sigma(SM)}$ where $\alpha = \Delta g, \Delta\kappa, \lambda$. The data points on figure 4.7 are the cross section given by Herwig++ for different aTGC parameters, the solid line is the expectation from equation 4.26.

Figure 4.8 shows the LO diboson pair mass m_{VV}, the p_T spectrum of the positron produced in the W^+ boson decay, the rapidity η distribution of the W^+ boson and the $\cos\theta^*$ distribution for e^+ from the W^+ boson decay for different anomalous coupling values. θ^* is the angle of the charged lepton decaying from the parent boson defined in the rest-frame of that boson. As a general trend, it can be seen that anomalous coupling values enhance the cross section at high p_T and large invariant pair mass values. The η distribution shows the approximate radiation zero, mentioned in the previous chapter, and the presence of aTGCs fills in this dip because the SM gauge cancellations are spoiled. The $\cos\theta^*$ distributions are found to be symmetric for lepton pairs from the same parent. This means that the ν_e (e^-)

[7] The branching ratios (BR) for leptonic boson decays is small compared to hadronic decays. For completeness, the BR used in Herwig++ are BR($W^+ \to e^+\nu_e$) = BR($W^+ \to \mu^+\nu_\mu$) = 0.108059 and BR($Z \to e^+e^-$) = BR($Z \to \mu^+\mu^-$) = 0.03362. Hadronic decays can easily be switched off by including a file in the source code with `set V->q, qbar;:OnOff Off`.

[8] An analogous treatment for anomalous $WW\gamma$ couplings with more explanations on this weighting method can be found in reference [107].

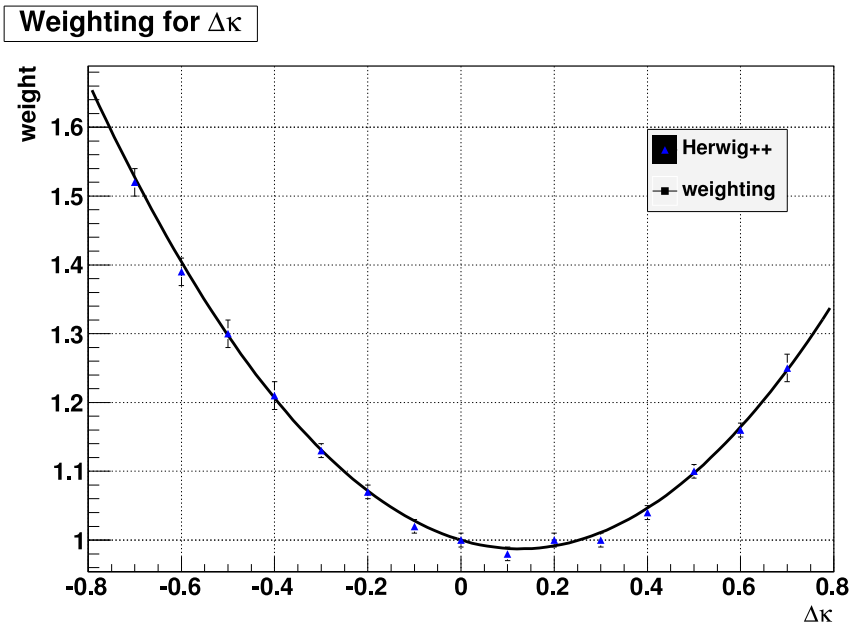

Figure 4.7: Parabolic behaviour of the LO cross section as a function of the aTGC parameter $\Delta\kappa^Z$.

distribution is a mirror image of the e^+ distribution from the W^+ (Z) boson decay. These angular distributions might be an interesting quantity for aTGC studies, aside from the more common p_T or η distributions. A comparison of the LO $\cos\theta^*$ distribution to MC@NLO has been made and good agreement found, which indicate that NLO corrections do not have a big influence on spin correlations.

Moving on to NLO results, the distributions shown here only include anomalous couplings at the Born and real corrections level. The virtual corrections use SM couplings; the calculation and possible approach for a future implementation of aTGC virtual corrections was discussed in section 4.4. The NLO analysis code stores all the leptons and partons separately and checks that there are exactly four lepton entries. It then makes sure all the leptons have bosonic parents and orders the bosons and leptons according to a certain consistent order. The jets are ordered according to their p_T using FastJet [108], a jet finder that implements the longitudinally invariant k_T, anti-k_T and Cambridge/Aachen jet algorithms. The name is justified by the fact that the algorithmic complexity of most jets finders is proportional to n^3 whereas for FastJet it is proportional to $n \ln n$, n being the number of particles in an ensemble. This is especially useful for a high multiplicity environment like the LHC. For simplicity, QED radiation is switched off for the W and Z bosons so that no photon radiation is added around the final state leptons from the boson decays. In the analysis, it is assumed that the bosons decay into a pair of leptons and not into leptons plus photons. The code reconstructs the mass of each boson by adding lepton momenta which will not be done correctly if there are additional photons around. The analysis runs at parton level with the `HadronizationHandler` switched off.

Figure 4.9(a) compares the LO to the NLO leptonic p_T distribution and figure 4.9(b)

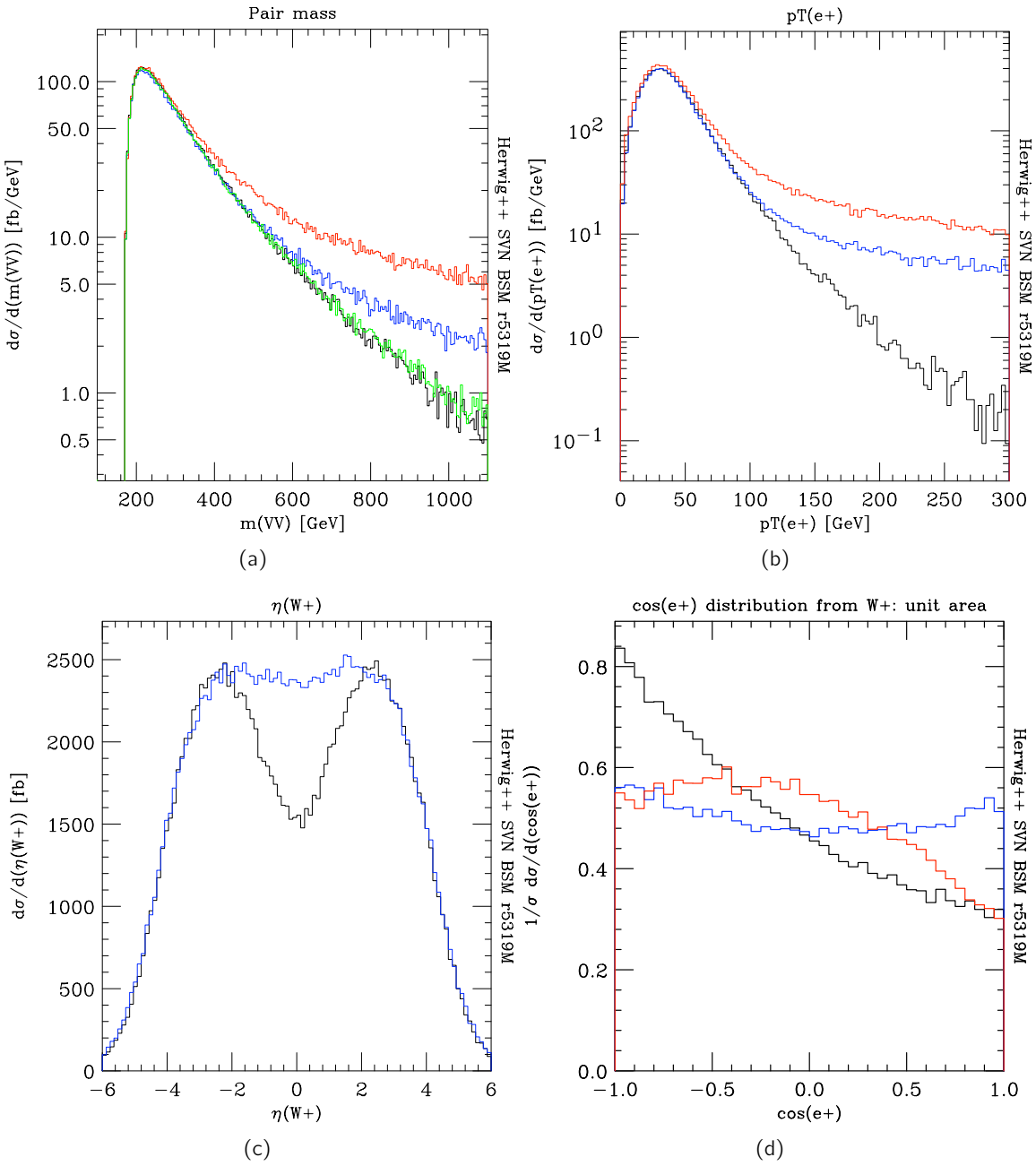

Figure 4.8: LO distributions for various anomalous coupling values, all normalised to cross section, (d) has a different colour coding: black=SM, red=$\kappa^Z = 2$, blue=$\lambda = 1$.

shows the θ_1 distribution. This is one of the so-called Born variables in the POWHEG implementation and is defined as the angle between $\vec{p}_1$, the momentum of the incoming quark, and $\vec{k}_1$, the momentum of the outgoing boson, in the partonic centre-of-mass frame obeying the following relation

$$t = (p_1 - k_1)^2 = m_V^2 - \frac{m_{VV}^2}{2}(1 - \beta \cos\theta_1) \tag{4.27}$$

where

$$\beta = \sqrt{1 - \frac{4m_V^2}{m_{VV}^2}}. \tag{4.28}$$

This variable might be harder to analyse experimentally but it is a good quantity to compare the POWHEG implementation to other methods.

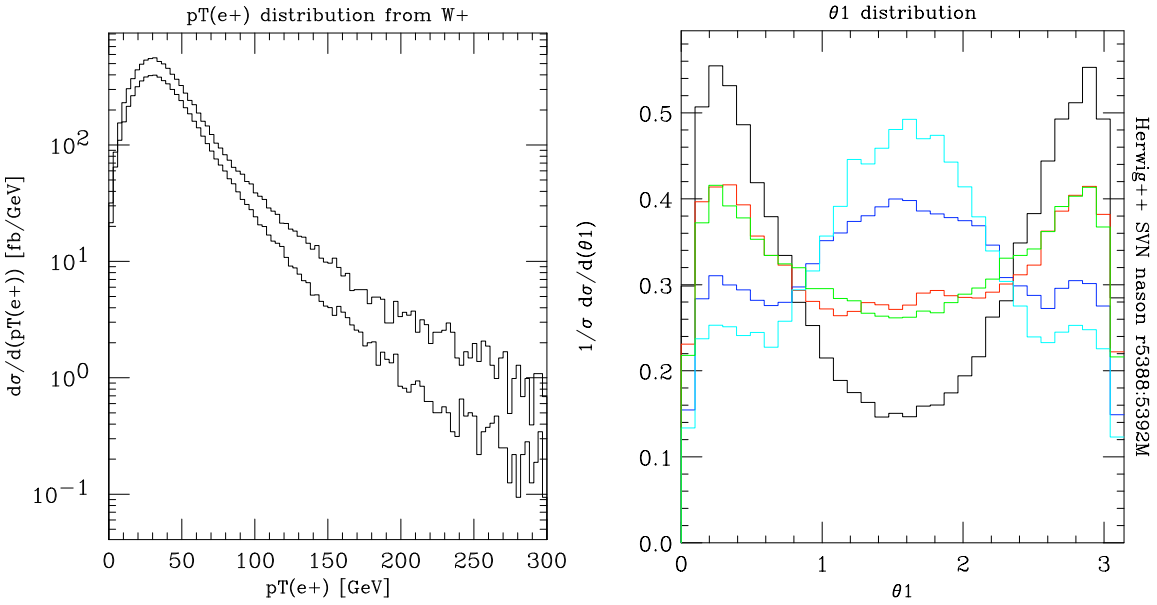

(a) (b)

Figure 4.9: (a) Comparison of the LO to NLO p_T distribution of the charged lepton from the W boson decay and (b) the θ_1 distribution at NLO for various anomalous coupling values.

As a finishing note, the comparison of POWHEG and MC@NLO will be discussed briefly. Like POWHEG, MC@NLO is a method to match the NLO calculation to a SMC to generate fully exclusive events. The parton shower is started from Born, virtual and real configurations distributed according to the NLO cross section. There is, however, a problem of double counting as the virtual and real contributions are divergent and the shower evolution of the Born term already contains a NLO approximation in the collinear limit which is also included in the real corrections term. To avoid this double counting, the NLO shower approximation is subtracted from the exact NLO calculation. This then gives finite terms but also negative weights. Several papers have been published to compare these two methods for different

processes. The general common features are that the POWHEG p_T distributions are harder in the high p_T region and that the MC@NLO jet rapidity distributions exhibit a dip around zero. However both of these differences are understood. Due to the form of its differential cross section given in equation 4.8, POWHEG will have contributions at large p_T that are higher than the pure NLO result by a factor of $\bar{B}/B$. Hence, POWHEG generally agrees better with the NNLO result in the high p_T region and MC@NLO generally has higher rates at low p_T. A rather striking example is Higgs production from gluon fusion [109] which has a rather large k-factor. The difference is not as striking for diboson production as the k-factor is smaller. MC@NLO typically has a dip in the distribution of the difference of the jet rapidity and the rapidity of the main quantity considered, in this case the rapidity of the boson pair $y_{jet} - y_{VV}$. It inherits this dip from Fortran HERWIG and fills it in somewhat but not completely, whereas POWHEG irons out the mismatch by generating the full NLO result itself.

Chapter 5

The Large Hadron Collider

The experimental results reported in this thesis use data collected with the ATLAS detector at the LHC in 2011 and 2012. In this chapter, the design and performance of the LHC are presented and in the following chapter the ATLAS detector is described in detail.

The LHC is located at the Franco-Swiss border close to Geneva, Switzerland. It is the largest, highest energy and highest luminosity particle accelerator to date and is designed for proton and ion beam collisions. It is built in an underground tunnel ring that was previously used by the Large Electron-Positron (LEP) experiment, which started being operational in 1989 and was dismantled in 2000. In December 1994, the CERN Council approved the construction of the LHC which took place from 1998 to 2008.

The four main experiments – ALICE, ATLAS, CMS and LHCb – located around the LHC ring are shown in figure 5.1. ATLAS ("A Toroidal LHC ApparatuS") [60, 110–112] and CMS ("Compact Muon Solenoid") [113, 114] are general purpose experiments whose main goals are to find or exclude the Higgs boson[1], to provide precise measurements of the SM predictions and to search for possible new physics such as SUSY. LHCb ("Large Hadron Collider beauty") [115, 116] is a single-arm forward spectrometer designed to study heavy flavour physics to help understand the matter-antimatter asymmetry in the universe, in particular through precision measurements of CP violation and rare decays of beauty and charm hadrons. ALICE ("A Large Ion Collider Experiment") [117] focuses on the strong interaction and studies the quark-gluon plasma at very high temperatures and energy densities in heavy ion collisions. These are mostly lead-lead collisions but the programme also includes collisions with lighter ions and proton-ion runs. The LHC ring is divided into octants: the ATLAS and CMS caverns, located at Point 1 and Point 5, respectively, were newly excavated whereas ALICE and LHCb, at Point 2 and Point 8, respectively, sit in pre-existing caverns used by LEP.

5.1 Design

The excavation work for the original LEP tunnel took place from 1984 to 1989. The ring has a circumference of 26.7 km, a depth varying between 45 m and 170 m underground and a gradient of 1.4%. It was decided to build the LHC in this existing tunnel to considerably

[1] At the Moriond 2013 conference, ATLAS and CMS officially announced the discovery of "a Higgs boson".

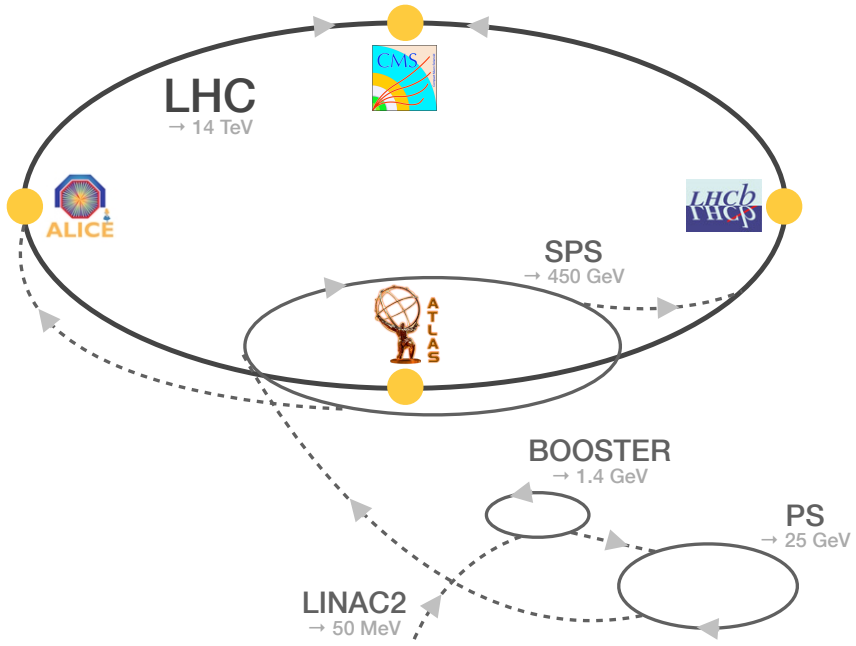

Figure 5.1: Layout of the CERN accelerators and the four main LHC detectors.

lower the construction costs, even though a hadron collider generally benefits from a larger radius and does not suffer as much from synchrotron radiation as a circular lepton collider.

The LHC [118–122] is designed to produce proton-proton collisions up to a centre of mass energy of $\sqrt{s} = 14$ TeV. To accelerate the particles to the desired energy the beam is injected through a succession of machines which accelerate the particles to gradually higher energies. This accelerator chain is shown in figure 5.1.

The protons, produced by a duoplasmatron source [123] through stripping hydrogen atoms of their orbiting electrons, are injected in the only linear accelerator in the chain, the Linac2, where they get accelerated to an energy of 50 MeV. The beam is then firstly fed into the Proton Synchrotron (PS) Booster, which has a radius of 25 m and accelerates the particles to 1.4 GeV, secondly into the PS, the oldest part of the chain first used in 1959, where an energy of 25 GeV is obtained, and finally into the Super PS (SPS), which has a circumference of 6.9 km, where the particles are accelerated to 450 GeV. The particles have now reached the LHC injection energy and are fed into the LHC ring via two transfer lines that circulate in opposite directions. It takes approximately 4 minutes to fill each of the two LHC rings. The particles are then accelerated for 20 minutes by electric fields in superconducting radio-frequency (RF) cavities operating at 400 MHz with a 5 MV/m gradient located around Point 4 to reach the design energy of 14 TeV. Once the particles are circulating around the ring at the nominal beam energy, they will lose about 7 keV of synchrotron radiation per turn. The RF cavities provide energy corrections to the beams to account for this loss. The accelerator chain can also accelerate lead ions which are passed through a Low Energy Ion Ring and are from there transferred through the PS and the SPS. In the LHC ring, they get accelerated to

maximally 2.76 TeV per nucleon. It should be noted that the LHC has not reached its design energy yet, it has been running at 7 and 8 TeV in 2011 and 2012, respectively.

To get an idea of how fast the particles at the LHC are moving, the relativistic kinetic energy of a particle moving at a speed v can be written down as

$$K = (\gamma - 1)m \tag{5.1}$$

where m is the particle's rest mass, the speed of light c has been set to 1 and

$$\gamma = \frac{1}{\sqrt{1 - v^2}}. \tag{5.2}$$

Table 5.1 shows this relation between the speed of a proton, whose rest mass is 0.938 GeV, and its kinetic energy at each of the different CERN accelerators. It can be seen that at high energies, a large increase in energy only causes a small increase in speed.

Accelerator	Kinetic energy	Speed (%)
Linac2	50 MeV	31.4
Booster	1.4 GeV	91.6
PS	25 GeV	99.93
SPS	450 GeV	99.9998
LHC	14 TeV	99.9999998

Table 5.1: Kinetic energy and percentage of the speed of light of a proton while travelling through the various stages of the CERN accelerators.

The protons are kept on a circular path around the LHC ring using 1232 superconducting NbTi dipole magnets providing magnetic fields up to peak values of 8.6 T. Additionally, there are 392 superconducting quadrupole magnets to correct the mean position of the beam and to focus the beams at the interaction points (IP). To ensure superconductivity, all magnets are cooled down to 1.9 K using liquid helium.

Since the LHC is a particle-particle collider, it is made of two rings with counter-rotating beams. Opposite magnetic fields are needed so that the two beams can collide. A twin-bore magnet design is used which means that the two rings are placed within the same cryostat and mechanical structure. This solves spatial and financial limitations but is less flexible as the rings become magnetically and mechanically coupled, leading to a very complicated magnet design.

The protons enter the LHC in bunches, one bunch is a group of about 1.1×10^{11} protons. The RF cavities allow bunches of a well-defined energy. The LHC is designed to store up to 2808 bunches per ring. The bunches come in so-called bunch trains, which each contain 72 bunches and are separated in time by 25 ns. This corresponds to a bunch crossing frequency of 40 MHz. To increase the particle flux, each bunch can be compressed transversally down to a design radius of 16 μm at the IP. Beams usually do not collide head on but at a slight angle of about 150-200 μrad so as not to produce "bad" collisions close to but not at the IP.

Once the machine is filled, the beams can circulate for many hours before they are dumped. The longest continuous stable beam conditions in one fill were achieved on June 2,

2012 and lasted for 22.8 hours [124]. The beams cross at four IPs where the main experiment caverns are located.

The machine luminosity depends on a certain number of beam parameters and, assuming a Gaussian beam distribution, it can be expressed as

$$\mathcal{L} = \frac{N}{\sigma} = \frac{n_b N_b^2 f_{\text{rev}} \gamma}{4\pi \epsilon_n \beta^*} F \tag{5.3}$$

where N is the number of events, σ the cross section of the event under study, n_b the number of bunches per beam, N_b the number of particles per bunch, f_{rev} the revolution frequency, γ as defined in equation 5.2, ϵ_n the normalised transverse beam emittance, β^* the beta function at the collision point and F the geometric luminosity reduction factor which takes into account that the region of interaction is reduced due to the fact that the beams have a certain crossing angle at the IP. The design luminosities for p-p collisions at the four main LHC experiments are 10^{34} cm^{-2}s^{-1} for ATLAS and CMS, 10^{32} cm^{-2}s^{-1} for LHCb and 10^{30} cm^{-2}s^{-1} for ALICE.

5.2 Performance

The first $\sqrt{s} = 7$ TeV p-p collisions took place at the LHC on March 30, 2010 followed by the first 8 TeV collisions on April 5, 2012. The highest peak luminosities reached were 3.6×10^{33} cm^{-2}s^{-1} (7.73×10^{33} cm^{-2}s^{-1}) and the maximum number of colliding bunches was 1331 (1380) for 7 (8) TeV data. The bunch spacing was, for the majority of the time, 50 ns and the average transverse beam width was about 30 μm. The LHC delivered a total luminosity of 5.6 (23.3) fb^{-1} in 2011 (2012) and ATLAS recorded this data with a $\sim 94\%$ efficiency. The delivered and recorded luminosities as a function of date can be seen in figure 5.2. The luminosity measurement and uncertainty determination are described in chapter 6, section 6.7.

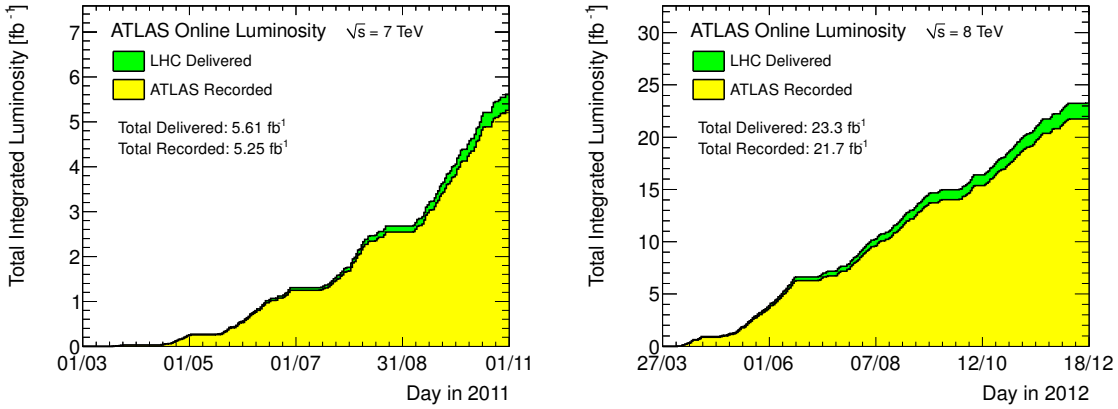

(a) (b)

Figure 5.2: Total integrated luminosity delivered by the LHC and recorded by ATLAS at (a) 7 TeV in 2011 and at (b) 8 TeV in 2012.

An increasing challenge for LHC data is in- and out-of-time pile-up. In-time pile-up refers to multiple protons from each bunch interacting in a given bunch crossing whereas out-of-time pile-up refers to the presence of energy from surrounding bunch crossings in the read-out window of the considered bunch crossing. The recorded luminosity as a function of the average number of interactions per bunch crossing $\langle\mu\rangle$ in 2011 and 2012 can be seen in figure 5.3. The average μ is 9.1 (20.0) for 7 (8) TeV data. Pile-up increases the track and vertex multiplicity as well as the overall energy in an event. This renders the reconstruction of physics objects like tracks, vertices and jets very challenging. To avoid large systematic uncertainties, a precise pile-up modelling is therefore crucial for successful physics analyses.

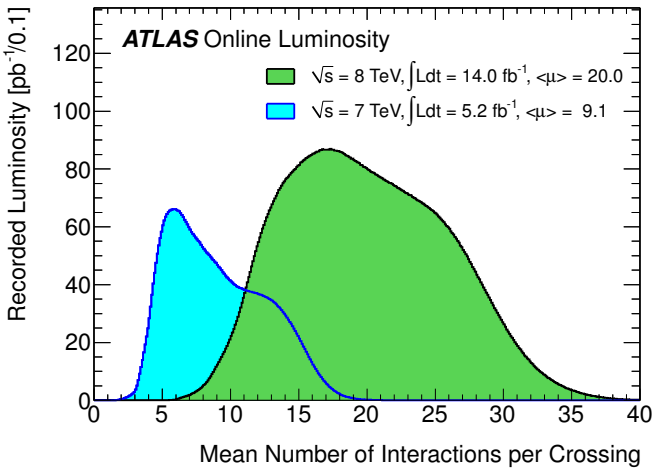

Figure 5.3: The average number of interactions per bunch crossing in 7 and 8 TeV data.

Chapter 6

The ATLAS Detector

ATLAS [60, 110–112] is a general purpose experiment that was designed to probe a large range of physics from soft QCD, precision electroweak and top quark measurements to searches for the Higgs boson and new physics at the TeV scale. To this end, ATLAS is built in a layered structure with cylindrical geometry and almost complete hermetic coverage. A schematic of the detector can be seen in figure 6.1. ATLAS is 44 m long, 25 m tall and weighs about 7000 tonnes. Starting from its core and moving outwards, there is the inner detector (ID) that is structured in three layers and is responsible for precisely measuring the momentum of charged particles moving in a 2 T solenoidal magnetic field, followed by the electromagnetic and hadronic calorimeters which measure the energy deposition of electrons, photons and hadrons and also infer the missing transverse energy from neutrinos and other undetected particles, and lastly a precise muon spectrometer (MS) which provides tracking and triggering of muons in a toroidal magnetic field. This complex structure will be described in more detail in this chapter.

The detector took fifteen years to design, build and install. The ATLAS collaboration counts about 3000 people from 178 institutions in 38 countries. ATLAS recorded its first collisions in 2009, after a one-year shutdown due to an LHC magnet quenching accident, and has been running successfully until the beginning of 2013 when it was shutdown for a two year upgrade period.

6.1 Detector Coordinates and Nomenclature

In terms of a right-handed cartesian coordinate system, the z direction is defined by the beam direction and the x-y plane is transverse to the beam direction. The nominal IP is defined as the origin of the coordinate system. The positive x direction is pointing from the IP to the inside of the ring and the positive y direction is pointing upwards. The positive z direction is defined along the anti-clockwise beam direction and is commonly referred to as the A-side, whereas the negative z direction is called the C-side. The azimuthal angle ϕ is measured around the beam pipe in the x-y plane with $\phi = 0$ on the positive x axis. The polar angle θ is the angle from the beam axis measured with respect to the positive z direction so that $\theta = 0$ points into the anti-clockwise beam circulation direction. The pseudorapidity η is

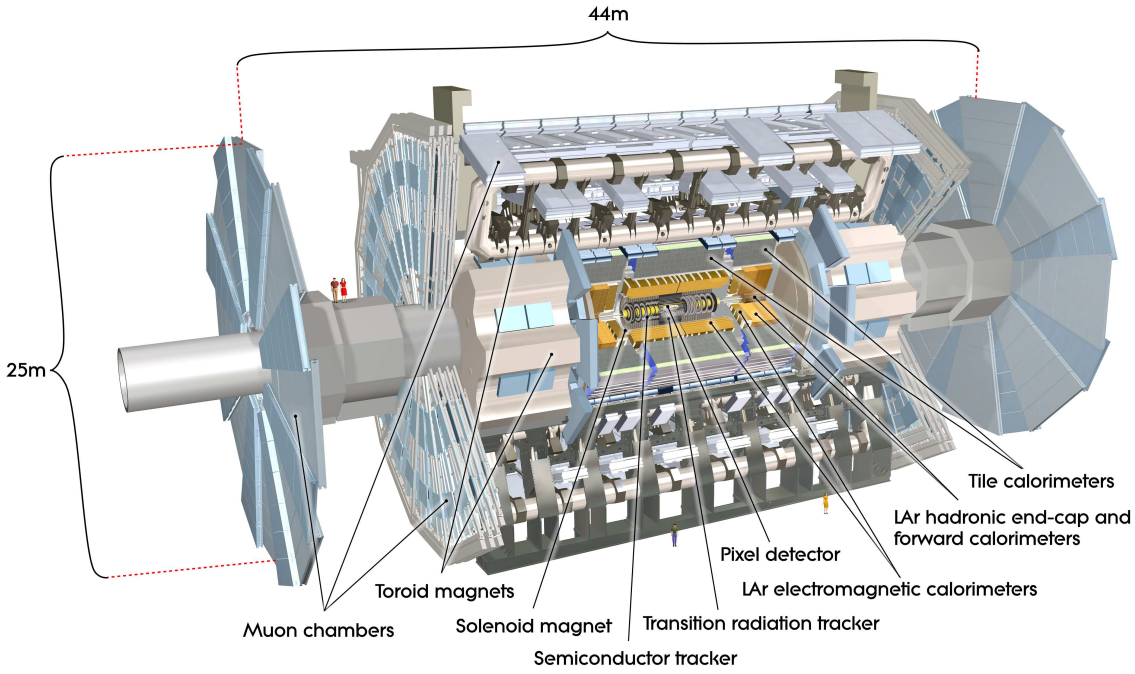

Figure 6.1: Cut-away schematic of the ATLAS detector [112].

defined as

$$\eta = -\ln \tan \frac{\theta}{2} \tag{6.1}$$

and the rapidity y, often used for massive objects like jets, is defined as

$$y = \frac{1}{2} \ln \left(\frac{E + p_z}{E - p_z} \right). \tag{6.2}$$

It should be noted that rapidity as well as pseudorapidity differences are Lorentz invariant. The distance ΔR in pseudorapidity-azimuthal angle space between two particles is defined as

$$\Delta R = \sqrt{(\Delta\eta)^2 + (\Delta\phi)^2}. \tag{6.3}$$

The transverse momentum of a particle is defined in the transverse x-y plane with a magnitude equal to

$$p_T = \sqrt{p_x^2 + p_y^2} = |p| \sin\theta. \tag{6.4}$$

The Cartesian components can be recovered via

$$p_x = p_T \cos\phi \tag{6.5}$$

$$p_y = p_T \sin\phi. \tag{6.6}$$

Similarly, the transverse energy is defined as

$$E_T = E \sin\theta \tag{6.7}$$

while the missing transverse energy $E_{\mathrm{T}}^{\mathrm{miss}}$ denotes an energy imbalance in the detector, due to the production of neutrinos that cannot be measured or other particles produced outside the detector acceptance. Lastly, the transverse mass $m_{\mathrm{T}} = \sqrt{E_1 E_2 - \mathbf{p}_1 \cdot \mathbf{p}_2}$ of a parent particle X, decaying into two daughter particles 1 and 2, is often used in case one of the daughters does not have a measured z component, like the neutrino. The transverse mass can then, in the case of massless daughters or of negligible mass compared to the mass of the parent, be approximated by

$$m_{\mathrm{T}} = \sqrt{2E_{\mathrm{T},1}E_{\mathrm{T},2}(1 - \cos(\phi_1 - \phi_2))}. \tag{6.8}$$

6.2 Magnet System

The ATLAS magnet system is composed of four large superconducting magnets, one central solenoid and three toroids, which are shown in red in figure 6.2(a). The magnetic field for the ID and the MS is generated by the solenoid and the toroids, respectively. The field is used for bending the trajectory of charged particles and measuring the particle momenta.

The *solenoid* is a superconducting magnet located between the ID and the calorimeter system and it provides a 2 T field in the z direction. It is designed to be as thin as possible to ensure that the electromagnetic calorimeter can still perform optimally and so that the particles traversing the solenoid lose as little energy as possible before hitting the calorimeter. Additionally, the solenoid and the liquid argon (LAr) calorimeter share a common vacuum vessel which means that two less vacuum walls are needed. The 1154 turn coil is a single layer made of aluminium-stabilised NbTi conductors. The dimensions of the solenoid are an axial length of 5.8 m, an inner radius of 1.23 m and a thickness of 10 cm. The coil weighs 5.4 tonnes and it can store an energy of 40 MJ. The solenoid is cooled to 4.5 K by a flow of liquid helium.

There are three large superconducting air-core *toroids* installed around the calorimeters, one in the barrel and one in either end-cap. They each have eight independent coils distributed radially and symmetrically around the beam axis. Each barrel coil has 120 turns, whereas each end-cap coil has 116. The toroids produce a magnetic field in the MS of 0.5 T and 1 T for the barrel and end-caps, respectively, whereas the maximal magnetic fields can reach up to 3.9 T and 4.1 T, respectively. The end-cap toroids are twisted by 22.5° with respect to the barrel toroid so as to ensure an ideal overlap in the radial direction and to achieve the best possible bending power in the transition region between $1.3 < |\eta| < 1.6$. The toroid is cooled to 4.6 K and all the eight barrel coils have their own cryostat whereas the end-cap coils share one cryostat on each side.

The amount by which a particle's trajectory deviates from a straight line depends directly on the strength of the magnetic field and the distance travelled transverse to the field. The bending power is defined as the field integral $\int B \cdot dl$, where B is the component of the magnetic field normal to the direction of motion and dl is the distance travelled, assuming infinite momentum. Since the solenoid and toroid fields are in the z and ϕ directions respectively, the bending occurs in the ϕ and η directions respectively. It should be noted however that the toroid field strength is not homogenous and hence the bending power in the toroid varies significantly. It can be seen in figure 6.2(b) that for different values of ϕ, a muon can either point in between two coils in the barrel and at a single coil in the end-cap or

vice versa. In the transition region the bending power is significantly lower and can even be negative, meaning that the particle is bent in the opposite direction.

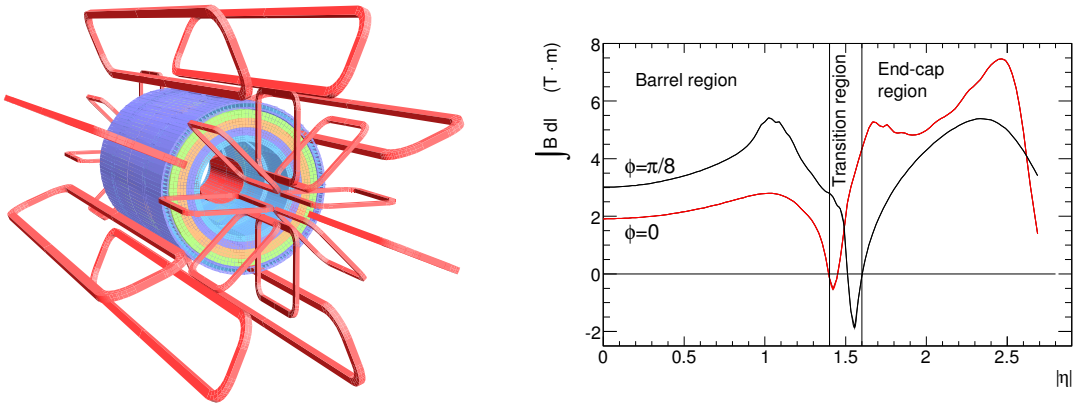

(a) (b)

Figure 6.2: (a) The solenoid windings, lying inside the tile calorimeter, and the barrel and end-cap toroid magnet coils of the ATLAS detector. (b) Predicted bending power as a function of $|\eta|$ in one toroid octant of the muon spectrometer [112].

6.3 Inner Tracking Detector

The ID, shown in figure 6.3(a), is contained within a cylinder of 7 m length and 1.15 m radius and is fully immersed within the 2 T magnetic field provided by the solenoid. The large track density at the LHC calls for a very good momentum resolution and precise vertex reconstruction, both for primary vertices from the hard collision and for secondary vertices from long-lived particles such as kaons, τ leptons or jets produced by heavy flavour quarks. The ID detects particles by measuring the interaction of a particle with the surrounding material at discrete space points up to $|\eta| < 2.5$. It can only detect electromagnetically charged particles which leave a track, neutral particles are not detected in the ID. The direction of the curvature gives the charge of the particle, the degree of curvature gives the momentum.

The ID is composed of three subsystems, the pixel detector, the semiconductor tracker (SCT) and the transition radiation tracker (TRT). It combines high resolution silicon pixel layers and silicon microstrip detectors in the inner part and continuous straw-tube detectors in the outer part. The silicon sensors need to be kept cool, at a temperature of about $-5°$ to $-10°$ C, using non-flammable octafluoropropane (C_3F_8) to keep the noise at a manageable level after radiation damage. The TRT can operate at room temperature. The overall resolution performance goal for the ID tracking is $\sigma_{p_T}/p_T = 0.05\%\ p_T \oplus 1\%$, where p_T is in GeV and $\oplus$ indicates a sum in quadrature. The three different subsystems will now be described in order of increasing distance from the beam line.

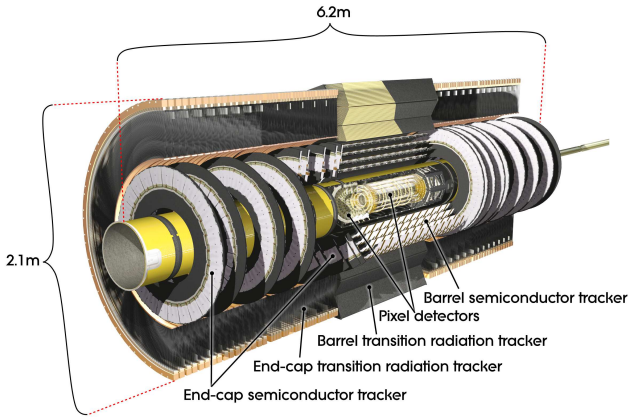

(a)

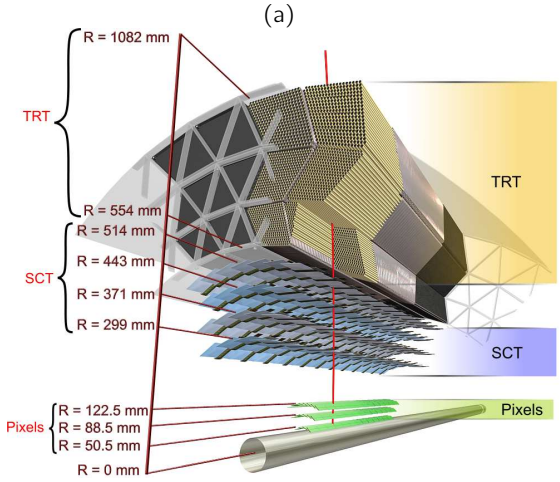

(b)

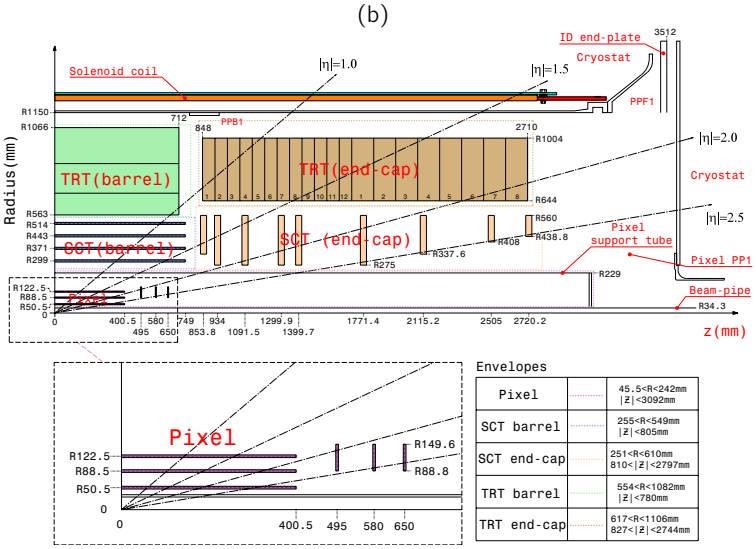

(c)

Figure 6.3: (a) View of the ATLAS inner detector. (b) Zoomed view on the layered structure of the pixel, SCT and TRT subsystems. (c) Dimensions of the barrel and end-cap ID layers [112].

6.3.1 Pixel Detector

Out of the three ID subsystems, the pixel system is the one located closest to the beam line. Its innermost layer, often called the B-layer, is positioned at 5 cm from the IP. The pixel detector has the highest granularity and gives very precise measurements of track impact parameters which help with the identification of displaced vertices from B-hadron or τ lepton decays.

The pixel detector contains 80% of all the read-out channels of the whole ATLAS detector, namely 80.4 million channels distributed over 1744 modules. All the modules are identical and each module has external dimensions of 19×63 mm^2. There are three concentric pixel layers in the barrel and three disks perpendicular to the beam pipe in each end-cap. The radial distances from the beam pipe can be seen in figure 6.3(b). Each layer is made of silicon sensors that have a thickness of 250 μm. About 90% of the individual pixels have a r-ϕ-by-z size of 50×400 μm^2, where r is the radial distance from the beam line. Some "long" pixels measure 50×600 μm^2 and are needed to cover the gaps between neighbouring front-end chips [125]. This allows for an intrinsic accuracy of 10 μm by 115 μm in the r-ϕ by z or r directions for the barrel or end-cap, respectively. A total of 2880 individual pixel cells are connected to one chip and 16 chips are mounted on one module. Every pixel is connected through bump-bonding to a read-out element on the front-end electronics of the module.

The initial bias voltage on the pixel detector is 150 V which needs to be increased up to 600 V as operation time increases due to radiation damage. For the same reason the performance of the pixel detector will decrease over time, especially the innermost layer which is planned to be reinforced by an additional Insertable B-layer (IBL) even closer to the beam line during the long shutdown in 2013 and 2014.

6.3.2 Semiconductor Tracker

The SCT is a silicon microstrip detector located around the pixel detector. It uses essentially the same detection technique and material as the pixel detector, namely semiconductor silicon, but it is organised in larger and cheaper strip sensors rather than small rectangular pixels. The strips are organised in four cylindrical layers in the barrel and nine disks in each of the end-caps, the exact location of these layers in terms of r and z can be seen in figure 6.3(c).

The SCT is designed to provide at least eight hit measurements per track. The silicon strips are made of two 6 cm long daisy-chained sensors with a strip pitch of 80 μm, which is chosen based on optimal granularity, digitisation precision and noise performance for the expected high particle occupancy. In total, there are 768 of these 12 cm long strips which are then assembled back-to-back so that each SCT layer is equipped with two modules at a small relative rotation angle of 40 mrad to increase the spatial resolution of a hit and to measure both r and ϕ coordinates. The intrinsic accuracy of SCT hit measurements is 17 μm by 580 μm in the r-ϕ by z or r directions for the barrel or end-cap, respectively. In total there are 4088 SCT modules leading to about 6.3 million read-out channels.

6.3.3 Transition Radiation Tracker

The TRT is the outermost component of the ID and allows tracking up to $|\eta| < 2.0$ but only provides r-ϕ information. It is composed of about 351000 drift tubes, also called straw tubes, which have a 2 mm radius, a wall thickness of 35 μm and are mechanically stabilised using carbon fibres. The straws are up to 144 cm long and oriented parallel to the beam in the barrel, whereas in the end-caps the straws are up to 37 cm long and laid out radially. The TRT has a lower material budget and a lower cost than the silicon. Each straw is filled with a gas mixture of 70% Xe, 27% CO_2 and 3% O_2 that becomes ionised when a particle passes through. The gold-plated tungsten anodes are 31 μm in diameter and connected to the front-end electronics. The anodes are kept at ground potential and the cathodes are operated at a voltage of -1530 V. As the particles travel through the straws, they ionise the gas inside the tubes and the electric field makes the ionised electrons drift towards the anode. The maximum electron collection time under standard operating conditions is 48 ns. From this time of arrival a drift radius, the radius of closest approach to the anode, is measured which gives an intrinsic resolution of 130 μm per straw. This is about a factor of ten less accurate than the other two ID subsystems, but the lower precision is compensated for by a much higher number of measurements. An average of 36 hits per track over a large bending radius provides almost continuous following of tracks and significantly improves the resolution of the ID as a whole.

The TRT is valuable for the detection of photon conversions and electron identification, which is improved greatly by the measurement of transition radiation (TR). This radiation is due to photons that are emitted when highly relativistic particles are traveling through materials with different relative permittivities in the xenon based gas mixture in the straws. Since electrons are very light they emit much more TR than heavier particles such as pions. The photons from TR will create a larger signal amplitude in the straws and so the TR can be distinguished from the initial charged particles on a straw-by-straw basis using two different thresholds in the front-end electronics, a low threshold for the tracking signals of the hard interaction and a high threshold for the TR.

6.4 Calorimetry

The ATLAS calorimeter system is composed of an electromagnetic and a hadronic sampling calorimeter covering a range up to $|\eta| < 4.9$. It uses various detection techniques adjusted to the different physics processes to be measured. The different components of the calorimeter are shown in figure 6.4. The purpose of the calorimeter is to measure the energy of charged and neutral particles, like electrons, photons, τ leptons and quark or gluon jets, ranging from energies of a few GeV all the way to several TeV, as well as to measure the $E_{\mathrm{T}}^{\mathrm{miss}}$ due to undetected particles.

The electromagnetic (EM) calorimeter has a very fine granularity which allows for shower shape analysis needed for electron and photon identification. The remainder of the calorimeter lies outside the EM calorimeter radially, or in the forward direction. This is the hadronic calorimeter which has a coarser granularity but is still suitable to reconstruct jets and $E_{\mathrm{T}}^{\mathrm{miss}}$.

An important requirement is that the calorimeters can fully contain the EM and

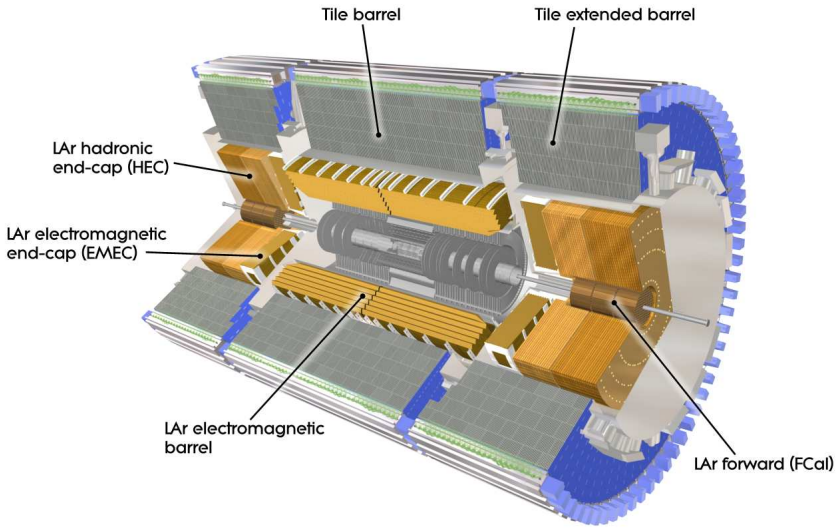

Figure 6.4: Schematic of the ATLAS calorimeter system [112].

hadronic showers and thus minimise punch-through, which occurs when a jet does not deposit all its energy in the calorimeter and therefore reaches the MS. This is why the depth of the calorimeter has to be significantly large. A particle traversing the EM calorimeter will pass through more than 22 (24) radiation lengths X_0 in the barrel (end-cap) and, after having passed through the whole calorimeter, an average of 10 interaction lengths λ. This allows a high resolution for very energetic jets and reduces punch-through into the MS below the irreducible level from prompt or decay muons. The λ dependence on η is shown in figure 6.5. This thick calorimeter layer combined with the almost hermetic coverage in η allows good $E_{\mathrm{T}}^{\mathrm{miss}}$ measurements.

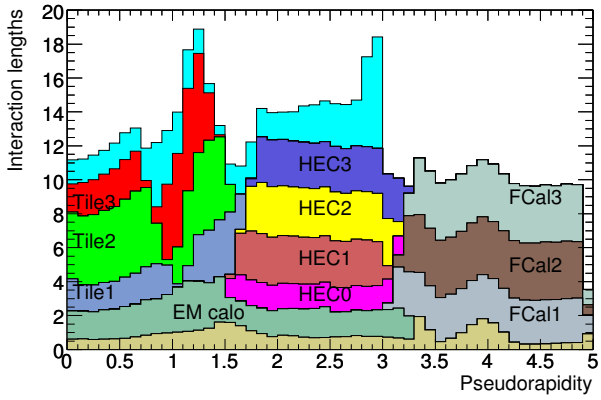

Figure 6.5: The amount of material expressed in units of interaction lengths λ as a function of pseudorapidity η for the different layers of the calorimeter [112].

6.4.1 Electromagnetic Calorimeter

The EM sampling calorimeter is divided into a barrel component up to $|\eta| < 1.475$ and two end-cap sections covering $1.375 < |\eta| < 3.2$. All three of these sections have their own cryostat. The barrel part comprises two half-barrels divided by a 4 mm gap at $z = 0$. Each half-barrel is 3.2 m long, weighs 57 tonnes and the inner (outer) radius measures 2.8 m (4 m). Each of the two end-cap parts is made of two coaxial wheels where the inner and outer wheels cover the ranges $1.375 < |\eta| < 2.5$ and $2.5 < |\eta| < 3.2$, respectively. A wheel has a width of 63 cm and weighs 27 tonnes.

The EM calorimeter is a LAr detector with accordion-shaped electrodes made of Kapton, a polyimide, and lead absorber plates whose thickness is optimised for energy resolution. The accordion-shaped arrangement allows for a full coverage in ϕ without any cracks and ensures that every particle traveling through the detector will cross approximately the same amount of material. As charged particles hit the absorber plates, they produce EM showers of electrons and photons, the latter of which can in turn pair-produce electrons. These showers ionise the LAr and the ionised electrons drift to the read-out electrodes. The latter are installed between the absorbers and are surrounded by copper plates that are held at a potential of 2000 V, leading to a drift time of 450 ns. The signal size on the electrode, which is roughly proportional to the number of electrons reaching the electrode, determines the energy measurement and so directly influences the resolution. It is therefore important to prevent large resolution from leakage fluctuations. The additional electrons from the containment of the full shower in the longitudinal direction also improve the sampling resolution. A presampler detector is installed within $|\eta| < 1.8$ to correct for inhomogeneous energy losses of electrons and photons traveling through the ID and support structures. It is made of a thin, active LAr layer of 1.1 cm (0.5 cm) width in the barrel (end-cap).

The high granularity of the EM calorimeter leads to a very good position and energy resolution of $\sigma_E/E = 10\%/\sqrt{E} \oplus 0.7\%$, where E is in GeV. The accordion structure has multiple layers. There are three in the $0 < |\eta| < 2.5$ region for precision measurements, also called compartments and shown in figure 6.6, and two in the $2.5 < |\eta| < 3.2$ region. The three longitudinal layers in the barrel have a thickness of $4.3X_0$, $16X_0$ and $2X_0$ moving outwards. The first layer has fine segments in the η direction with a spacing of $\Delta\eta = 0.0031$. The $\Delta\phi \times \Delta\eta$ granularity of the cells in the second and third layer are 0.0245×0.025 and 0.0245×0.05, respectively. The location of the active photon cluster in the first and second layers determines the η direction of a photon.

6.4.2 Hadronic Calorimeter

The hadronic calorimeter is composed of the tile (TileCal), LAr end-cap (HEC) and LAr forward (FCal) calorimeters.

The TileCal lies in the $|\eta| < 1.0$ barrel region and the $0.8 < |\eta| < 1.7$ end-cap region, where the crack region in between is used for services. The inner (outer) radius is 2.28 m (4.25 m). Steel is used as the absorbent material and tile scintillators as the active material. The TileCal is made of three layers of varying thickness, 1.5λ, 4.1λ, 1.8λ in the barrel and 1.5λ, 2.6λ, 3.3λ in the end-cap, adding up to a total of 7.4 interaction lengths in both cases. In the TileCal, wavelength shifting fibres are attached to each side of a scintillator tile, which

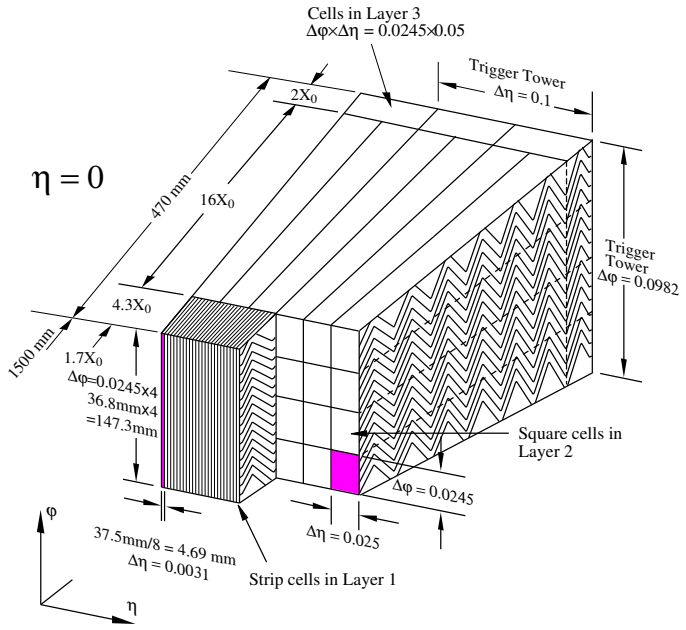

Figure 6.6: Granularity of a barrel module in the EM calorimeter [112].

are read out into two independent photomultiplier tubes.

The LAr HEC covers the range $1.5 < |\eta| < 3.2$ and is located in the same cryostat and uses the same technology and material as the EM calorimeter. There is a good coverage between the EM and HEC since the EM calorimeter extends up to the same η. The HEC has two wheels in each end-cap of the detector, both of which are divided into two longitudinal direction, and uses 25-50 cm thick copper plate absorbers. They alternate with 8.5 mm gaps filled with LAr and read-out wires.

The special LAr forward calorimeters are located close to the beam line and cover the very forward range of $3.1 < |\eta| < 4.9$. The forward calorimeters are designed to detect every interacting particle and to withstand the harsh radiation damage close to the beam line. This part of the hadronic calorimeter is about 10λ deep and is divided into three slices along the beam direction, the inner one being a copper absorber and the outer two being tungsten. All three slices alternate with LAr gaps as small as 0.25 mm. The materials are chosen to insure optimal EM and hadronic shower measurements.

Overall, the hadronic calorimeter has a very good jet and $E_{\mathrm{T}}^{\mathrm{miss}}$ performance. The resolution for jets is $\sigma_E/E = 50\%/\sqrt{E} \oplus 3\%$ in the barrel and end-cap regions and $\sigma_E/E = 100\%/\sqrt{E} \oplus 10\%$ in the forward region.

6.5 Muon Spectrometer

The MS is the outermost part of the ATLAS detector and it is composed of four different technologies shown in figure 6.7. The monitored drift tubes (MDT) and cathode strip chambers (CSC) are designed for precision tracking of the muon direction and momentum

measurement based on the deflection of tracks in a magnetic field whereas the resistive plate chambers (RPC) in the barrel and the thin gap chambers (TGC) in the end-caps are for triggering and precisely measuring the ϕ coordinate. The η coverage as well as the total number of chambers and channels of the four different components is summarised in table 6.1.

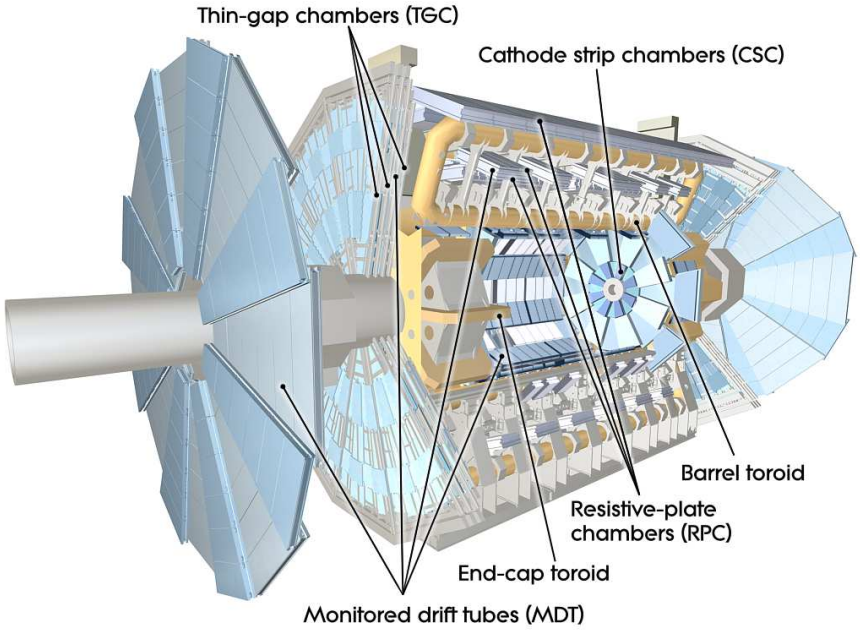

Figure 6.7: Layout of the ATLAS muon spectrometer [112].

	Coverage	Chambers	Channels
MDT	$\|\eta\| < 2.7$	1088	339000
CSC	$2.0 < \|\eta\| < 2.7$	32	31000
RPC	$\|\eta\| < 1.05$	544	359000
TGC	$1.05 < \|\eta\| < 2.7$	3588	318000

Table 6.1: Installation parameters of the four different MS components.

The barrel and two end-cap parts of the large super-conducting toroid magnets were already described in section 6.2. Within $|\eta| < 1.4$ and $1.6 < |\eta| < 2.7$ the bending of charged particles occurs via the barrel and the two smaller end-cap toroids, respectively. In the transition region $1.4 < |\eta| < 1.6$ the bending is due to a combination of barrel and end-cap fields. The bending power along the muon direction needs to be known to a few parts per thousand. Overall, the field is mostly perpendicular to the muon trajectory. Multiple scattering effects, which worsen the resolution, are minimised by the strong magnetic fields within an open structure with low material content. The magnetic field in the MS is permanently monitored with approximately 1800 Hall probes that are distributed throughout the spectrometer. Their

readings help to reconstruct the relative spatial position of the magnetic coils and to account for any possible perturbations from the TileCal or other nearby metallic support structures.

The tracks are measured by three layers of chambers organised cylindrically around the beam in the barrel and four wheels installed perpendicularly to the beam in the transition and end-cap regions. They are spatially organised so that a high momentum muon typically traverses three layers giving a so-called three station coincidence. The barrel layers are located at radii of 5 m, 7.5 m and 10 m from the beam and the end-cap disks at $|z|$ coordinates of 7.4 m, 10.8 m, 14 m and 21.5 m from the IP. The muon chambers reflect the layout of the toroid coils and are also organised in octants. Each octant is made of a small and a large chamber, resulting in 16 sectors, to have as few gaps as possible and to allow a measurement of the relative alignment using neighbouring sectors in the small and the large chambers. This organisation can be seen more easily in figure 6.8.

In the region around $\eta \approx 0$, there is a gap to allow access for services to the ID, solenoid and calorimeter. The size of the gap changes depending on the sector, with the large chambers having the biggest gap of about 1-2 m. Sectors 12 and 14 have further gaps called the "feet" region, which is where the ATLAS detector stands on the ground. All these uninstrumented regions deteriorate the muon efficiency in the barrel which will be discussed in more detail in sections 7.4 and 8.5.

The muon p_{T} resolution is excellent with a standalone (independent of the ID) precision $\sigma_{p_{\mathrm{T}}}/p_{\mathrm{T}}$ of about 10% for a muon p_{T} of 1 TeV. Such a muon will have a sagitta along z of 500 μm with a resolution of ≤ 50 μm. The different components that contribute to the resolution of a muon reconstructed in the MS is shown in figure 6.9.

The trigger chambers have a very fast response time but only extend up to $|\eta| < 2.4$. They provide precise p_{T} thresholds, bunch-crossing identification and measure the η and ϕ components of a track. This makes them complementary to the precision chambers in the sense that they also precisely measure the muon coordinate orthogonal to the direction measured by the MDTs and CSCs. A very good alignment of the chambers with respect to each other and with respect to the detector is needed as the overall performance of the MS depends on it. This is done by precision mechanical-assembly techniques and optical alignment systems within and between the chambers. For example, standalone muons require a 30 μm precision on the relative alignment within a layer and between adjacent layers in order to achieve the design resolution. The relative positioning accuracy of non-adjacent towers is a few mm. This positioning is established during the installation of the chambers. The relative alignment of the barrel or end-cap MS with the calorimeter and the ID relies on high-momentum muon tracks.

6.5.1 Monitored Drift Tubes

An MDT chamber, as shown in figure 6.10(a), is made of two sets of three or four drift tube layers bounded by read-out electronics and high voltage supplies, and separated by four optical rays that allow the internal monitoring of the alignment of a chamber based on an optical deviation from a straight line. Each chamber also has sensors to monitor the local temperature and magnetic field. The MDT chambers cover a range up to $|\eta| < 2.7$ except in the innermost layer which only extends up to $|\eta| < 2.0$. The size of a chamber depends on its

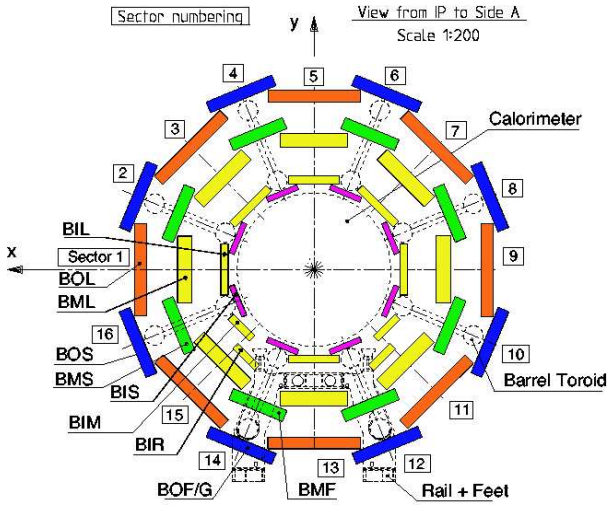

(a)

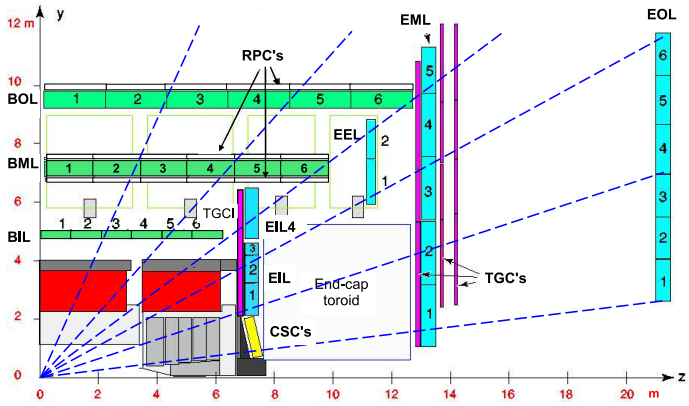

(b)

Figure 6.8: Cross sectional views of the MS along the (a) non-bending and (b) bending planes. To explain the sector nomenclature, B/E stands for barrel/end-cap, I/M/O for inner/middle/outer and L/S for long/short [112].

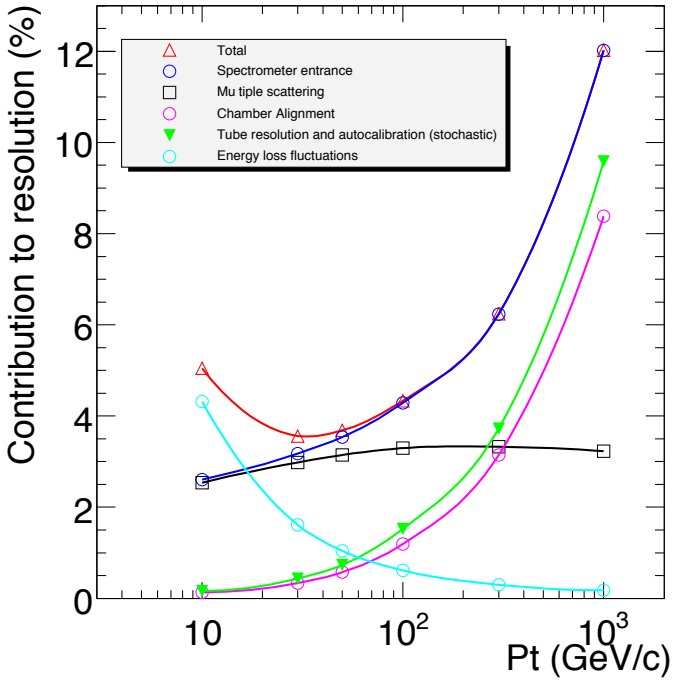

Figure 6.9: Contributions to the MS resolution within $|\eta| < 1.5$ as a function of p_T [60].

position in the detector. The length and width of a chamber vary between 1-6 m and 1-2 m, respectively. Altogether, the MDTs cover an area of about 5500 m^2.

The aluminium drift tubes have a radius of 15 mm and are filled with a Ar/CO_2 mixture in a 93%/7% ratio and are pressurised to 3 bar. A muon passing through an MDT is shown in figure 6.10(b). As it passes, the muon ionises the gas and the ionised electrons drift towards a central tungsten-rhenium anode wire which has a radius of 25 μm and is kept at a 3080 V potential, leading to a maximal drift time of about 700 ns. This electron avalanche causes a voltage drop at the wire and a so-called hit in the MDT. The time of arrival of the hit, as well as the charge deposition are then read out and converted into a drift radius measurement. Each tube (chamber) has an average hit resolution of 80 μm (35 μm). No ϕ information is recorded as the tubes are laid out along this direction.

Mechanically isolated drift tubes have several advantages. First of all, a single tube is quite stiff which makes it robust and reliable, and if one individual tube fails the remaining tubes are not affected. The cylindrical geometry of a tube produces a radial electric field and so a hit measurement does not depend strongly on the angle of incidence of a track onto the plane of the MDT chamber, which is especially important for high p_T muons.

6.5.2 Cathode Strip Chambers

The CSCs are located at a radius of 7 m from the IP covering the $2.0 < |\eta| < 2.7$ end-cap region with a total area of about 65 m^2. Rather than using another MDT layer, the CSCs were chosen because of their better resolution due to a higher granularity and their

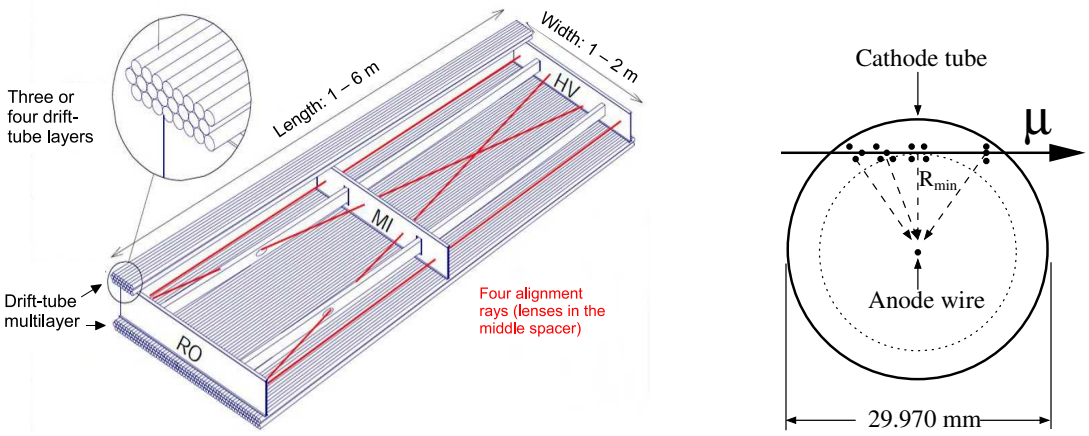

Figure 6.10: (a) Structure of an MDT chamber. (b) Cross section view of a muon traversing an MDT tube and ionising the gas mixture [112].

ability to cope with the very high particle flux close to the beam pipe[1].

The CSCs are multi-wire proportional chambers with radial anode wires of 30 μm diameter kept under a 1900 V voltage and cathode planes that are segmented into strips. The chambers are filled with a 80%/20% Ar/CO_2 gas mixture and they are slightly tilted towards the IP, as the resolution is optimal for a normal angle of incidence. The CSCs have the same structure as the MDTs, they are also organised in octants in ϕ with small and large chambers, where the former (latter) have 250 (420) wires per chamber. One chamber has four CSC planes which give four independent η-ϕ measurements per track. This means that the number of CSC hits per track is lower than the number of MDT hits but the faster response time of the CSCs increases the tracking efficiency.

There are two types of cathodes, one where the strips are perpendicular to the wires with a 5 mm strip spacing and one where the strips are parallel to the wires and a coarser 16 mm strip spacing. The former is for the longitudinal measurement (η) and the latter for the transverse coordinate (ϕ). The exact position is then a relative measurement determined by interpolating between the charges induced on two adjacent strips. The resolution in the bending direction is 60 μm per CSC plane. The coarser segmentation in the non-bending direction leads to a resolution of about 5 mm.

6.5.3 Resistive Plate Chambers

The cylindrical RPC layers are located in three trigger stations in the barrel region within $|\eta| < 1.05$, where the magnetic field is fairly homogenous. Their location with respect to the MDTs can be seen in figure 6.8(b).

An RPC trigger chamber, called a unit, contains no wires and each station has two independent, parallel resistive plates made of phenolic-melaminic plastic laminate that are

[1]MDTs can take counting rates up to 150 Hz/cm^2 whereas CSCs can take rates up to 1000 Hz/cm^2.

separated by 2 mm and an electric field of 4.9 kV/mm. The thickness of a unit varies between 96 mm and 122 mm. The gaps are filled with a non-flammable and cheap 94.7%/5%/0.3% $C_2H_2F_4$/Iso-C_4H_{10}/SF_6 gas mixture.

A signal is generated when a muon traverses the gaps and ionises the gas. The primary ionisation causes an avalanche of electrons that is read out, through capacitive coupling, to metallic strips installed on the outer layer of the plates. The strips on either side of the gap are orthogonal so that each layer can measure η and ϕ coordinates. This means that if a muon hits all three stations, there will be six measurements of η and ϕ over a long lever arm. The strip pitch is between 25-35 mm with a space and time resolution of 10 mm and 5 ns, respectively. This very fast trigger signal can be used for the hardware-based Level 1 trigger.

6.5.4 Thin Gap Chambers

The TGCs provide ϕ coordinate measurements in the end-cap region $1.05 < |\eta| < 2.7$ with triggering up to $|\eta| = 2.4$. They use the same detection principle as the CSCs and are chosen in this region over RPCs for their higher granularity and higher rate tolerance, both important in the dense particle flux environment in the end-caps. Four TGC layers are installed to increase the trigger robustness in the presence of higher backgrounds; their locations can again be seen in figure 6.8(b).

A big TGC wheel is made of 12 sectors of 30° in ϕ, giving a geometrical coverage of almost 99%. A chamber is made of two cathode plates with a separation distance of 2.8 mm. The chambers are filled with a 55%/45% CO_2/C_5H_{10} gas mixture. An anode wire is placed between the cathodes under a 3.1 kV voltage which creates fast signals due to a small drift time. The spacing from one wire to the next is 1.8 mm. The spatial resolution is 2-6 mm in η and 3-7 mm in ϕ.

6.6 Trigger and Data Acquisition

At the design luminosity of 10^{34} $cm^{-2}s^{-1}$ and a 25 ns bunch-spacing, the LHC bunch crossing (BC) rate is 40 MHz, which is too much data to fully reconstruct and store. Therefore, very fast but careful decisions need to be made about whether an event is of interest and should be recorded so that the overall data flow is reduced but only a minimal fraction of physics events is lost. The majority of collision events, called minimum bias events, do not have any high p_T objects or other interesting features and can therefore be safely discarded.

The ATLAS Trigger is composed of three levels, the hardware-based Level 1 (L1) trigger and the software-based Level 2 (L2) and Event Filter (EF) triggers, collectively called the high level trigger (HLT). As shown in figure 6.11, the overall rate is reduced stepwise at every trigger level down to a rate of about 200 Hz after the final EF stage. At the same time, the decision and selection criteria are refined at every stage.

After an event passes the L1 trigger decision it is transferred to the data acquisition (DAQ) system, which stores the data in temporary buffers to pass it on to the L2 trigger. Events that pass the L2 and EF triggers, which run reconstruction checks at different levels of accuracy, are written to a permanent data storage unit where they remain available for physics

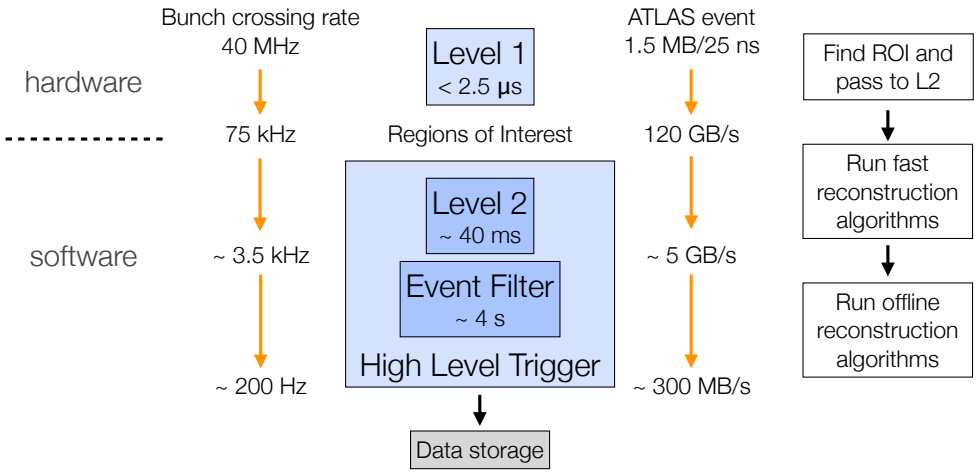

Figure 6.11: Setup of the ATLAS trigger and read-out chain.

analysis. The DAQ system, in addition to insuring the flow of data, also allows the control and monitoring of different hardware and software components.

6.6.1 Level 1 Trigger

The L1 trigger needs to make decisions extremely quickly and send the outcome to the front-end electronics within 2.5 μs per event. This decision time is also called the latency. Such a short time is only possible if the decision is based only on a subset of the full detector information. The overall rate is thereby reduced down to 75 kHz.

The L1 trigger searches for high momentum objects like muons, electrons, photons or jets or events with large $E_{\mathrm{T}}^{\mathrm{miss}}$ or scalar-summed E_{T}. The L1 trigger uses information from subdetectors but at a reduced granularity. L1 muon triggers use information from the RPC and TGC trigger chambers, all other objects use calorimeter information from trigger towers that have a $\Delta\eta \times \Delta\phi$ granularity of 0.1×0.1. The acquired information is processed by a central trigger processor (CTP) which puts together a so-called trigger menu that contains all the different selected trigger chains. Prescales[2] can be applied to make optimal use of the available bandwidth between the various trigger chains as the luminosity and run conditions change.

If an event passes the L1 trigger decision then it is passed to DAQ via point-to-point read-out links. In each of these events the L1 trigger has defined regions-of-interest (RoI) in η-ϕ space to indicate where the physical objects of interest are located. One RoI makes up only about 2% of a full event.

[2] A prescale of x means that only every x^{th} event passing a certain trigger chain requirement will be accepted. Prescales can be applied at all trigger levels, not only at L1.

6.6.2 High Level Trigger

The HLT part of the trigger is software-based and therefore will not be explained in extensive detail here. More information will be given in chapters 7 and 8.

The L2 trigger is seeded by the L1 RoIs which contain p_{T}, η and ϕ information. The L2 algorithms use the full granularity and precision available within the RoI and reduce the rate further down to about 3.5 kHz, spending about 40 ms on an event. The drop in rate is mostly achieved by more precise p_{T} measurements deduced from information from the precision chambers and calorimeter isolation requirements. The L2 trigger also has the possibility to require a match of an MS track with an ID track.

The EF trigger is the final stage of event selection. It further reduces the rate to about[3] 200 Hz and fully reconstructs every event using procedures similar to the offline reconstruction algorithms while spending about 4 s per event. The EF trigger uses about three times more computing nodes than the L2 trigger. The EF can also perform more complex computations like vertex measurements and tagging of b quark jets. If an event passes the EF trigger decision, it is permanently written to tape and organised according to different trigger streams (Muon, Egamma etc.).

6.7 Luminosity

The luminosity gives the scaling between the number of observed events and the cross section of a specific process. Any uncertainty on the luminosity will directly feed into the uncertainty on the cross section and make the measurement less precise. It further plays a role when estimating background levels and determining the sensitivity to new physics. It is therefore important to have several independent detectors and algorithms within ATLAS to determine the recorded luminosity. The combination of different methods can help to reduce the systematic uncertainty on the final luminosity uncertainty [126–129].

The luminosity at a proton-proton collider can be written as

$$\mathcal{L} = \frac{R_{\mathrm{inel}}}{\sigma_{\mathrm{inel}}} = \frac{\mu n_b f_r}{\sigma_{\mathrm{inel}}}, \tag{6.9}$$

where R_{inel} is the rate of inelastic collisions, σ_{inel} the inelastic p-p cross section, μ the average number of inelastic interactions per BC, n_b the number of bunch pairs colliding per revolution and f_r the revolution frequency of the bunches. The last two parameters are known so the aim is to measure μ and σ_{inel}. Both of these quantities can be replaced by their visible counterparts μ_{vis} and σ_{vis}, where the relation between the inelastic and visible quantity is just the efficiency ϵ for an inelastic collision to be detected or selected. As μ and σ appear in a ratio in equation 6.9, ϵ will cancel.

Since μ_{vis} is experimentally measurable, the determination of σ_{vis} for a specific detector will give a calibration for the luminosity scale. After the detectors are calibrated, mostly using beam parameter measurements, the event rates on the detectors can be converted into estimates of μ from which the luminosity can be determined.

[3] This is the design output rate, the average rate during 2011 and 2012 data taking was closer to 400 Hz.

To measure μ_{vis}, most of the ATLAS algorithms rely on simple event counting where an event passes if it satisfies certain criteria indicating that it has at least one inelastic p-p interaction. However, in the presence of pile-up, the relation between μ_{vis} and the number of events is not linear and the event counting method is no longer valid if all BCs contain events. Here the method of hit counting can be used, where, instead of counting how many BCs contain at least one p-p interaction, the number of readout channels above a certain threshold is counted.

The instantaneous luminosity scale calibration through σ_{vis} is realised from direct measurements of the beam parameters which allow the derivation of an absolute luminosity. Equation 6.9 can be rewritten as

$$\mathcal{L} = \frac{n_b f_r n_1 n_2}{2\pi \Sigma_x \Sigma_y} \tag{6.10}$$

where n_1 and n_2 are the number of protons per bunch for beams 1 and 2 determined by external LHC measurements of the total beam current and the current variations between different bunches. Σ_x and Σ_y are the beam widths and can be determined by beam-separation scans, so-called van der Meer (vdM) scans, where the beams are incrementally separated by a known horizontal or vertical distance δ. Σ_x is given by

$$\Sigma_x = \frac{1}{\sqrt{2\pi}} \frac{\int R_x(\delta) d\delta}{R_x(0)} \tag{6.11}$$

where $R_x(0)$ is the observed event rate for no beam separation, meaning the maximum rate. Σ_y is a similar quantity but for the vertical direction.

The vdM scans used for the results presented here were performed on May 15, 2011. They used fewer bunches than for normal data-taking conditions, namely 14 colliding bunches, no bunch trains and an average μ of 2.3. The profile of a horizontal scan for one specific BC is shown in figure 6.12.

The systematic uncertainties on the luminosity measurement are decreased using several luminosity sensitive detectors. The beam condition monitor (BCM) is located about 2 m longitudinally from the IP on either side and it is made from four diamond sensors, grouped vertically and horizontally into pairs. The BCM is designed to measure hit rates. LUCID is a Cherenkov detector installed at 17 m from the IP on either side in the very forward direction $5.6 < |\eta| < 6.0$. Both detectors can provide bunch-by-bunch luminosity measurements. For the results presented in this thesis using 7 (8) TeV data, the preliminary luminosity uncertainty is 1.8% (3.6%). In previous LHC measurements the uncertainty was dominated by the understanding of the bunch charge product $n_1 n_2$, whereas now it is dominated by the accuracy of the vdM calibration procedure.

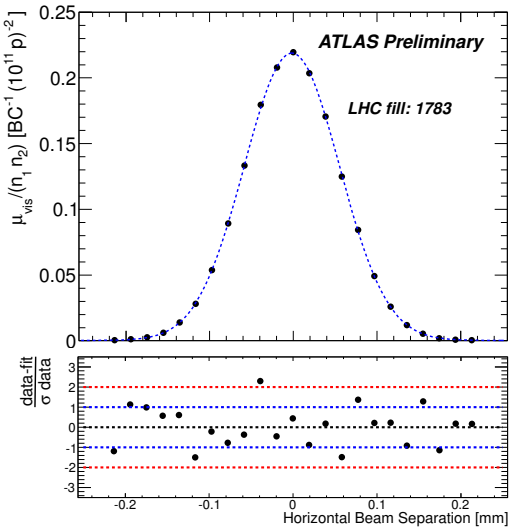

Figure 6.12: Specific interaction rate from a single BC as a function of the horizontal beam separation [128].

Chapter 7

Physics Object Reconstruction

This chapter aims to give a general overview of how physics objects are reconstructed from detector signals in ATLAS. As this thesis describes two analyses using different data sets, 4.6 fb^{-1} and 7.2 fb^{-1} taken at $\sqrt{s} = 7$ TeV and $\sqrt{s} = 8$ TeV respectively, the specific selection details will be described in the relevant chapters.

The simulation software used in ATLAS to model particles passing through matter is based on the Geant4 toolkit [130, 131]. It uses over 10^7 events from a large variety of physics processes ranging from energies as low as 250 eV up to the TeV range. It simulates the full ATLAS detector and allows one to account for the alignment of the subdetectors, irregularities in the magnetic field or the material and distortions in the calorimeters.

Figure 7.1 shows a slice through the detector being traversed by different particles. Charged particles leave tracks in the ID, electrons, photons and jets deposit energy in the calorimeters, muons propagate all the way into the MS and neutrinos exit without being detected.

7.1 Inner Detector Tracks

In cylindrical coordinates, a track is defined by a state vector with components $(r, z, \theta, \phi, q/p)$, where r is the radial distance from the beam pipe, q is the charge and p the momentum of the track. The remaining components were defined in section 6.1. The spatial components correspond to the distance of closest approach to the beam line of the track helix. Tracks from charged particles are reconstructed in the ID within $|\eta| < 2.5$. The efficiency at low momentum is reduced due the large amount of material in the ID. Tracks are for example needed for vertex, electron and muon reconstruction, which are all crucial to the analyses described in this thesis. The ID track reconstruction software uses a common ATLAS Event Data Model (EDM) [132–134] which makes it possible to use one model across the different subdetectors and encourages the use of a common software for online and offline reconstruction. The EDM contains a track class which is common for combined tracks in the ID and in the MS. In the track reconstruction algorithm, track fitting is a part of pattern recognition. They happen simultaneously because of the complex magnetic field, the need to extrapolate tracks out through the field and the need to estimate energy loss in material.

The ID track reconstruction works in two sequences. The first one is the so-called

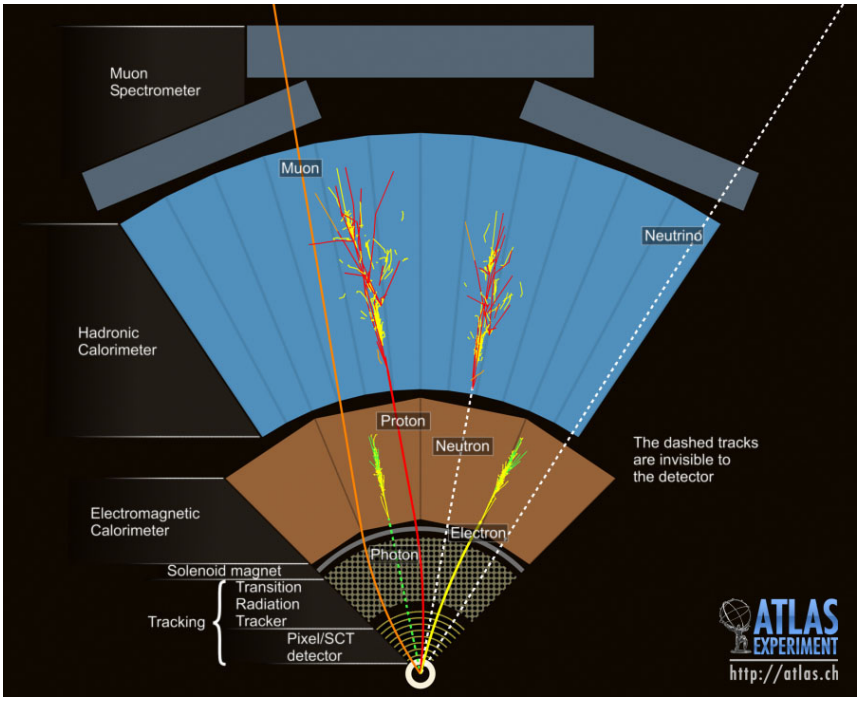

Figure 7.1: Cross sectional slice of the detector showing the flow of particle identification.

inside-out method. It first creates a space point which is a three dimensional (3D) representation of the measurements in the silicon detectors. The pixel detector gives a two dimensional ($\phi - z$) measurement on a surface at a given r, while the SCT clusters cannot be directly converted to 3D since an SCT module only gives a measurement perpendicular to the SCT strip. However, since the SCT modules have a back-to-back structure, as described in the previous chapter, these two inputs together with a beam spot constraint will give a 3D space point. These space point collections are then used to seed the track reconstruction. A Kalman filter is used to propagate the trajectory and include successive hits into the track candidate fit to form a track segment. As it progresses, the track information and the covariance matrices are updated. Since a silicon detector element usually has more than one hit per event, the most likely extension of the trajectory in terms of χ^2 is used. At the same time, outliers are identified by their large contribution to χ^2 and excluded to improve the track quality. If no hit is found, the algorithm proceeds to the next layer. The tracks are then extended to the TRT by searching for sets of TRT measurements that are compatible with the silicon seeds. The inside-out method can fail due to photon conversions which will cause the track to not have hits in the inner pixel layer needed for seeding or due to displaced vertices from a decay in flight. To cover such cases, the *outside-in* method is used after the inside-out method has finished. It starts with a segment-finding algorithm from the TRT hits[1] and a back-tracking of these segments into the silicon detectors. A third track sequence, the second stage pattern

[1]TRT drift tube measurements do not give any coordinate information along the direction of the straw and so techniques need to be used to find straight line patterns. Here a so-called Hough transform is used.

recognition, is implemented to deal with Bremsstrahlung which causes a kink in the track.

7.2 Primary Vertices

The primary vertex (PV) [135, 136] of an event is the main IP where the hard collision happens. The PV reconstruction is divided into two steps. The primary vertex finding algorithm associates reconstructed tracks to a vertex candidate and the vertex fitting algorithm reconstructs the vertex position plus its error matrix. The decision about whether a track originates from a vertex is based on the transverse and longitudinal impact parameters d_0 and z_0, the number of pixel and SCT hits and only uses tracks with $p_{\mathrm{T}} > 400$ MeV. In a bunch crossing, the PV is defined as the vertex with the highest $\sum_{\mathrm{tracks}} p_{\mathrm{T}}^2$.

Once the tracks are associated to common vertices, the position of each vertex is determined from a vertex seed using a so-called adaptive vertex fitting algorithm which is again χ^2 based. As with outlier hits in the track reconstruction, outlier tracks are given a lower weight and tracks that are incompatible with the vertex by more than 7σ are removed completely. This process is repeated until every track has been associated to a vertex or until no additional vertices can be found.

The vertex resolution as determined in 7 TeV [137] and 8 TeV [138] collision data for PVs with $\sqrt{p_{\mathrm{T}}^2} > 12$ GeV is $\sim 20\mu$m ($\sim 40\mu$m) in the x and y (z) directions.

7.3 Electrons

Electrons are reconstructed up to $|\eta| < 2.47$ excluding the crack region within $1.37 < |\eta| < 1.52$, which is a transition region in the calorimeter between the barrel and the end-caps containing dead-material used for services. The electron reconstruction algorithm [139, 140] starts by building so-called towers. This is done by dividing calorimeter clusters into a grid of $\Delta\eta \times \Delta\phi = 0.025 \times 0.025$ fixed-size rectangles and summing over all layers. Then, a sliding window the size of one rectangle searches for the position which gives the maximum local energy above a 3 GeV threshold. These cells form a so-called pre-cluster from which the final electron cluster is formed. The cluster size varies in the barrel and in the end-caps, being 3×7 or 5×5 cells respectively, to contain as much energy but as little noise as possible. In the barrel, the magnetic field bends the trajectory in the ϕ direction and so the cluster is chosen to be longer in that direction. Likewise, e^+e^- pairs from photon conversions also spread in the ϕ direction. The effect of the magnetic field and the cell size is smaller in the end-caps and thus the cluster size is larger in η but smaller in ϕ than in the barrel.

The electron direction can either be taken from the ID track or the calorimeter cluster depending on the number of silicon hits of the ID track. If it is a high quality track which has a large number of hits, the η and ϕ track coordinates are used. If the track has less than four silicon hits, the electron direction is taken from the cluster as the barycenter in the middle layer of the EM calorimeter. This direction gets propagated to the transverse energy which is equal to $E_{\mathrm{T}} = E_{\mathrm{cluster}}/\cosh\eta$, where η is chosen as just described.

The electrons are then classified using three different quality criteria – *loose++*, *medium++* and *tight++* – whose definitions have changed slightly between 2011 and 2012

data. For simplicity, the 2011 quality definitions will be described here. The main difference in the 2012 menu is that it relies more heavily on pile-up robust variables, details can be found in reference [141]. The selection cuts are chosen to ensure a good discrimination between physics objects. Electrons and photons can be distinguished by matching calorimeter clusters to ID tracks and by discrimination of shower shape distributions. Transition radiation from the TRT is used to distinguish electrons from hadrons. Stricter qualities generally have higher background rejection but lower efficiency.

- Loose++ applies cuts on shower shape variables in the first (strip) and second layers of the EM calorimeter, as well as on the hadronic leakage. It requires track quality hits in the pixel and SCT layers and loose track-cluster matching of $|\Delta\eta| < 0.015$. The loose++ efficiency derived from Z tag-and-probe studies is about 95%.

- Medium++ has tighter shower shape cut values, tighter track-cluster matching of $\Delta\eta < 0.005$ and an impact parameter cut of $d_0 < 5$ mm. It further applies stricter B-layer and pixel hit requirements and cuts on the TRT H_T fraction, which is the scalar sum of all transverse energies in the cluster. The efficiency is about 85%.

- Tight++ has shower shape cuts that are the same as or tighter than medium++ and additionally it imposes cuts on the cluster energy to track momentum ratio E/p, $\Delta\phi$ track-cluster matching and $d_0 < 1$ mm. The efficiency is about 78%.

In order to accurately reconstruct the energy deposited in the EM calorimeter, the electron cluster energy is calibrated by accounting for the energy deposited in the material before the EM calorimeter, in the cluster itself, outside the cluster as lateral leakage and beyond the EM calorimeter as longitudinal leakage. The overall scale is refined using test-beam data and the Z boson mass in $Z \to e^+e^-$ events. Systematic uncertainties associated to electron reconstruction, identification and trigger will be discussed in the relevant analyses in chapters 8 and 9.

7.4 Muons

The ATLAS muon reconstruction algorithms use the ID, the calorimeter and the MS. The ID can track up to $|\eta| < 2.5$ and the MS up to $|\eta| < 2.7$. There are two main muon reconstruction algorithms used within ATLAS which lead to two different muon collections called Muid [142] and Staco [143, 144]. The track reconstruction and the matching procedure is different for these two algorithms but the resolution and efficiency performance for physics analysis is comparable. In this thesis, only Staco muons were used and so this algorithm will be described in detail. The reconstruction distinguishes between four different muon types which are shown in figure 7.2.

- *Standalone* (SA) (also called *MuonBoy* in the Staco collection) muons are reconstructed if there is only a track reconstructed in the MS. The track is then back-extrapolated to the IP while taking into account multiple scattering and energy loss dE/dx in the ID and the calorimeter. This method is relevant for high momentum as very low momentum muons may not penetrate to the MS stations.

- *Calo-tagged* muons are reconstructed if ID tracks can be matched with calorimeter energy deposits of minimum ionising particles[2]. They are most effective at low p_T.
- *Segment-tagged* (ST – also called *MuTag* in the Staco collection) muons are reconstructed if hits in the MS can be matched to reconstructed ID tracks. This is done by extrapolating the ID track into the inner MS station and associating it to nearby reconstructed track segments. These muons are useful because not every MS layer might have recorded hits due to extended dead material in the transition and feet regions of the MS and for low p_T (< 6 GeV) which might not reach the middle or outer layer as they can get bent outside of the detector acceptance.
- *Combined* (CB – often simply referred to as *Staco* muons in the Staco collection) muons are reconstructed if ID tracks can be matched with MS tracks, the measurements from the two systems are then combined. These muons have the best resolution and the lowest fake rate, as the combination of tracks significantly improves the resolution for $p_T < 100$ GeV and suppresses backgrounds from punch-through or from pion or kaon decays in flight.

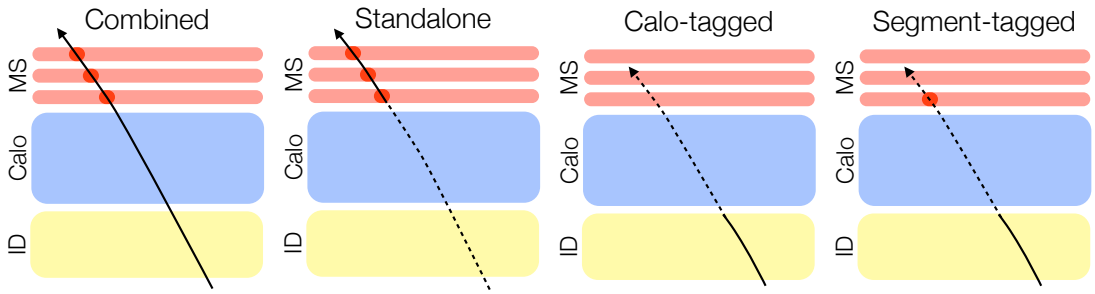

Figure 7.2: Different reconstructed muon types.

The muon reconstruction starts with building seeds to search for segments in the MS. This is done by looking for hits in the RPC and TGC trigger chambers in windows of 0.4×0.4 in $\eta \times \phi$ space. The raw data from all the muon chambers are then pre-processed and used for pattern finding and to build segments. A segment is defined as a straight line in a single chamber. The segments from the different stations are combined to form a muon track candidate using 3D tracking in the magnetic field and global track fitting using full hit information.

The reconstructed muons can have different quality levels [145]. Staco combined muons are of *tight* quality whereas MuTag muons can be of *loose* or *tight* quality depending on the quality of the segments. If a MuTag only has one segment in the $|\eta| > 1.05$ region without any TGC ϕ hits then the quality is loose. If a MuTag muon has at least three TGC ϕ hits in its segments or it has at least two segments then the quality is tight.

In the analyses described here, CB and ST muons of loose and tight quality are used and additional information is therefore given for these muon types. CB muons are identified

[2] A muon can traverse and will deposit energy in every calorimeter layer but only with a small signal. Low p_T hadrons will deposit most energy in the first layers and almost none in the last layers, high p_T hadrons and electrons will deposit a lot of energy and can be vetoed [60].

by a χ^2 match, defined as the difference between MS and ID track vectors weighted by their combined covariance matrix. This gives a measure of the quality of the match and the pairs with the lowest χ^2 are kept. The combined track vector is formed by statistical combination of the MS and ID track vectors. The ST muon reconstruction only uses segments that are not used for SA or CB muons. It matches these segments to ID tracks in the η and ϕ directions, which are taken from the ID track measurement only. The algorithm extrapolates all ID tracks above a certain momentum out to the first MS station and looks for close-by segments. It defines a tag χ^2 using the difference between the prediction from the track extrapolation and any nearby segment.

There is an additional segment-tagging algorithm, called MuGirl [146], which is used in the trigger and works in a similar way but uses an artificial neural network to identify hits rather than a χ^2. An important difference in the reconstruction chain between MuTag and MuGirl is that MuGirl uses all ID tracks and reruns the segment finding close to the track whereas MuTag only uses ID tracks and MS segments that were not used by Staco. MuTag is therefore complementary to Staco whereas MuGirl tries to reconstruct all muons itself.

7.5 Jets

In the $W^{\pm}Z \to \ell^{\pm}\nu\ell^{+}\ell^{-}$ analysis, jets are only used to ensure good $E_{\mathrm{T}}^{\mathrm{miss}}$ reconstruction by removing events, in data and in simulation, with jets that have a poor calorimeter performance. These are so-called "bad looser" jets which are most likely not associated to real energy deposits in the calorimeters. They can be caused by hardware problems or they are background events from LHC beam conditions or cosmic-ray showers. For the graviton search, jets with a default size of $R = 0.4$ are used and cuts on jet p_{T} and jet mass are applied. It is therefore necessary to take into account a set of systematic uncertainties associated to jet energy scale (JES), jet energy resolution (JER) and additionally jet mass scale (JMS) and jet mass resolution (JMR). Only the first of these will be touched on briefly here, more details will be given in chapter 9.

Jets are built from topological clusters (topo-clusters) which are formed from a set of calorimeter cells according to a three-step algorithm. First, the algorithm identifies a list of seeds. These are all the calorimeter cells that have a signal (usually the cell energy deposition) to noise (the expected RMS of the electronics noise) ratio above a certain threshold t_{seed}. The contribution from pile-up is taken into account here and added in quadrature to the noise. Secondly, all the cells neighbouring these seeds are added if they in turn satisfy a certain signal to noise ratio with a threshold $t_{\mathrm{neighbour}}$. Lastly, all the neighbours of the so-formed clusters are added if they are above t_{cell}. In the case of hadronic calorimeter clusters, the standard ATLAS parameters for the $t_{\mathrm{seed}}/t_{\mathrm{neighbour}}/t_{\mathrm{cell}}$ thresholds[3] are in the ratio 4/2/0 [139, 147]. This threshold approach of the algorithm efficiently suppresses calorimeter noise. The topo-clusters at the electromagnetic scale, which is determined from the response of electrons in the LAr and Tile calorimeters in test beam data, are the input for the anti-k_{T} jet reconstruction algorithm [108, 148] with a distance parameter of $R = 0.4$ (or $R = 0.6$) which is infrared and

[3]Since t_{cell} is taken as 0 for the hadronic cluster this is essentially equivalent to adding all the cells adjacent to a cluster. For EM clusters the ratios are 6/3/3.

collinear safe. The lowest p_{T} threshold for jet reconstruction is 7 GeV.

The jets are calibrated based on their p_{T} and η to correct for energy losses due to the applied thresholds, detector acceptance and dead material. The aim of the calibration is to, on average, provide a correct measurement of the energy across the detector independent of pile-up. The simplest calibration scheme, called the EM+JES calibration scheme, estimates the systematic uncertainty from single hadron response measurements and systematic MC variations. The JES correction relates the calorimeter response to the true jet energy at production. The EM+JES scheme consists of three subsequent steps, a pile-up correction, a vertex correction and a jet energy and direction correction.

The η and p_{T} dependent JES systematic uncertainty is estimated by using the p_{T} balance between central and forward jets in dijet events and by computing variations between different MC simulations. For $|\eta| < 0.8$ the uncertainty is less than 2.5% for jets with $60 \leq p_{\mathrm{T}} < 800$ GeV jets, while for $3.2 \leq |\eta| < 4.5$ it can be up to 14% for $p_{\mathrm{T}} < 30$ GeV.

7.6 Missing Transverse Energy

$E_{\mathrm{T}}^{\mathrm{miss}}$ is computed using information from energy depositions in the calorimeter topo-clusters and muons reconstructed in the MS [149, 150]. The missing transverse component is built from the missing x and y components according to

$$E_{\mathrm{T}}^{\mathrm{miss}} = \sqrt{\left(E_x^{\mathrm{miss}}\right)^2 + \left(E_y^{\mathrm{miss}}\right)^2} \tag{7.1}$$

where the missing x and y components in turn are

$$E_{x(y)}^{\mathrm{miss}} = E_{x(y)}^{\mathrm{miss,calo}} + E_{x(y)}^{\mathrm{miss},\mu} \tag{7.2}$$

and the azimuthal angle of the $E_{\mathrm{T}}^{\mathrm{miss}}$ is

$$\phi^{\mathrm{miss}} = \arctan\left(\frac{E_y^{\mathrm{miss}}}{E_x^{\mathrm{miss}}}\right). \tag{7.3}$$

The calorimeter term is made of many independently calibrated terms of all objects that deposit energy in the calorimeter as follows

$$E_{x(y)}^{\mathrm{miss,calo}} = E_{x(y)}^{\mathrm{miss,e}} + E_{x(y)}^{\mathrm{miss},\gamma} + E_{x(y)}^{\mathrm{miss},\tau} + E_{x(y)}^{\mathrm{miss,jets}} + E_{x(y)}^{\mathrm{miss,softjets}} + E_{x(y)}^{\mathrm{miss,cellout}} + \left(E_{x(y)}^{\mathrm{miss,calo}\mu}\right). \tag{7.4}$$

These objects are electrons, photons, hadronically decaying τ leptons, all with $p_{\mathrm{T}} > 10$ GeV, soft ($7 < p_{\mathrm{T}} < 20$ GeV) and hard ($p_{\mathrm{T}} > 20$ GeV) jets. The cellout term is to account for energy deposits in cells that are not associated to a specific physics object. The calorimeter muon term accounts for energy lost by muons in the calorimeter, this term is not always added and the different cases will be discussed below. Each term is built by taking the negative sum over all the calibrated calorimeter cells contributing to this object up to $|\eta| < 4.5$ as

$$E_x^{\mathrm{miss,term}} = -\sum_{i=1}^{N_{\mathrm{cells}}^{\mathrm{term}}} E_i \sin\theta_i \cos\phi_i \tag{7.5}$$

$$E_y^{\text{miss,term}} = -\sum_{i=1}^{N_{\text{cells}}^{\text{term}}} E_i \sin\theta_i \sin\phi_i. \tag{7.6}$$

The muon term

$$E_{x(y)}^{\text{miss},\mu} = -\sum_{\text{muons}} p_{x(y)}^{\mu} \tag{7.7}$$

is calculated using the momenta of all reconstructed muon tracks within $|\eta| < 2.7$. This includes CB and ST muons as well as SA muons within $2.5 < |\eta| < 2.7$ where no ID tracks are available. The isolation of a muon is determined by the amount of energy in calorimeter cells or ID tracks within $\Delta R < 0.3$ of the muon. For isolated muons, the combined ID and MS momentum measurement is used, which already takes into account the energy in the calorimeter, and so the last term in equation 7.4 is not needed. For non-isolated muons, the energy deposited in the calorimeter cells cannot be unambiguously associated to the muons and so the MS momentum measurement is used. The muon has already lost energy in the calorimeter when the MS track is determined and so the $E_{x(y)}^{\text{miss,calo}\mu}$ term needs to be added back. If there is however a significant mis-match between the combined and MS measurement, the combined value is used and a parametrized muon calorimeter term subtracted.

Chapter 8

$W^{\pm}Z \to \ell^{\pm}\nu\ell^{+}\ell^{-}$ Analysis

This chapter presents a measurement of $W^{\pm}Z$ production in p-p collisions at $\sqrt{s} =$ 7 TeV with the ATLAS detector. The analysis uses fully leptonic events with electrons, muons and missing transverse momentum in the final state. The first $W^{\pm}Z$ cross section measurement and limits on anomalous couplings in ATLAS used 1.0 fb^{-1} of 7 TeV data [92]. The result documented in this thesis supersedes this previous measurement and uses the full 4.6 fb^{-1} of data collected in 2011. A more precise cross section measurement, more stringent aTGC limits and the first unfolded diboson distributions in ATLAS are presented [151]. Extensive motivation for studying diboson production was given in chapter 3. Other than being an important, irreducible background for Higgs boson production and NP searches, $W^{\pm}Z$ production tests the electroweak structure of the SM at high energies, and precise inclusive and differential cross section measurements help frame EW predictions. $W^{\pm}Z$ production is directly sensitive to the WWZ TGC vertex which offers a generic test of the TeV scale.

This chapter is organised as follows. Section 8.1 defines the $W^{\pm}Z$ signal and theoretical cross section in detail, sections 8.2 and 8.3 list the data and MC samples and section 8.4 covers the lepton triggers used in the analysis. Sections 8.5 and 8.6 explain how physics objects and events are selected and section 8.7 shows the resulting selection acceptance. The $W^{\pm}Z$ signal in fully leptonic channels is small but the selection also results in relatively small backgrounds. The main backgrounds, discussed in section 8.8, can be separated into two categories: those with three or more prompt leptons, such as ZZ production, for which the detector acceptance and kinematic distributions are well modelled in MC, and those that contain two prompt leptons and at least one "fake" lepton. These are mainly Z+jets and $t\bar{t}$ production where the background rates depend on jet production and jet fragmentation, which are not well modelled in MC and are therefore estimated using data-driven techniques. Section 8.9 describes the systematic uncertainties taken into account for this analysis and section 8.10 presents the resulting numbers of observed and expected events as well as kinematic distributions of different variables. The fiducial and total cross section extraction, explained in section 8.11, relies on a maximum likelihood fit using the number of observed events in each channel. Section 8.12 presents the aTGC frequentist limit setting procedure and results using the Z boson p_{T} spectrum. Section 8.13 shows the unfolded $W^{\pm}Z$ distributions which can be compared to a specific model or to data from other experiments. They complement the aTGC limits, which do not rely on a specific physics model but are sensitive to the ATLAS detector

reconstruction.

8.1 Signal and Theoretical Cross Section

The LO diagrams contributing to the $W^{\pm}Z$ process are shown in figure 8.1. The higher-order diagrams have been discussed in chapter 3 and NLO corrections are on the order of 75% of the LO cross section. The contributions from incoming $q\bar{q}$ and qg annihilation is estimated to be about 85% and 15%, respectively, while the $\bar{q}g$ contribution is negligible as expected from the PDF content at the LHC [71].

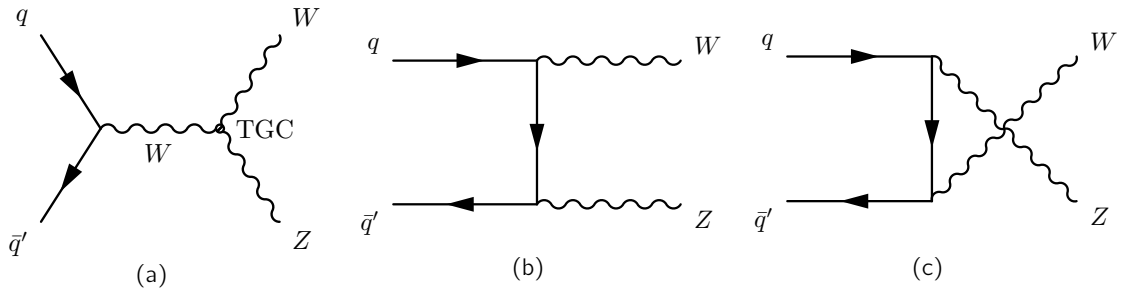

Figure 8.1: The SM tree-level Feynman diagrams for $W^{\pm}Z$ production through the (a) s-, (b) t-, and (c) u-channel exchanges in $q\bar{q}$ interactions at hadron colliders.

The branching ratios (BR) for $W^{\pm}Z$ production can be derived by multiplication of the separate $W^{\pm}$ and Z boson decay BRs [32]. The exact numbers for leptonic, hadronic and invisible decays are listed in table 8.1 and visualised in figure 8.2. This measurement uses fully leptonic final states with electrons, muons and $E_{\mathrm{T}}^{\mathrm{miss}}$ which leads to the four channels $e\nu ee$, $e\nu\mu\mu$, $\mu\nu ee$ and $\mu\nu\mu\mu$[1], and an experimentally available branching fraction of about 1.5%.

Given the presence of Z/γ^* interference in $W^{\pm}Z$ production, the concept of a "total $W^{\pm}Z$ cross section" needs to be defined carefully. Figure 8.3 shows the $W^{\pm}Z$ cross section as a function of the dilepton invariant mass, $m_{\ell\ell}$, for the MC@NLO [80] and `POWHEG BOX` [84] generators. The latter includes the γ^* contribution whereas the former does not. In this figure, a $m_{\ell\ell} > 10$ GeV requirement is applied, since without such a cut the cross section has a singularity at zero. Since most of the Z boson mass peak is contained within this range and for consistency with previous ATLAS measurements of the inclusive Z boson cross section, a window of $66 < m_{\ell\ell} < 116$ GeV is chosen for the total $W^{\pm}Z$ cross section.

The motivation for measuring a *fiducial* cross section and the exact definition of the fiducial phase space will be detailed in section 8.11.1. For completeness, the fiducial cross section expectation will be quoted here along with the total cross section expectation. For sake of comparison of MC@NLO to MCFM, for which no particle-level samples are available, only parton-level four-vector information is used for the numbers quoted in this section. This implies that they do not take into account FSR or parton showering and differ from the final state

[1] In the following, this is often abbreviated to eee, $e\mu\mu$, μee and $\mu\mu\mu$ where the presence of a neutrino from the $W^{\pm}$ boson decay is assumed.

Decay mode	Branching fraction [%]
$W^{\pm} \to \ell^{\pm}\nu$	10.80 ± 0.09
$W^{\pm} \to q\bar{q}'$	67.60 ± 0.27
$Z \to \ell^{+}\ell^{-}$	3.3658 ± 0.0023
$Z \to \nu\bar{\nu}$	20.00 ± 0.06
$Z \to q\bar{q}$	69.91 ± 0.06
$W^{\pm}Z \to \ell^{\pm}\nu\ell'^{+}\ell'^{-}$	0.364 ± 0.003
$W^{\pm}Z \to \ell^{\pm}\nu\nu\bar{\nu}$	2.16 ± 0.02
$W^{\pm}Z \to \ell^{\pm}\nu q\bar{q}$	7.55 ± 0.06
$W^{\pm}Z \to q\bar{q}'\ell^{+}\ell^{-}$	2.275 ± 0.009
$W^{\pm}Z \to q\bar{q}'\nu\bar{\nu}$	13.52 ± 0.07
$W^{\pm}Z \to q\bar{q}'q\bar{q}$	47.26 ± 0.19

Table 8.1: Branching fractions for $W^{\pm}$, Z and $W^{\pm}Z$ production. For leptonic decays the numbers are per lepton flavour.

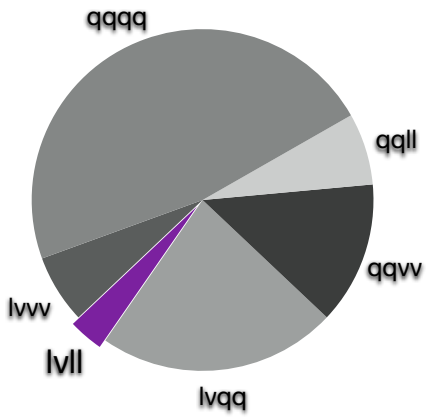

Figure 8.2: Branching fractions for $W^{\pm}Z$ production. For leptonic decays the numbers include all three lepton flavours.

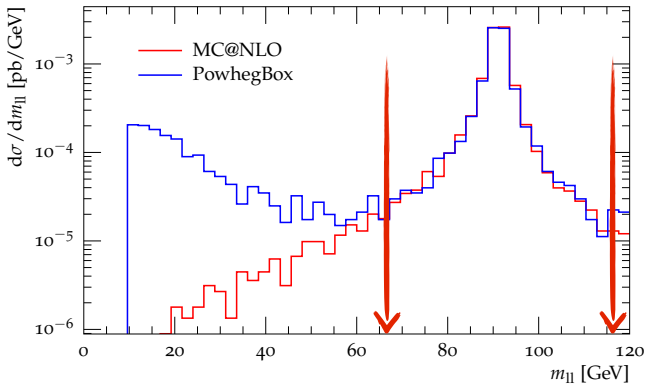

Figure 8.3: $m_{\ell\ell}$ distribution for $W^{\pm}Z$ production for MC@NLO and `POWHEG BOX`.

particle-level fiducial cross section. This difference is taken into account and will be explained in section 8.7. Table 8.2 summarises the SM cross section computed with MCFM and MC@NLO. CT10 is used as the nominal PDF. The QCD renormalization μ_r and factorization μ_f scales in MCFM are set to

$$\mu_r = \mu_f = \frac{1}{2}(m_W + m_Z) = 85.7863 \text{ GeV} \tag{8.1}$$

and in MC@NLO they are dynamically set event-by-event to

$$\mu^2 = \frac{1}{2}\left[m_W^2 + p_{\mathrm{T},W}^2 + m_Z^2 + p_{\mathrm{T},Z}^2\right]. \tag{8.2}$$

	σ(MCFM) [pb]		σ(MC@NLO) [pb]	
PDF	total	fiducial	total	fiducial
CT10	17.61±0.03	6.18±0.03	17.28	6.14
CTEQ6.6	17.39±0.03	6.10±0.03	17.07	6.02
MSTW 2008	17.98±0.03	6.39±0.04	17.69	6.31
NNPDF2.0	17.67±0.03	6.22±0.02	17.42	6.18
NNPDF2.1	18.11±0.03	6.34±0.03	17.82	6.32

Table 8.2: The SM cross sections for $pp \to W^{\pm}Z$ at $\sqrt{s} = 7$ TeV computed with MCFM and MC@NLO. The uncertainties are statistical.

The systematic uncertainties on the MCFM cross sections have been evaluated.

- The statistical uncertainties are negligible.
- The PDF uncertainty is computed using the CT10 eigenvectors ($i = 1 \ldots 52$) and adding

the differences in quadrature, separately for positive and negative, as

$$\sigma_{+} = \sum_{i=1}^{52} \max(\sigma_{WZ}^{i} - \sigma_{WZ}^{\text{default}}, 0)^2, \quad (8.3)$$

$$\sigma_{-} = \sum_{i=1}^{52} \min(\sigma_{WZ}^{i} - \sigma_{WZ}^{\text{default}}, 0)^2. \quad (8.4)$$

The resulting uncertainty is $^{+3.1}_{-3.9}$% for the total cross section and $^{+2.1}_{-6.5}$% for the fiducial cross section. It should be noted that this procedure is prone to accumulation of statistical fluctuations and may lead to an overestimation of the result. The nominal CT10 set is compared to other PDF sets, the largest variation occurring for NNPDF2.1 and CTEQ 6.6 which give a larger and smaller cross section, respectively. The change from CT10 to NNPDF2.1 is +2.1% for the total and fiducial cross sections while CTEQ 6.6 has been superseded by CT10. It was checked that no other PDF set produces smaller cross sections than CT10. Since these changes to other sets are covered by the PDF uncertainties computed with the CT10 eigenvectors as described above, they are not included separately in the systematic uncertainty estimation.

- The μ_r and μ_f scales are varied simultaneously up and down by factors of $\times 2$ and $\times 0.5$. The resulting differences are $^{+5.3}_{-4.0}$% for the total cross section and $^{+4.7}_{-4.2}$% for the fiducial cross section. As already mentioned, MCFM and MC@NLO differ in the treatment of the renormalization and factorization scales. In MC@NLO, the scale is chosen for each event according to equation 8.2 while MCFM does not offer this setting out of the box. It does however offer a possibility of using the $W^{\pm}Z$ invariant mass as the scale. For $W^{\pm}Z$ production, this results in $\mu > m_W + m_Z$ and a reduction of the predicted cross section by up to -6.7%. The effect of fixed versus dynamic scale was investigated by manually implementing equation 8.2 into MCFM 6.2. The difference was -2.3% in the total cross section which is considered covered by the scale uncertainty of $^{+5.3}_{-4.2}$% evaluated earlier.

- The strong coupling constant α_s is varied by ± 0.001 which results in changes of the total and fiducial cross section of $^{+0.2}_{-0.5}$% and $^{+0.6}_{-0.8}$%, respectively.

Combining all the above, the SM predictions for the NLO fiducial and total $W^{\pm}Z$ cross sections are found to be $\sigma_{WZ}^{\text{fid}} = 6.18^{+0.35}_{-0.48}$ pb and $\sigma_{WZ}^{\text{tot}} = 17.6^{+1.1}_{-1.0}$ pb, respectively.

8.2 Data Samples

This analysis uses a data sample of proton-proton collisions collected with the ATLAS detector at the LHC between April and October 2011 at $\sqrt{s} = 7$ TeV. Based on the date of collection, the data is organised into so-called data periods labelled from D to M. An event is selected for physics analysis based on certain data quality criteria required per luminosity block, the so-called *Good Runs List* (GRL)[2] [152]. This ensures good performance of the

[2]For completeness, the specific GRL used is
`data11_7TeV.periodAllYear_DetStatus-v36-pro10_CoolRunQuery-00-04-08_WZjets_allchannels_DtoM.xml`.

magnets, the different subdetectors (ID, calorimeter, MS, luminosity detectors) and the TDAQ system. The GRL also ensures that a collision took place in the event by requiring that every colliding bucket contains protons. The resulting integrated luminosity as reported by the ATLAS luminosity calculation tool [153] is 4.64 fb^{-1}. The preliminary luminosity uncertainty for 2011 data is 1.8% [129].

The analysis uses two different data streams recorded by the muon and electron trigger menus. By construction, an event can appear in both streams. In the analysis, this potential overlap is handled by removing an event from the electron stream if it already appeared in the muon stream. The exact trigger chains used will be listed in section 8.4. The offline reconstruction is performed with Athena [154] release 17.0. The reconstruction takes into account the six missing front-end boards of the calorimeter during data periods E to H.

8.3 Monte Carlo Samples

8.3.1 Signal

The $W^{\pm}Z$ diboson signal samples with fully leptonic decays are modelled by the MC@NLO 4.0 [80] event generator using the CT10 PDF set. MC@NLO incorporates the full NLO QCD matrix element calculation with the parton shower by interfacing to the HERWIG /Jimmy [155] programs. The smooth matching between the hard emission and the parton shower ensure that there is no double-counting. As mentioned in chapter 3, full spin correlations and $W^{\pm}$ and Z boson widths are included in the generator but the γ^* interference contribution is not. The gauge-boson decays into τ leptons are included in the event generator and the τ-lepton decays to all possible final states are simulated with Tauola [156]. Photos [157] is used to model QED FSR. Table 8.3 lists the $W^{\pm}Z$ MC signal samples used in this analysis. Samples with MC ID 126089-126106 are produced at aTGC values $\Delta g_1^Z = 0$, $\Delta\kappa^Z = 0$, $\lambda^Z = 0.13$ and a cut-off value of $\Lambda = 100$ TeV. The SM samples are used in the cross section analysis to calculate the selection acceptance and efficiency. The aTGC samples are used for the aTGC limit extraction. The signal cross sections listed in table 8.3 are not used for the final cross section prediction as the signal samples are scaled to the predicted MCFM cross section quoted in the previous section to account for the contribution from Z/γ^* interference.

8.3.2 Backgrounds

Major backgrounds to $W^{\pm}Z$ production, listed in order of decreasing importance, come from $W^{\pm}$ or Z boson production in association with jets (V+jets), ZZ production, top quark events and $W^{\pm}$ or Z boson production in association with a photon. V+jets samples, listed in tables 8.5 and 8.6, and events with dileptons from Drell-Yan production in the range $10 < m_{\ell\ell} < 40$ GeV, listed in table 8.5, are simulated using Alpgen [158]. Top quark related samples are listed in table 8.4. MC@NLO is used to model $t\bar{t}$ and single top events, MadGraph [159] for $t\bar{t} + V$ events. Events with heavy flavour dijets, listed in table 8.4, are modeled with PythiaB [160] which provides a convenient front-end to Pythia to filter and speed up the simulation of B physics events. The diboson processes are listed in table 8.7. WW

and ZZ are modelled with HERWIG and Pythia respectively, where the latter includes Z/γ^* contributions for both Z bosons with a mass cut of $m_{Z/\gamma^*} > 12$ GeV. $W/Z + \gamma$ production is modelled with Sherpa [161] for $\ell = e, \mu$ or with MadGraph for $\ell = \tau$. The background MC samples generally correspond to about 5-1000 fb^{-1} of integrated luminosity.

For all upcoming sample tables, the different columns list the MC ID run number, the physics process, the MC event generator name used to produce the events, the number of events in the sample, the k-factor, the filter efficiency and the cross section. Whenever LO event generators are used, the cross-sections are multiplied by k-factors to correct to NLO or NNLO (if available) matrix element calculations [162]. The MC filter is an event selection applied at the generator level and the corresponding filter efficiencies ϵ_{filter} are given in the table. The listed cross sections do not include k-factors or filter efficiencies.

MCID	Process	Generator	Events	k-factor	ϵ_{filter}	σ [pb]
126053	$W^+Z \to e\nu ee$	MC@NLO	49999	1.0	1.0	0.04114
126054	$W^-Z \to e\nu ee$	MC@NLO	50000	1.0	1.0	0.02243
126055	$W^+Z \to e\nu\mu\mu$	MC@NLO	49999	1.0	1.0	0.04114
126056	$W^-Z \to e\nu\mu\mu$	MC@NLO	49900	1.0	1.0	0.02243
126057	$W^+Z \to e\nu\tau\tau$	MC@NLO	50000	1.0	1.0	0.04114
126058	$W^-Z \to e\nu\tau\tau$	MC@NLO	49950	1.0	1.0	0.02243
126059	$W^+Z \to \mu\nu ee$	MC@NLO	49999	1.0	1.0	0.04114
126060	$W^-Z \to \mu\nu ee$	MC@NLO	50000	1.0	1.0	0.02243
126061	$W^+Z \to \mu\nu\mu\mu$	MC@NLO	49950	1.0	1.0	0.04114
126062	$W^-Z \to \mu\nu\mu\mu$	MC@NLO	50000	1.0	1.0	0.02243
126063	$W^+Z \to \mu\nu\tau\tau$	MC@NLO	49950	1.0	1.0	0.04114
126064	$W^-Z \to \mu\nu\tau\tau$	MC@NLO	50000	1.0	1.0	0.02243
126065	$W^+Z \to \tau\nu ee$	MC@NLO	49999	1.0	1.0	0.04114
126066	$W^-Z \to \tau\nu ee$	MC@NLO	49949	1.0	1.0	0.02243
126067	$W^+Z \to \tau\nu\mu\mu$	MC@NLO	50000	1.0	1.0	0.04114
126068	$W^-Z \to \tau\nu\mu\mu$	MC@NLO	50000	1.0	1.0	0.02243
126069	$W^+Z \to \tau\nu\tau\tau$	MC@NLO	49950	1.0	1.0	0.04114
126070	$W^-Z \to \tau\nu\tau\tau$	MC@NLO	50000	1.0	1.0	0.02243
126089-97	$W^+Z \to \ell\nu\ell\ell$	MC@NLO	$\approx$ 49995	1.0	1.0	0.05516
126098-106	$W^-Z \to \ell\nu\ell\ell$	MC@NLO	$\approx$ 49995	1.0	1.0	0.02849

Table 8.3: The $W^{\pm}Z$ MC signal samples, ℓ denotes e, μ and τ.

8.3.3 Pile-up Reweighting

The dense bunch train structure of the proton beams at the LHC leads to pile-up, which are multiple inelastic collisions in a given bunch crossing. The MC reconstruction needs to take these additional events into account and simulates pile-up events on top of each hard scattering collision. The MC simulation is divided into four periods to reflect data-taking conditions as closely as possible. The fraction of data represented by the different periods is 3.2% for periods B – D, 17.4% for periods E – H, 25.8% for periods I – K and 53.5% for periods L – M. The bunch spacing is 50 ns and the average number of interactions per bunch crossing μ for the different periods is shown in figure 8.4(a). These simulated conditions are

MCID	Process	Generator	events	k-factor	ϵ_{filter}	σ [pb]
105200	$t\bar{t}$	MC@NLO	14983835	1.0	0.55551	166.8
119353	$t\bar{t} + W^{\pm}$	MadGraph	100000	1.3	1.0	0.12444
119355	$t\bar{t} + Z$	MadGraph	99997	1.3	1.0	0.095581
108340	t-channel$\to$e	MC@NLO	299998	1.0	1.0	7.1522
108341	t-channel$\to \mu$	MC@NLO	299999	1.0	1.0	7.1767
108342	t-channel$\to \tau$	MC@NLO	299999	1.0	1.0	7.1277
108343	s-channel$\to$e	MC@NLO	299948	1.0	1.0	0.46856
108344	s-channel$\to \mu$	MC@NLO	299998	1.0	1.0	0.46837
108345	s-channel$\to \tau$	MC@NLO	299899	1.0	1.0	0.46978
108346	Wt	MC@NLO	899694	1.0	1.0	13.102
105757	bbcc $\mu\mu$	PythiaB	296599	1.0	1.0	2830.3
105758	bbcc μe	PythiaB	795695	1.0	1.0	4017.1
105759	bbcc ee	PythiaB	290995	1.0	1.0	1693.0

Table 8.4: MC samples used to model top (including $t\bar{t}$ and single top) quark production and dijet backgrounds.

an expected projection done before data taking and do not exactly reflect the data conditions. This can be seen by comparing figure 8.4(a) to figure 5.3.

An event-by-event pile-up reweighting is applied to MC to take this pile-up difference correctly into account. It attempts to make the average μ distribution in MC look as much as possible like the average μ distribution in data while keeping the total sum of weights unchanged. It should be noted that the granularity of the μ distribution in MC is coarser than in data. The pile-up weight is determined based on the luminosity of data collected for a certain μ value. Figure 8.4(b) shows the number of primary vertices in $Z \to ee$ and $Z \to \mu\mu$ events that satisfy $|m_{\ell\ell} - m_Z| < 10$ GeV for data and for pile-up reweighted MC distributions. The exact selection requirements for these samples will be described in sections 8.5 and 8.6.

8.4 Trigger

8.4.1 Trigger Chains

The ATLAS trigger system was described in detail in section 6.6. The p_{T} thresholds of single lepton triggers was low enough during 2011 data taking that these chains could be used for the $W^{\pm}Z$ analysis without any decrease in signal acceptance. The three high p_{T} leptons in $W^{\pm}Z$ events push the probability for event triggering close to the 100% mark. A $W^{\pm}Z$ candidate can be recorded by a single muon or a single electron trigger.

The trigger chains used in this analysis vary for different data taking periods. The single muon trigger chains used are EF_mu18_MG during periods D – I and EF_mu18_MG_medium during periods J – M. The single electron trigger chains used are EF_e20_medium during periods D – J, EF_e22_medium during period K and EF_e22vh_medium1 || EF_e45_medium1, where vh indicates that hadronic leakage and dead material corrections were applied at the L1 trigger stage, during periods L – M. The OR in the last electron trigger helps to increase the trigger efficiency at high p_{T}. The L1 trigger seeds are L1_MU10 and L1_MU11 for muon

MCID	Process	Generator	Events	k-factor	ϵ_{filter}	σ [pb]
107650	$Z \to ee$ Np0	Alpgen	6618284	1.25	1.0	668.32
107651	$Z \to ee$ Np1	Alpgen	1334897	1.25	1.0	134.36
107652	$Z \to ee$ Np2	Alpgen	2004195	1.25	1.0	40.54
107653	$Z \to ee$ Np3	Alpgen	549949	1.25	1.0	11.16
107654	$Z \to ee$ Np4	Alpgen	149948	1.25	1.0	2.88
107655	$Z \to ee$ Np5	Alpgen	50000	1.25	1.0	0.83
107660	$Z \to \mu\mu$ Np0	Alpgen	6615230	1.25	1.0	668.68
107661	$Z \to \mu\mu$ Np1	Alpgen	1334296	1.25	1.0	134.14
107662	$Z \to \mu\mu$ Np2	Alpgen	1999941	1.25	1.0	40.33
107663	$Z \to \mu\mu$ Np3	Alpgen	549896	1.25	1.0	11.19
107664	$Z \to \mu\mu$ Np4	Alpgen	150000	1.25	1.0	2.75
107665	$Z \to \mu\mu$ Np5	Alpgen	50000	1.25	1.0	0.77
107670	$Z \to \tau\tau$ Np0	Alpgen	10613179	1.25	1.0	668.40
107671	$Z \to \tau\tau$ Np1	Alpgen	3334137	1.25	1.0	134.81
107672	$Z \to \tau\tau$ Np2	Alpgen	1004847	1.25	1.0	40.36
107673	$Z \to \tau\tau$ Np3	Alpgen	509847	1.25	1.0	11.25
107674	$Z \to \tau\tau$ Np4	Alpgen	144999	1.25	1.0	2.79
107675	$Z \to \tau\tau$ Np5	Alpgen	45000	1.25	1.0	0.77
116250	$Z \to ee$ Np0	Alpgen/Jimmy	994949	1.22	1.0	3051.62
116251	$Z \to ee$ Np1	Alpgen/Jimmy	299998	1.22	1.0	87.87
116252	$Z \to ee$ Np2	Alpgen/Jimmy	999946	1.22	1.0	41.10
116253	$Z \to ee$ Np3	Alpgen/Jimmy	149998	1.22	1.0	8.38
116254	$Z \to ee$ Np4	Alpgen/Jimmy	40000	1.22	1.0	1.85
116255	$Z \to ee$ Np5	Alpgen/Jimmy	10000	1.22	1.0	0.46
116260	$Z \to \mu\mu$ Np0	Alpgen/Jimmy	999849	1.22	1.0	3051.62
116261	$Z \to \mu\mu$ Np1	Alpgen/Jimmy	300000	1.22	1.0	87.87
116262	$Z \to \mu\mu$ Np2	Alpgen/Jimmy	999995	1.22	1.0	41.45
116263	$Z \to \mu\mu$ Np3	Alpgen/Jimmy	150000	1.22	1.0	8.38
116264	$Z \to \mu\mu$ Np4	Alpgen/Jimmy	39999	1.22	1.0	1.85
116265	$Z \to \mu\mu$ Np5	Alpgen/Jimmy	10000	1.22	1.0	0.46
109300	$(Z \to ee)bb$ Np0	Alpgen/Jimmy	409999	1.25	1.0	6.57
109301	$(Z \to ee)bb$ Np1	Alpgen/Jimmy	160000	1.25	1.0	2.48
109302	$(Z \to ee)bb$ Np2	Alpgen/Jimmy	60000	1.25	1.0	0.89
109303	$(Z \to ee)bb$ Np3	Alpgen/Jimmy	30000	1.25	1.0	0.39
109305	$(Z \to \mu\mu)bb$ Np0	Alpgen/Jimmy	409949	1.25	1.0	6.56
109306	$(Z \to \mu\mu)bb$ Np1	Alpgen/Jimmy	155000	1.25	1.0	2.47
109307	$(Z \to \mu\mu)bb$ Np2	Alpgen/Jimmy	60000	1.25	1.0	0.89
109308	$(Z \to \mu\mu)bb$ Np3	Alpgen/Jimmy	29999	1.25	1.0	0.39

Table 8.5: MC samples used to model Z+X processes, including Z+jets, Zbb+jets and Drell-Yan samples. NpX (X = 0...5) refers to the number of additional partons in the final state. Samples 116250-116265 have the following cuts applied, $10 < m_{\ell\ell} < 40$ GeV and $p_{\mathrm{T}} > 20$ GeV for at least one lepton.

MCID	Process	Generator	Events	k-factor	ϵ_{filter}	σ [pb]
107680	$W \to e\nu$ Np0	Alpgen	6952874	1.2	1.0	6921.60
107681	$W \to e\nu$ Np1	Alpgen	4998487	1.2	1.0	1304.30
107682	$W \to e\nu$ Np2	Alpgen	3768632	1.2	1.0	378.29
107683	$W \to e\nu$ Np3	Alpgen	1008947	1.2	1.0	101.43
107684	$W \to e\nu$ Np4	Alpgen	250000	1.2	1.0	25.87
107685	$W \to e\nu$ Np5	Alpgen	69999	1.2	1.0	7.0
107690	$W \to \mu\nu$ Np0	Alpgen	3462942	1.2	1.0	6919.60
107691	$W \to \mu\nu$ Np1	Alpgen	4998236	1.2	1.0	1304.20
107692	$W \to \mu\nu$ Np2	Alpgen	3768737	1.2	1.0	377.83
107693	$W \to \mu\nu$ Np3	Alpgen	1008446	1.2	1.0	101.88
107694	$W \to \mu\nu$ Np4	Alpgen	254950	1.2	1.0	25.75
107695	$W \to \mu\nu$ Np5	Alpgen	70000	1.2	1.0	6.92
107700	$W \to \tau\nu$ Np0	Alpgen	3418296	1.2	1.0	6918.60
107701	$W \to \tau\nu$ Np1	Alpgen	2499194	1.2	1.0	1303.20
107702	$W \to \tau\nu$ Np2	Alpgen	3750986	1.2	1.0	378.18
107703	$W \to \tau\nu$ Np3	Alpgen	1009946	1.2	1.0	101.51
107704	$W \to \tau\nu$ Np4	Alpgen	249998	1.2	1.0	25.64
107705	$W \to \tau\nu$ Np5	Alpgen	65000	1.2	1.0	7.04

Table 8.6: MC samples used to model W+jets processes. NpX (X = 0...5) in the process name refers to the number of additional partons in the final state.

MCID	Process	Generator	Events	k-factor	ϵ_{filter}	σ [pb]
105985	$W^{+}W^{-}$	HERWIG	2489244	1.52	0.38863	29.592
109292	ZZ	Pythia	149999	1.40	0.6235	0.07494
126013	$(W \to e\nu)\gamma$	Sherpa	399899	1.0	1.0	75.5
126014	$(W \to \mu\nu)\gamma$	Sherpa	399948	1.0	1.0	75.5
106003	$(W^{+} \to \tau\nu)\gamma$	Pythia /MadGraph	49999	1.75	1.0	25.4
108290	$(W^{-} \to \tau\nu)\gamma$	Pythia /MadGraph	50000	1.83	1.0	16.8
126015	$(Z \to ee)\gamma$	Sherpa	199899	1.0	1.0	14.7
126016	$(Z \to \mu\mu)\gamma$	Sherpa	199950	1.0	1.0	14.7
108325	$(Z \to \tau\tau)\gamma$	Pythia /MadGraph	49949	1.41	0.15	9.41

Table 8.7: MC samples used to model diboson backgrounds, including WW, ZZ, $W\gamma$ and $Z\gamma$. The Sherpa samples include up to one jet.

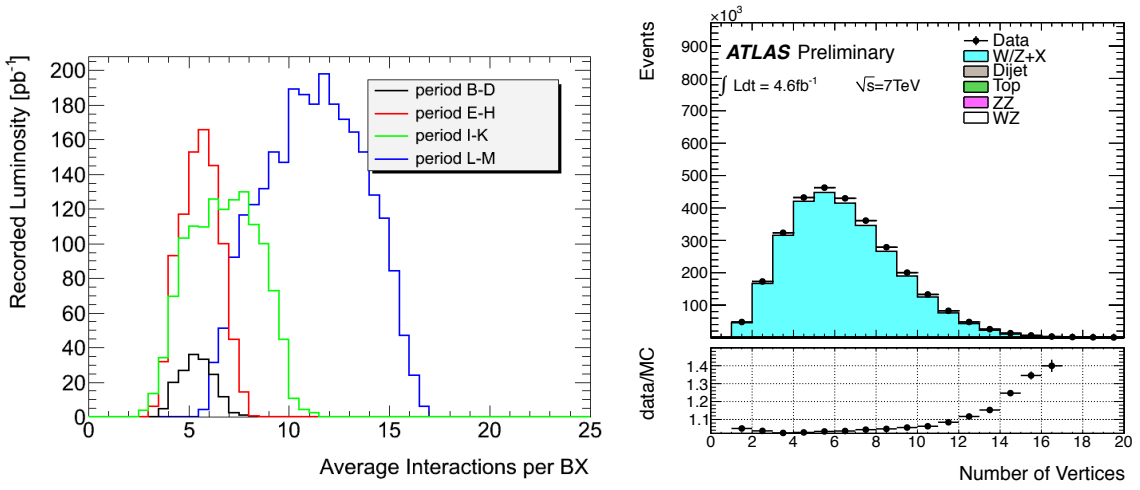

(a) (b)

Figure 8.4: (a) The average number of interactions per bunch crossing as a function of recorded luminosity for the four different period divisions in MC samples. (b) The number of primary vertices after pile-up reweighting has been applied for $Z \to \ell^{+}\ell^{-}$ events.

chains and L1_EM14, L1_EM16 and L1_EM16VH for the electron chains, listed in the same period categorisation as for the EF triggers. The L2 triggers have the same nomenclature as the EF triggers.

As an example, the efficiencies of the EF_mu18_MG_medium and EF_e20_medium triggers are shown in figures 8.5 and 8.6. The muon trigger efficiency is only about 70% in the barrel due to detector geometry discussed earlier, whereas the efficiency in the end-caps is above 90%. The electron efficiency is high and around 95% in the plateau region. For an event to be selected as a candidate at least one of the three final state muons (electrons) must be matched to a trigger object within $\Delta R < 0.1$ (0.15). To ensure that the trigger matching is not strongly p_{T} dependent, the matched lepton must lie in the trigger plateau region and has to satisfy p_{T} >20 (25) GeV for muons (electrons). Due to the presence of three leptons with large p_{T} the trigger efficiencies for $W^{\pm}Z$ events is higher than the single lepton trigger efficiency.

The efficiencies of these trigger chains are established using the Z boson tag-and-probe (ZTP) method, which is illustrated in figure 8.7. The basic idea relies on the fact that leptonically decaying Z bosons are "standard candles" that are easy to reconstruct with a high efficiency. As a first step, one of the leptons, called the tag lepton, needs to pass certain lepton quality requirements and be matched to a trigger object within a defined ΔR. Then, the corresponding lepton from the Z boson decay, called the probe lepton, is searched for. This lepton needs to fulfil the same quality requirements as the tag lepton except a trigger match is not required. The probe lepton additionally needs to have opposite charge to the tag lepton and together they need to make an invariant mass close to the Z boson pole mass. Once all these conditions are satisfied, the number of probes N_{p} is counted. The probe lepton is then

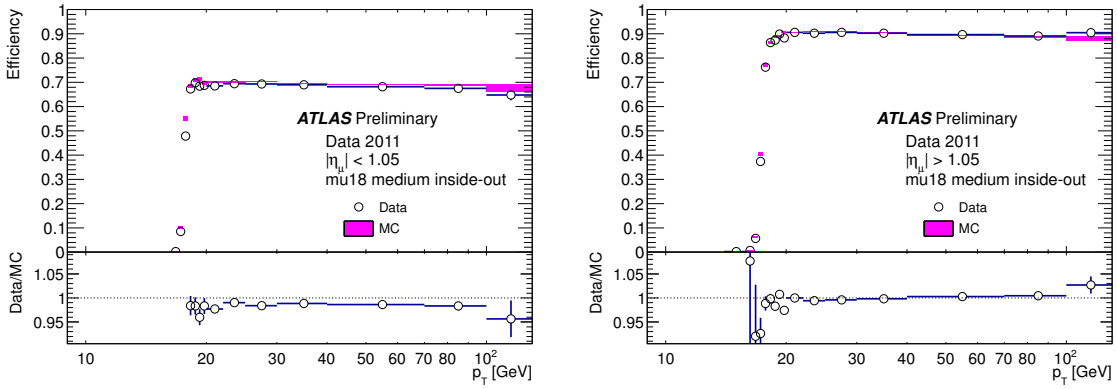

Figure 8.5: Muon trigger efficiency of the mu18_MG_medium chain as a function of p_{T} in the barrel (left) and in the end-caps (right) for 7 TeV data.

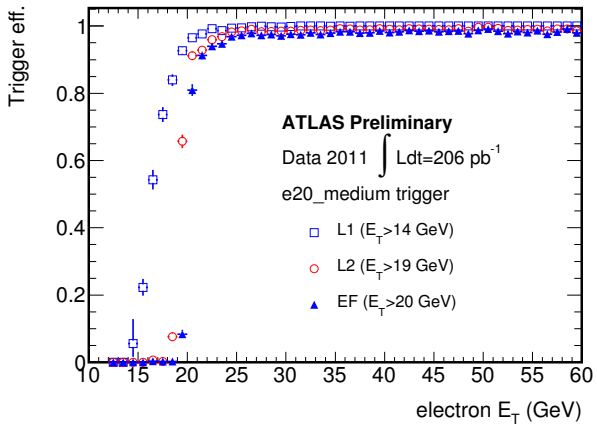

Figure 8.6: Trigger efficiency of the e20_medium chain as a function of E_{T} for 7 TeV data.

checked for a match with a trigger object within a certain ΔR and if this check is successful the probe is counted towards the number of matched probes N_{mp}. Finally, the efficiency of a trigger chain is deduced by taking the ratio of these two numbers $\epsilon = N_{\text{mp}}/N_{\text{p}}$. In event with two tag leptons, each is considered as a tag with the other as the probe.

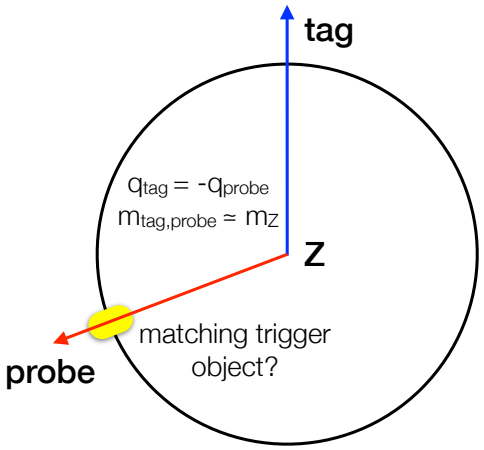

Figure 8.7: Schematic of the tag-and-probe method using $Z \to \ell^{+}\ell^{-}$ events.

8.4.2 Trigger Scale Factors

To account for differences in the modelling of the trigger efficiencies in data and MC samples, scale factors (SF) derived using ZTP are applied to simulated samples. The per event SF depends on the lepton flavour and p_{T} and can be written as

$$\text{SF} = \frac{1 - \prod_{n=1}^{N_\ell}(1 - \epsilon_{\text{Data},\ell_n})}{1 - \prod_{n=1}^{N_\ell}(1 - \epsilon_{\text{MC},\ell_n})} \tag{8.5}$$

where $N_\ell = 3$ in the $W^{\pm}Z$ case and $\epsilon_{\text{Data},\ell_n}$ ($\epsilon_{\text{MC},\ell_n}$) is the data (MC) trigger efficiency determined with ZTP for lepton ℓ_n. The SFs are binned in η-ϕ for muons and in η-E_{T} for electrons. Figure 8.8 shows the η-ϕ distribution of the scale factors for the mu18_MG_medium chain [163]. The extraction of trigger efficiencies and the application of SFs is described in detail in reference [164] and the package used is TrigMuonEfficiency-00-01-11.

The SFs are applied to the leptons forming the $W^{\pm}$ and Zcandidates and satisfying the threshold p_{T} cut. The trigger efficiencies, defined as the ratio of events passing the whole selection when applying or not applying a trigger requirement, determined with the $W^{\pm}Z$ signal MC samples after all selection cuts, are listed in table 8.8. The efficiencies are close to or above 99% in all channels, with efficiencies increasing with the number of electrons in the event. The statistical uncertainty on this efficiency is $\sim 1\%$. Systematic uncertainties due to the application of SFs are studied independently for electron and muon triggers and are combined as uncorrelated sources to a per-channel uncertainty of $\leq 0.3\%$ in all channels.

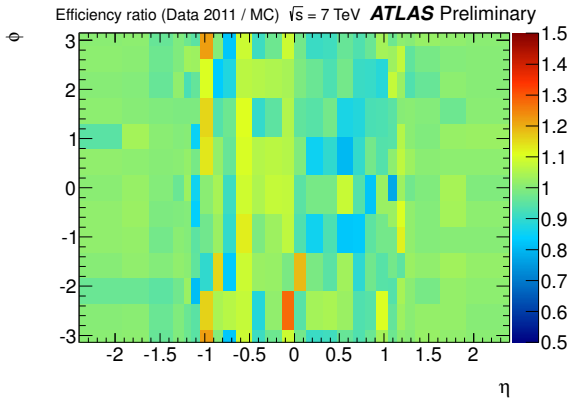

Figure 8.8: Muon trigger scale factors for 7 TeV in barrel and end-cap.

Channel	Trigger Efficiency [%]	Systematic Uncertainty [%]
eee	99.7	$\pm$ <0.05
$ee\mu$	99.5	$\pm$ 0.08
$e\mu\mu$	98.9	$\pm$ 0.16
$\mu\mu\mu$	98.4	$\pm$ 0.29

Table 8.8: Trigger efficiencies and systematic uncertainties for the four $W^{\pm}Z$ channels.

8.5 Object Selection

8.5.1 Muons

In this analysis, the reconstructed muons can either be of the CB or ST type, as described in section 7.4. The selected muons are required to have $p_{\mathrm{T}} > 15$ GeV and $|\eta| < 2.5$. To ensure that the muons originate from the primary vertex and to reduce backgrounds from heavy flavour decays, the muon tracks must satisfy certain distance requirements with respect to the primary vertex. The absolute longitudinal impact parameter $|z_0|$ must be less than 1 mm and the ratio of the transverse impact parameter d_0 to its uncertainty, the so-called d_0 significance, must be less than three. ID tracks must additionally have a minimum number of hits in each silicon sub-detector. There need to be at least one hit in the pixel B-layer, two in all the pixel layers, six in the SCT and there cannot be more than two holes[3] in all silicon layers. For the three first hit conditions, dead sensors are counted as observed hits, not as holes. Finally, an $|\eta|$ dependent condition on the TRT hits and outliers is applied. For $|\eta| < 1.9$, the number of hits and outliers is required to be greater than five and the outlier fraction, defined as $N_{\mathrm{outliers}}/(N_{\mathrm{outliers}} + N_{\mathrm{hits}})$, must be less than 0.9. For $|\eta| > 1.9$, if the number of hits and outliers is greater than six, the outlier fraction has to be less than < 0.9. Lastly, the muons originating from the decay of a $W^{\pm}$ or Z boson need to be isolated. The ID track of the muon must therefore be isolated from surrounding tracks to reject secondary

[3] A hole is an expected but missing hit on a silicon layer crossed by the ID track.

muons from hadronic jets and heavy flavour decays. The isolation requires that the p_{T} scalar sum of all ID tracks within a cone of $\Delta R = 0.3$ around the muon, but not including the muon, must be less than 15% of the muon p_{T}. To reduce the contribution from and the isolation uncertainty due to pile-up, all ID tracks are required to originate from the primary vertex. The muon matched to a trigger object must have $p_{\mathrm{T}} > 20$ GeV as explained in section 8.4.

As recommended by the Muon Combined Performance group [165], several corrections are applied to the MC to match the observed muons in $W^{\pm}$ and Z boson data. The packages used to apply these corrections, that will now be described, are MuonEfficiencyCorrections-01-01-03, MuonMomentumCorrections-00-05-03 and IsoIPSF-00-00-06. Associated systematic uncertainties are taken into account and will be covered in section 8.9.

- The muon reconstruction efficiency has been measured in data and MC using ZTP as described in detail in reference [166]. The tag is always required to be a CB muon whereas the probe is an ID track that has to be matched within $\Delta R < 0.01$ to a CB or ST track of the same charge to deduce the efficiency. Figure 8.9 shows the muon reconstruction efficiency in data and MC for CB and ST muons [167]. The efficiency is greatly enhanced by the inclusion of ST muons especially in the central and transition regions resulting in a SF close to 1 over the full coverage. The event weights of MC samples are scaled to match the measured efficiency for each CB and ST muon. The event level reconstruction SF is the product of the single lepton reconstruction SFs.

- The width and location of the Z boson mass peak in $Z \to \mu^{+}\mu^{-}$ data and MC events is used to measure the muon momentum resolution and scale, respectively. Resolution smearing mainly occurs due to the limited accuracy of calibration and alignment constants. Inaccurate descriptions of the material distribution and the magnetic field can also lead to a worse resolution at low momenta. Since a change in resolution directly affects the acceptance, it is crucial to ensure good modelling in the MC. To account for data/MC differences, the muon p_{T} is smeared in MC while keeping the direction fixed. The exact smearing is determined by a χ^2 minimisation when comparing a MC Z boson mass template to data. The smearing for MS and ID tracks is independent, whereas the smearing for CB muons is a linear combination of the MS and ID contributions. Figure 8.10 shows the MS, ID and CB resolution for data and MC in different η bins [168].

- The efficiency of isolation and impact parameter (IsoIP) cuts has been computed using ZTP and is equal to the ratio of the number of probes passing the IsoIP cuts in question to the number of all selected probes. SFs have been calculated in p_{T}-η bins for loose and combined muons and are shown in figure 8.11 [169].

8.5.2 Electrons

Electrons are required to have a so-called author of 1 or 3, which selects the standard electron collection, and they need to satisfy the loose++ electron identification requirements as defined in section 7.3. The electron candidates have to pass an object quality cut that checks a bitmask for dead front-end boards in the first two LAr calorimeters layers, a dead

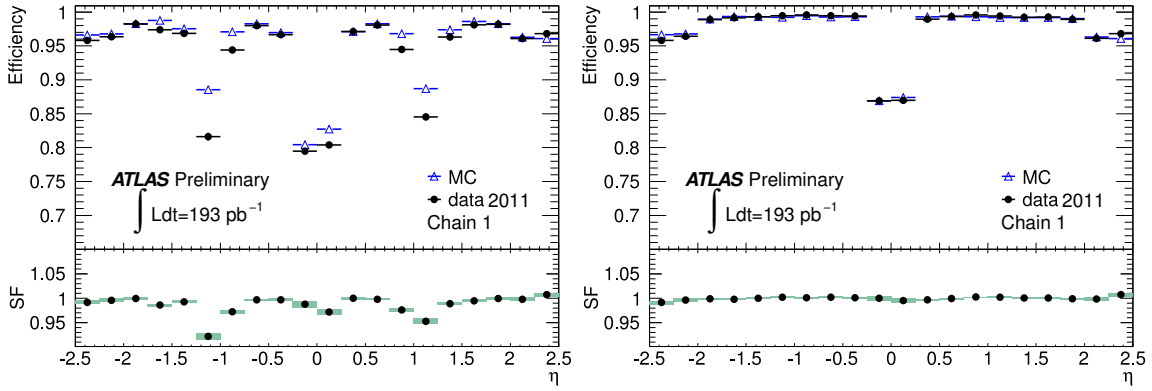

(a) (b)

Figure 8.9: Muon reconstruction efficiency as a function of η for (a) combined and (b) combined or segment-tagged muons. Chain 1 refers to the Staco collection.

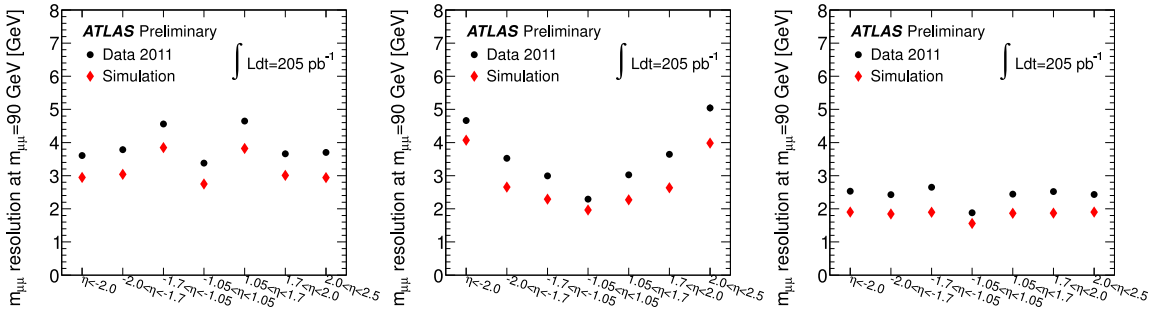

(a) (b) (c)

Figure 8.10: Muon resolution as a function of η for (a) SA, (b) ID and (c) combined tracks.

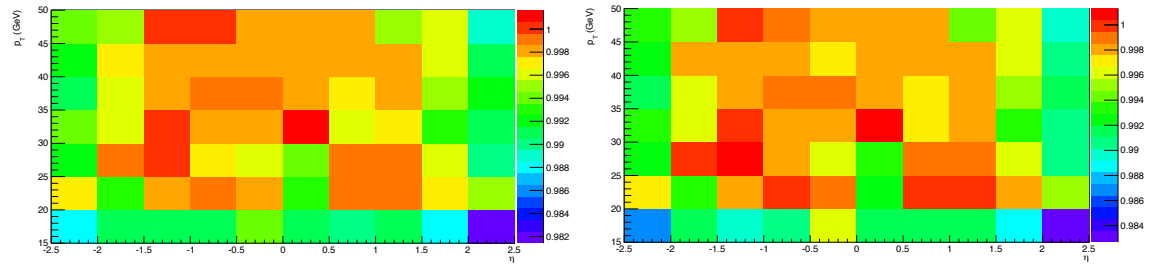

(a) (b)

Figure 8.11: The combined isolation and impact parameter scale factor as a function of p_{T} and η for (a) loose and (b) combined muons.

region affecting all three EM calorimeter layers or masked cells in the calorimeter. The electron transverse energy has to satisfy $E_{\mathrm{T}} > 15$ GeV. The electron cluster pseudorapidity must be in the ranges $|\eta| < 1.37$ or $1.52 < |\eta| < 2.47$ to ensure good containment of the electromagnetic shower in the calorimeters by avoiding the transition region between the barrel and end-cap calorimeters. The $|z_0|$ with respect to the primary vertex must be less than 1 mm and the d_0/σ_{d_0} ratio must be less than 10 to ensure that the electron tracks originate from the primary vertex. Lastly, the electron candidates need to pass calorimeter and track isolation requirements. The total calorimeter E_{T} in a cone of $\Delta R = 0.3$ around the electron candidate, but not including the energy of the candidate itself, and corrected for p_{T} leakage and the number of primary vertex candidates in the event (pile-up), must be less than 14% of the electron cluster E_{T}. The p_{T} sum of all tracks with $p_{\mathrm{T}} > 1$ GeV in a cone of $\Delta R = 0.3$ around the electron candidate, not including the momentum of the candidate itself, must be less than 13% of the electron track p_{T}. A matched electron is ensured to be in the trigger efficiency plateau if $E_{\mathrm{T}} > 25$ GeV.

As for the muons, various corrections need to be applied to MC to make the electron performance match that observed in data. Associated systematics are again described in section 8.9. The package used to apply these corrections is egammaAnalysisUtils-00-02-76.

- The electron reconstruction efficiency is defined as the efficiency to reconstruct an electron cluster candidate and to match it to an ID track. The electron identification efficiency denotes the efficiency for a reconstructed electron to pass the various quality requirements. The efficiencies only apply for $E_{\mathrm{T}} > 15$ GeV and are derived from ZTP, details can be found in reference [170]. Both the reconstruction and identification efficiencies are binned in η-E_{T}. The reconstruction SFs are consistent with one over the full η range except in the forward $2.01 < |\eta| < 2.47$ region where the deviation from one is maximally about 2%. Figure 8.12 shows the identification efficiency in data and MC for the three different quality criteria [171]. Tight++ is less efficient than loose++ as expected from the more stringent selection criteria. The identification efficiencies are only weakly dependent on pile-up and vary by about 1% over the whole 2011 dataset. If there are multiple electrons in the event, the SFs for the different electrons are multiplied. The reconstruction and identification SFs are also multiplied.

- In data, a residual energy scale calibration is applied to electrons. The correction factors are calculated in 26 η bins from a sample of 2011 $Z \to e^{+}e^{-}$ events and are less than 0.5% (1%) in the barrel (end-cap). In MC, the electron energy is smeared, while keeping the electron direction fixed, to match the resolution observed in data. The resulting invariant mass distribution is shown in figure 8.13 [172].

- The IsoIP SFs for electrons are derived in the same way as for muons and are shown in figure 8.14 for loose++ and tight++ electrons.

8.5.3 Missing Transverse Energy

The $E_{\mathrm{T}}^{\mathrm{miss}}$ used in this analysis is built from other reconstructed objects as described in section 7.6. The exact configuration of the calibration is referred to as MET_RefFinal [173].

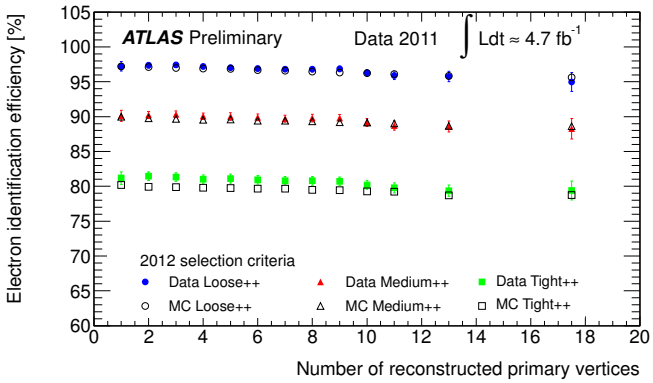

Figure 8.12: Electron identification efficiencies for the different electron quality criteria in data and MC as a function of the number of reconstructed PV.

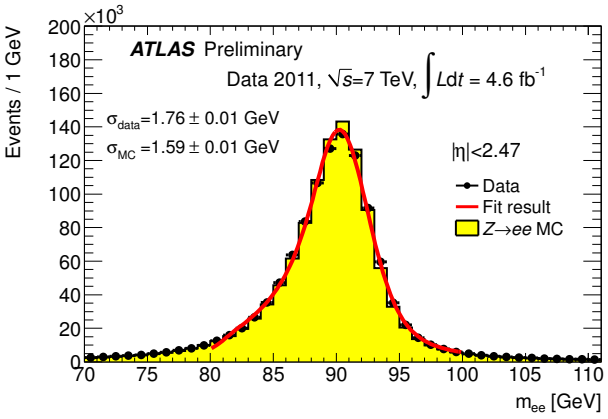

Figure 8.13: Invariant mass distribution in $Z \to e^{+}e^{-}$ events shown for MC, data and fit to data using the full 2011 dataset.

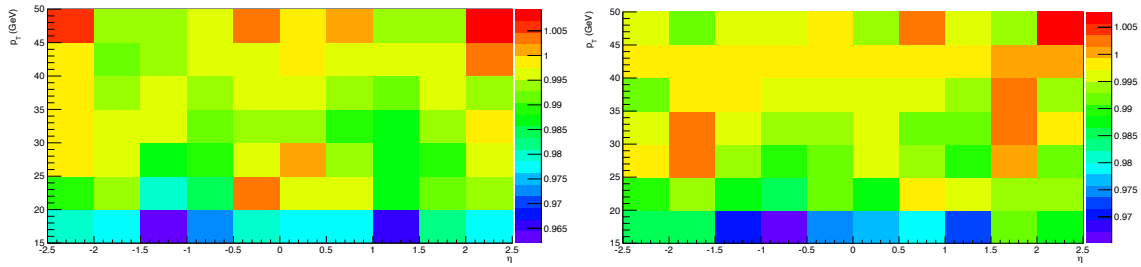

(a) (b)

Figure 8.14: Isolation and impact parameter scale factors as a function of p_{T} and η for (a) loose++ and (b) tight++ electrons.

8.5.4 Jets

In this analysis, jets are only used to ensure good calorimeter performance as will be explained in the next section. Jets are reconstructed at the EM scale using topo-clusters and calibrated to the hadronic scale as described in section 7.5. They are built using the anti-k_T algorithm with a distance parameter $R = 0.4$ and must have $p_T > 20$ GeV.

8.6 Event Selection

Once the electrons, muons, jets and E_T^{miss} have been defined and selected as described in the previous section, a candidate event needs to satisfy the following criteria:

1. **Good Runs List:** The event needs to be on the GRL, this is only relevant for data.
2. **Trigger:** The event must have fired the single electron or single muon trigger chains listed in section 8.4.
3. **Primary vertex:** The event has to contain at least one primary vertex as defined in section 7.2 that is reconstructed with at least three good tracks.
4. **Overlap removal:** If an electron candidate is found within $\Delta R = 0.1$ of a muon candidate, the electron candidate is removed. This mainly removes FSR, where a photon can be misidentified as an electron, and jets from pile-up that can be misidentified as electrons. If two electrons are selected within $\Delta R = 0.1$ of each other, the electron with the lower p_T is removed[4]. Jets within $\Delta R = 0.3$ of a selected electron or muon are also removed.
5. **Event cleaning:** The event must have a well-measured E_T^{miss} and therefore it should not contain any badly measured jets. To ensure this, selected jets are tested for the "looser bad" jet criteria [174], which assess the jet quality by testing for noise spikes, coherent noise, non-collision or cosmic backgrounds.
6. **Event cleaning:** The event must not have a data quality flag indicating noise in the LAr calorimeter.
7. **Z boson candidate:** The event has to contain two same flavour, opposite charge leptons that satisfy $|m_{\ell\ell} - 91.1876| < 10$ GeV. If there is more than one possible combination, the one that gives an invariant mass closest to the Z boson pole mass is retained.
8. **Three leptons:** It is required that the event contains at least three leptons that pass the selection criteria described in section 8.5. The lepton not associated to the Z boson decay must have $p_T > 20$ GeV and satisfy more stringent quality criteria, namely be a CB muon or a tight++ electron.
9. **Missing transverse energy:** The E_T^{miss} in the event must be greater than 25 GeV.

[4] This cut removes less than one electron in 10^7 in the full dataset.

10. **W boson candidate:** The transverse mass of the W boson candidate, formed from the non-Z boson candidate lepton and the $E_{\mathrm{T}}^{\mathrm{miss}}$ as defined in equation 6.8, must be greater than 20 GeV.

11. **Trigger matching:** At least one of the three selected leptons must match an online reconstructed muon or electron trigger object and have a p_{T} greater than 20 or 25 GeV, respectively.

An $W^{+}Z$ candidate event passing all selection cuts is shown in figure 8.15. The event was selected in the $e\mu\mu$ channel. The two muon tracks can be seen in red with hits in all three muon chambers. The electron energy deposit in the calorimeter is shown as a green rectangle and the $E_{\mathrm{T}}^{\mathrm{miss}}$ is indicated with a blue arrow.

Figure 8.16 shows various distributions when all cuts except the one on the variable shown have been applied. They are distributions of the $m_{\ell\ell}$, p_{T} of the lepton associated to the W boson decay, $E_{\mathrm{T}}^{\mathrm{miss}}$ and m_{T} of the reconstructed W boson candidate. The stacked histograms show expectations from simulation for the signal and the ZZ and $Z\gamma$ backgrounds. For the Z+jets and $t\bar{t}$ backgrounds, the expected shape is taken from simulation but the normalisation is taken from the data-driven estimates that will be described in section 8.8. From these distributions, it can be seen that the cuts were chosen so as to eliminate significant background contributions while maximising the signal acceptance. The observed m_{T}^{W} distribution appears narrower than the simulation prediction. The events with $70 < m_{\mathrm{T}}^{W} < 80$ GeV have been extensively tested for signs of experimental problems[5] and no issues have been found. The limited $E_{\mathrm{T}}^{\mathrm{miss}}$ resolution makes it unlikely that the observed excess is a narrow peak.

8.7 Selection Acceptance

The expected number of events in $\mathcal{L} = 4.64$ fb^{-1} after each cut for the $W^{\pm}Z$ signal MC are summarized in table 8.9. The last row includes all the MC corrections listed in sections 8.4 and 8.5. The expectation has been normalised to the theoretical $W^{\pm}Z$ cross section prediction from MCFM listed in section 8.1. In addition, the relative acceptance of each cut is listed in table 8.10. The absolute acceptance increases with the number of muons in the final state as expected because the reconstruction efficiency for muons is higher than for electrons. Lastly, the contribution from $W^{\pm}Z$ events where at least one of the bosons decays to τ leptons, which subsequently decays into an electron or a muon, is shown in table 8.11 and added to the signal expectation in table 8.9 for the cross section extraction.

8.8 Background Estimation

This section will describe how the different backgrounds to the $W^{\pm}Z$ signal are estimated. They can be classified according to how similar they are to the signal. ZZ diboson

[5] These tests include splitting the events up by channel, raising the $E_{\mathrm{T}}^{\mathrm{miss}}$ and the W lepton p_{T} cuts, separating events from positive and negative η or ϕ regions and plotting the number of events as a function of the $\Delta\phi$ separation between the $E_{\mathrm{T}}^{\mathrm{miss}}$ and the closest jet.

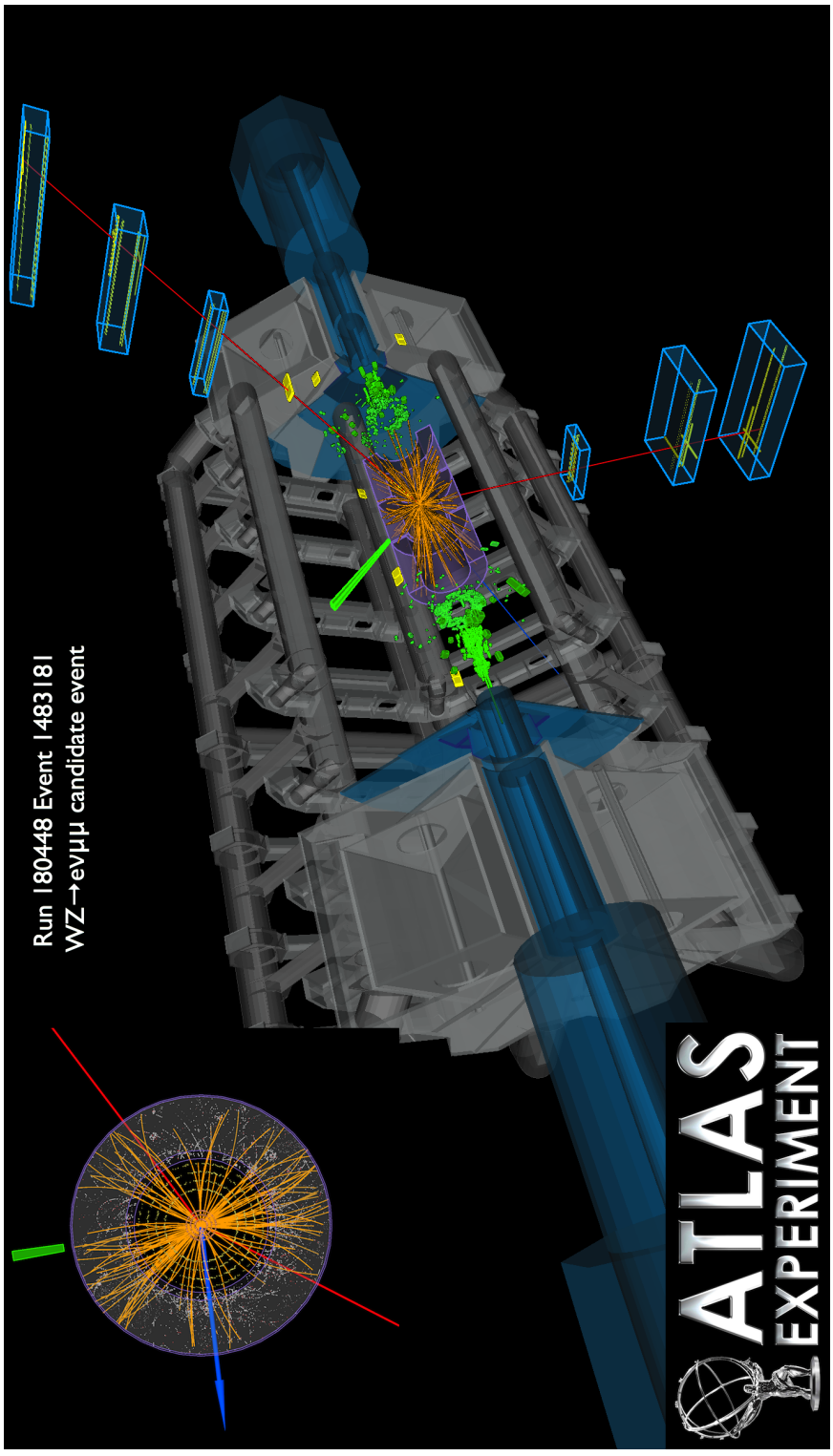

Figure 8.15: An event display of a $W^{+}Z \to e^{+}\nu\mu^{+}\mu^{-}$ candidate event.

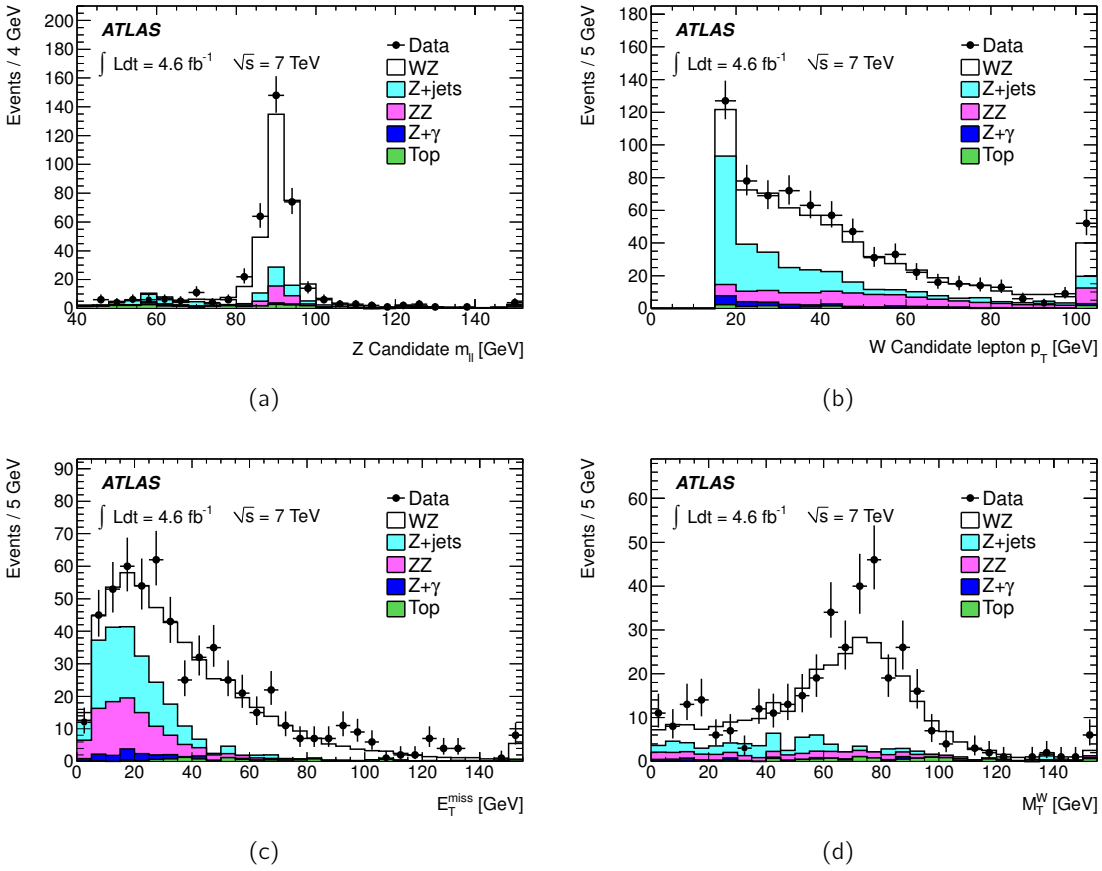

Figure 8.16: (a) Dilepton invariant mass distribution of the Z boson candidate, (b) p_{T} of the lepton attributed to the W boson candidate, (c) $E_{\mathrm{T}}^{\mathrm{miss}}$ distribution and (d) m_{T}^{W} distribution of the W boson candidate.

Cutflow	Events			
	eee	$ee\mu$	$\mu\mu e$	$\mu\mu\mu$
All	1202.26			
Muon or electron trigger	1120.78			
Primary vertex	1117.91			
$E_{\mathrm{T}}^{\mathrm{miss}}$ cleaning	1116.16			
Z cut	218.88		317.37	
Three leptons	51.22	70.55	74.82	106.55
$E_{\mathrm{T}}^{\mathrm{miss}}$ cut	40.50	57.00	59.17	86.44
m_{T}^{W} cut	38.07	54.05	55.67	81.85
Trigger match	38.04	53.99	55.29	81.67
Scale factors	37.24	51.77	54.20	78.32

Table 8.9: Expected number of MC signal events in $\mathcal{L} = 4.64$ fb^{-1} after each cut.

Cutflow	Acceptance (%)			
	eee	$ee\mu$	$\mu\mu e$	$\mu\mu\mu$
All	100			
Muon or electron trigger	93.22			
Primary vertex	99.74			
$E_{\mathrm{T}}^{\mathrm{miss}}$ cleaning	99.84			
Z cut	19.61		28.43	
Three leptons	23.40	32.23	23.57	33.57
$E_{\mathrm{T}}^{\mathrm{miss}}$ cut	79.07	80.80	79.09	81.12
m_{T}^{W} cut	93.99	94.82	94.08	94.70
Trigger match	99.93	99.90	99.31	99.78
Scale factors	97.89	95.89	98.04	95.89

Table 8.10: Relative acceptance of MC signal events after each cut.

Cutflow	Events			
	eee	$ee\mu$	$\mu\mu e$	$\mu\mu\mu$
All	1502.83			
Muon or electron trigger	950.01			
Primary vertex	947.66			
$E_{\mathrm{T}}^{\mathrm{miss}}$ cleaning	942.34			
Z cut	107.07		152.36	
Three leptons	2.98	4.02	4.39	5.62
$E_{\mathrm{T}}^{\mathrm{miss}}$ cut	2.42	3.12	3.44	4.44
m_{T}^{W} cut	1.77	2.38	2.46	3.49
Trigger match	1.76	2.38	2.44	3.50
Scale factors	1.71	2.28	2.37	3.35

Table 8.11: Expected number of MC signal events in $\mathcal{L} = 4.64$ fb^{-1} after each cut for $W^{\pm}Z \to \tau + X$.

production has three real leptons and can include $E_{\mathrm{T}}^{\mathrm{miss}}$ if, for example, the fourth lepton falls outside of the detector acceptance. High statistics MC is used to estimate both the expected ZZ shape and acceptance, which is normalised by the theoretical cross-section prediction. $Z\gamma$ diboson production can contribute as a background if the photon is misidentified as an electron. This contribution is estimated using simulation. The next class of backgrounds contain two prompt leptons from vector boson decays and one so-called "fake" lepton which can originate from an in-flight pion or kaon decay, a heavy-flavour (b or c) quark decay or a jet faking a lepton. Z+jets, $t\bar{t}$, single top and WW production fall into this category. Leptons produced by a real W or Z boson include leptonically decaying τ leptons and decays from the top quark, which is heavy enough to decay to a real W boson, which can subsequently decay leptonically. Leptons from gauge boson decays are mostly isolated whereas leptons from b or c quark decays tend to be spatially correlated with jets so that they will fail the isolation requirement. The residual background is estimated using data since the MC may not model jet fragmentation well. For Z+jets, a full data-driven estimate is performed based on measurements of the rate of jets faking leptons. For $t\bar{t}$, the shape of the MC prediction is normalised by a scale factor derived from data. Lastly, there are backgrounds with one prompt lepton and two leptons from a fake or heavy flavour decay. The category contains mainly W+jets but also single top, semi-leptonic $t\bar{t}$ or QCD multi-jet production. These processes all have relatively large cross sections but the probability of getting two fake leptons is very small and the three isolated leptons requirement excludes several backgrounds. The contribution from W+jets, WW, single-top and QCD dijet production has been checked in MC samples and no or no statistically significant number of events remain after the selection and so these backgrounds are not included subsequently. In summary, Z+jets, ZZ, $t\bar{t}$ and $Z\gamma$ production are the main $W^{\pm}Z$ backgrounds and will now be described in decreasing order of importance.

8.8.1 Z+jets

For Z+jets production to contribute as a background to $W^{\pm}Z$ production, an isolated lepton must be reconstructed from one of the jets, this is a so-called *fake* lepton. Such events are the largest background to the $W^{\pm}Z$ signal. The lepton fake rates are expected to depend strongly on event kinematics. The aim is therefore to measure them in a sample with event kinematics as similar as possible to the signal region, namely a Z boson plus additional lepton sample. The schematic in figure 8.17 illustrates the basic outline of the fake factor method used in this analysis.

To avoid signal contamination, the fake factor is derived in a region that explicitly excludes selected $W^{\pm}Z$ events. The background sample is required to pass all selection cuts but fail the $E_{\mathrm{T}}^{\mathrm{miss}}$ selection. These low $E_{\mathrm{T}}^{\mathrm{miss}}$ events are then separated into two categories by requiring the presence of an extra muon or electron that passes either a "loose" or a "tight" object definition. A "loose" object is one that passes the majority of the previously listed object selection requirements but fails a specific cut that is chosen to maximise the separation between leptons from jets and leptons from boson decays. As such, a tight muon passes all cuts whereas a loose muon fails the isolation requirement. A tight electron passes the whole selection whereas a loose electron fails either the loose++ quality identification or the isolation requirements. The resulting sample is then used to measure the electron fake factor and the muon isolation efficiency. These factors, derived in the low $E_{\mathrm{T}}^{\mathrm{miss}}$ region, are then applied to Z

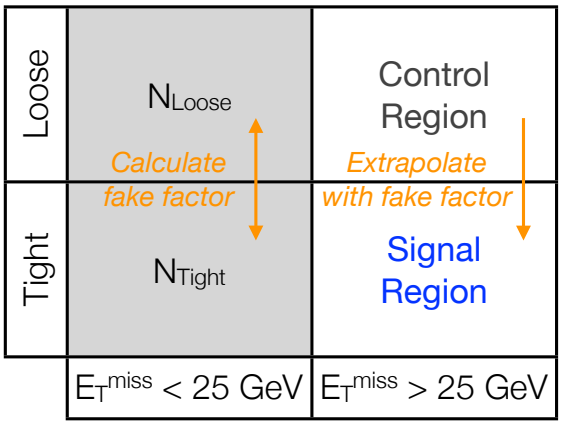

Figure 8.17: Illustration of the data-driven Z+jets background estimation method.

boson plus extra object events in the high $E_{\mathrm{T}}^{\mathrm{miss}}$ region to obtain a data-driven measurement of the backgrounds from fake leptons.

To get a better understanding of the meaning of the fake factor, a few explanations should be added. As described in section 7.3, electrons are reconstructed by matching clusters in the EM calorimeter to ID tracks. A charged particle in a hadronic jet can interact in the EM calorimeter and also deposit significant amounts of energy, thereby faking an electron. To minimise such contamination, selected electrons are required to pass a calorimeter isolation requirement as well as several quality requirements on their tracks, cluster shower shapes and the energy fraction deposited in the hadronic calorimeter as explained in section 8.5. The fake factor is the rate at which such "electron-like" jets mimic electrons and it is measured by counting the number of selected electron candidates and dividing it by the number of "electron-like" jets. The rate of fake muon identifications, however, is expected to be small and so the focus for muons is on backgrounds which contain real muons. To distinguish between muons from a W or Z boson decay and muons from a particle decay in jets, the muon is required to be isolated. The muon isolation efficiency is calculated in a similar way as the electron fake factor by computing the ratio of the number of isolated to non-isolated muons in a Z boson plus extra object sample with low $E_{\mathrm{T}}^{\mathrm{miss}}$. For electrons and muons, the fake factor is then defined as

$$f_{\mathrm{lepton}} = \frac{N_{\mathrm{tight\ lepton}}}{N_{\mathrm{loose\ lepton}}}. \tag{8.6}$$

Processes which produce three real leptons contribute to both the numerator and denominator of this fake factor and their contribution, estimated from MC, is subtracted. This correction is less than 1% of the fakeable object counts and a sizeable correction of the tight object counts for both electrons and muons, the major contribution to the latter coming from WZ and ZZ production. Generally, the fake factor does not have to be measured as a function of p_{T} because the p_{T} spectrum of the fakeable object is similar to that of the $W^{\pm}Z$ signal. Pure QCD events are not expected to contribute a significant background to the $W^{\pm}Z$ signal and so the fake rate measured in Z plus extra object events is expected to also be a good

description of fake leptons in W+jets backgrounds.

The number of fakeable and tight electrons and the number of non-isolated and isolated muons in data and MC in the low $E_{\mathrm{T}}^{\mathrm{miss}}$ region as a function of p_{T} are shown in figure 8.18. The fake factor in data is calculated using these distributions and equation 8.6. As mentioned, contributions from sources other than Z+jets are subtracted using MC.

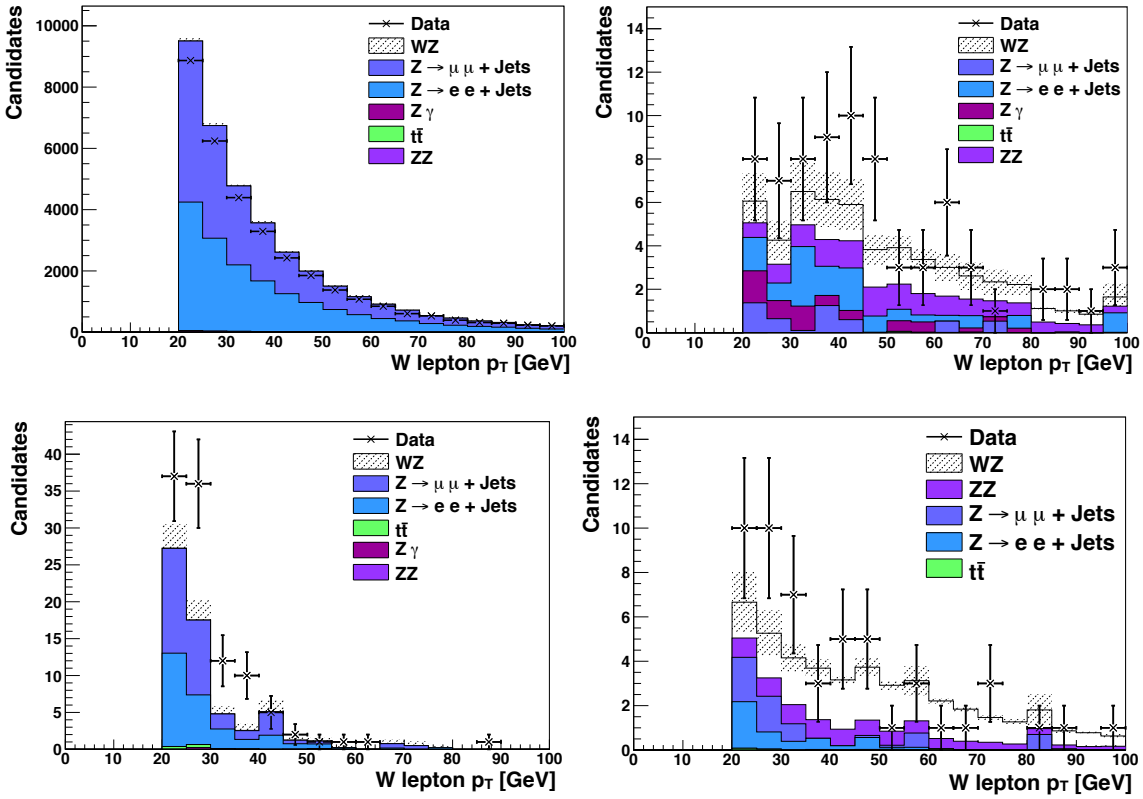

Figure 8.18: Number of electron (top) and muon (bottom) candidates passing the loose (left) and tight (right) lepton requirements as a function of p_{T} in events with a Z boson plus an extra object and failing the $E_{\mathrm{T}}^{\mathrm{miss}}$ cut.

The loose, high $E_{\mathrm{T}}^{\mathrm{miss}}$control region, to which the fake factor is applied, is taken from data events with a loose lepton associated to the W boson. However, in the $\mu\mu\mu$ and eee channels different combinations are possible and the fake lepton might therefore not be associated to the W boson but wrongly to the Z boson. While this mis-association from real $W^{\pm}Z$ events is expected to be very small and at the percent level, it is expected to be larger for Z+jets events. The leptons associated to the Z boson are therefore required to pass $p_{\mathrm{T}} > 15$ GeV, while the lepton associated to the W boson must have $p_{\mathrm{T}} > 20$ GeV. This reduces the problem because the jet p_{T} spectrum of Z+jets events is strictly falling from 15 GeV to 20 GeV and there are therefore more fakeable leptons at 15 GeV than at 20 GeV. For the eee channel, this mis-association can be measured in data where 10% of the Z+jets background is found to come from events with a loose Z lepton. The Z+jets MC prediction

is 8%. For the $\mu\mu\mu$ channel, this cannot be measured in data because the loose Z region is completely dominated by $t\bar{t}$ events. Therefore, a correction derived from MC is applied in the $\mu\mu\mu$ case. The MC is trusted to do a reasonable job of modelling the relative proportion of loose Z and loose W events in Z+jets simulation, because the problem is one of lepton kinematics, not fake-ability. No correction is needed in the $ee\mu$ and $\mu\mu e$ channels because the Z lepton assignment is unambiguous due to flavour.

For the aTGC limit extraction and unfolding of the p_{T}^{Z} distribution, the Z+jets background estimates are derived in bins of p_{T}^{Z}. It is possible that the fake factor may not be flat as a function of p_{T}^{Z}, since the study of dijet data has shown that the fake factor is a function of jet p_{T}, which in turn is correlated with the p_{T}^{Z} in Z+ jets events. Therefore, the fake factor is calculated independently in bins of p_{T}^{Z}. The method for the differential fake factor estimation is the same as for the inclusive estimation except that the sample is divided according to the p_{T} of the Z boson in the event. The measured fake factor as a function of p_{T}^{Z} is shown in figure 8.19 for electrons and muons. Additionally, the fake factor from MC is shown as a comparison. A clear dependence on p_{T}^{Z} is observed in data and MC. Due to a dearth of data in the last two p_{T}^{Z} bins, the fake factor is calculated for the last three bins together for both the muon and electron cases. To unfold the reconstructed m_{WZ} distribution, a data-driven bin-by-bin estimate of the Z+jets background is performed in a similar way.

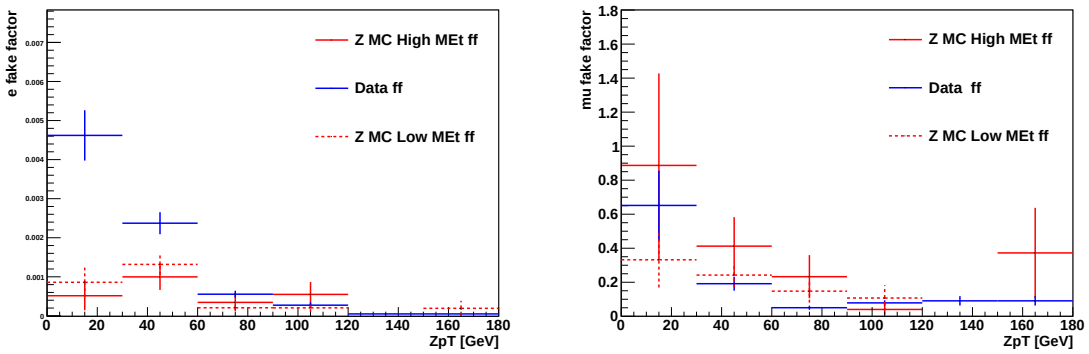

(a) (b)

Figure 8.19: The fake factor for (a) electrons and (b) muons in Z+ jets events as measured in data and predicted in simulation as a function of p_{T}^{Z}. The last bin is omitted from this plot since the fake factor is the same as for the second-to-last bin.

The important difference between the region in which the fake factor is calculated and the signal region is the size of the $E_{\mathrm{T}}^{\mathrm{miss}}$. If there were a correlation between the $E_{\mathrm{T}}^{\mathrm{miss}}$ and the fake factor, this would require a correction between the measured fake factor in the low $E_{\mathrm{T}}^{\mathrm{miss}}$ region in order to apply it to the control sample of Z plus fakeable leptons in the high $E_{\mathrm{T}}^{\mathrm{miss}}$ region. However, the reason why this correlation is difficult to test in data is twofold. Firstly, the statistics in a Z boson plus third lepton data sample are too low to extract a correlation before the sample becomes dominated by the $W^{\pm}Z$ signal. Secondly, the $E_{\mathrm{T}}^{\mathrm{miss}}$ miss-scaling of the fake factor cannot be tested in dijet data in bins of p_{T}^{Z} because there is no good proxy for p_{T}^{Z} in dijet data. Therefore, the possibility of a correlation between $E_{\mathrm{T}}^{\mathrm{miss}}$

and the fake factor is treated as a systematic uncertainty on the measurement of the fake factor. The systematic uncertainty is taken either as the deviation from unity in the ratio between the fake factor in the high to the low $E_{\mathrm{T}}^{\mathrm{miss}}$ regions in the Z+jets MC or as the statistical uncertainty on the ratio in MC, depending on which quantity is larger. For the inclusive muon and electron fake factors, this uncertainty is 35% and 20%, respectively. An additional systematic uncertainty on the fake factor comes from the subtraction of the non-Z+jets samples in the data control regions used to calculate the fake factor. These samples include $W^{\pm}Z$, ZZ, $Z\gamma$ and $t\bar{t}$ simulation. To estimate the uncertainty that this subtraction has on the final estimate of Z+jets background, the $W^{\pm}Z$ and ZZ samples are varied by the uncertainty on the measured cross sections in the most recent ATLAS results, which are 20% for $W^{\pm}Z$ and 15% for ZZ. The $t\bar{t}$ cross section is varied by 100% since the $t\bar{t}$ contribution to these samples includes $t\bar{t}$ events where the third lepton is a fake which is not necessarily well modelled by the simulation. The uncertainty is taken as half of the difference between the data-driven estimate with the MC sample varied by cross section and the data-driven estimate with the nominal MC samples. Final background and uncertainty estimates obtained with this method are given in tables 8.19 and 8.20.

8.8.2 ZZ

ZZ events with fully leptonically decaying Z bosons are a major background to the $W^{\pm}Z$ signal in all four channels. For a ZZ event to pass the $W^{\pm}Z$ event selection it must have $E_{\mathrm{T}}^{\mathrm{miss}} > 25$ GeV. The source of this $E_{\mathrm{T}}^{\mathrm{miss}}$ can be from mis-measured jets, from the tail of the $E_{\mathrm{T}}^{\mathrm{miss}}$ distribution or from a leptonic Z boson decay outside the fiducial detector acceptance. To assess how well this background is modelled in simulation, the lepton kinematics are studied using MC truth information. Figure 8.20 shows the η distributions of truth muons and electrons which fail a $\Delta R < 0.1$ match with a reconstructed muon or electron in $ZZ \to 4\ell$ events but pass the full selection. This indicates that only three of the four leptons have been reconstructed in the detector while the fourth "missing" lepton is a source of $E_{\mathrm{T}}^{\mathrm{miss}}$. This is particularly true for muons whose momentum is not measured fully by the MS and the η distribution of "missing" muons in figure 8.20(a) confirms this. The largest contribution comes from ZZ events with a muon near $\eta = 0$, where the MS has a gap in coverage to allow services to enter, or with a muon outside of the MS coverage at $|\eta| > 2.7$. A smaller contribution comes from the transition regions $|\eta| \sim 1.4$. The η distribution of "missing" electrons in figure 8.20(b) shows peaks in the transition region between the calorimeters at $|\eta| \sim 1.4$. The coverage is otherwise hermetic and no other obvious features can be seen.

The ZZ acceptance is known to be well described by simulation and the theoretical modelling uncertainties, presented in the next section, are relatively small. The shape of this background is therefore estimated from simulation by applying the full selection criteria as well as pile-up reweighting, trigger scale factors and all lepton related corrections described in section 8.5. The LO generation in Pythia is used as it includes contributions from off-shell Z/γ^{*} bosons. The total number of events is determined by scaling the ZZ sample by a k-factor which includes the correction to the theoretical NLO cross-section value estimated by MCFM and the contribution from gg fusion. The total estimated background contribution from the ZZ process is listed in tables 8.19 and 8.20.

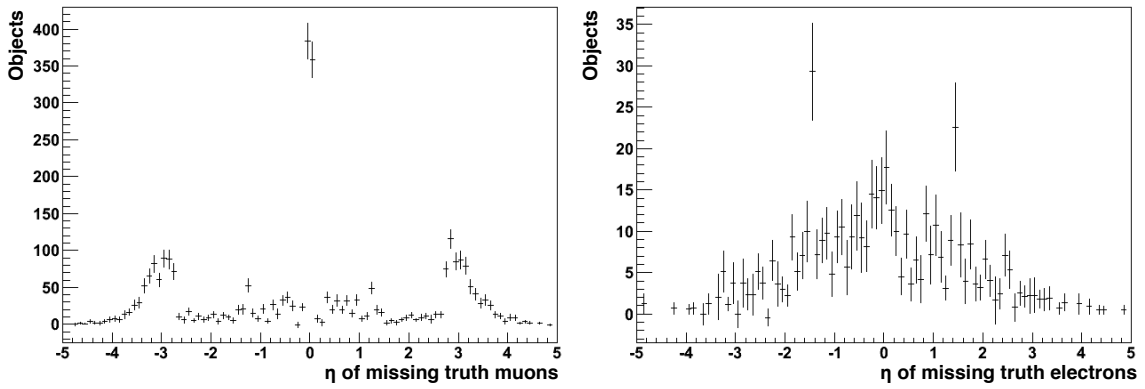

(a) (b)

Figure 8.20: The η distribution of (a) truth muons and (b) truth electrons that do not have a corresponding reconstructed object within $\Delta R < 0.1$ in $ZZ \to 4\ell$ events passing the full $W^{\pm}Z$ selection.

8.8.3 $t\bar{t}$

Electroweak decays of top quarks can produce multiple leptons through subsequent leptonic decays of the W boson and semi-leptonic decays of the b quark. Even if the W boson decays hadronically, particles within the jets can be identified as electrons if they deposit energy in the EM calorimeter. The leptonic W boson decay will further ensure the presence of real $E_{\mathrm{T}}^{\mathrm{miss}}$ making the background even more signal-like.

A large part of the top background can be eliminated by rejecting reconstructed leptons from either b quark or light quark jets through lepton isolation requirements. No significant single top contribution and about 3 $t\bar{t}$ events remain in MC after the full selection. The isolation or quality selection efficiencies may however not be well modelled in MC and therefore it is desirable to apply data-driven corrections derived in $t\bar{t}$-enriched control regions. In order to avoid substantially changing the main selection cuts and thereby potentially inducing large uncertainties, the $t\bar{t}$ control region is obtained by modifying only the opposite charge requirement on the lepton candidates from the Z boson decay and applying a same charge requirement instead. The fact that $t\bar{t}$ events do not contain a real Z boson is exploited and so this charge requirement should only have a weak effect on $t\bar{t}$ events. Figure 8.21 shows that the invariant mass distribution of the two leptons closest to the Z boson mass and the $E_{\mathrm{T}}^{\mathrm{miss}}$ distribution in $t\bar{t}$ MC events after all selection cuts look comparable for same and opposite charge requirements. Processes containing a real Z boson on the other hand would show a strong difference. It should be noted that only the two channels where the leptons from the W and Z bosons have different flavours, namely $e\mu\mu$ and μee, are used in this estimation to eliminate combinatorial errors.

Figure 8.22 shows the simulated $E_{\mathrm{T}}^{\mathrm{miss}}$ distribution in the $t\bar{t}$ control region. It can be seen that $t\bar{t}$ is the only significant contribution with a purity of 88.8% in the $e\mu\mu$ channel and 61.6% in the $ee\mu$ channel for $E_{\mathrm{T}}^{\mathrm{miss}}$ values less than 200 GeV. The purity in the $ee\mu$ channel is enhanced to 80.5% if only events with $E_{\mathrm{T}}^{\mathrm{miss}}$ above 60 GeV are considered, which will be used

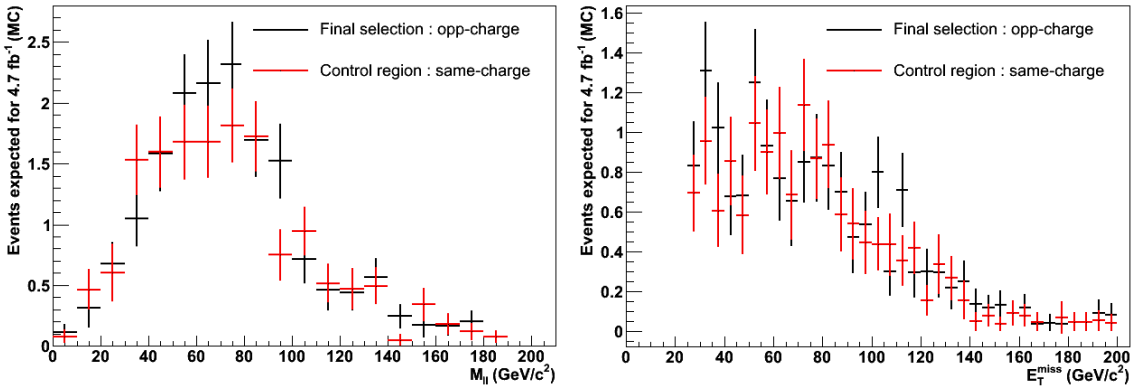

(a) (b)

Figure 8.21: (a) The invariant mass distribution for the same flavor lepton pair closest to the Z boson mass and (b) the $E_{\mathrm{T}}^{\mathrm{miss}}$ distribution in simulated $t\bar{t}$ events for opposite and same sign selections.

for this estimation. The MC prediction shows a deficit compared to data, the ratio of data to MC in the control region is 2.06 $\pm$ 0.77 and 2.32 $\pm$ 1.13 for the $e\mu\mu$ and $ee\mu$ channels, respectively. From this, an average rescaling factor of 2.2 $\pm$ 1.0 is defined.

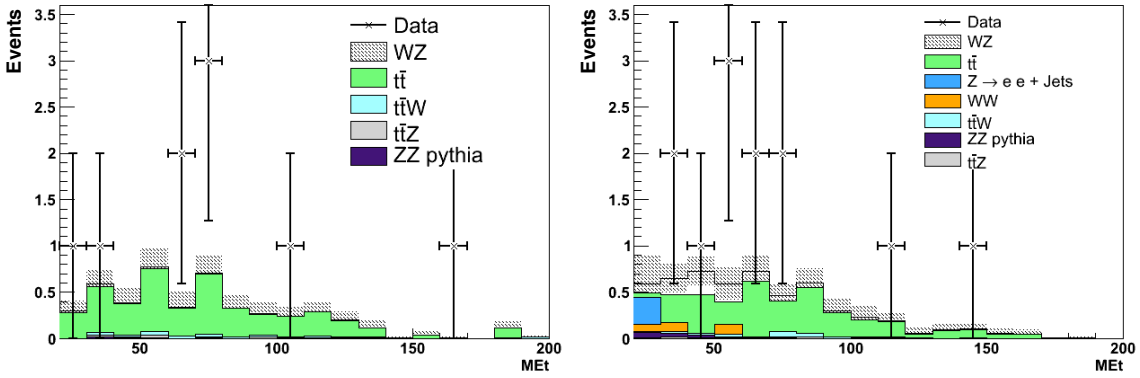

(a) (b)

Figure 8.22: The $E_{\mathrm{T}}^{\mathrm{miss}}$ distribution in (a) $e\mu\mu$ and (b) μee events passing all $W^{\pm}Z$ selection cuts but requiring the leptons associated to the Z boson to have the same charge.

A fully data-driven estimate of the $t\bar{t}$ background as the one described for Z+jets is not feasible with the small statistics remaining after all selection cuts. However, an estimate obtained by relaxing the d_0 significance cut, which is very powerful in removing the $t\bar{t}$ background, shows a data/MC ratio of 15/7 which is compatible with the rescaling value quoted above.

The final estimates for $t\bar{t}$ background, listed per channel and per p_{T}^{Z} bin in table 8.12, are obtained by multiplying the original numbers from simulation by the correction factor cal-

culated above. Uncertainties on the estimates have been split in two terms for illustration. The two uncertainties listed are first the statistical MC uncertainty multiplied by the rescaling factor and secondly the systematic uncertainty obtained by multiplying the original MC estimate by the uncertainty on the rescaling factor. The final uncertainty is the sum in quadrature of the statistical and systematic uncertainties.

The MC@NLO $t\bar{t}$ sample used for the background estimation is NLO in QCD and includes QED corrections but it does not include weak boson radiation. Therefore contributions from $t\bar{t}W^{\pm}$ and $t\bar{t}Z$ production must be added separately and are estimated from simulation. The production cross section of these processes is much lower but both can produce events with three prompt leptons and significant $E_{\mathrm{T}}^{\mathrm{miss}}$ and are hence less likely to be rejected by the lepton selection cuts. Due to the presence of a real Z boson, $t\bar{t}Z$ production gives a final event yield that is comparable to $t\bar{t}$, as shown in table 8.12. $t\bar{t}W^{\pm}$ events have an additional prompt lepton which increases their probability to pass the selection cuts. However, since they do not contain a real Z boson, like $t\bar{t}$ they are mostly rejected by the dilepton invariant mass cut. Their final yield is thus smaller than $t\bar{t}Z$ and is also listed in table 8.12. The $t\bar{t}W^{\pm}$ and $t\bar{t}Z$ uncertainties are statistical. $t\bar{t}W^{\pm}W^{\pm}$ and $t\bar{t}t\bar{t}$ samples have also been considered but, due to their even lower production cross sections, they do not give any significant event yield.

channel	$t\bar{t}$	$t\bar{t}W^{\pm}$	$t\bar{t}Z$
eee	0.4±0.3±0.2	0.1±0.02	0.6±0.1
$ee\mu$	1.7±0.5±0.8	0.1±0.02	1.1±0.1
$\mu\mu e$	2.3±0.5±1.0	0.1±0.03	1.2±0.1
$\mu\mu\mu$	2.4±0.5±1.1	0.1±0.03	1.5±0.1
p_{T}^{Z} [GeV]	$t\bar{t}$	$t\bar{t}W^{\pm}$	$t\bar{t}Z$
0 − 30	1.1±0.4±0.5	0.04±0.02	0.3±0.04
30 − 60	2.0±0.5±0.9	0.1±0.02	0.8±0.1
60 − 90	2.0±0.4±0.9	0.1±0.03	0.7±0.1
90 − 120	1.0±0.4±0.5	0.1±0.03	0.7±0.1
120 − 150	0.5±0.2±0.2	0.02±0.01	0.4±0.1
150 − 180	0.03±0.1±0.01	0.01±0.01	0.4±0.1
180 − 2000	0.1±0.1±0.1	0.01±0.01	1.0±0.1

Table 8.12: Number of expected $t\bar{t}$ and $t\bar{t}V$ background events per decay channel and p_{T}^{Z} bin.

8.8.4 $Z\gamma$

Leptonic decays of $W^{\pm}$ or Z bosons produced in association with photons can mimic the three lepton signature if a photon undergoes conversion into an $e^{+}e^{-}$ pair when interacting with the material of the detector and is then wrongly identified with an ID track. Such a final state is different from those in the data-driven method for "lepton-like" jets described above as the photon does not have to be associated to a jet. Therefore, the contribution from $W/Z\gamma$ diboson production has to be added specifically when using that method. Ideally, this contribution would also be estimated using a data-driven method, however this background is

expected to be very small and it is for simplicity estimated using MC. The processes are simulated using Sherpa for boson decays into electron or muons. The matrix element calculation of the MadGraph generator is used for boson decays into τ leptons, together with Pythia for the parton shower and hadronization, Photos for photon radiation, Tauola for τ-lepton decays, and Geant4 for the detector simulation of photon conversions. No events passed the selection for the $W\gamma$ samples and so for simplicity this background will henceforth be referred to as $Z\gamma$, whose final contributions are shown in tables 8.19 and 8.20.

8.9 Systematic Uncertainties

This section discusses the various sources of systematic uncertainties considered in this analysis. They are calculated separately for each source and consist of uncertainties related to physics object reconstruction, trigger efficiencies and theoretical predictions like cross sections, PDFs, QCD scale and generator modelling. The size of the uncertainties is computed by varying the systematic uncertainty of a specific source in the signal MC and taking the fractional difference between the nominal yield and the systematically varied yield. This is different for theoretical uncertainties for which the procedure will be described in subsection 8.9.4. The systematic uncertainties from the same source are treated as fully correlated for the different channels. The relative uncertainties calculated on signal samples are propagated for background uncertainties to ensure sufficient statistics.

Systematic uncertainties that have been previously discussed will not be repeated here. They include the 1.8% luminosity uncertainty discussed in section 6.7, trigger efficiency uncertainties listed in section 8.4 and uncertainties on the data-driven background estimates presented in section 8.8.

8.9.1 Muons

Section 8.5 described the three types of muon corrections that are applied to simulation. The systematic uncertainties related to reconstructed muon objects that are taken into account are listed in detail below and the values are summarised in table 8.13. The main source of uncertainty is related to the muon reconstruction efficiency. Event yields are computed by varying the efficiency SFs, which are applied per muon, in MC within recommended uncertainties [165]. The number of events varies symmetrically around the nominal values and scales roughly with the number of muons in each channel. The uncertainty related to the muon momentum scale and resolution is established by varying the p_{T} smearing of the muons in the MS and ID according to the uncertainty on the p_{T} scale and resolution observed in data. The ID and MS systematic uncertainties are the means of the absolute ID up, ID down and MS up, MS down variations, respectively. The final value used is the sum in quadrature of ID and MS systematic uncertainties. Lastly, event yields are computed by varying the muon isolation and impact parameter scale factors. The effect of this variation is again symmetrical around the nominal values and scales with the number of muons in the event. The IsoIP SF is an overall factor applied per muon and depends on the muon p_{T} and η values. The total muon reconstruction systematic uncertainty is also listed in table 8.13 and is the sum in quadrature of each of the individual sources. This number is provided to indicate the overall

size of uncertainties but in the cross section extraction, discussed in section 8.11, each source of uncertainty is treated as a separate nuisance parameter.

Source		μee	$\mu\mu e$	$\mu\mu\mu$
Reconstruction efficiency		$^{+0.27}_{-0.27}$	$^{+0.53}_{-0.53}$	$^{+0.79}_{-0.8}$
p_{T} smearing	ID	0.03	0.01	0.04
	MS	0.02	0.05	0.04
	combination	0.04	0.05	0.06
Isolation & impact parameter efficiency		$^{+0.2}_{-0.2}$	$^{+0.43}_{-0.43}$	$^{+0.61}_{-0.62}$
Total		0.34	0.68	1.01

Table 8.13: Muon reconstruction systematic uncertainties (%) in $W^{\pm}Z$ MC, τ lepton contributions are included.

8.9.2 Electrons

The contribution of the electron systematics to the signal acceptance is evaluated in MC by taking into account the uncertainties associated with the electron reconstruction and identification efficiency, energy scale, energy smearing and calorimeter isolation as described in section 8.5. Each source is varied within its associated uncertainty and the fractional change in the number of events passing the selection is observed [175]. The results are listed in table 8.14. The largest source of uncertainty is due to electron reconstruction and identification efficiencies. The uncertainty on the reconstruction efficiency SF is provided in eleven η bins and is close to 0.4% for most of the η range. The electron identification efficiency SFs and their uncertainties are determined from W, Z and J/ψ electron measurements as a function of η and E_{T}. The uncertainties of the η and E_{T} dependent SFs are added in quadrature to obtain the combined electron identification uncertainty. The systematics on the energy scale derived from 2011 data are used on the MC to obtain the associated uncertainty on the signal acceptance. Since the MC does not reproduce the observed energy resolution in data, a smearing is applied to it. The systematics uncertainties related to isolation and impact parameter cuts are determined by varying the IsoIP SFs within their provided uncertainties and observing the change in acceptance.

8.9.3 Missing Transverse Energy

A prescription to calculate the $E_{\mathrm{T}}^{\mathrm{miss}}$ related systematic uncertainties is described in reference [173]. Since the $E_{\mathrm{T}}^{\mathrm{miss}}$ used in this analysis is built from other reconstructed objects, the uncertainties on those objects can be easily propagated to the $E_{\mathrm{T}}^{\mathrm{miss}}$. As an example, the uncertainty due to the jet energy scale on the $E_{\mathrm{T}}^{\mathrm{miss}}$ can be calculated by varying the energy scale of the jets since they are used directly in the $E_{\mathrm{T}}^{\mathrm{miss}}$ calculation. The main sources of systematic uncertainty, which enter the analysis as systematic uncertainties on the

Source	eee	$ee\mu$	$e\mu\mu$
Energy scale	0.5	0.3	0.3
Energy smearing	0.1	0.1	0.0
Reconstruction efficiency	2.5	1.7	0.8
Identification efficiency	3.5	2.3	1.2
Isolation & impact parameter efficiency	1.5	1.1	0.4
Total	4.5	3.1	1.5

Table 8.14: Electron reconstruction systematic uncertainties (%) in $W^{\pm}Z$ MC.

acceptance of the $E_{\mathrm{T}}^{\mathrm{miss}}$ and m_{T}^{W} cuts, are the uncertainty on the topological cluster (or topo-cluster) energy scale, muon energy scale and resolution, electron energy scale and resolution, jet energy scale and the description of pile-up in MC. The standard procedure of estimating the uncertainty on the topo-cluster energy scale as a function of the cluster p_{T} and η is used [149] and applied to the simulation to obtain an estimate of the systematic uncertainty for each source. Similar procedures are used for the other uncertainties, and the uncertainties are propagated to the $E_{\mathrm{T}}^{\mathrm{miss}}$ to obtain uncertainties due to these sources. The uncertainties from propagating the muon and electron scale and resolution uncertainties are included in the muon and electron uncertainties, and are not considered here. The uncertainty due to pile-up, estimated to be 6.6% on the calorimeter terms of $E_{\mathrm{T}}^{\mathrm{miss}}$, is obtained by studying the H_{T} dependence of the number of pile-up interactions in Z boson events. Table 8.15 summarises the systematic uncertainties considered for $E_{\mathrm{T}}^{\mathrm{miss}}$.

Source	eee	$ee\mu$	$e\mu\mu$	$\mu\mu\mu$
Topo-cluster energy scale	0.40	0.17	0.57	0.18
Jet energy scale	0.11	0.08	0.10	0.08
Jet energy resolution	0.28	0.30	0.39	0.25
Pile-up	0.32	0.11	0.32	0.13

Table 8.15: $E_{\mathrm{T}}^{\mathrm{miss}}$ reconstruction systematic uncertainties (%) in $W^{\pm}Z$ MC.

8.9.4 Theoretical

The uncertainties taken into account on the fiducial and total signal cross section have been described in section 8.1. The latter is summarised in table 8.16 with uncertainties on the theoretical cross section for various background MC samples [162, 176–178].

Sample	$W^{\pm}Z$	$W^{+}W^{-}$	ZZ	$Z\gamma$	$t\bar{t}$
Uncertainty (%)	$^{+6.3}_{-5.7}$	$^{+5.5}_{-4.5}$	$^{+5.0}_{-4.1}$	± 5.0	$^{+7.0}_{-9.6}$

Table 8.16: Uncertainties on theoretical cross sections for MC samples used in the analysis.

In this analysis, a fiducial cross section is measured whose benefit it is to be mostly free of theoretical uncertainties, parton distribution functions (PDF), renormalization and factorisation scales, or deviations in the signal modelling arising from different MC generators. However, to extrapolate from the fiducial to the total cross section, systematic uncertainties that affect the fiducial acceptance A_{WZ} need to be considered. Three different sources of uncertainty are considered and will be described in the remainder of this section.

- The central value of A_{WZ} is calculated based on events generated with MC@NLO using the CT10 NLO PDF and the corresponding ATLAS tune. The calculation of the acceptance uncertainties due to PDFs is itemized below:
  - The uncertainty due to the nominal CT10 PDF set is obtained by following a standard procedure described in the CTEQ manual [179]. The symmetric uncertainty is evaluated by averaging positive and negative uncertainties like
  $$\frac{\sqrt{\sum_{i=1}^{n}[max(A_i - A_{WZ}, 0)]^2} + \sqrt{\sum_{i=1}^{n}[max(A_{WZ} - A_i, 0)]^2}}{2A_{WZ}}, \tag{8.7}$$
  where i runs over the 52 CT10 error eigenvectors.
  - The uncertainty between different PDF sets is estimated by comparing the CT10 set to the central MSTW2008 NLO 68% CL PDF set. This is done by an event-by-event PDF reweighting technique of the $W^{\pm}Z$ signal samples.

  The uncertainty calculated from the 52 CT10 error eigenvectors is $\sim$0.8% and the central value deviation from MSTW2008 NLO is $\sim$0.8%. The statistical uncertainty is $\sim$0.3%. The final systematic uncertainty on A_{WZ} due to PDFs is obtained by a sum in quadrature of those three terms and equal to 1.2%.

- To determine the uncertainty on A_{WZ} due to μ_r and μ_f, various MC@NLO samples were produced in which the scale was multiplied by a factor of 2 and a factor 0.5. In MC@NLO, as discussed earlier, this is a dynamic scale and equal to the average of the transverse mass squared of the W and Z bosons. The difference between the change in the expected number of events in the fiducial volume and the change in cross section is 0.4%.

- The A_{WZ} dependence on generator modelling is cross checked by a comparison between MC@NLO + HERWIG and `POWHEG BOX` [84] + Pythia and the differences were found to be $\sim$ 0.4%.

For both the scale and generator uncertainty on A_{WZ}, privately produced `evgen` level samples are used, which means that these samples are after parton showering but before full ATLAS Geant4 simulation and reconstruction. In table 8.17 the scale and generator uncertainties are only on the acceptance A_{WZ}. In table 8.18, scale and generator uncertainties on the shape of the p_{T}^{Z} spectrum are shown. For the generator uncertainty, the cross sections predicted by MC@NLO and `POWHEG BOX` are normalised so as to only account for shape differences, not differences in cross section prediction. This is done in order to avoid double counting of the γ^* contribution, already accounted for by scaling MC@NLO samples to the MCFM cross section.

8.9.5 Summary

Tables 8.17 and 8.18 summarize the systematic uncertainties on the acceptance used per channel, as input for the cross section extraction, and in bins of p_{T}^{Z}, as input for the aTGC limit setting and the unfolding measurement.

Source	$\mu\mu\mu$	$e\mu\mu$	$ee\mu$	eee
μ reconstruction efficiency	0.8	0.53	0.27	-
μ p_{T} scale & resolution	0.06	0.05	0.04	-
μ isolation & impact parameter efficiency	0.62	0.43	0.2	-
e reconstruction efficiency	-	0.8	1.7	2.5
e identification efficiency	-	1.2	2.3	3.5
e isolation & impact parameter efficiency	-	0.4	1.1	1.5
e energy scale	-	0.3	0.3	0.5
e energy resolution	-	0.0	0.1	0.1
$E_{\mathrm{T}}^{\mathrm{miss}}$ cluster energy scale	0.18	0.57	0.17	0.40
$E_{\mathrm{T}}^{\mathrm{miss}}$ jet energy scale	0.08	0.10	0.08	0.11
$E_{\mathrm{T}}^{\mathrm{miss}}$ jet energy resolution	0.25	0.39	0.30	0.28
$E_{\mathrm{T}}^{\mathrm{miss}}$ pile-up	0.13	0.32	0.11	0.32
Trigger - μ	0.29	0.15	0.07	-
Trigger - e	-	<0.05	<0.05	<0.05
Generator	0.4	0.4	0.4	0.4
PDF	1.2	1.2	1.2	1.2
Scale	0.4	0.4	0.4	0.4
Luminosity	1.8	1.8	1.8	1.8

Table 8.17: Summary of all relative acceptance uncertainties (%) per channel.

8.10 Results

This section presents the overall number of observed and expected events as well as kinematic distributions of the final number of candidates.

8.10.1 Observed and Expected Events

The number of expected and observed events, with statistical and systematic uncertainties, after applying all selection cuts are shown per channel in table 8.19 and per p_{T}^{Z} bin in table 8.20. All numbers are calculated with three but rounded up to two decimal places. The listed backgrounds are estimated as described in section 8.8. The Z+jets background is estimated using data-driven methods, the top quark production is estimated with MC and rescaled to data and all other predictions are taken from MC simulation. For each channel or p_{T}^{Z} range and each process, the fractional systematic uncertainties are calculated by combining different sources listed in tables 8.17 and 8.18 in quadrature and then applying to the central value of MC estimates. The uncertainty on the rescaling method used for the top background estimate is added in quadrature to that systematic uncertainty. For the Z+jets background, the systematic uncertainties are the ones from the data-driven estimate. In particular, the systematic uncertainties with a $W \to \mu\nu$ are summed linearly since the uncertainties for the

Source	0-30	30-60	60-90	90-120	120-150	150-180	180-2000
μ reconstruction efficiency	0.55	0.56	0.57	0.58	0.59	0.61	0.63
μ p_{T} scale &resolution	0.07	0.03	0.07	0.18	0.35	0.15	0.25
μ isolation & impact parameter efficiency	0.32	0.43	0.49	0.53	0.55	0.57	0.55
e reconstruction efficiency	0.97	0.97	1.19	1.03	1.06	0.10	1.13
e identification efficiency	1.35	1.44	0.94	1.44	1.37	0.55	1.30
e isolation & impact parameter efficiency	0.41	0.56	0.79	0.70	0.70	0.03	0.73
e energy scale	-0.16	0.16	0.10	0.38	0.40	-0.43	1.10
e energy resolution	0.05	0.02	-0.28	-0.07	0.09	0.51	-0.14
$E_{\mathrm{T}}^{\mathrm{miss}}$ cluster energy scale	-0.00	0.20	0.41	0.47	0.19	0.06	-0.12
$E_{\mathrm{T}}^{\mathrm{miss}}$ jet energy scale	-0.07	-0.09	-0.23	0.04	-0.16	0.35	0.04
$E_{\mathrm{T}}^{\mathrm{miss}}$ jet energy resolution	-0.01	0.01	0.27	0.36	-0.07	0.05	0.61
$E_{\mathrm{T}}^{\mathrm{miss}}$ pile-up	0.04	0.10	0.35	0.36	0.08	0.04	-0.21
Trigger - μ	0.14	0.16	0.16	0.16	0.15	0.14	0.14
Trigger - e	0.02	0.03	0.03	0.03	0.02	0.02	0.02
Generator	-0.58	-2.97	3.90	1.11	1.10	4.28	-1.45
PDF	4.28	4.19	4.09	4.00	4.16	4.02	4.24
Scale	2.60	2.60	4.80	8.70	6.70	7.30	8.00
Luminosity	1.8	1.8	1.8	1.8	1.8	1.8	1.8

Table 8.18: Summary of all relative acceptance uncertainties (%) in bins of p_{T}^{Z} [GeV].

muon fakes are correlated in both channels. The same applies to the estimates in the channels with a $W \to e\nu$. The two sets of Z+jets systematic uncertainties are then summed in quadrature since the uncertainties associated with fake electrons and fake muons are uncorrelated. The systematic uncertainties for the subtracted MC estimates are added linearly since they are correlated across channels. These are summed in quadrature with the systematic uncertainties from the Z+jets background estimation.

The systematic uncertainties listed in table 8.19 are not used in the cross section fit and are just for illustrative purposes. The fit procedure accounts for the full granularity and correlation of systematic sources across the different channels, as will be described in the next section.

In rough numbers, a total of 317 $W^{\pm}Z$ candidates are observed in data with an expectation of 231 ± 8 signal[6] and 68 ± 10 background events. There are 206 $W^{+}Z$ and 111 $W^{-}Z$ candidates which is consistent with an expectation of 186 ± 11 and 110 ± 6 events, respectively.

8.10.2 Kinematic Distributions

Figures 8.23 and 8.24 show kinematic distributions of various quantities after the complete set of $W^{\pm}Z$ selection cuts has been applied. The backgrounds shown in these plots are taken from simulation except for backgrounds from Z+jets and $t\bar{t}$ production, where the expected shape is taken from simulation but the normalisation is taken from the data-driven estimates. Figure 8.23 shows the number of leptons, the W charge, the p_{T} distribution of the leading lepton in the event, the p_{T} distribution of the W boson candidate, the three-body mass reconstructed using the three selected leptons and the jet multiplicity. Figure 8.24 shows two

[6] This includes boson decays into τ leptons.

Final State	$eee + E_{\mathrm{T}}^{\mathrm{miss}}$	$ee\mu + E_{\mathrm{T}}^{\mathrm{miss}}$	$e\mu\mu + E_{\mathrm{T}}^{\mathrm{miss}}$	$\mu\mu\mu + E_{\mathrm{T}}^{\mathrm{miss}}$	Combined
Observed	56	75	78	108	**317**
Z+jets	$8.8\pm2.1^{+1.9}_{-1.9}$	$3.7\pm1.7^{+1.6}_{-1.6}$	$10.2\pm2.4^{+2.2}_{-2.2}$	$9.1\pm3.9^{+3.9}_{-3.9}$	$31.9\pm5.3^{+7.5}_{-7.5}$
ZZ	$3.2\pm0.1\pm0.2$	$4.9\pm0.1\pm0.2$	$5.0\pm0.1\pm0.1$	$7.9\pm0.1\pm0.2$	$21.0\pm0.2\pm0.7$
Top	$1.1\pm0.3\pm0.2$	$2.9\pm0.5\pm0.8$	$3.5\pm0.5\pm1.0$	$4.0\pm0.5\pm1.1$	$11.5\pm0.9\pm3.4$
$Z\gamma$	$1.4\pm0.7\pm0.1$	–	$2.3\pm0.9\pm0.1$	–	$3.7\pm1.1\pm0.1$
Total Background	$14.5\pm2.2^{+1.9}_{-1.9}$	$11.5\pm1.8^{+1.8}_{-1.8}$	$21.0\pm2.6^{+2.4}_{-2.4}$	$21.0\pm3.9^{+4.0}_{-4.0}$	$68.1\pm5.5^{+8.2}_{-8.2}$
Expected Signal	$38.9\pm0.5\pm2.0$	$54.0\pm0.5\pm2.1$	$56.6\pm0.6\pm1.6$	$81.7\pm0.7\pm2.0$	$231.2\pm1.1\pm7.8$
Expected S/B	2.7	4.7	2.7	3.9	**3.4**

Table 8.19: Summary of observed events and expected signal and background contributions in the four channels and combined. The first uncertainty is statistical while the second is systematic.

p_{T} (Z) [GeV]	[0, 30]	[30, 60]	[60, 90]	[90, 120]	[120, 150]	[150, 180]	[180, 2000]	Combined
Observed	73	111	69	24	14	13	13	317
Z+jets	$12.2\pm4.0^{+2.6}_{-2.6}$	$11.5\pm2.4^{+2.1}_{-2.1}$	$3.3\pm1.9^{+0.6}_{-0.6}$	$1.5\pm1.0^{+0.3}_{-0.3}$	$0.5\pm0.5^{+0.2}_{-0.2}$	$0.4\pm0.5^{+0.1}_{-0.1}$	$0.6\pm0.6^{+0.2}_{-0.2}$	$30.0\pm5.2^{+7.5}_{-7.5}$
ZZ	$4.8\pm0.1\pm0.3$	$7.4\pm0.1\pm0.5$	$4.3\pm0.1\pm0.3$	$2.1\pm0.1\pm0.2$	$1.0\pm0.0\pm0.1$	$0.6\pm0.0\pm0.1$	$0.8\pm0.0\pm0.1$	$21.0\pm0.2\pm0.7$
Top	$1.4\pm0.4\pm0.5$	$2.9\pm0.5\pm0.9$	$2.9\pm0.4\pm0.9$	$1.8\pm0.4\pm0.5$	$0.9\pm0.2\pm0.2$	$0.4\pm0.1\pm0.04$	$1.1\pm0.1\pm0.1$	$11.5\pm0.9\pm3.4$
$Z\gamma$	$0.4\pm0.4\pm0.0$	$2.0\pm0.8\pm0.1$	$0.3\pm0.3\pm0.0$	$1.0\pm0.6\pm0.1$	$0.0\pm0.0\pm0.0$	$0.0\pm0.0\pm0.0$	$0.0\pm0.0\pm0.0$	$3.7\pm1.1\pm0.1$
Bkg (total)	$18.7\pm4.0^{+2.6}_{-2.6}$	$23.8\pm2.6^{+2.4}_{-2.4}$	$10.8\pm2.0^{+1.2}_{-1.2}$	$6.4\pm1.2^{+0.6}_{-0.6}$	$2.4\pm0.5^{+0.3}_{-0.3}$	$1.5\pm0.5^{+0.2}_{-0.2}$	$2.5\pm0.6^{+0.2}_{-0.2}$	$68.1\pm5.5^{+8.2}_{-8.2}$
Expected signal	$52.1\pm0.6\pm3.0$	$76.3\pm0.7\pm4.8$	$49.4\pm0.5\pm3.9$	$24.7\pm0.4\pm2.5$	$12.0\pm0.3\pm1.0$	$7.2\pm0.2\pm0.7$	$9.4\pm0.2\pm0.9$	$231.2\pm1.1\pm7.8$
Expected S/B	2.8	3.2	4.6	3.8	4.9	4.9	3.8	3.4

Table 8.20: Summary of observed events and expected signal and background contributions in different p_{T}^{Z} ranges and combined. The first uncertainty is statistical while the second is systematic.

dimensional distributions of the p_{T} of the Z boson candidate versus the p_{T} of the W boson candidate, the transverse mass of the W boson candidate, the $E_{\mathrm{T}}^{\mathrm{miss}}$ and the transverse mass of the diboson system.

Figure 8.25 shows the p_{T} distribution of the Z boson, which is used for the aTGC limit extraction and the unfolding measurement, and the diboson invariant mass distribution, which is used for the unfolding measurement. The invariant mass of the $W^{\pm}Z$ system cannot be fully reconstructed since the information of $p_{z,\nu}$, the neutrino momentum in the z-direction, is missing. However, by assuming the W boson mass to be fixed to $m_W = 80.385$ GeV and the lepton and neutrino to be massless, it is possible to derive m_{WZ} by solving a second order equation for $p_{z,\nu}$. The W boson is built from the lepton and neutrino as $p_W = p_\nu + p_\ell$. With the above assumptions this can be rewritten as,

$$\frac{m_W^2}{2} = E_\nu E_\ell - \vec{p_\nu}\vec{p_\ell}. \tag{8.8}$$

Using $p_x = p_{\mathrm{T}} \cos\phi$ and $p_y = p_{\mathrm{T}} \sin\phi$ in the coordinate system defined earlier gives

$$\vec{p_\nu}\vec{p_\ell} = p_{\mathrm{T},\nu} p_{\mathrm{T},\ell}(\cos\phi_\nu \cos\phi_\ell + \sin\phi_\nu \sin\phi_\ell) + p_{z,\nu} p_{z,\ell}. \tag{8.9}$$

Combining the above two equations, making use of some trigonometric properties, letting $X = \frac{m_W^2}{2} + \cos(\phi_\nu - \phi_\ell) p_{\mathrm{T},\nu} p_{\mathrm{T},\ell}$ and solving for $p_{z,\nu}$ then gives

$$p_{z,\nu}^{\pm} = \frac{X p_{z,\ell} \pm E_\ell \sqrt{X^2 + p_{\mathrm{T},\nu}^2 (p_{z,\ell}^2 - E_\ell^2)}}{(E_\ell^2 - p_{z,\ell}^2)}. \tag{8.10}$$

If there are two real solutions, the solution with the smaller magnitude is chosen as studies show that this choice gives a better reproduction of the truth distribution. If there is no real solution, the real part of the solution with the smaller magnitude is chosen. The $W^{\pm}Z$ mass can then be computed by simple four vector addition. In 27% of the $W^{\pm}Z$ candidate events, the measured transverse mass is larger than the nominal W boson mass and therefore no real solutions exist for $p_{z,\nu}$. The most likely cause for this is that the measured $E_{\mathrm{T}}^{\mathrm{miss}}$ is larger than the actual neutrino p_{T}. In this case, the best estimate is obtained by following the prescription described above and choosing the real part of the complex solutions. This essentially reduces the magnitude of $E_{\mathrm{T}}^{\mathrm{miss}}$ until a physical solution appears.

8.11 Cross Section Measurement

In this analysis, fiducial and total cross section measurements are presented. This section discusses the ingredients needed to compute such quantities, explains the exact definitions and extraction procedure and finally lists the measured cross section results.

8.11.1 A_{WZ} and C_{WZ}

The ATLAS detector has a limited phase space coverage, which is even more reduced when selection cuts are applied. An extrapolation from the detector acceptance to the total

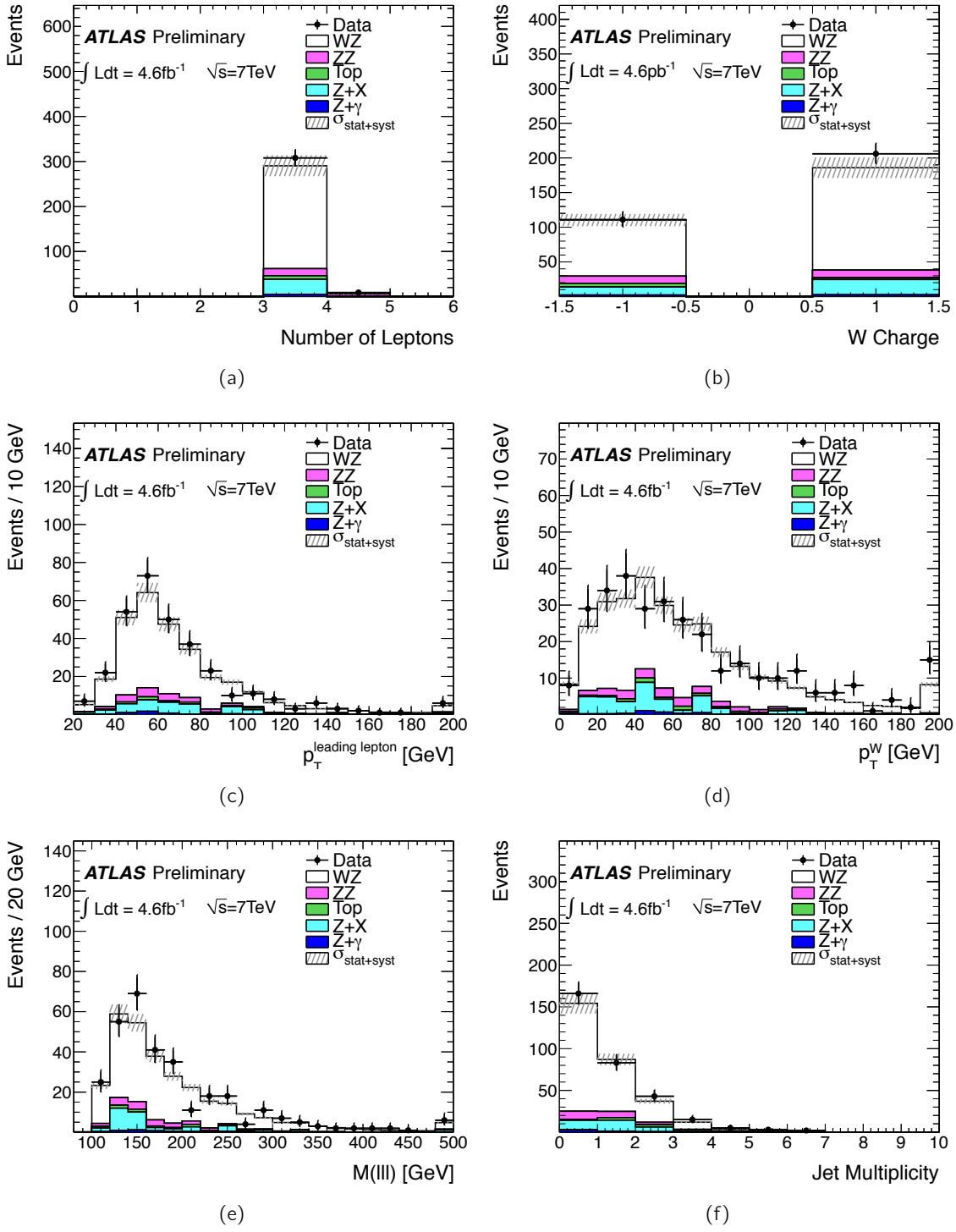

Figure 8.23: Distributions of (a) the number of leptons, (b) the W charge, (c) the p_{T} distribution of the leading lepton in the event, (d) the p_{T} distribution of the W boson candidate, (e) the three-body mass reconstructed using the three selected leptons and (f) the jet multiplicity after the full $W^{\pm}Z$ selection.

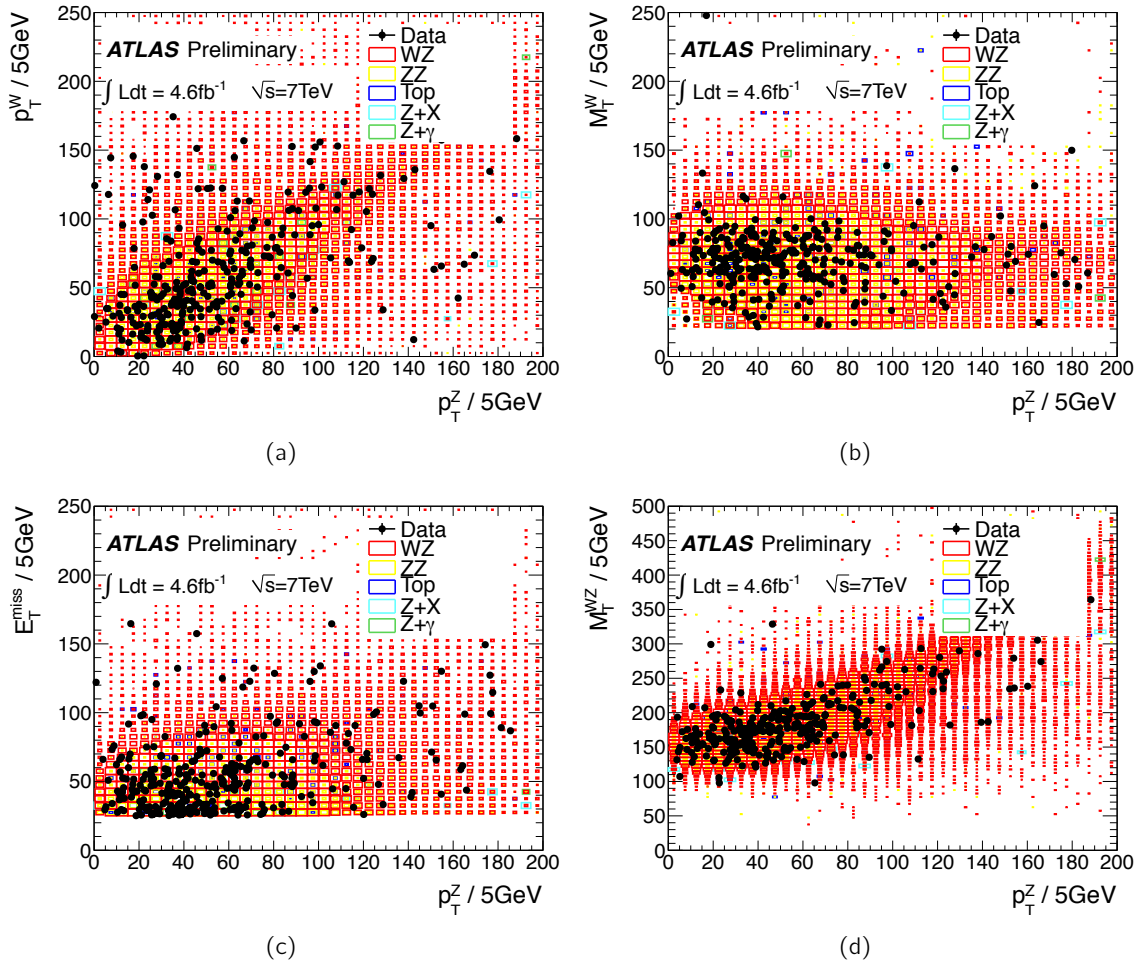

Figure 8.24: Two dimensional distributions of the p_{T} of the Z boson candidate versus (a) the p_{T} of the W boson candidate, (b) the transverse mass of the W boson candidate, (c) the $E_{\mathrm{T}}^{\mathrm{miss}}$ and (d) the transverse mass of the diboson system after the full $W^{\pm}Z$ selection.

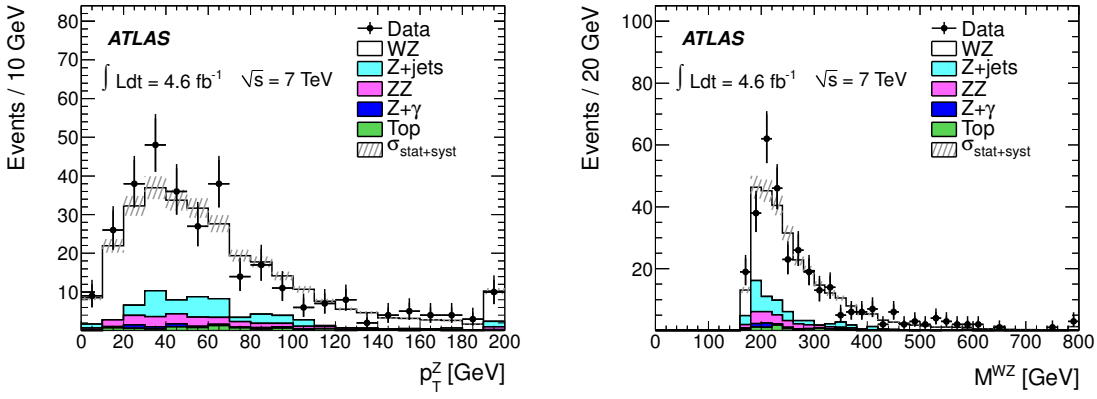

(a) (b)

Figure 8.25: Distributions of (a) the Z boson p_{T} and (b) the diboson invariant mass after the full $W^{\pm}Z$ selection.

phase space must therefore be applied to calculate a total cross section. This extrapolation is made using information from simulation and is accompanied by theoretical uncertainties. A fiducial cross section measurement, without the full extrapolation and with reduced uncertainties, and a total cross section measurement are presented in this thesis.

For a fiducial cross section measurement, a fiducial phase space and a fiducial efficiency correction term must be defined. The former aims to take into account the limited detector acceptance and the effect of kinematic cuts made after the reconstruction. Since the object selection cuts for electrons and muons are not exactly the same, the fiducial phase space for the four different $W^{\pm}Z$ channels will vary. To make it possible to compute a combined fiducial cross section, an additional extrapolation to a common fiducial volume would first have to be performed in which the combined cross section can then be extracted. To avoid such a compilation in this measurement, a common fiducial phase space for the individual channels is defined as follows:

- $p_{\mathrm{T}}^{\ell} > 15\,\mathrm{GeV}$ for the two leptons associated to the Z boson decay,
- $p_{\mathrm{T}}^{\ell} > 20\,\mathrm{GeV}$ for the lepton associated to the W boson decay,
- $|\eta^{\ell}| < 2.5$ for the three leptons,
- $p_{\mathrm{T}}^{\nu} > 25\,\mathrm{GeV}$ for the neutrino,
- $|m_{\ell\ell} - m_Z| < 10\,\mathrm{GeV}$ for the Z boson candidate,
- $m_{\mathrm{T}}^{W} > 20\,\mathrm{GeV}$ for the W boson candidate,
- $\Delta R(\ell,\ell) > 0.3$ for all three leptons.

These cuts are defined only for direct electrons and muons which implies that the fiducial phase space is strictly defined without τ leptons, whose contribution will be accounted for as explained in the following subsection. It should be noted that these cuts are defined for

truth MC objects and that "dressed" final state leptons are used. A dressed final state lepton, electron or muon, has all photons within $\Delta R < 0.1$ added to its Lorentz vector. This procedure is applied to ensure that the final state leptons are physically well-defined and less dependent on the modelling of soft and collinear photon radiation.

The fiducial efficiency correction term C_{WZ} is used to correct the reconstruction-level cross section to a truth-level cross section defined in the fiducial phase space. The advantage of such a correction is that it is less sensitive to theoretical uncertainties such as PDF or QCD scale uncertainties. C_{WZ} approximately gives the probability of reconstructing an event, assuming that all the objects in the event are in the detector and pass all the selection cuts at production, and it is defined as

$$C_{WZ\to\ell\nu\ell\ell} = \epsilon_{\text{trig}} \times \epsilon_{\text{event}} \times \epsilon_{\text{lep}} \times \alpha_{\text{reco}} \tag{8.11}$$

where ϵ_{trig} is the trigger efficiency, ϵ_{event} the efficiency of the event level cuts, $\epsilon_{\text{lep}} = \prod_{i=1}^{3} \epsilon_{\text{lep},i}$ the product of the individual efficiencies for the three leptons to pass the object selection cuts and α_{reco} the reconstruction to generator level fiducial phase space correction which includes smearing and resolution corrections. In practice, C_{WZ} can be calculated by applying the necessary corrections to the signal MC and computing the ratio of the number of events passing the reconstruction level cuts to the number of events passing the fiducial phase space cuts at the generator level as

$$C_{WZ\to\ell\nu\ell\ell} = \frac{N^{\text{Pass Reco Cuts}}_{\text{MC Reco } WZ\to\ell\nu\ell\ell} \times \text{SF}}{N^{\text{Pass Fid Cuts}}_{\text{MC Truth } WZ\to\ell\nu\ell\ell}} \tag{8.12}$$

where the SF is applied on an event-by-event basis and corrects for discrepancies in trigger and reconstruction efficiency between data and MC as

$$\text{SF} = \frac{\epsilon^{\text{data}}_{\text{trig}}}{\epsilon^{\text{MC}}_{\text{trig}}} \times \frac{\epsilon^{\text{data}}_{\text{reco}}}{\epsilon^{\text{MC}}_{\text{reco}}} \tag{8.13}$$

with $\epsilon_{\text{reco}} = \epsilon_{\text{lep}} \times \epsilon_{\text{event}}$. C_{WZ} will need to be calculated for each decay channel separately. It should be noted that this extrapolates from reconstructed level to truth fiducial level values within the given channel and branching ratios are needed to combine channels and obtain a total cross section.

The $\Delta R(\ell,\ell) > 0.3$ cut is applied to the fiducial phase space to mimic the isolation cut that is applied to the reconstructed quantities and to ensure that the efficiency does not drop in the high energy regime. This point is illustrated in figure 8.26 which shows C_{WZ} as a function of the Z boson p_{T}. If the $\Delta R(\ell,\ell)$ cut is not applied the efficiency drops significantly in the high energy tail as the Z boson becomes boosted and the two decay leptons cannot be well separated anymore. The application of the $\Delta R(\ell,\ell)$ cut prevents this from happening.

The value and systematic uncertainty of C_{WZ} also needs to be checked for the aTGC limits, which are derived by comparing the signal yield in the reconstructed data sample to the expectation computed with aTGC. Within the studied aTGC parameter ranges, the expected signal yields and the corresponding fiducial cross sections increase by nearly a factor of two. However, C_{WZ} remains relatively stable, the average C_{WZ} varies at most by 4%. This means that the experimental systematic uncertainties on C_{WZ} evaluated for the SM can also be used in the aTGC limit setting.

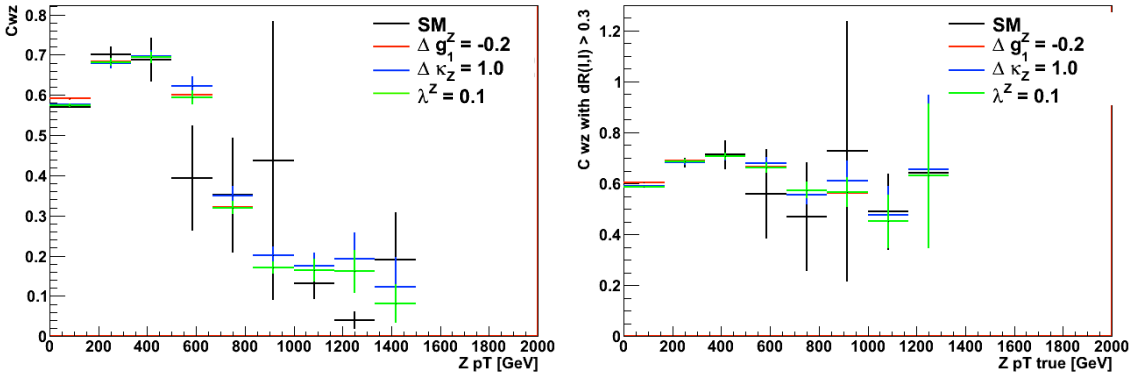

(a) (b)

Figure 8.26: C_{WZ} as a function of p_{T}^{Z} (a) without and (b) with a $\Delta R(\ell,\ell) > 0.3$ cut.

A further correction factor is needed to calculate a total cross section as the reconstruction level cross section must be corrected to the full phase space of possible truth level quantities. This is done by applying an acceptance correction A_{WZ} from the fiducial truth phase space to the full truth phase space defined as

$$A_{WZ\to\ell\nu\ell\ell} = \frac{N^{\text{Pass Fid Cuts}}_{\text{MC Truth } WZ\to\ell\nu\ell\ell}}{N^{\text{All}}_{\text{MC Truth } WZ\to\ell\nu\ell\ell}}, \tag{8.14}$$

which will again be calculated for each channel separately. Consequently, the theoretical uncertainties will primarily affect $A_{WZ\to\ell\nu\ell\ell}$ and only lead to small uncertainties on $C_{WZ\to\ell\nu\ell\ell}$. The total acceptance correction will be the product $A_{WZ\to\ell\nu\ell\ell} \times C_{WZ\to\ell\nu\ell\ell}$.

$A_{WZ\to\ell\nu\ell\ell}$ is calculated relative to the theoretical total cross section predicted by MCFM using the fiducial cross section from MC@NLO with HERWIG showering, after dressing the final state leptons with all final state photons within $\Delta R < 0.1$. A correction factor of 1.018 is applied and taken from a comparison of the fiducial cross sections calculated by MC@NLO before showering and MCFM to account for the missing Z/γ^{*} interference in the MC@NLO samples. $C_{WZ\to\ell\nu\ell\ell}$ is calculated using the signal MC samples. The calculated values are summarised in table 8.21. The differences in A_{WZ} after showering are due to FSR photons emitted outside $\Delta R = 0.1$ around electrons. The A_{WZ} values have been cross checked with the `POWHEG BOX` generator [84] and differences were found to be 0.4%, which is taken as a generator uncertainty, as already mentioned in section 8.9.4.

8.11.2 Cross Section Definition

For a given $W^{\pm}Z \to \ell\nu\ell\ell$ channel, where ℓ is e or μ, the fiducial cross section is defined as

$$\sigma^{\text{fid}}_{WZ\to\ell\nu\ell\ell} = \frac{N_{\text{obs}} - N_{\text{bkg}}}{\mathcal{L} \times C_{WZ\to\ell\nu\ell\ell}} \times \left(1 - \frac{N^{MC}_{\tau}}{N^{MC}_{\text{sig}}}\right). \tag{8.15}$$

	$\mu\mu\mu$	$e\mu\mu$	$ee\mu$	eee
A_{WZ} (pre-showering)	0.352	0.352	0.352	0.352
A_{WZ} (post-showering)	0.338	0.333	0.332	0.330
C_{WZ}	0.780	0.548	0.525	0.380
$A_{WZ} \times C_{WZ}$	0.263	0.182	0.174	0.125

Table 8.21: Fiducial and total acceptance corrections per channel.

N_{obs} and N_{bkg} denote the number of observed and expected background events, respectively, $\mathcal{L}$ is the luminosity and $C_{WZ\to\ell\nu\ell\ell}$ is the correction factor defined in section 8.11.1. N_{τ}^{MC} is the number of accepted MC $W^{\pm}Z$ events where at least one of the bosons decays into a τ lepton and N_{sig}^{MC} is the number of accepted MC $W^{\pm}Z$ events with decays into any lepton flavour. Since the fiducial volume is defined by the leptonic kinematics, the fiducial cross section calculated is specifically for leptonic decays of $W^{\pm}Z$ and therefore must include the branching ratio.

The cross section for the total phase space in each channel can be calculated as

$$\sigma_{WZ}^{\text{tot}} = \frac{\sigma_{WZ\to\ell\nu\ell\ell}^{\text{fid}}}{BR_{WZ\to\ell\nu\ell\ell} \times A_{WZ\to\ell\nu\ell\ell}} \tag{8.16}$$

where $A_{WZ\to\ell\nu\ell\ell}$ is the acceptance correction factor defined in section 8.11.1 and $BR_{WZ\to\ell\nu\ell\ell}$ is the branching ratio for a W boson to decay to $\ell\nu$ and a Z boson to decay to $\ell\ell$.

In practice, equations 8.15 and 8.16 are not used to do the cross section extraction. Instead a minimum log-likelihood approach is used to calculate both the single channel and combined cross section. This approach takes into account the Poisson statistics of the samples and allows one to readily include the $W^{\pm}Z \to \tau + X$ contribution as will be discussed below.

8.11.3 Cross Section Calculation

The number of observed and expected events as well as the number of estimated background events are needed to calculate a cross section. Systematic uncertainties are taken into account as nuisance parameters x_k which affect N_s^i, the number of expected signal events, and N_b^i, the number of expected background events, as follows

$$N_s^i(\sigma, \mathbf{x}) = N_s^i(\sigma, 0)\left(1 + \sum_{k=1}^{n} x_k S_k^i\right) \tag{8.17}$$

$$N_b^i(\mathbf{x}) = N_b^i(0)\left(1 + \sum_{k=1}^{n} x_k B_k^i\right). \tag{8.18}$$

Each systematic uncertainty is assumed to be a normal distribution with zero mean and unit variance. The parameters S_k^i and B_k^i are the relative systematic uncertainties due to the k^{th} source of systematic uncertainty in channel i on the signal and background, respectively.

The number of signal events can be written as a function of the fiducial cross section

$$N_s^i\left(\sigma^{\text{fid}}_{WZ\to\ell\nu\ell\ell}, \mathbf{x}\right) = \frac{\sigma^{\text{fid}}_{WZ\to\ell\nu\ell\ell}}{\sigma^{\text{tot}}_{MC,\ WZ\to\ell\nu\ell\ell} \times A_{WZ\to\ell\nu\ell\ell}} \times \left(N^{MC}_{WZ\to\ell\nu\ell\ell} + N^{MC}_{WZ\to\tau+X}\right) \times (1 + \sum_{k=1}^{n} x_k S_k^i) \tag{8.19}$$

or as a function of the total cross section

$$N_s^i(\sigma^{\text{tot}}_{WZ}, \mathbf{x}) = \frac{\sigma^{\text{tot}}_{WZ}}{\sigma^{\text{tot}}_{MC,\ WZ}} \times \left(N^{MC}_{WZ\to\ell\nu\ell\ell} + N^{MC}_{WZ\to\tau+X}\right) \times (1 + \sum_{k=1}^{n} x_k S_k^i). \tag{8.20}$$

where $WZ \to \ell\nu\ell\ell$ does not include τ leptons unless explicitly specified. A negative log-likelihood function can be defined as

$$-\ln\ L(\sigma, \mathbf{x}) = \sum_{i=1}^{4} -\ln\left(\frac{e^{-\left(N_s^i(\sigma,\mathrm{x}) + N_b^i(\mathrm{x})\right)} \times \left(N_s^i(\sigma,\mathbf{x}) + N_b^i(\mathbf{x})\right)^{N^i_{\text{obs}}}}{(N^i_{\text{obs}})!}\right) + \sum_{k=1}^{n} \frac{x_k^2}{2} \tag{8.21}$$

where N^i_{obs} is the number of observed events after the full selection. In equation 8.21, the expression inside the logarithm is essentially the Poisson probability that the expected number of signal and background events produce the observed number of events. The final term in the likelihood equation is the product of the Gaussian constraints on the nuisance parameters x_k. If two systematic uncertainty sources are correlated, their linear sum is used. A single random variable x_k is used over all channels for signal and background as the effect of each systematic uncertainty is 100% correlated across channels and between signal and background. It should be noted that if a systematic uncertainty k^* only affects a single channel, or only signal and not background, only the $S^i_{k^*}$ and $B^i_{k^*}$ which are affected by the systematic uncertainty k^* are non-zero. Furthermore, it should be noted that, as each parameter x_k has a Gaussian constraint, the number of degrees of freedom of the fit is unchanged.

In equations 8.19 and 8.20, MC is used to determine the total number of events expected in a given channel. This number is then scaled by the ratio of the measured cross section to the MC generator cross section used to produce the MC expectations. This means that the data is used to drive the measurement to find the best rescaling of the expected signal contributions and thus allows the extraction of a cross section.

To find the most probable value of the fiducial or total cross section σ, the log-likelihood function is minimised simultaneously over σ and all the nuisance parameters x_k. The uncertainties are estimated by taking the difference of the cross section at the minimum to the cross section where the log-likelihood is 0.5 units above the minimum along the direction of the parameter σ. This calculation is performed in the positive and negative directions separately and can therefore give different positive and negative uncertainties. As the nuisance parameters account for the systematic uncertainties on the measurement, this uncertainty is the combined statistical and systematic uncertainty on the measurement. The minimization and uncertainty calculation is performed with the Minuit package [180].

Lastly, to calculate the fiducial or total cross section in a single channel i, only the Poisson probability in channel i is used rather than the product over all channels. The Gaussian constraint terms are unchanged.

8.11.4 Calculation of Systematic Uncertainties on the Cross Section

All the systematic uncertainties will automatically be taken into account by the full likelihood function with nuisance parameters and be propagated to the final uncertainty. To estimate separately the contribution from each systematic uncertainty, the specific uncertainty can be propagated by hand to the final cross section acceptance. This is done by varying the signal and background acceptance in the likelihood function up and down by 1σ and re-minimizing the likelihood function, without nuisance parameters, to find a new cross section value. The specific translations are

$$C_{WZ} \rightarrow C_{WZ} \times (1 + \Delta_s) \tag{8.22}$$

$$N_{WZ\to\tau+X} \rightarrow N_{WZ\to\tau+X} \times (1 + \Delta_\tau) \tag{8.23}$$

$$N_{\text{bkg}} \rightarrow N_{\text{bkg}} \times (1 + \Delta_b) \tag{8.24}$$

where Δ_s, Δ_τ and Δ_b are the fractional changes in the $W^{\pm}Z \to \ell\nu\ell\ell$, the $W^{\pm}Z \to \tau + X$ and the background estimations. The cross section difference between the central value and the one obtained after adjusting the acceptance in the likelihood function is taken as the estimate of the systematic uncertainty on the cross section.

This variation of every source of systematic uncertainty is performed for each channel and for the combined measurement. The systematic uncertainties on the fiducial and total cross sections thus obtained are summarised in tables 8.22 and 8.23. All systematic uncertainties are added in quadrature to give the total uncertainty quoted in the last line, excluding the luminosity uncertainty.

8.11.5 Cross Section Results

The final results for the fiducial and total $W^{\pm}Z$ cross section measurements in each channel and for the combined measurement are shown in tables 8.24 and 8.25. The systematic uncertainties include all sources except luminosity, which is listed separately.

8.12 Anomalous Triple Gauge Couplings

$W^{\pm}Z$ production can probe the WWZ TGC vertex specifically and set limits on anomalous TGCs as described in section 3.2. The Lagrangian used to derive these limits is given in equation 3.9. Only charge and parity conserving terms as well as operators up to dimension six are considered which leads to three free parameters to test g_1^Z, κ^Z and λ^Z or, expressed in terms of their deviation from the SM values, Δg_1^Z, $\Delta\kappa^Z$ and λ^Z.

Any deviation of the couplings from their SM values will lead to a change in the production rate as predicted by the SM. If such deviations occur and aTGCs are present, the consistency between the observed data and the MC prediction for an aTGC signal must be tested. This is measured by establishing the aTGC parameter set that reproduces the observed data at the 95% confidence interval (C.I.). The C.I. is determined with a frequentist approach, also called a Neyman construction [181] or a Feldman-Cousins method [182]. A likelihood function, analogous to the one used in the cross section calculation, is built that

Source	$\mu\mu\mu$	$e\mu\mu$	$ee\mu$	eee	Combined
μ reconstruction efficiency	$^{+0.88}_{-0.87}$	$^{+0.57}_{-0.56}$	$^{+0.32}_{-0.32}$	$^{+0.00}_{-0.00}$	$^{+0.52}_{-0.53}$
μ p_T smearing	$^{+0.11}_{-0.11}$	$^{+0.11}_{-0.11}$	$^{+0.00}_{-0.00}$	$^{+0.00}_{-0.00}$	$^{+0.07}_{-0.07}$
μ isolation & IP efficiency	$^{+0.66}_{-0.65}$	$^{+0.45}_{-0.45}$	$^{+0.22}_{-0.22}$	$^{+0.00}_{-0.00}$	$^{+0.39}_{-0.40}$
e reconstruction efficiency	$^{+0.00}_{-0.00}$	$^{+0.91}_{-0.90}$	$^{+1.86}_{-1.80}$	$^{+2.84}_{-2.71}$	$^{+1.12}_{-1.11}$
e identification efficiency	$^{+0.00}_{-0.00}$	$^{+1.37}_{-1.34}$	$^{+2.53}_{-2.42}$	$^{+4.02}_{-3.76}$	$^{+1.61}_{-1.57}$
e energy smearing	$^{+0.00}_{-0.00}$	$^{+0.00}_{-0.00}$	$^{+0.11}_{-0.11}$	$^{+0.11}_{-0.11}$	$^{+0.04}_{-0.04}$
e energy scale	$^{+0.00}_{-0.00}$	$^{+0.34}_{-0.34}$	$^{+0.32}_{-0.32}$	$^{+0.56}_{-0.55}$	$^{+0.25}_{-0.25}$
e isolation & IP efficiency	$^{+0.00}_{-0.00}$	$^{+0.34}_{-0.34}$	$^{+1.20}_{-1.17}$	$^{+1.58}_{-1.53}$	$^{+0.62}_{-0.63}$
$E_{\mathrm{T}}^{\mathrm{miss}}$ jet energy scale	$^{+0.11}_{-0.11}$	$^{+0.11}_{-0.11}$	$^{+0.11}_{-0.11}$	$^{+0.11}_{-0.11}$	$^{+0.11}_{-0.11}$
$E_{\mathrm{T}}^{\mathrm{miss}}$ jet energy resolution	$^{+0.22}_{-0.22}$	$^{+0.45}_{-0.45}$	$^{+0.32}_{-0.32}$	$^{+0.33}_{-0.33}$	$^{+0.32}_{-0.32}$
$E_{\mathrm{T}}^{\mathrm{miss}}$ cluster energy	$^{+0.22}_{-0.22}$	$^{+0.68}_{-0.67}$	$^{+0.22}_{-0.22}$	$^{+0.45}_{-0.44}$	$^{+0.36}_{-0.37}$
$E_{\mathrm{T}}^{\mathrm{miss}}$ pile-up	$^{+0.11}_{-0.11}$	$^{+0.34}_{-0.34}$	$^{+0.11}_{-0.11}$	$^{+0.33}_{-0.33}$	$^{+0.20}_{-0.20}$
Trigger μ	$^{+0.33}_{-0.33}$	$^{+0.23}_{-0.23}$	$^{+0.11}_{-0.11}$	$^{+0.00}_{-0.00}$	$^{+0.20}_{-0.20}$
Signal stat. (MC)	$^{+0.86}_{-0.85}$	$^{+1.07}_{-1.05}$	$^{+0.93}_{-0.92}$	$^{+1.30}_{-1.27}$	$^{+0.50}_{-0.51}$
Bkg stat. (MC)	$^{+0.11}_{-0.11}$	$^{+1.59}_{-1.59}$	$^{+0.16}_{-0.16}$	$^{+1.70}_{-1.70}$	$^{+0.43}_{-0.42}$
Bkg stat. (data-driven)	$^{+4.52}_{-4.52}$	$^{+4.30}_{-4.30}$	$^{+2.79}_{-2.79}$	$^{+5.12}_{-5.12}$	$^{+2.30}_{-2.23}$
Data-driven method Z+jets	$^{+4.43}_{-4.44}$	$^{+3.85}_{-3.86}$	$^{+2.46}_{-2.47}$	$^{+4.59}_{-4.57}$	$^{+3.05}_{-3.04}$
Data-driven method $t\bar{t}$	$^{+1.26}_{-1.26}$	$^{+1.75}_{-1.75}$	$^{+1.26}_{-1.26}$	$^{+0.48}_{-0.48}$	$^{+1.26}_{-1.26}$
Total (no lumi)	$^{+6.63}_{-6.64}$	$^{+6.68}_{-6.67}$	$^{+5.31}_{-5.24}$	$^{+8.93}_{-8.75}$	$^{+4.67}_{-4.62}$

Table 8.22: Relative systematic uncertainties (%) on the fiducial cross section for each channel.

Source	$\mu\mu\mu$	$e\mu\mu$	$ee\mu$	eee	Combined
μ reconstruction efficiency	$^{+0.88}_{-0.88}$	$^{+0.57}_{-0.56}$	$^{+0.32}_{-0.32}$	$^{+0.00}_{-0.00}$	$^{+0.53}_{-0.53}$
μ p_{T} smearing	$^{+0.10}_{-0.12}$	$^{+0.11}_{-0.11}$	$^{+0.00}_{-0.00}$	$^{+0.00}_{-0.00}$	$^{+0.07}_{-0.07}$
μ isolation & IP efficiency	$^{+0.65}_{-0.66}$	$^{+0.45}_{-0.45}$	$^{+0.22}_{-0.21}$	$^{+0.00}_{-0.00}$	$^{+0.40}_{-0.40}$
e reconstruction efficiency	$^{+0.00}_{-0.00}$	$^{+0.91}_{-0.89}$	$^{+1.86}_{-1.79}$	$^{+2.87}_{-2.72}$	$^{+1.10}_{-1.09}$
e identification efficiency	$^{+0.00}_{-0.00}$	$^{+1.37}_{-1.34}$	$^{+2.53}_{-2.41}$	$^{+4.06}_{-3.77}$	$^{+1.57}_{-1.55}$
e energy smearing	$^{+0.00}_{-0.00}$	$^{+0.00}_{-0.00}$	$^{+0.11}_{-0.11}$	$^{+0.11}_{-0.12}$	$^{+0.04}_{-0.04}$
e energy scale	$^{+0.00}_{-0.00}$	$^{+0.34}_{-0.34}$	$^{+0.32}_{-0.32}$	$^{+0.56}_{-0.56}$	$^{+0.24}_{-0.24}$
e isolation & IP efficiency	$^{+0.00}_{-0.00}$	$^{+0.34}_{-0.34}$	$^{+1.19}_{-1.17}$	$^{+1.58}_{-1.54}$	$^{+0.61}_{-0.60}$
$E_{\mathrm{T}}^{\mathrm{miss}}$ jet energy scale	$^{+0.10}_{-0.12}$	$^{+0.11}_{-0.11}$	$^{+0.11}_{-0.11}$	$^{+0.11}_{-0.12}$	$^{+0.11}_{-0.11}$
$E_{\mathrm{T}}^{\mathrm{miss}}$ jet energy resolution	$^{+0.21}_{-0.23}$	$^{+0.45}_{-0.45}$	$^{+0.32}_{-0.32}$	$^{+0.33}_{-0.34}$	$^{+0.32}_{-0.32}$
$E_{\mathrm{T}}^{\mathrm{miss}}$ cluster energy	$^{+0.21}_{-0.23}$	$^{+0.68}_{-0.67}$	$^{+0.22}_{-0.21}$	$^{+0.44}_{-0.45}$	$^{+0.36}_{-0.36}$
$E_{\mathrm{T}}^{\mathrm{miss}}$ pile-up	$^{+0.10}_{-0.12}$	$^{+0.34}_{-0.34}$	$^{+0.11}_{-0.11}$	$^{+0.33}_{-0.34}$	$^{+0.20}_{-0.20}$
Trigger μ	$^{+0.32}_{-0.34}$	$^{+0.23}_{-0.23}$	$^{+0.11}_{-0.11}$	$^{+0.00}_{-0.00}$	$^{+0.20}_{-0.20}$
Generator	$^{+0.40}_{-0.41}$	$^{+0.40}_{-0.40}$	$^{+0.40}_{-0.40}$	$^{+0.40}_{-0.40}$	$^{+0.40}_{-0.40}$
PDF	$^{+1.22}_{-1.20}$	$^{+1.21}_{-1.18}$	$^{+1.21}_{-1.18}$	$^{+1.22}_{-1.20}$	$^{+1.21}_{-1.18}$
μ_r and μ_f scale	$^{+0.40}_{-0.41}$	$^{+0.40}_{-0.40}$	$^{+0.40}_{-0.40}$	$^{+0.40}_{-0.40}$	$^{+0.40}_{-0.40}$
Signal stat. (MC)	$^{+0.86}_{-0.86}$	$^{+1.07}_{-1.05}$	$^{+0.93}_{-0.91}$	$^{+1.31}_{-1.28}$	$^{+0.50}_{-0.50}$
Bkg stat. (MC)	$^{+0.11}_{-0.12}$	$^{+1.59}_{-1.59}$	$^{+0.16}_{-0.16}$	$^{+1.70}_{-1.71}$	$^{+0.43}_{-0.42}$
Bkg stat. (data-driven)	$^{+4.52}_{-4.51}$	$^{+4.30}_{-4.29}$	$^{+2.78}_{-2.78}$	$^{+5.06}_{-5.11}$	$^{+2.31}_{-2.21}$
Data-driven method Z+jets	$^{+4.42}_{-4.44}$	$^{+3.85}_{-3.85}$	$^{+2.46}_{-2.46}$	$^{+4.54}_{-4.57}$	$^{+3.06}_{-3.02}$
Data-driven method $t\bar{t}$	$^{+1.26}_{-1.27}$	$^{+1.75}_{-1.75}$	$^{+1.25}_{-1.25}$	$^{+0.48}_{-0.49}$	$^{+1.26}_{-1.25}$
Total (no lumi)	$^{+6.76}_{-6.77}$	$^{+6.81}_{-6.78}$	$^{+5.47}_{-5.37}$	$^{+9.00}_{-8.86}$	$^{+4.85}_{-4.76}$

Table 8.23: Relative systematic uncertainties (%) on the total cross section for each channel.

Channel	Cross section [fb]
$\mu\mu\mu$	$23.03^{+2.84}_{-2.66}(\text{stat})\ ^{+1.53}_{-1.53}(\text{syst})\ ^{+0.46}_{-0.45}(\text{lumi})$
$e\mu\mu$	$21.46^{+3.46}_{-3.20}(\text{stat})\ ^{+1.43}_{-1.43}(\text{syst})\ ^{+0.44}_{-0.43}(\text{lumi})$
$ee\mu$	$24.98^{+3.57}_{-3.25}(\text{stat})\ ^{+1.33}_{-1.31}(\text{syst})\ ^{+0.49}_{-0.48}(\text{lumi})$
eee	$22.53^{+4.29}_{-3.85}(\text{stat})\ ^{+2.01}_{-1.97}(\text{syst})\ ^{+0.46}_{-0.44}(\text{lumi})$
Combined	$92.31^{+6.66}_{-6.33}(\text{stat})\ ^{+4.31}_{-4.26}(\text{syst})\ ^{+1.85}_{-1.79}(\text{lumi})$

Table 8.24: Measured fiducial $W^{\pm}Z$ cross sections for each channel and combined.

Channel	Cross section [pb]
$\mu\mu\mu$	$18.74^{+2.31}_{-2.17}(\text{stat})\ ^{+1.27}_{-1.27}(\text{syst})\ ^{+0.38}_{-0.36}(\text{lumi})$
$e\mu\mu$	$17.72^{+2.86}_{-2.64}(\text{stat})\ ^{+1.21}_{-1.20}(\text{syst})\ ^{+0.37}_{-0.35}(\text{lumi})$
$ee\mu$	$20.69^{+2.97}_{-2.69}(\text{stat})\ ^{+1.13}_{-1.11}(\text{syst})\ ^{+0.41}_{-0.39}(\text{lumi})$
eee	$18.78^{+3.58}_{-3.20}(\text{stat})\ ^{+1.69}_{-1.66}(\text{syst})\ ^{+0.38}_{-0.37}(\text{lumi})$
Combined	$19.00^{+1.38}_{-1.30}(\text{stat})\ ^{+0.92}_{-0.90}(\text{syst})\ ^{+0.38}_{-0.37}(\text{lumi})$

Table 8.25: Measured total $W^{\pm}Z$ cross sections for each channel and combined in agreement with a SM prediction of $\sigma_{WZ}^{\text{tot}} = 17.6^{+1.1}_{-1.0}$ pb.

can predict the number of events not as a function of the cross section but as a function of the aTGC parameters. This smooth prediction for any aTGC values can be realised using the event-by-event reweighting procedure available in MC@NLO and described in section 8.12.3.

In addition to affecting the total $W^{\pm}Z$ production cross-section, aTGCs can also change the expected distribution of measured observables. Since Δg_1^Z and λ^Z are proportional to $\hat{s}$ and $\Delta\kappa^Z$ is proportional to $\sqrt{\hat{s}}$, any observables that are sensitive to $\hat{s}$ will be sensitive to the presence of aTGCs. As mentioned in section 3.2, a derivative in the couplings in the effective Lagrangian translates into a gauge boson momentum dependence on the aTGC parameters. It can therefore be beneficial to not just count the total number of events but extract the aTGC limits using the distribution of a specific variable. The following section discusses the aTGC dependence of several observables and justifies the choice of the Z boson p_{T} to extract aTGC limits in this analysis.

Unitarity violation was discussed in section 3.2. The consensus in ATLAS and CMS is to express aTGC limits without a form factor, which is essentially equivalent to setting the cutoff scale Λ to infinity. The aTGC MC samples used in this analysis were generated with $\Lambda = 100$ TeV. The reweighting procedure, described in section 8.12.3, can be used to move the cutoff scale to a different value or remove it completely.

8.12.1 Selection of p_{T}^Z

Figure 8.27 shows the aTGC dependence of the inclusive $W^{\pm}Z$ cross section and of the distributions of several observables at MC truth level. The $W^{\pm}Z$ cross section has a quadratic aTGC dependence and the leading lepton p_{T} distribution, the mass of the $W^{\pm}Z$ system and the Z boson p_{T} spectrum all show large deviations from the SM distributions in the high tail. These distributions have been normalised to the same area to allow shape comparisons and can be considerably more sensitive to aTGCs than the cross section.

A study using 1 fb^{-1} of data showed that the limits on Δg_1^Z, $\Delta\kappa^Z$, and λ^Z improve, on average, by 42%, 23% and 41% when using the p_{T}^Z spectrum instead of the cross section [183]. The particular choice of kinematic distribution is based on optimising the sensitivity to aTGC parameters, if they exist, while achieving the most stringent limits, if they do not.

A toy study is performed to compare the distribution of expected limits using different observables and assuming no aTGC signal. A simplified version of the limit setting procedure, which will be detailed in section 8.12.4, is used. The actual limit extraction procedure uses a frequentist approach to determine the 95% C.I. based on a likelihood function describing how likely the data is, given a particular value of an aTGC parameter. While this limit extraction gives exact coverage, it is computationally slow. To approximate the limit extraction for this optimization study, the 95% C.I. is calculated using the best fit value varied up or down by the uncertainties computed by setting the delta log-likelihood function equal to 1.92. This method has been found to slightly under-cover but it can still be used to compare the limits found by studying different variables and binnings.

Four different distributions sensitive to aTGCs are tested. They are the Z boson p_{T} spectrum, the invariant mass of the three selected leptons, the p_{T} spectrum of the leading lepton and the diboson invariant mass distribution. Each of these distributions is then divided into four bins. Since the aTGC dependence is strongest in the high tail, the sensitivity to aTGCs depends strongly on the ratio of the number of expected SM to aTGC events in

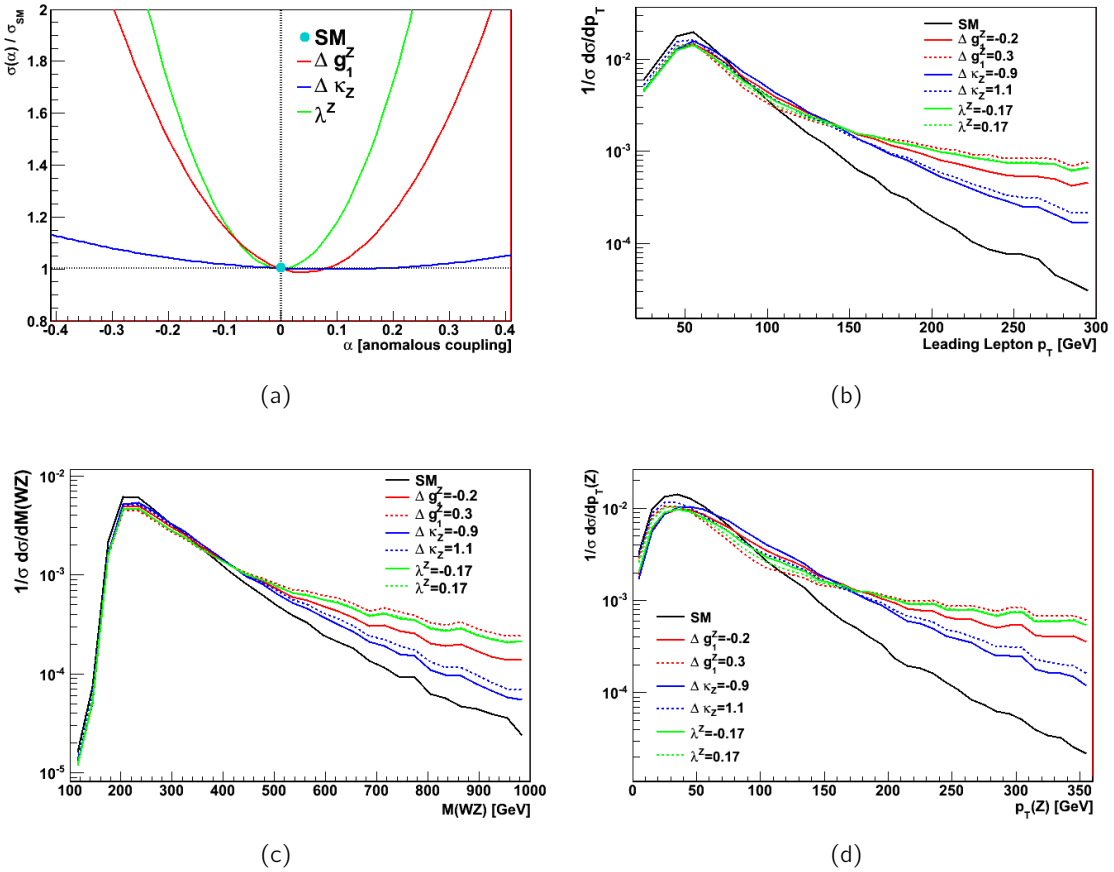

Figure 8.27: The impact of aTGCs on the truth MC distributions of (a) the aTGC to SM cross section ratio, (b) the p_{T} of the leading lepton, (c) the diboson invariant mass and (d) the p_{T} of the Z boson. A form factor with $\Lambda = 2$ TeV is used in these distributions.

the last bin or simply on the number of expected SM events in the last bin. To exclude a potential bin-related bias and to only compare the sensitivity of each observable to aTGCs, the binning for each distribution is selected so that each bin has the same number of expected SM $W^{\pm}Z$ events across all observables.

The width of the 95% C.I. is then calculated for each aTGC parameter and each observable, using 5000 toy experiments and the delta log-likelihood method described above. In each toy experiment, the number of "observed" data events per bin is randomly sampled from a Poisson distribution with mean equal to the number of data and background events in each bin. The signal to background ratio is assumed to be the same for each kinematic distribution and the limits are calculated considering only statistical uncertainties. The cutoff scale is set to 3 TeV for this comparison. The resulting widths of the expected aTGC limits in the absence of an aTGC signal are shown in figure 8.28. They indicate that the aTGC sensitivity varies between the different kinematic distributions. In particular, the p_{T}^{Z} distribution shows the narrowest expected limits for all three aTGC parameters.

It makes qualitative sense that the measured p_{T}^{Z} distribution is the most sensitive to aTGCs since the p_{T}^{Z} distribution is a proxy for the $W^{\pm}Z$ mass, which is directly sensitive to $\sqrt{\hat{s}}$. A disadvantage of the $W^{\pm}Z$ mass is that it cannot be directly reconstructed and some information is lost in the process, as described in section 8.10. The p_{T}^{Z} distribution, however, can be built directly from the reconstructed leptons and it has a further advantage in that it has a good shape discrimination for positive and negative aTGC values, which can be seen in figure 8.27. Therefore, if aTGCs happen to be measured the p_{T}^{Z} distribution is also sensitive to the sign of the parameter. In summary, the p_{T}^{Z} distribution is chosen to search for the presence of aTGCs due to the narrowness of the expected limits in the absence of an aTGC signal, the possibility to distinguish the sign of aTGC parameters if they exist and the good experimental resolution.

8.12.2 Binning Optimization

As visible in figure 8.27(d), the deviation between the predicted SM distribution and the aTGC distribution grows for larger values of p_{T}^{Z} and therefore the ratio of expected events between the SM and aTGC prediction depends on the binning of the distribution.

An initial study is performed to choose a binning for the p_{T}^{Z} distribution that can be used for the extraction of aTGC limits and it is based on statistical uncertainties and MC background estimations only. The procedure used to test the sensitivity to different p_{T}^{Z} binnings is the same delta log-likelihood method as described in the previous section. The last bin is required to contain 10% or more of the total number of expected events, to ensure that the statistical uncertainty in that bin is below 25%. The initial optimization finds a maximum in expected sensitivity for a binning of [0-30-60-120-500] GeV. Moving from four to eight bins is not found to significantly increase the expected sensitivity. From the four nominal bins, all systematic uncertainties and data-driven background estimates can be calculated and used to proceed with further optimization.

For the second round of optimization, the expected aTGC sensitivity is tested by comparing the distribution of expected limits for different binnings. All four bin boundaries are moved and tested. The systematic uncertainties are kept at the same relative size in each bin as the bin boundaries are changed. For the data-driven background estimates, the size of the

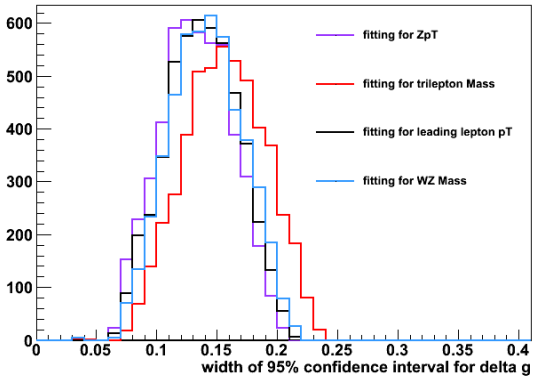

(a)

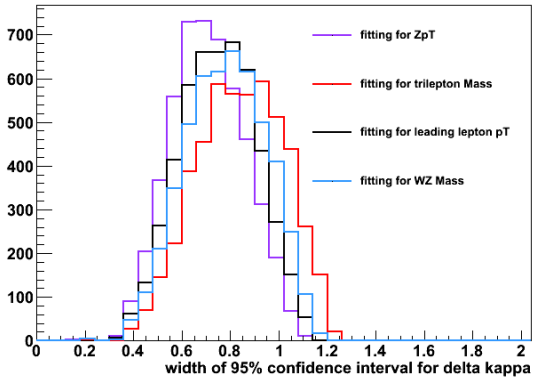

(b)

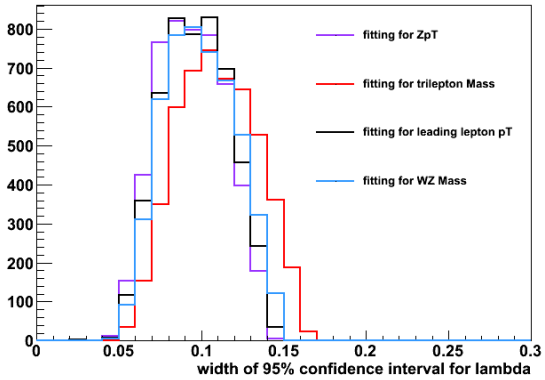

(c)

Figure 8.28: The 95% C.I. widths of different variables for the (a) Δg_1^Z, (b) $\Delta\kappa^Z$ and (c) λ^Z parameters. The *y*-axis shows the number of events.

background in the new binning is smoothly varied from the nominal binning by assuming that the backgrounds follow the same shape as the signal. This is done because the actual data-driven backgrounds are based on control regions with limited statistics and would therefore suffer from statistical fluctuations. The aim is to optimise based on the size of expected background, not based on false minima arising from real data fluctuations. The expected number of SM and aTGC signal events is recalculated for each new binning using MC. The aTGC sensitivity is found to increase for all three parameters as the upper bin boundary is moved from 500 GeV to 2 TeV. No additional expected SM events are gained by enlarging this bin whereas aTGC events continue to contribute up until 2 TeV. No additional aTGC events are predicted above 2 TeV and so increasing the bin any further will not lead to an improvement of the sensitivity. Moving the lower two boundaries at 30 and 60 GeV has no effect while moving the lower boundary of the last bin to 180 GeV improves the expected limits significantly and keeps more than five expected SM events in all bins.

So far the optimization has used four bins but in a last round additional bins are added and found to increase the expected sensitivity as well as to improve the visual presentation of the data. The upper limit on the number of bins is chosen based on two considerations. Firstly, the ability to calculate estimated backgrounds in data in all bins with reasonable uncertainty and secondly, the amount of time it takes to perform a fit. Since the computation of two dimensional and expected limits require a large number of pseudo-experiments, increasing the number of bins significantly drastically decreases the turn-around time of the analysis. A total of seven bins is found to be an optimal consensus between expected sensitivity, visual presentation, ability to do data-driven background estimates and time required to perform the fits. A final binning of [0-30-60-90-120-150-180-2000] GeV is chosen.

The widths of the expected aTGC limits in absence of an aTGC signal are compared in the left column of figure 8.29 for the nominal four bins and the optimised four bins. Two versions of the optimised binning are shown, in purple the toy study with the smoothly-varied systematic uncertainties and data-driven background estimates and in red the actual systematic uncertainties and fully data-driven background estimates recalculated after the first optimization. The right column of figure 8.29 compares the width of expected aTGC limits for the optimised binning with four and seven bins, respectively.

Figure 8.30 shows the p_{T}^{Z} distribution in the seven chosen bins. Data and the expected background and signal events, assuming the SM, are shown. The expected distribution for three aTGC values, that correspond to the upper limit of the 99% expected C.I., are also plotted. These values are chosen for display purposes to get a better sense of discrimination between the different parameters. The sensitivity to anomalous couplings in the last bin of p_{T}^{Z} is evident and the three anomalous couplings additionally have different p_{T}^{Z} shapes. The last bin is shortened for display purposes and includes events up to 2 TeV. The aTGC distributions are plotted with a cutoff scale of 2 TeV.

8.12.3 Reweighting

In MC@NLO version 4.0 [80] it is possible to generate $W^{\pm}Z$ events with any Δg_1^Z, $\Delta\kappa^Z$ or λ^Z aTGC parameter value. Each event is given a vector of ten weights $\{w_0 \ldots w_9\}$ which can be reweighted to another aTGC phase space point. The weight at a new point is

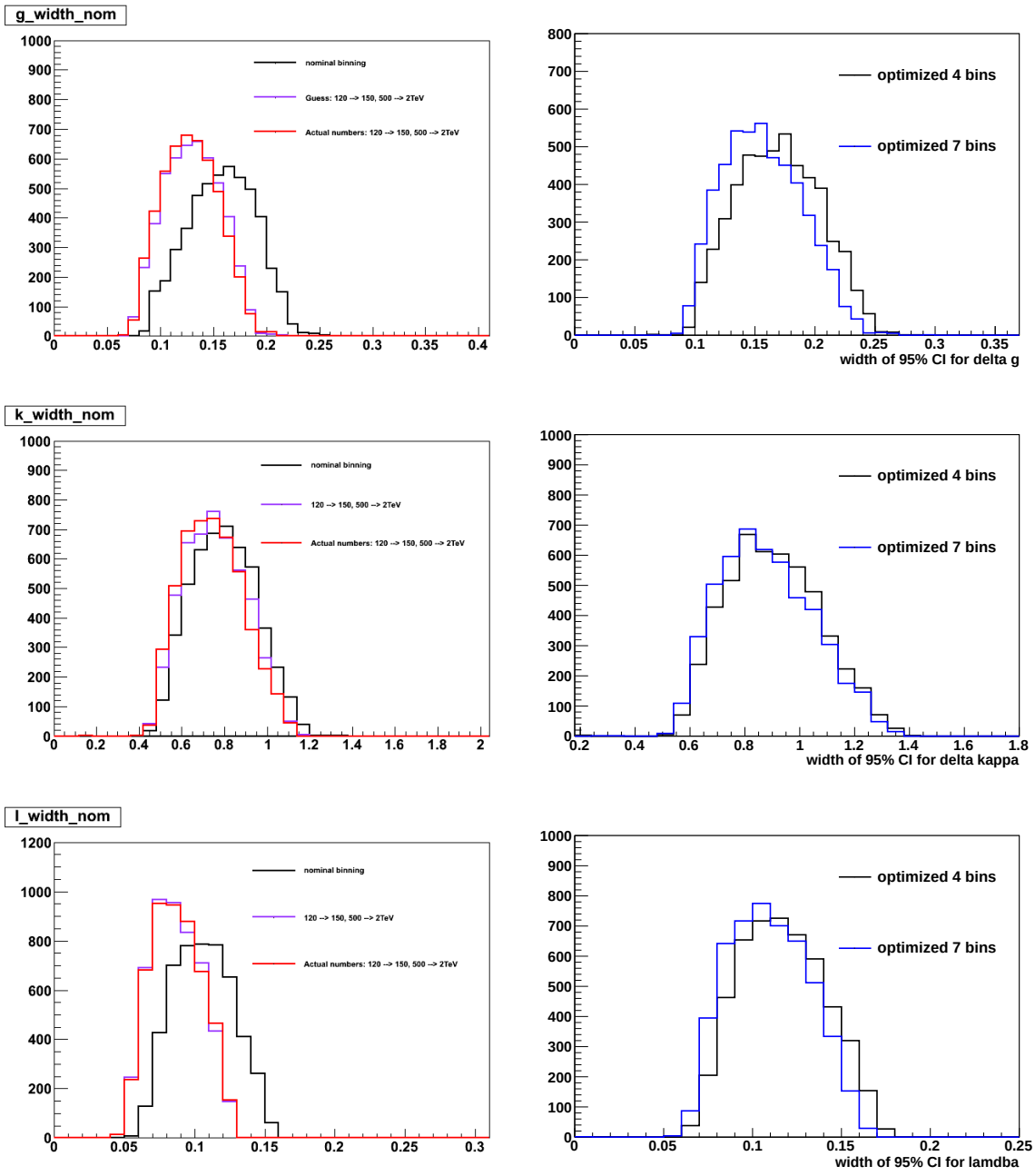

Figure 8.29: The 95% C.I. widths comparing, in the left column, the nominal and optimised four bin distributions and, in the right column, the optimised four and seven bin distributions for Δg_1^Z, $\Delta\kappa^Z$ and λ^Z in the top, middle and bottom rows. The cutoff scale is 100 TeV and 2 TeV for the left and right columns respectively. The y-axis shows the number of events.

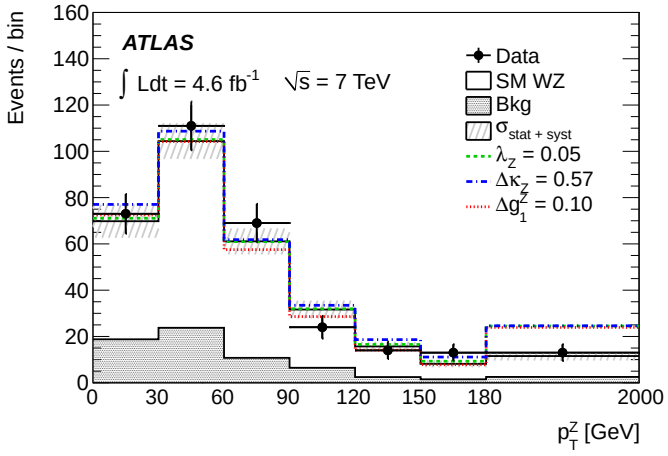

Figure 8.30: p_{T}^{Z} distribution of $W^{\pm}Z$ candidate events for data, SM and aTGC MC.

given by

$$\begin{aligned} w(\Delta g_1^Z, \Delta\kappa^Z, \lambda^Z) = w_0 \quad &+ \quad (\Delta g_1^Z)^2 w_1 + (\Delta\kappa^Z)^2 w_2 + (\lambda^Z)^2 w_3 \\ &+ \quad 2\Delta g_1^Z w_4 + 2\Delta\kappa^Z w_5 + 2\lambda^Z w_6 \\ &+ \quad 2\Delta g_1^Z \Delta\kappa^Z w_7 + 2\Delta g_1^Z \lambda^Z w_8 + 2\Delta\kappa^Z \lambda^Z w_9. \end{aligned} \tag{8.25}$$

where w_0 is the SM weight and the other weights come from aTGC contributions. All the weights w_i are aTGC independent and depend only on the initial and final state kinematics. This equation is derived from squaring the aTGC amplitude expression which is a linear sum of the SM amplitude plus three additional amplitudes, one for each aTGC parameter.

In order to change or remove the form factor, the aTGC parameters Δg_1^Z, $\Delta\kappa^Z$, and λ^Z are multiplied by a factor of $(1+\hat{s}/\Lambda^2)$ to remove the old form factor, in this case $\Lambda = 100$ TeV, and divided by a factor of $(1+\hat{s}/\Lambda'^2)$, where Λ' is the new form factor. This is equivalent to adjusting the event weights $\{w_0 \ldots w_9\}$ as

$$w_i \to \begin{cases} w_i & \text{for } i = 0 \\ w_i(1+\hat{s}/\Lambda^2)^2/(1+\hat{s}/\Lambda'^2)^2 & \text{for } i = 4,5,6 \\ w_i(1+\hat{s}/\Lambda^2)^4/(1+\hat{s}/\Lambda'^2)^4 & \text{for } i = 1,2,3,7,8,9. \end{cases} \tag{8.26}$$

The form factor is removed completely by setting the new cutoff scale to infinity and $(1+\hat{s}/\Lambda'^2) \to 1$.

A few other multiplicative factors are applied to the MC sample, namely the MC generator weights from MC@NLO, pile-up weights as well as trigger and reconstruction scale factors. After applying these factors, the event weights are accumulated for the MC signal events that pass the selection. The end result is the expected number of signal events N_s^i in the data sample in the form of

$$\begin{aligned} N_s^i(\Delta g_1^Z, \Delta\kappa^Z, \lambda^Z) = W_0^i \quad &+ \quad (\Delta g_1^Z)^2 W_1^i + (\Delta\kappa^Z)^2 W_2^i + (\lambda^Z)^2 W_3^i \\ &+ \quad 2\Delta g_1^Z W_4^i + 2\Delta\kappa^Z W_5^i + 2\lambda^Z W_6^i \\ &+ \quad 2\Delta g_1^Z \Delta\kappa^Z W_7^i + 2\Delta g_1^Z \lambda^Z W_8^i + 2\Delta\kappa^Z \lambda^Z W_9^i \end{aligned} \tag{8.27}$$

for each p_{T}^{Z} bin. The W^{i}_{j} coefficients are used as input to the aTGC limit setting procedure described next.

8.12.4 Limit Setting Procedure

A frequentist limit setting approach [184] is adopted to extract limits on the aTGC parameters. The 95% C.I. for each anomalous coupling is determined separately with the other couplings set to their SM values. The reweighting procedure described in the previous section allows one to express the expected number of signal events N_{s}^{i} in p_{T}^{Z} bin i as a function of aTGC parameters. The p-value of the aTGC values which give anomalous cross sections inside of the 95% C.I. of the cross section establishes the 95% C.I. of the anomalous couplings. The procedure for determining the 95% C.I. is as follows.

1. The likelihood function $L(n|\sigma,\beta)$, used for the cross section extraction and described in section 8.11, is modified by replacing the cross section σ with one of the aTGC parameters $\alpha = \Delta g_{1}^{Z}$, $\Delta\kappa^{Z}$, or λ^{Z}. Furthermore, the sum over channels $i = 1...4$ is replaced by a sum over p_{T}^{Z} bins $i = 1...7$. The N_{s}^{i} in p_{T}^{Z} bin i is expressed as a quadratic function of α using the reweighting method described in the previous section. The symbol n stands for the number of observed data events and β are the nuisance parameters which represent the Gaussian constrained systematic uncertainties.

2. A test statistic $q(\alpha)$ is constructed by taking the ratio of the profile maximum likelihood at a test aTGC parameter value α to the full maximum likelihood as

$$q(\alpha) = \frac{L(n|\alpha,\hat{\hat{\beta}})}{L(n|\hat{\alpha},\hat{\beta})} \tag{8.28}$$

   where $\hat{\hat{\beta}}$ is the maximum likelihood estimator of β that maximises the numerator for the fixed test value of α. Similarly, $\hat{\alpha}$ and $\hat{\beta}$ are the values of α and β which maximise the denominator.

3. From the number of observed data events n_{obs} for each value of the test aTGC parameter, the observed value of the test statistic, $q_{\mathrm{obs}}(\alpha)$, is found by scanning a range of values of α and determining the value of the test statistic for each α.

4. To determine how often an outcome at least as unlikely as the actual observation is expected, a large number (10^{4}) of pseudo experiments is generated for each test value of α. The test statistic $q_{\mathrm{pe}}(\alpha)$ is then computed for each pseudo experiment to generate a probability distribution of $q(\alpha)$. To generate each pseudo experiment, first, the nuisance parameters β are Gaussian fluctuated around the mean value of $\hat{\hat{\beta}}(\alpha)$. The numbers of "observed" events N_{pe}^{i} is then drawn randomly from a Poisson distribution whose mean is computed from the value of α and β. The number of pseudo experiments is chosen to ensure that a p-value of 5% can be determined to a reasonable statistical precision of $\pm 0.2\%$.

5. The p-value at each α value is calculated as the fraction of pseudo experiments whose test statistic $q_{\mathrm{pe}}(\alpha)$ is smaller than the observed value $q_{\mathrm{obs}}(\alpha)$.

6. All aTGC parameter values for which $p(\alpha) \geq 5\%$ can be determined by scanning α. These define the 95% C.I. of α for the observed data.

7. The expected sensitivity is computed by using the SM expectations for the signal and background to generate a large number of toy MC observed data sets, $n_{\text{obs}}^{\text{toy}}$. From these sets, the distribution of the 95% C.I. for the aTGC parameters can be studied.

As N_s^i is a quadratic function of α, $N_s^i(\alpha)$ has a minimum near, but not exactly at, the SM point $\alpha = 0$ and increases for both positive and negative values of α. Consequently, there can be one or two optimum values of α that best describe the observed data. This depends on whether N_{obs} is smaller or larger than the minimum expected value. This means that the 95% C.I. of α can either be a single continuous region or two disjoint regions.

The observed limits are computed in two different scenarios. In the first scenario, one dimensional (1D) limits are set on each parameter by setting the value of the other two aTGC parameters to zero. In the second scenario, one aTGC parameter is set to zero, and the 95% confidence contour for the other two parameters are fit simultaneously, allowing for a confidence interval in a two dimensional (2D) phase space. In the latter case, the best-fit value can have non-zero couplings in two parameters. The 2D limits are extracted using the same method as for the 1D limits. First, the best-fit value in the 2D aTGC parameter space is found and, from that point, 1D limits are extracted along radial lines moving out from the best-fit value. The 95% confidence contour is the contour connecting the set of points which correspond to the 95% limits on the many radial spokes.

8.12.5 Observed and Expected Limits

Table 8.26 summarises the observed 95% C.I. on the Δg_1^Z, $\Delta\kappa^Z$, and λ^Z aTGC parameters for a cutoff values of $\Lambda = 2$ TeV and without a cutoff, which is equivalent to setting $\Lambda \to \infty$. These 1D limits are obtained by varying one aTGC parameter at a time and setting the others to zero. Figure 8.31 visualises the 1D observed limits and compares them to the Tevatron results[7]. The 95% C.I. for the 2D fitting scenario with no form factor are shown as contours in figure 8.32. The horizontal and vertical lines inside each contour correspond to the limits found in the 1D fit procedure.

The expected sensitivity of the measurement is evaluated by generating a large number of toy MC datasets assuming the SM. Table 8.26 shows the 95% C.I. of the expected aTGC limits. The left column of figure 8.33 shows the distributions of the 95% C.I. obtained from the toy experiments, as well as the actual C.I. from the data. The right column of figure 8.33 shows the widths of the 95% C.I.. If a toy experiment gives two separate C.I., the sum of the two widths is plotted. The poorest limits, in terms of the total width of the C.I., are expected when the measured cross section is at the border between single and double intervals – which happens to be the case for this measurement.

[7] It can be seen that the Tevatron limits, aside from using the same amount or more data, are not much weaker than the ATLAS limits even though one might naively expect much better limits from the LHC as it runs at a higher centre of mass energy, which directly affects the aTGCs. It is important to keep in mind that this plot shows the observed, not the expected, limits. In the last bin, which is most sensitive to aTGCs, DØ expected 2 events and saw none, whereas ATLAS expected 9.4 and saw 13.

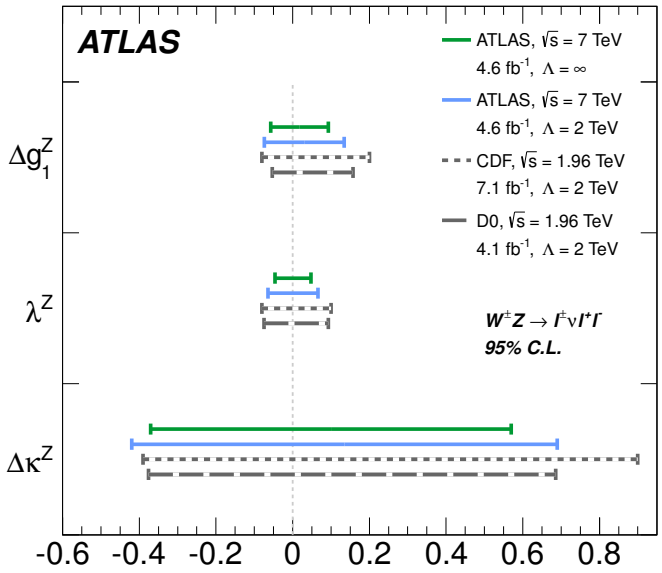

Figure 8.31: Observed aTGC limits from ATLAS and Tevatron experiments. Luminosiy, centre of mass energy and cutoff Λ for each experiment are shown and the limits are for 95% C.I.

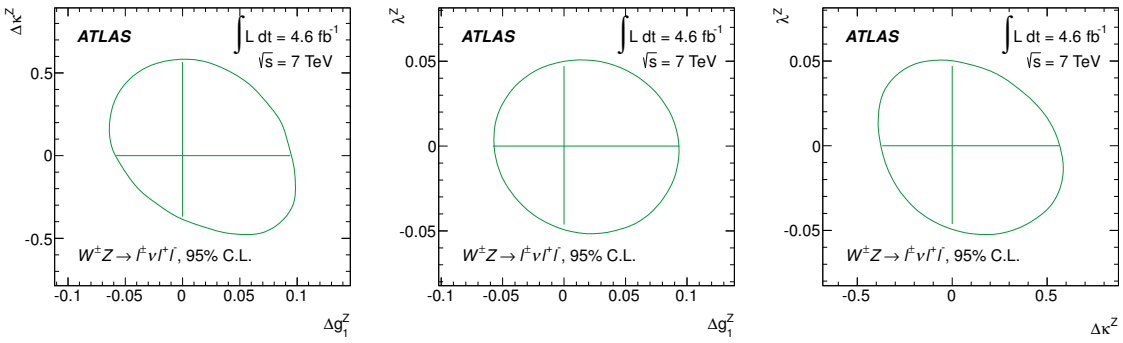

Figure 8.32: Observed 2D 95% confidence contours with no cutoff.

	Observed 95% C.I. $\Lambda = 2$ TeV	Expected 95% C.I. $\Lambda = 2$ TeV	Observed 95% C.I. no cutoff	Expected 95% C.I. no cutoff
Δg_1^Z	$[-0.074, 0.133]$	$[-0.059, 0.110]$	$[-0.057, 0.093]$	$[-0.046, 0.080]$
$\Delta\kappa^Z$	$[-0.42, 0.69]$	$[-0.37, 0.57]$	$[-0.37, 0.57]$	$[-0.33, 0.47]$
λ^Z	$[-0.064, 0.066]$	$[-0.056, 0.055]$	$[-0.046, 0.047]$	$[-0.041, 0.040]$

Table 8.26: Observed and expected 95% C.I. on Δg_1^Z, $\Delta\kappa^Z$, and λ^Z.

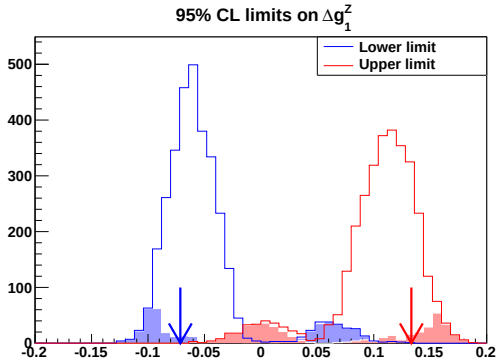

(a) 95% CL limits on Δg_1^Z

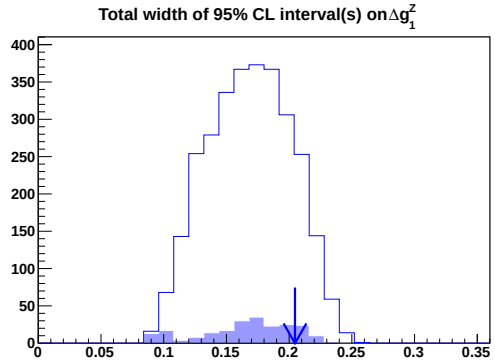

(b) Total width of 95% CL limits on Δg_1^Z

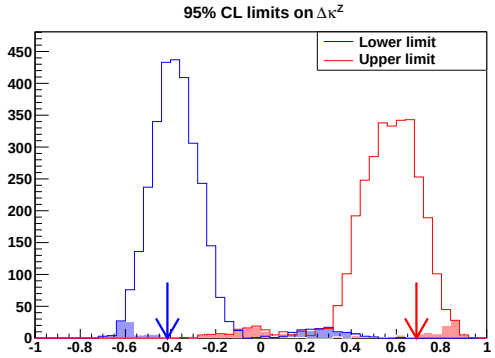

(c) 95% CL limits on $\Delta\kappa^Z$

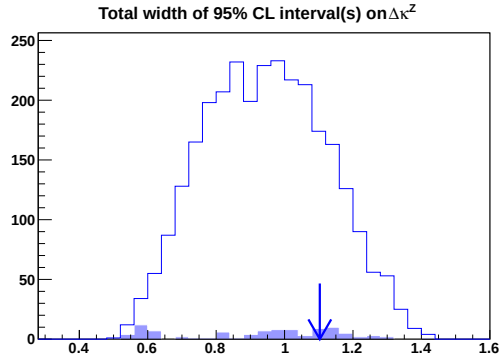

(d) Total width 95% CL limits on $\Delta\kappa^Z$

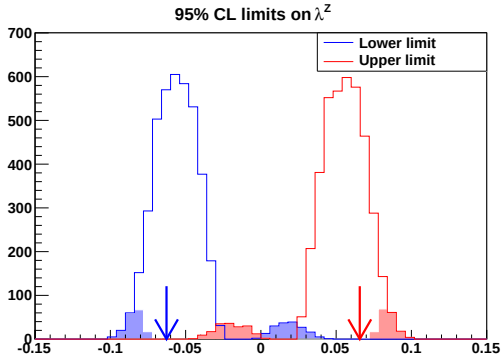

(e) 95% CL limits on λ^Z

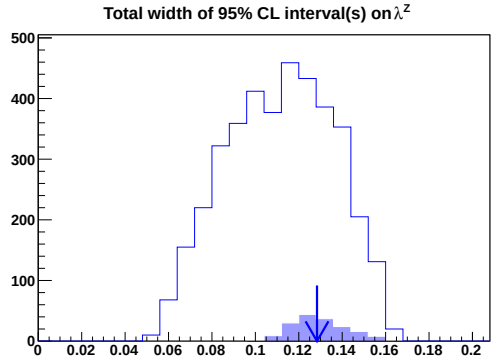

(f) Total width 95% CL limits on λ^Z

Figure 8.33: The left (right) column shows the upper and lower limits (total widths) of the 95% C.I. of Δg_1^Z, $\Delta\kappa^Z$ and λ^Z in the top, middle and bottom rows obtained from toy MC samples. The shaded areas indicate the cases in which two split C.I. were found. The blue and red arrows show the actual limits (widths) obtained from data. The limits are for a cutoff scale of 2 TeV. The y-axis shows the number of events.

8.13 Unfolding

The aTGC limit extraction, described in the previous section, uses an effective Lagrangian approach to probe the SM behaviour and search for new physics in a generic way with little model dependence. The data used for this extraction however still carries information specific to the ATLAS detector reconstruction. Unfolding gives a complementary approach to this as it allows to convert the measured distributions to the true underlying distributions that are detector independent and can be easily compared to a specific model or data from a different experiment.

The method applied in this analysis is iterative Bayesian unfolding [185]. A response matrix is used to model the detector acceptance and resolution. It is combined with the measured spectrum to form a likelihood which in turn is multiplied by a prior distribution to produce the posterior probability of the true spectrum. The goal is to achieve stable unfolding without any excessive sensitivity to statistical fluctuations or to the details of the unfolding technique. This is generally ensured if the response matrix is close to diagonal. The statistical uncertainty is taken as the RMS of a large number of Poisson fluctuated pseudo experiments which are all unfolded. The systematic uncertainty is obtained by varying the response matrix for each source of uncertainty and combining the variations in the unfolded distribution.

8.13.1 Introduction

The goal in measuring a physical observable is to determine its true underlying distribution whereas experimentally measured quantities are smeared and distorted by detector effects such as limited acceptance, imperfect efficiency, and finite resolution. In general, an observable x distributed according to a probability density function (p.d.f.) $f(x)$ cannot be measured perfectly due to both experimental and statistical uncertainties. Instead of measuring x, what is often done is to measure a different variable y distributed according to a different p.d.f. $g(y)$ and the relation between $f(x)$ and $g(y)$ can be expressed as a convolution of the true distribution $f(x)$ with a kernel $A(y,x)$ as

$$\int A(y,x)f(x)\mathrm{d}x = g(y). \tag{8.29}$$

The kernel $A(y,x)$ is a so-called response function which describes the detector effects on the measurement. The full analytic parameterisations of $g(y)$ and $A(y,x)$ are not necessarily known and only discretised samplings of the distributions are available in the form of histograms. The convolution equation 8.29 can be rewritten in matrix form by treating each bin of a histogram as a vector or matrix element

$$\mathbf{Ax} = \mathbf{y}, \tag{8.30}$$

which can be solved for $\mathbf{x}$, given $\mathbf{y}$. The vector $\mathbf{y}$ with n elements represents the data histogram of measured quantities y and the distribution $f(x)$ is represented by a histogram of the vector $\mathbf{x}$ with m elements. $\mathbf{A}$ is the $n \times m$ response matrix that transforms $\mathbf{x}$ into $\mathbf{y}$. The elements of the response matrix a_{ij} give the probability for a true value x_j to be measured as a value y_i.

Even if an analytic parameterisation of $\mathbf{A}$ is not available, it is possible to model these detector effects with MC simulations of the underlying physics processes and detector simulations of particles interacting with the detector material.

Once the response matrix is built, there are two methods of determining the true underlying distribution from a measured spectrum:

- *Smearing*: The underlying physics model parameters can be smeared with the detector model and compared to the measured data. The best set of smeared values determines the true measured distribution. In other words, one can simulate and vary $\mathbf{x}$, smear $\mathbf{x}$ with the response matrix $\mathbf{A}$ and find values of $\mathbf{x}$ which best describe $\mathbf{y}$.

- *Unfolding*: Using MC based detector smearing, the smearing effects of the measured data can be inverted to produce directly a measured true distribution. This means looking for a solution of the form $\mathbf{x} = \mathbf{A}^{-1}\mathbf{y}$.

If the main aim is to compare the measurement with an existing theory, smearing provides a mathematically simpler solution. However, without unfolding it is still difficult to compare results with other experiments or with theoretical models. Furthermore, for complex detectors, smearing can become extremely computationally intensive. As a result, unfolding is chosen for this measurement.

There are many unfolding procedures to determine the true underlying distribution of the measured data [185–188], only the main methods will be described here briefly. The following notation is adopted.

- One dimensional histograms or vectors are denoted by small letters (e.g. $\mathbf{x}$, $\mathbf{y}$).

- Two dimensional histograms or matrices are denoted by capital letters (e.g. $\mathbf{A}$).

- Bold letters indicate a vector or matrix (e.g. $\mathbf{x}$, $\mathbf{A}$).

- Regular (non-bold) letters indicate a scalar (e.g. τ).

- Regular letters with indices indicate vector or matrix elements (e.g. x_j, A_{ij})

- Summation is not implied over repeated indices but is explicit (e.g. $\sum_j A_{ij}x_j$).

- Covariance matrices are indicated by a bold and capital $\mathbf{V}$ followed by the variable in parentheses or as a subscript (e.g. for vector $\mathbf{y}$ the covariance matrix is $\mathbf{V}(\mathbf{y})$ or $\mathbf{V}_y$).

Bin-by-bin unfolding is one of the simplest unfolding techniques. A correction factor c_i is calculated for each bin in the observed vector $\mathbf{y}$ from a control sample, typically from MC simulation, that describes the ratio of observed to true events. Given a simulated sample of observed $\mathbf{y}^{\text{sim}}$ and true $\mathbf{x}^{\text{sim}}$ measurements, the c_i are calculated as $y_i^{\text{sim}}/x_i^{\text{sim}}$. For an observed data sample $\mathbf{y}^{\text{data}}$, the final unfolded result is equal to $x_i^{\text{data}} = y_i^{\text{data}}/c_i$. The advantages of this method are that it is conceptually simple, it does not involve complicated uncertainty computations or bin-to-bin correlations and it is not computationally intensive. However, it also has a number of disadvantages. The most important one being that all of the corrections are within each bin, which means that bin-to-bin migrations are not corrected for. As a result,

if bin purities are low, the unfolded result is highly biased to the control sample used to produce the bin-by-bin corrections. This method is usually considered safe if the bin purity exceeds 80%, such that the majority of reconstructed events stay within the bin in which they were generated.

The *Bayesian* unfolding technique does not suffer from this disadvantage. An outline of the Bayesian unfolding technique is given below. A detailed description can be found in reference [185]. Fundamentally, Bayesian unfolding is an iterative unfolding algorithm that uses Bayes theorem to perform unfolding, treating the response matrix as a description of the probability of observed data given the true distribution. Mathematically, the algorithm tries to determine the probability distribution of true events given the observed data and the response matrix as

$$P(\mathbf{x} \mid \mathbf{y}, \mathbf{A}, I) \tag{8.31}$$

where the new variable I contains the underlying assumptions of the analysis, which are usually left implicit. Equation 8.31 can be rewritten using Bayes theorem as

$$P(\mathbf{x} \mid \mathbf{y}, \mathbf{A}, I) \propto P(\mathbf{y} \mid \mathbf{x}, \mathbf{A}, I) \cdot P(\mathbf{x} \mid I). \tag{8.32}$$

The first term on the right is the likelihood of the observed data and the second term is the prior on the underlying truth distribution. This equation carries a difficulty in that the unfolded value will be strongly dependent on the underlying prior distribution. In particular, if a certain MC model is used to produce a prior, the unfolded value will be biased towards the truth distribution of the simulation used. This method can further suffer from problems related to regularized matrix inversion, specifically, oscillations due to amplified statistical uncertainties. As a solution to both of these problems, Bayesian unfolding uses an iterative smoothing approach, which uses the number of iterations as a regularization parameter. The first iteration solves equation 8.32 using the given MC truth distribution as the prior distribution. For subsequent iterations, the result from the previous iteration is used as the prior. The bias from the MC truth distribution becomes smaller as more iterations are performed. However, at the same time, the statistical uncertainty increases because the statistical fluctuations are amplified due to the positive feedback nature of the system. Therefore, the number of iterations is used to balance the strength of the bias with the size of the oscillations. The number of iterations is generally small as otherwise the statistical uncertainties become large. There are several advantages to this technique. Firstly, it is implemented in the RooUnfold package, which simplifies integration with ROOT based analysis. Secondly, it contains only one free parameter, the number of iterations, which is easily understood and optimised, because good solutions occupy a relatively small range in this parameter. Thirdly, the algorithm is very fast, which makes uncertainty calculations via pseudo experiments computationally feasible. Lastly, the prior distribution does not degrade the ability of the algorithm to correctly unfold steeply falling distributions. This analysis therefore uses iterative Bayesian unfolding for its final result.

8.13.2 Methodology

Having established the basic concepts of unfolding, the general methodology used in this analysis will now be discussed. A specific distribution with n bins is denoted as $\mathbf{z}$ and

the content of bin i is written as z_i. **z** can stand for the measured data distribution **d**, the expected background **b**, the signal distribution **y** or the unfolded distribution **x**.

The measured distribution can be transformed into the unfolded distribution using the following three quantities, defined with fully simulated MC signal samples.

- The response matrix **A** accounts for bin-to-bin migrations between the reconstructed and the truth distribution. It is only defined for events which pass all reconstruction level cuts and which fall within the fiducial phase space.

- The correction factors for each bin i of the unfolded distribution are defined as the ratio of reconstructed events N_i^{reco} in bin i over the number of truth events N_i^{truth} in bin i

$$c_i = \frac{N_i^{\text{reco}}}{N_i^{\text{truth}}}|_{\text{in fid.}} \tag{8.33}$$

  where all events are required to fall within the fiducial region defined at truth level. Note that bin i is defined here by the truth value of the unfolding variable. The correction factors account for acceptance and efficiency losses at the reconstruction level.

- The fiducial factors for each bin i of the reconstructed distribution are defined as the ratio of events which fall within the fiducial region on truth level $N_i^{\text{in fid.}}$ over the total number of events N_i

$$f_i = \frac{N_i^{\text{in fid.}}}{N_i}|_{\text{is reco.}} \tag{8.34}$$

  where all events are required to pass all reconstruction level cuts. Note that bin i is defined here by the reconstructed value of the unfolding variable. The fiducial factors correct for reconstructed events that fall outside the fiducial region and hence have no corresponding truth value which can be used during the unfolding.

y_i and x_i can then be defined as

$$y_i = (d_i - b_i)f_i \tag{8.35}$$

and

$$x_i = (A_{ij}^{-1}y_i)c_i. \tag{8.36}$$

The unfolding procedure is schematically illustrated in figure 8.34. The central value of the unfolded distribution is based on the nominal signal MC samples, including all detector-related efficiency, scale or resolution corrections. For completeness, the following information for each signal MC event is used and stored in an event-by-event array, a so-called signal NTuple.

- MCTruthValue is the MC truth value of the quantity to be unfolded.

- MCTruthWeight is the MC truth weight of the quantity to be unfolded.

- MCTruthIsFiducial is a boolean that indicates whether or not the event falls within the fiducial phase space region defined at MC truth level.

- RecoValue is the reconstructed value of the quantity to be unfolded.

- RecoWeight is the event weight at reconstruction level. In addition to MCTruthWeight it contains the reconstruction and trigger efficiency scale factors.
- RecoIsReconstructed is a boolean that indicates whether or not the event passes the full signal selection at reconstruction level.

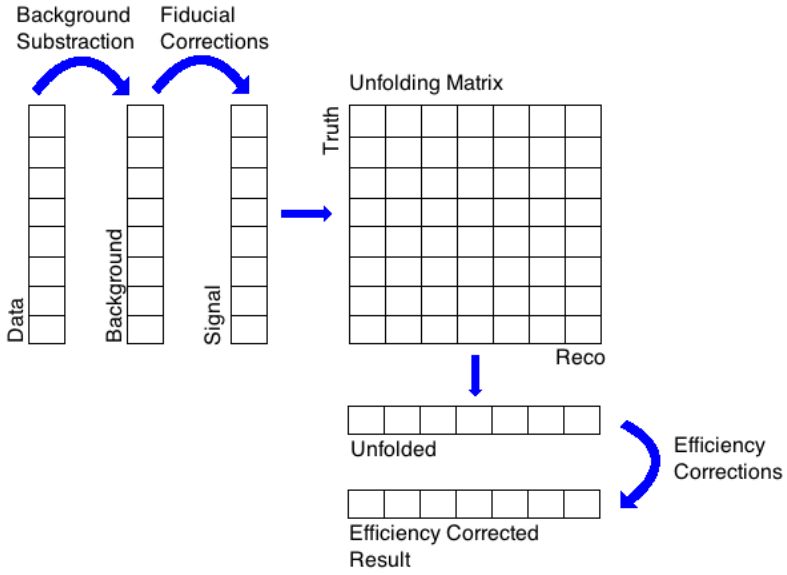

Figure 8.34: Pictorial description of the unfolding method for a distribution in a fiducial volume.

The statistical uncertainty of the unfolded distribution is determined by toy MC tests. Each measured data entry d_i is Poisson fluctuated and the full nominal unfolding procedure is applied. This is repeated 2000 times and the RMS of the resulting unfolded values x_i is taken as the statistical uncertainty. For each systematic uncertainty source, a new signal NTuple is produced for which the corresponding systematic variation has been applied. In a second step, the quantities $\mathbf{A}$, c_i and f_i are defined with the signal NTuple, each corresponding to one systematic variation. The measured data distribution is then unfolded for all instances separately, leading to one $\mathbf{x}^{\text{sys}}$ distribution per source of systematic uncertainty. The difference $\delta_i^{\text{sys}} = x_i - x_i^{\text{sys}}$ is defined as the systematic uncertainty in each bin. The corresponding covariance matrix for bins i and j is defined as

$$\text{Cov}_{ij} = \delta_i^{\text{sys}} \times \delta_j^{\text{sys}}. \tag{8.37}$$

The covariance matrices from different systematic uncertainties can be added linearly. The global bin-by-bin correlation matrix is defined as

$$C_{ij} = \frac{\text{Cov}_{ij}}{\sqrt{\text{Cov}_{ii}}\sqrt{\text{Cov}_{jj}}}. \tag{8.38}$$

Most systematic uncertainties are split into an upwards and a downwards variation of 1σ around the nominal value. Since these two variations are fully correlated and to give a conservative estimate during the first round of this measurement, the larger value of δ_i^{sys} is taken for both variations of the systematic uncertainty. The corresponding correlations are estimated using the MC sample including the larger variation.

The systematic uncertainties due to background estimations are evaluated in a similar manner. For each systematic variation of the background $\mathbf{b}^{\text{sys}}$ the full unfolding based on the nominal signal NTuple is performed and the differences $\delta_i^{\text{bkg}} = x_i - x_i^{\text{bkg}}$ are defined as systematic uncertainties. The corresponding covariance and correlation matrices are defined accordingly. It is assumed that all background variations and detector systematic variations can be treated as uncorrelated.

The stability of the unfolding procedure is tested by comparing the Bayesian unfolding algorithm with two iterations to the same algorithm with one additional iteration. The difference of both results is taken as systematic uncertainty due to the unfolding itself.

This implementation provides the initialisation, the efficiency and fiducial corrections, the final systematic and statistical uncertainty estimations as well as the final unfolded results. The core unfolding problem of solving the response matrix is based on RooUnfold.

8.13.3 Results

In this analysis, the variables being unfolded are the transverse momentum of the Z boson, p_{T}^{Z}, using the same binning as for the aTGC limit setting, namely [0-30-60-90-120-150-180-2000] GeV and the diboson invariant mass, m_{WZ}, using a binning of [170-270-405-2500] GeV. The unfolded distributions are normalised to unity within the given kinematic range, which means that the measured quantities are $\Delta\sigma_{\text{fid}}(p_{\text{T}}^{Z})/\sigma_{\text{fid}}$ and $\Delta\sigma_{\text{fid}}(m_{WZ})/\sigma_{\text{fid}}$. The normalisation implies that detector corrections which are independent of the unfolding variable have no impact on the final result and only shape-dependent systematic uncertainties will have an effect. In addition, the normalisation leads to an additional constraint which also impacts the bin-by-bin correlation for the statistical uncertainties. This can most easily be understood by considering only two bins. In order to keep the overall normalisation constant, an upward fluctuation of one bin implies a downward fluctuation in the other bin.

Figure 8.35 shows the input distributions of the observed data and expected background events in bins of p_{T}^{Z} and m_{WZ} used for the unfolding. Figures 8.36 and 8.37 show the purity and the efficiency correction factors, respectively. The purity is above 85% for all p_{T}^{Z} bins, implying very small bin-to-bin migration effects, and almost 90% for the m_{WZ} bin containing the mass peak whereas the bins making up the tail of the distribution have a lower purity of around 60%. The efficiency correction factors are around 0.6 and close to flat as a function p_{T}^{Z} and around 0.5 and fairly flat as a function m_{WZ}. Figure 8.38 shows the MC signal distributions for truth and reconstructed quantities and figure 8.39 shows the response matrix. The fractions of events that migrate between two bins is 2-7% for p_{T}^{Z} and 13-17% for m_{WZ}. The unfolding procedure is tested via two closure tests. In the first test, the nominal signal NTuple is not only used for the definition of the unfolding procedure but also taken as the input signal distribution. A perfect closure, meaning full agreement with the corresponding truth distribution, is expected and confirmed in figure 8.40. For the second closure test, an aTGC MC sample is reweighted to SM values and unfolded in turn by the same proce-

dure. The difference is treated as an additional systematic uncertainty and is listed in table 8.27. The final unfolded distributions including the comparison to the generator prediction and the associated uncertainties are shown in figure 8.36. The corresponding numerical values and correlation matrices are shown in tables 8.27 – 8.30 and 8.31 – 8.34 for p_{T}^{Z} and m_{WZ} respectively. The uncertainties are split into statistical, systematic and background-related categories. Also shown are uncertainties from applying the Bayesian unfolding algorithm with an additional iteration (listed as "alternative unfolding") to test the stability and the uncertainties from a closure test using a SM reweighed aTGC MC sample, rather than a SM MC sample. A detailed list of the signal and background systematics is also given.

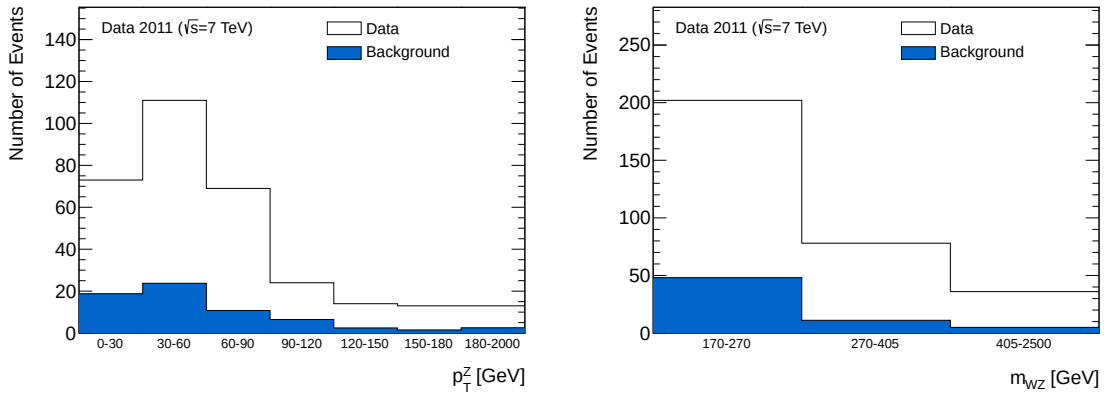

Figure 8.35: Data and background distributions for p_{T}^{Z} and m_{WZ}.

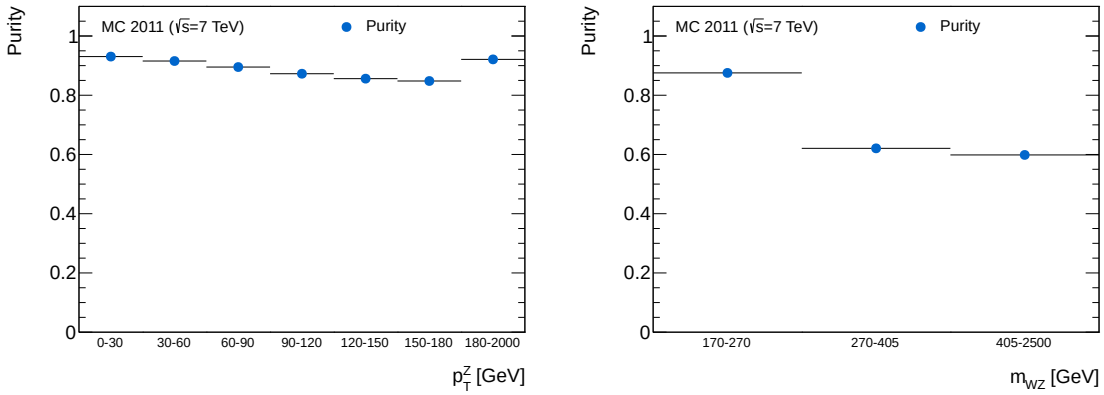

Figure 8.36: Purity for p_{T}^{Z} and m_{WZ}.

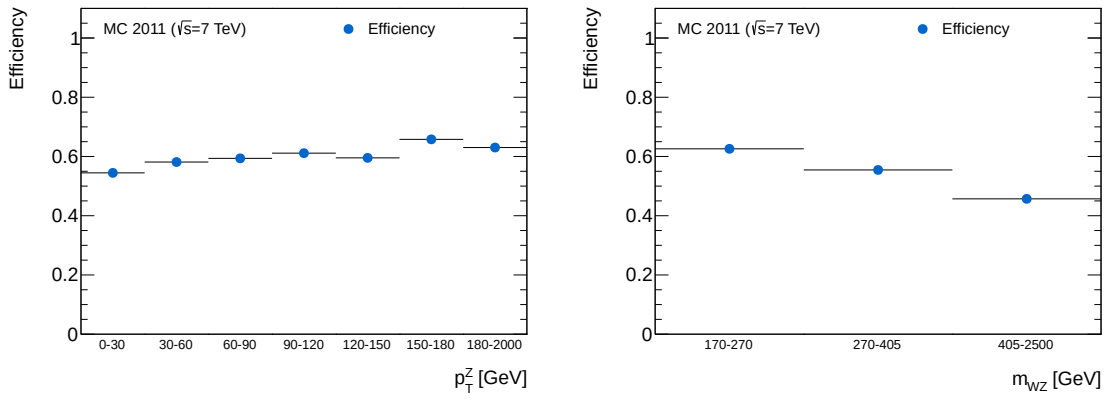

Figure 8.37: Efficiency for p_{T}^{Z} and m_{WZ}.

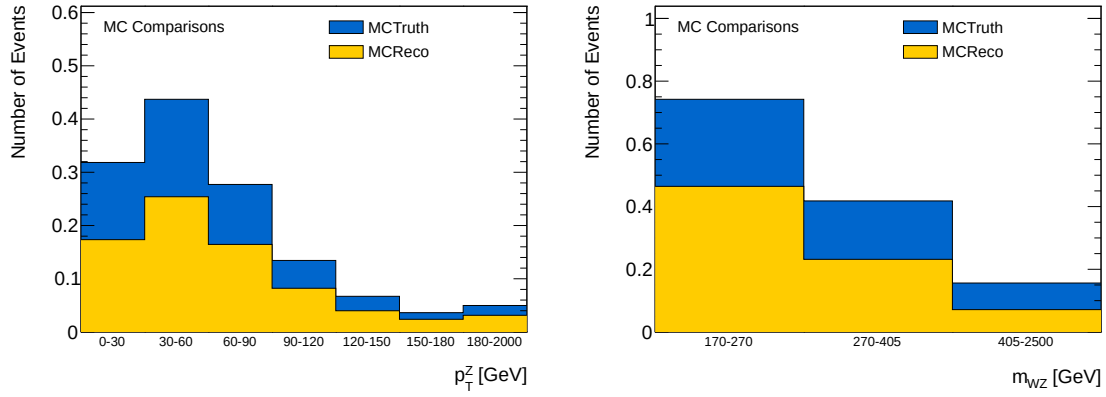

Figure 8.38: Truth versus reconstruction for p_{T}^{Z} and m_{WZ}.

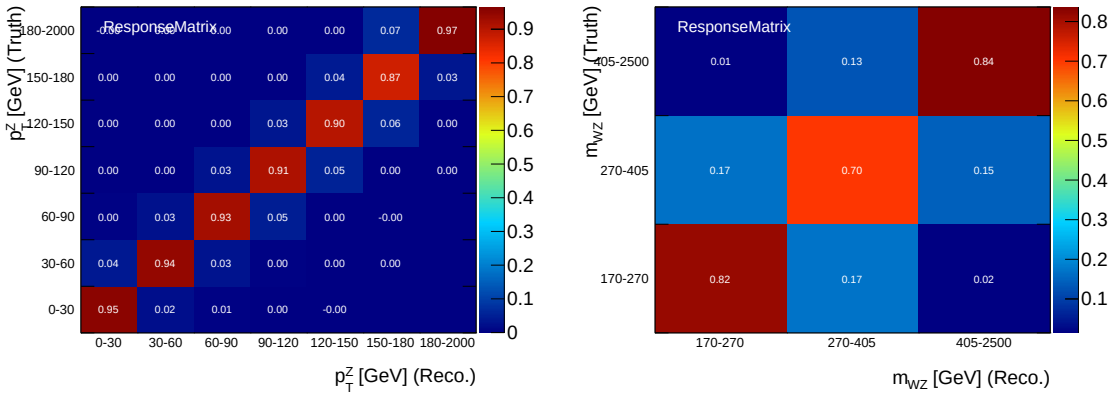

Figure 8.39: Response matrix for p_{T}^{Z} and m_{WZ}.

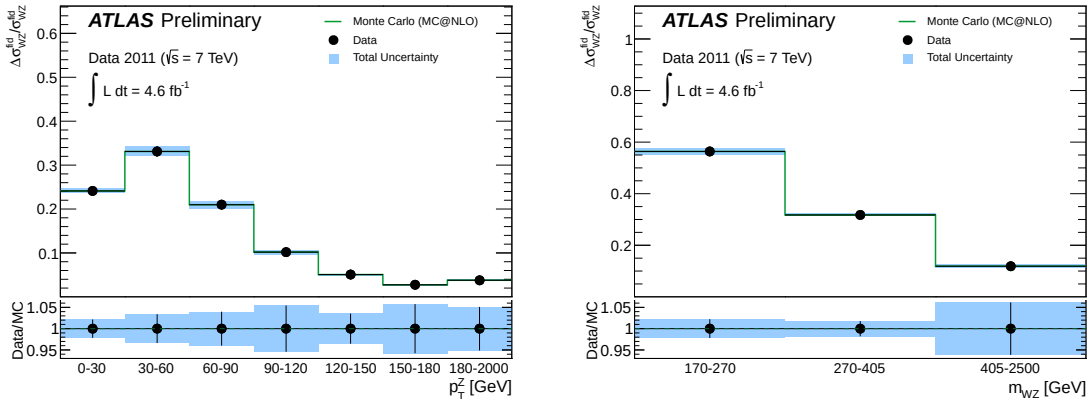

Figure 8.40: Result of closure test with nominal MC used as input for p_{T}^{Z} and m_{WZ}.

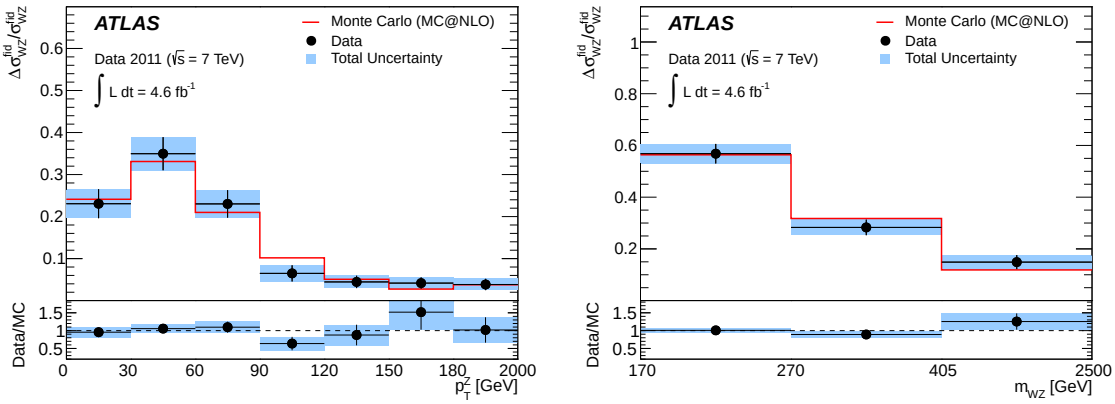

Figure 8.41: Final unfolded distributions for p_{T}^{Z} and m_{WZ} defined using "dressed" leptons.

p_{T}^{Z} Bin [GeV]	0 - 30	30 - 60	60 - 90	90 - 120	120 - 150	150 - 180	180 - 2000
$\Delta\sigma_{WZ}^{\mathrm{fid}}(p_{\mathrm{T}}^{Z})/\sigma_{WZ}^{\mathrm{fid}}$	0.231	0.350	0.230	0.065	0.045	0.042	0.038
Stat. Unc.	14.2%	10.6%	13.4%	28.8%	32.7%	31.7%	34.5%
Sys. Unc.	2.02%	3.32%	4.01%	5.84%	3.59%	6.09%	5.35%
Bkg. Unc.	4.01%	1.62%	1.97%	3.53%	1.47%	1.05%	1.28%
Second Closure Test	0.00%	0.00%	0.00%	0.13%	0.06%	0.09%	0.00%
Alternative Unfolding	0.10%	0.00%	0.54%	1.89%	0.40%	1.85%	0.93%
Signal Systematics							
Stat. Unc. (MC)	0.44%	0.31%	0.42%	0.77%	1.05%	1.15%	1.03%
Muon MS Smearing	0.00%	0.00%	0.09%	0.14%	0.37%	0.10%	0.40%
Muon ID Smearing	0.07%	0.00%	0.00%	0.29%	0.18%	0.14%	0.23%
Muon Efficiency	0.00%	0.00%	0.00%	0.00%	0.00%	0.00%	0.00%
Muon Isolation&IP	0.10%	0.00%	0.00%	0.07%	0.08%	0.09%	0.08%
Electron Isolation&IP	0.17%	0.00%	0.07%	0.13%	0.16%	0.16%	0.16%
Electron ID	0.05%	0.00%	0.00%	0.00%	0.00%	0.00%	0.11%
Electron Reconstruction	0.00%	0.00%	0.00%	0.00%	0.09%	0.10%	0.14%
Electron Scale	0.50%	0.12%	0.27%	0.31%	0.13%	0.39%	1.44%
Electron Smearing	0.11%	0.00%	0.16%	0.28%	0.26%	0.40%	0.18%
$E_{\mathrm{T}}^{\mathrm{miss}}$ Cluster	0.20%	0.07%	0.25%	0.47%	0.06%	0.24%	0.08%
$E_{\mathrm{T}}^{\mathrm{miss}}$ Pile-up	0.17%	0.00%	0.22%	0.47%	0.00%	0.27%	0.68%
$E_{\mathrm{T}}^{\mathrm{miss}}$ JES	0.05%	0.00%	0.00%	0.26%	0.30%	0.90%	0.19%
$E_{\mathrm{T}}^{\mathrm{miss}}$ JER	0.11%	0.26%	0.17%	0.41%	0.10%	0.26%	0.86%
Electron Trigger	0.00%	0.00%	0.00%	0.00%	0.00%	0.00%	0.00%
Muon Trigger	0.40%	0.20%	0.20%	0.42%	0.21%	0.38%	0.16%
PDF MSTW	0.00%	0.00%	0.00%	0.08%	0.27%	0.09%	0.11%
PDF CT10	0.13%	0.00%	0.12%	0.23%	0.13%	0.00%	0.40%
Generator	0.64%	2.82%	3.82%	1.19%	1.18%	4.14%	1.32%
Scale	1.71%	1.68%	0.76%	5.22%	3.12%	3.69%	4.56%
Background Systematics							
$t\bar{t}$	0.36%	0.38%	0.18%	2.05%	1.19%	0.30%	0.05%
Z+jets	4.00%	1.56%	1.93%	0.84%	0.00%	0.51%	0.97%
ZZ	0.00%	0.00%	0.06%	0.32%	0.10%	0.13%	0.00%
$Z\gamma$	0.17%	0.13%	0.33%	2.73%	0.85%	0.85%	0.83%

Table 8.27: Normalized unfolded fiducial results and uncertainties in p_{T}^{Z} bins.

1	-0.47	-0.28	-0.13	-0.12	-0.08	-0.12
-0.47	1	-0.42	-0.21	-0.11	-0.14	-0.13
-0.28	-0.42	1	-0.14	-0.11	-0.10	-0.07
-0.13	-0.21	-0.14	1	-0.09	-0.05	-0.04
-0.12	-0.11	-0.11	-0.09	1	0.05	-0.05
-0.08	-0.14	-0.10	-0.05	-0.05	1	0.07
-0.12	-0.13	-0.07	-0.04	-0.05	0.07	1

Table 8.28: Correlation matrix of statistical uncertainties for the p_{T}^{Z} distribution.

1	0.72	-0.49	-0.80	-0.81	-0.71	-0.66
0.72	1	-0.90	-0.63	-0.70	-0.87	-0.22
-0.49	-0.90	1	0.35	0.50	0.82	-0.06
-0.80	-0.63	0.35	1	0.93	0.61	0.81
-0.81	-0.70	0.50	0.93	1	0.76	0.77
-0.71	-0.87	0.82	0.61	0.76	1	0.37
-0.66	-0.22	-0.06	0.81	0.77	0.37	1

Table 8.29: Correlation matrix of systematic uncertainties for the p_{T}^{Z} distribution.

1	-0.95	-0.98	0.15	-0.04	-0.43	0.78
-0.95	1	0.91	-0.31	-0.25	0.48	-0.80
-0.98	0.91	1	-0.31	0.16	0.59	-0.63
0.15	-0.31	-0.31	1	0.03	-0.92	-0.29
-0.04	-0.25	0.16	0.03	1	0.23	0.42
-0.43	0.48	0.59	-0.92	0.23	1	0.14
0.78	-0.80	-0.63	-0.29	0.42	0.14	1

Table 8.30: Correlation matrix of background uncertainties for the p_{T}^{Z} distribution.

m_{WZ} Bin [GeV]	170 - 270	270 - 405	405 - 2500
$\Delta\sigma^{\text{fid}}_{WZ}(m_{WZ})/\sigma^{\text{fid}}_{WZ}$	0.568	0.283	0.149
Stat. Unc.	6.2%	9.6%	16.5%
Sys. Unc.	2.48%	4.45%	7.42%
Bkg. Unc.	0.27%	0.58%	0.63%
Second Closure Test	0.05%	0.33%	0.41%
Alternative Unfolding	0.97%	4.16%	4.20%
Signal Systematics			
Stat. Unc. (MC)	0.20%	0.37%	0.77%
Muon MS Smearing	0.06%	0.07%	0.22%
Muon ID Smearing	0.00%	0.00%	0.15%
Muon Efficiency	0.00%	0.00%	0.00%
Muon Isolation&IP	0.05%	0.00%	0.12%
Electron Isolation&IP	0.05%	0.00%	0.14%
Electron ID	0.00%	0.00%	0.07%
Electron Reconstruction	0.00%	0.00%	0.00%
Electron Scale	0.24%	0.13%	0.67%
Electron Smearing	0.00%	0.00%	0.00%
$E_{\text{T}}^{\text{miss}}$ Cluster	0.83%	0.81%	1.62%
$E_{\text{T}}^{\text{miss}}$ Pileup	0.54%	0.60%	0.94%
$E_{\text{T}}^{\text{miss}}$ Jes	0.00%	0.00%	0.17%
$E_{\text{T}}^{\text{miss}}$ Jer	0.19%	0.07%	0.59%
Electron Trigger	0.00%	0.00%	0.00%
Muon Trigger	0.26%	0.35%	0.32%
PDF MSTW	0.41%	0.18%	1.22%
PDF CT10	0.08%	0.00%	0.26%
Generator	1.89%	0.95%	5.41%
Scale	0.47%	0.38%	1.06%
Background Systematics			
$t\bar{t}$	0.15%	0.07%	0.45%
Z+jets	0.20%	0.57%	0.30%
ZZ	0.00%	0.00%	0.09%
$Z\gamma$	0.06%	0.00%	0.29%

Table 8.31: Normalized unfolded fiducial results and uncertainties in m_{WZ} bins.

1	-0.71	-0.63
-0.71	1	-0.09
-0.63	-0.09	1

Table 8.32: Correlation matrix of statistical uncertainties for the m_{WZ} distribution.

1	-0.65	-0.50
-0.65	1	-0.28
-0.50	-0.28	1

Table 8.33: Correlation matrix of systematic uncertainties for the m_{WZ} distribution.

1	-0.83	-0.17
-0.83	1	-0.41
-0.17	-0.41	1

Table 8.34: Correlation matrix of background uncertainties for the m_{WZ} distribution.

Chapter 9

$G^* \to ZZ \to \ell^+\ell^- q\bar{q}$ Analysis

9.1 Introduction

As mentioned in chapter 3, one of the biggest problems of the SM is the large hierarchy between the Planck and electroweak scales. Different models propose a solution to this problem by extending the SM and introducing warped extra dimensions [189–191], Theories of Everything [192] or dynamical EW symmetry breaking theories like Technicolor [193–195]. A common feature of many of these models is that they predict the existence of very massive resonances that can decay into vector boson pairs.

This chapter will describe a search for a new narrow resonance decaying into Z boson pairs [196]. One Z boson then decays leptonically, into electrons or muons, and the other Z boson decays hadronically. The advantage of semileptonic final states is a larger branching ratio due to the hadronic boson decay. Furthermore, it allows one to maximise the signal sensitivity by exploiting leptonic and hadronic topologies separately. However, semileptonic decays leads to a significant increase in background compared to fully leptonic final states.

This search is performed using 7.2 fb^{-1} of 8 TeV p-p collision data collected with the ATLAS detector in 2012. The benchmark model that is probed is a spin-2 Randall-Sundrum (RS) graviton G^* decaying to a Z boson pair as shown in figure 9.1. More specifically, the bulk RS model [46] is tested in which the SM particle fields propagate into the extra dimension. The bulk RS model is an extension to the original RS model, commonly referred to as RS1 [189, 190]. The extension addresses several issues of the RS1 model such as large contributions to flavour changing neutral currents. In the bulk RS model, fermion and boson fields can propagate into the extra dimension. The coupling of the graviton to light fermions is highly suppressed with respect to the RS1 model whereas the coupling to heavy quarks or bosons, like the top quark or the W, Z and Higgs bosons, is enhanced. The bulk RS cross section is only about 3-7% of the RS1 cross section but the branching ratio to Z boson pairs is enhanced by a factor of 2-7 for graviton masses ranging between 2000-300 GeV. The largest graviton mass has the smallest cross section and branching fraction ratio between the two models. A dimensionless coupling parameter $\kappa/\bar{m}_{\text{Planck}}$ is assumed, where the numerator is the curvature of the warped extra dimension and the denominator is the reduced Planck mass, defined as $m_{\text{Planck}}/\sqrt{8\pi}$. It should be noted that the G^* production cross section and decay width increase as the square of this coupling parameter.

If no significant deviation from a smoothly falling SM background prediction is observed in the reconstructed graviton invariant mass distribution, upper Bayesian limits on $\sigma(pp \to G^*) \times \mathrm{BR}(G^* \to ZZ)$ will be set. The limits extracted for this specific benchmark model are applicable to WZ resonances, as for example a W' boson, if the resonance width and kinematic properties of the boson decays are similar to those for the G^* signal.

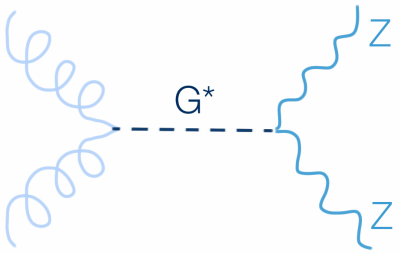

Figure 9.1: Feynman diagram of a bulk RS graviton resonance.

Many direct searches for diboson resonances have previously been performed at the Tevatron and the LHC in various channels and for various benchmark models. Table 9.1 summarises these results according to the experiment at which they were performed, which final state, model and coupling constant were used and finally what the derived limits are. A single number indicates a lower mass limit whereas a range of two numbers indicates an excluded range.

Experiment	Channel	Model	$\kappa/\bar{m}_{\mathrm{Planck}}$	Limit [GeV]	Reference
DØ	$W^+W^-/W^\pm Z \to \ell^\pm \nu q\bar{q}$	RS1	0.1	300-754	[197]
CDF	$W^+W^-/W^\pm Z \to e^\pm \nu q\bar{q}$	RS1	0.1	607	[198]
	$ZZ \to \ell^+\ell^-\ell^+\ell^- + \ell^+\ell^- q\bar{q}$	RS1	0.1	491	[199]
CMS	$ZZ \to \ell^+\ell^- q\bar{q}$	RS1	0.1	945	[200]
		RS1	0.05	720, 760-850	
		bulk RS	0.5	610	
	$W^\pm Z/ZZ \to \ell^+\ell^- J$	RS1	0.05	700-924	[201]
ATLAS	$ZZ \to \ell^+\ell^-\ell^+\ell^- + \ell^+\ell^- q\bar{q}$	RS1	0.1	325-845	[202]
	$W^+W^- \to \ell^+\nu\ell^-\nu$	RS1	0.1	1230	[203]
		bulk RS	0.1	840	

Table 9.1: Previous limits on graviton searches.

This chapter is organised as follows. In sections 9.2 – 9.4 the data and MC samples as well as the trigger chains used in this analysis are listed. Section 9.5 describes how physics objects, such as electrons, muons and jets, are selected and section 9.6 motivates the choice and definition of the signal and control regions. The Z+jets, $t\bar{t}$ and diboson MC as well as the data-driven QCD multijet background estimations are explained in section 9.7. Systematic uncertainties and the limit extraction procedure are described in sections 9.8 and 9.9, respectively, while section 9.10 presents the final results.

9.2 Data Samples

This analysis uses a data sample of proton-proton collisions collected in 2012 with the ATLAS detector at the LHC at $\sqrt{s} = 8$ TeV. A GRL [152] is used to ensure good performance of the detector and data quality. Table 9.2 summarises the different data taking periods and the integrated luminosity recorded throughout this time after application of the GRL[1]. In total, this amounts to 7.2 fb^{-1} of data. The preliminary luminosity uncertainty for the 2012 data is estimated to be 3.6% [128].

Data Period	Run Numbers	$\int \mathcal{L} dt$ [pb^{-1}]
A	200804 – 201556	738.2
B	202660 – 205113	5103.3
C	206248 – 207397	1321.4
Total	200804 – 207397	7162.9

Table 9.2: The integrated luminosity per data taking period and in total.

9.3 Monte Carlo Samples

MC event simulation and detector reconstruction is done analogously to the description in section 8.3. The background samples are passed through the full Geant4 [130] detector simulation. The signal samples are simulated with the ATLFAST II [204] fast detector simulation, which is less CPU intensive, and they are validated against full detector simulation at reference mass points.

The bulk RS graviton signal samples are produced with the `CalcHEP` [205] generator, which fully retains all spin correlation information, and the CTEQ6L1 [206] PDF set. The parton showering and hadronization steps are done with Pythia 8 [207]. The signal samples are generated for semileptonic $ZZ \to \ell\ell jj$ decays ($\ell = e, \mu, \tau$) and at graviton mass points ranging from 300 to 1000 GeV, in steps of 50 GeV, and from 1000 to 2000 GeV, in steps of 100 GeV. The coupling constant of the graviton is set to $\kappa/\bar{m}_{\text{Planck}} = 1.0$, which is the default[2] value in `CalcHEP`. A generator level event filter is applied after the τ lepton decay which requires at least two leptons, electrons or muons, with $p_{\text{T}} > 8$ GeV and $|\eta| < 2.8$.

The background samples used in this analysis include W/Z+jets, $t\bar{t}$ as well as WZ, ZZ and WW diboson production. The Z+jets samples are produced with Sherpa [161], a multi-leg LO generator, and the CT10 [179] PDF set. The distributions of the Sherpa samples are cross-checked with Alpgen [158] Z+jets samples generated with the CTEQ6L1 PDF set. Alpgen generates Z bosons with up to five additional partons in the final state. HERWIG [155] is used for parton showering and hadronization and Jimmy [208] is used for simulating the

[1] For completeness, the specific GRL configuration used is `All_Good_v4`.

[2] $\kappa/\bar{m}_{\text{Planck}} = 1$ was long perceived as the upper limit of the domain of validity of the model. This boundary has been reviewed in reference [46] and the edge of validity has been pushed to $\kappa/\bar{m}_{\text{Planck}} \approx 3$.

underlying event. $t\bar{t}$ events are generated with the CT10 PDF set and MC@NLO [209] interfaced to HERWIG and Jimmy. A generator level event filter, that requires at least one lepton with $p_T > 1$ GeV, is applied to select events where at least one W boson decays leptonically. WZ, ZZ and WW diboson processes are simulated with HERWIG and the CTEQ6L1 PDF set. Leptonic and hadronic W and Z boson decay modes are included. W+jets samples are simulated with the CTEQ6L1 PDF set and Alpgen interfaced to HERWIG for hadronization and Jimmy for underlying event simulation. The events are generated with up to five additional partons. Tables 9.3 – 9.6 summarise all these samples indicating the process name, the cross section multiplied by the branching ratio and MC filter efficiency, the MC identification number, the number of generated events and the name of the generator used for each sample. For the signal samples, the width of the resonance is also indicated.

Process	$\sigma \times \mathcal{B} \times \epsilon_{\text{filter}}$ [pb]	width [GeV]	ϵ_{filter}	MCID	Events	Generator
$m_{G^*} = 300$ GeV	5.62	8.49	0.646	158294	15000	CalcHEP
$m_{G^*} = 350$ GeV	2.77	8.87	0.660	158295	15000	CalcHEP
$m_{G^*} = 400$ GeV	1.19	11.6	0.674	158296	15000	CalcHEP
$m_{G^*} = 450$ GeV	0.540	15.3	0.685	158297	15000	CalcHEP
$m_{G^*} = 500$ GeV	0.272	19.3	0.696	158298	15000	CalcHEP
$m_{G^*} = 550$ GeV	0.149	23.3	0.710	158299	15000	CalcHEP
$m_{G^*} = 600$ GeV	0.0854	27.2	0.709	158300	15000	CalcHEP
$m_{G^*} = 650$ GeV	0.0517	31.1	0.711	158301	15000	CalcHEP
$m_{G^*} = 700$ GeV	0.0328	35.0	0.719	158302	15000	CalcHEP
$m_{G^*} = 750$ GeV	0.0213	38.7	0.718	158303	15000	CalcHEP
$m_{G^*} = 800$ GeV	0.0144	42.5	0.731	158304	15000	CalcHEP
$m_{G^*} = 850$ GeV	0.975E-2	46.1	0.723	158305	15000	CalcHEP
$m_{G^*} = 900$ GeV	0.679E-2	49.8	0.725	158306	15000	CalcHEP
$m_{G^*} = 950$ GeV	0.482E-2	53.3	0.726	158307	14000	CalcHEP
$m_{G^*} = 1000$ GeV	0.349E-2	56.9	0.734	158308	15000	CalcHEP
$m_{G^*} = 1100$ GeV	0.186E-2	63.9	0.732	158309	15000	CalcHEP
$m_{G^*} = 1200$ GeV	0.105E-2	70.8	0.739	158310	15000	CalcHEP
$m_{G^*} = 1300$ GeV	0.602E-3	77.6	0.740	158311	15000	CalcHEP
$m_{G^*} = 1400$ GeV	0.355E-3	84.3	0.738	158312	15000	CalcHEP
$m_{G^*} = 1500$ GeV	0.214E-3	91.0	0.738	158313	15000	CalcHEP
$m_{G^*} = 1600$ GeV	0.131E-3	97.7	0.734	158314	15000	CalcHEP
$m_{G^*} = 1700$ GeV	0.835E-4	104	0.745	158315	15000	CalcHEP
$m_{G^*} = 1800$ GeV	0.531E-4	111	0.748	158316	15000	CalcHEP
$m_{G^*} = 1900$ GeV	0.340E-4	117	0.740	158317	15000	CalcHEP
$m_{G^*} = 2000$ GeV	0.223E-4	124	0.744	158318	15000	CalcHEP

Table 9.3: MC samples used to model the $G^* \to ZZ \to \ell\ell q\bar{q}$ bulk Randall-Sundrum graviton signal. The k-factor is 1 for all these samples.

As described in section 8.3, the simulated events need to be reweighted to account for differences in the modelling of pile-up between data and MC. Figure 9.2 shows the distribution of interactions per bunch crossing for MC and figure 5.3 shows the same distribution for 8 TeV data. An enhanced description of the vertex multiplicity in MC is obtained by scaling the average number of interactions per bunch crossing by a factor of 1.11 [210]. The simulated

Process	$\sigma \times \mathcal{B} \times \epsilon_{\text{filter}}$ [pb]	MC ID	Events	Generator
$Z \to ee + \text{jets}$	1.208	147770	9999568	Sherpa
$Z \to \mu\mu + \text{jets}$	1.208	147771	9999975	Sherpa
$Z \to \tau\tau + \text{jets}$	1.207	147772	4999087	Sherpa

Table 9.4: MC samples used to model the Z+jets processes. The k-factor is 1 for all these samples.

Process	$\sigma \times \mathcal{B} \times \epsilon_{\text{filter}}$ [pb]	MCID	Events	Generator
$t\bar{t} \to \ell + X$	129.3	105200	14993322	MC@NLO
$WW \to \ell + X$	20.6	105985	2484694	HERWIG
$WZ \to \ell + X$	4.71	105987	999797	HERWIG
$ZZ \to \ell + X$	2.24	105986	249999	HERWIG

Table 9.5: MC samples used to model the top and diboson processes. The k-factor is 1 for all these samples.

Process	$\sigma \times \mathcal{B} \times \epsilon_{\text{filter}}$ [pb]	MCID	Events	Generator
$W \to e\nu$ Np0	8037.1	107680	3459894	Alpgen
$W \to e\nu$ Np1	1579.2	107681	2499491	Alpgen
$W \to e\nu$ Np2	477.2	107682	3769487	Alpgen
$W \to e\nu$ Np3	133.9	107683	1009997	Alpgen
$W \to e\nu$ Np4	35.6	107684	249999	Alpgen
$W \to e\nu$ Np5	10.6	107685	70000	Alpgen
$W \to \mu\nu$ Np0	8040.0	107690	3469692	Alpgen
$W \to \mu\nu$ Np1	1580.3	107691	2499694	Alpgen
$W \to \mu\nu$ Np2	477.2	107692	3769886	Alpgen
$W \to \mu\nu$ Np3	133.9	107693	1006698	Alpgen
$W \to \mu\nu$ Np4	35.6	107694	254999	Alpgen
$W \to \mu\nu$ Np5	10.6	107695	69900	Alpgen
$W \to \tau\nu$ Np0	8035.8	107700	3419992	Alpgen
$W \to \tau\nu$ Np1	1579.8	107701	2499793	Alpgen
$W \to \tau\nu$ Np2	477.2	107702	3765989	Alpgen
$W \to \tau\nu$ Np3	133.8	107703	1009998	Alpgen
$W \to \tau\nu$ Np4	35.6	107704	249998	Alpgen
$W \to \tau\nu$ Np5	10.5	107705	65000	Alpgen

Table 9.6: MC samples used to model the W+jets processes. The k-factor is 1.23 for all these samples.

events used in this analysis have a larger beamspot size along the beam line than the data. This leads to more merged vertices and less reconstructed vertices in data compared to MC. This means that, even after applying the scaling above, the distribution of the number of primary vertices in data and MC is not in perfect agreement. The scaling factor will however allow the reproduction of the average activity in the event.

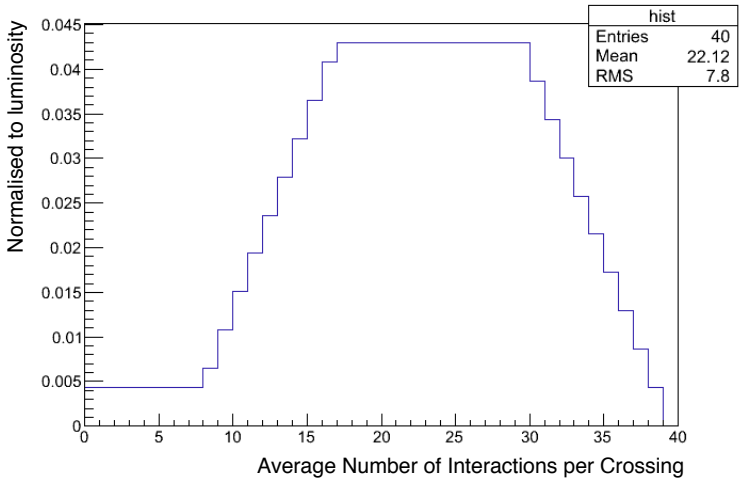

Figure 9.2: The number of interactions per bunch crossing for 8 TeV MC samples.

9.4 Trigger

As with the $W^{\pm}Z$ analysis, single lepton triggers are used in both the electron and the muon channels. The triggers, stable throughout the 2012 data taking periods, used in this analysis are EF_e24vhi_medium1 || EF_e60_medium1 for the electron triggers and EF_mu24i_tight || EF_mu36_tight for the muon triggers. The electron trigger efficiency [211] and the muon trigger scale factors [164] for these chains are shown in figures 9.3 and 9.4, respectively. At least one of the two selected leptons is required to be matched to a trigger object and have a $p_{\mathrm{T}} > 25$ GeV in the trigger plateau region. The systematic uncertainties related to the trigger are evaluated using the same method as described in section 8.4 for the $W^{\pm}Z$ analysis. They are less than or equal to 1% in the electron or muon channel, respectively. The package used to apply the Trigger SFs is TrigMuonEfficiency-00-02-13.

9.5 Object Selection

9.5.1 Electrons

The selection criteria for candidate electrons are very similar to the ones described in the $W^{\pm}Z$ analysis. For simplicity, only the cuts that have different cut values will be listed here, all other cuts are unchanged. An electron candidate is required to be of medium++ quality as defined in section 7.3, have an $E_{\mathrm{T}} > 20$ GeV, a $z_0 < 2$ mm and a d_0 significance

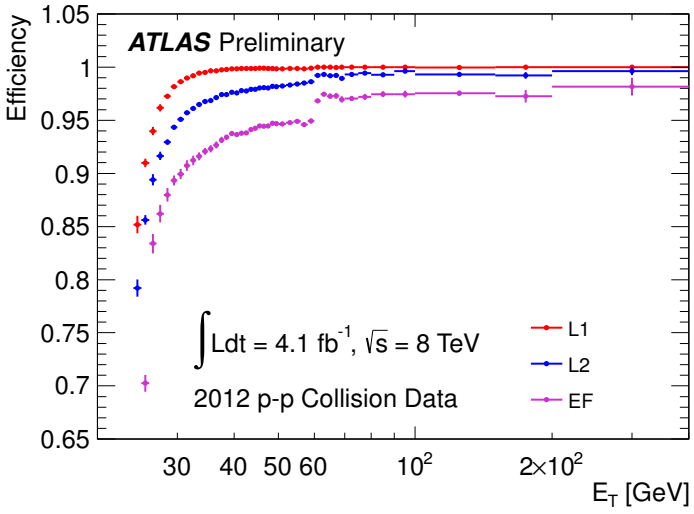

Figure 9.3: Electron trigger efficiency as a function of E_{T}.

less than six. The sum of transverse momenta of tracks with $p_{\mathrm{T}} > 1$ GeV surrounding the electron track in a cone of $\Delta R = 0.2$ must be less than 15% of the electron p_{T}. The sum of transverse energy of calorimeter clusters surrounding the cluster associated with the electron in a cone of $\Delta R = 0.2$ must be less than 30% of the electron E_{T}. Corrections for electron energy leakage from the electron cluster and pile-up contribution are taken into account for this cut. A smaller cone is chosen in this analysis as compared to the $W^{\pm}Z$ analysis since the aim is to probe large signal graviton masses. Optimisation studies showed that the signal acceptance increases with smaller isolation cone sizes as decay objects are expected to be boosted for large graviton masses. Similar smearing and scaling correction factors to those described in section 8.5 are applied to the electrons in this analysis to account for data and MC differences. The package used is egammaAnalysisUtils-00-03-46.

9.5.2 Muons

The muon selection criteria are also very similar to the $W^{\pm}Z$ selection and again only differences will be listed. In this analysis, only CB muons with a $p_{\mathrm{T}} > 20$ GeV are used. The number of ID hit requirements have changed slightly in that only one hit in all the pixel layers is required instead of two, only five SCT hits instead of six and a lower boundary for the $|\eta|$-dependent TRT hits has been added such that the requirements apply to $0.1 < |\eta| < 1.9$ and $|\eta| \leq 0.1$ or $|\eta| \geq 1.9$, respectively. High p_{T} searches are sensitive to precise momentum reconstruction and so a momentum consistency cut between the MS and ID tracks is applied. The charge q to momentum p ratio in the two detectors are required to satisfy $|(q/p)_{\mathrm{MS}} - (q/p)_{\mathrm{ID}}|/\sigma_C < 5$, where σ_C is the combined q/p uncertainty. The impact parameters must satisfy $|z_0| < 2$ mm and the d_0 significance must be less than 3.5. Lastly, the same track and calorimeter isolation requirements as for the electrons are applied. Similar smearing and scaling correction factors as described in section 8.5 are also applied to the muons in this analysis to account for data and MC differences. The packages used are

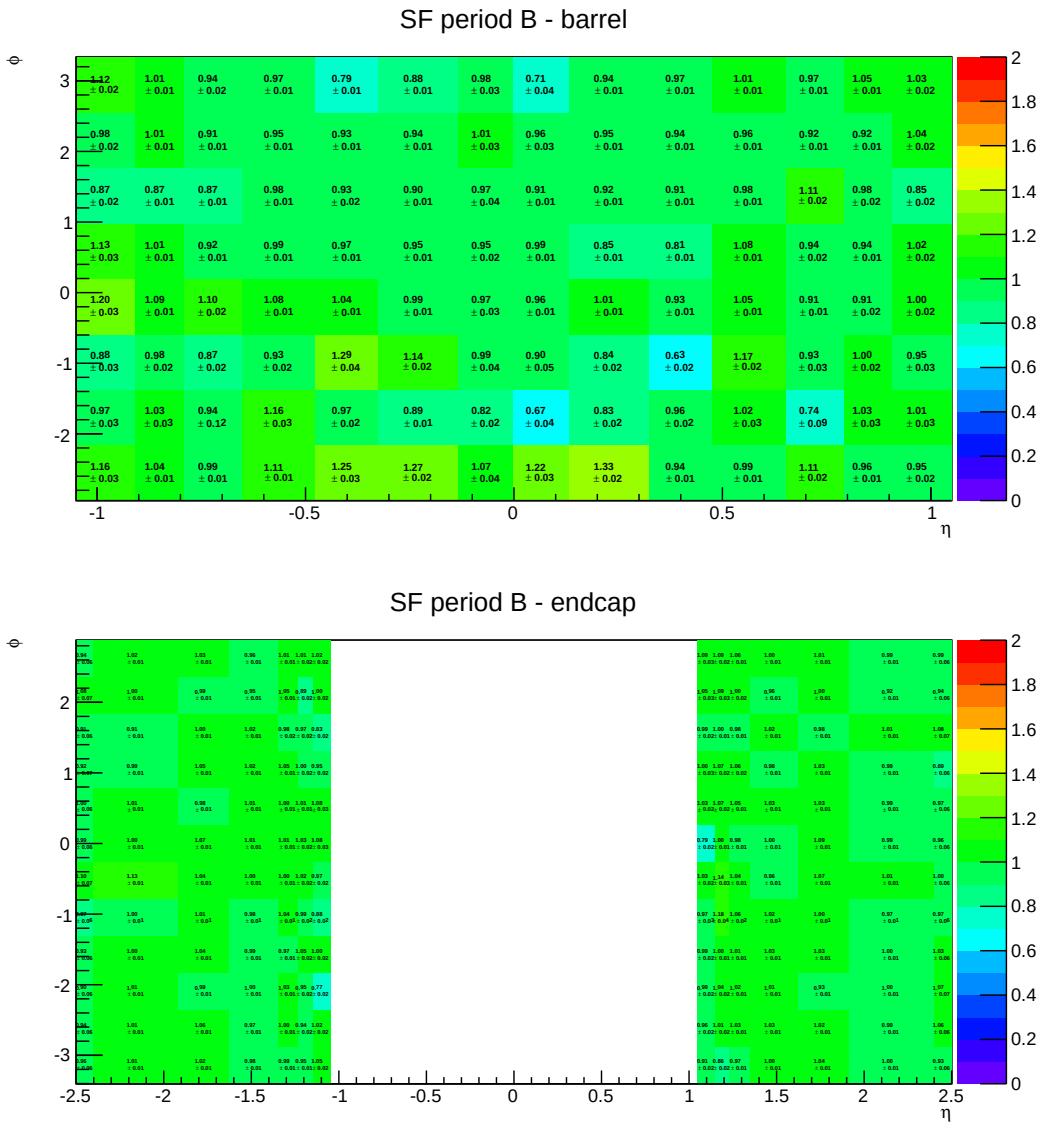

Figure 9.4: Muon trigger SFs in barrel (top) and end-cap (bottom) for period B. Fluctuations in the barrel are due to services and support structures in the detector as well as imperfect operation of the RPC during certain run periods of data taking.

MuonEfficiencyCorrections-02-01-02 and MuonMomentumCorrections-00-07-00.

9.5.3 Jets

In this analysis, jets are reconstructed from topological clusters using the anti-k_T jet clustering algorithm with a distance parameter of $R = 0.4$. The EM+JES calibration is applied to all jets as described in section 7.5. The jets need to further satisfy $p_T > 30$ GeV and $|\eta| < 2.1$ to ensure full containment in the tracker. They can not be of "bad looser" quality [174] and at least 50% of the total p_T from tracks associated to the jet, also known as the jet vertex fraction (JVF), must come from tracks associated to the primary vertex.

Lastly, an object overlap removal is applied because it is possible that two or more reconstructed objects overlap in η-ϕ space. Only one of these objects is retained and the others are removed as follows. The jet reconstruction algorithm does not distinguish between calorimeter energy deposit from an electron and from hadrons within a jet. Therefore, an electron is also reconstructed as a jet so jets that are within $\Delta R < 0.3$ of an electron are removed. Further, a muon can radiate a photon while traveling through the calorimeter. The photon is in turn reconstructed as a jet with a falsely associated track from the muon. Jets that are within $\Delta R < 0.3$ of a muon are therefore also removed.

9.6 Event Selection

This analysis selects final states with two high p_T electrons or muons from a Z boson decay and one or two reconstructed jets from the second Z boson decay. Once the electrons, muons and jets are selected as described in the previous section, the following event preselection cuts are applied.

1. The presence of a primary reconstructed vertex with at least three tracks is required to ensure that the event originated from a hard scatter.
2. The event must not have a data quality flag indicating noise in the LAr calorimeter.
3. Events with "looser bad" jets with calibrated $p_T > 20$ GeV are removed.
4. The event is vetoed if it contains a jet pointing into the $-0.2 < \eta < -0.1$ and $2.65 < \phi < 2.75$ regions close to a hot Tile calorimeter cell[3] that was not masked in the reconstruction and with more than 60% of the jet energy reconstructed in the second Tile calorimeter layer.
5. The event has to contain exactly two same flavour leptons. Opposite charge is only required for muons as the charge misidentification rate for electrons is higher and increases with p_T.
6. The event has to fire the single electron (muon) trigger for the electron (muon) channel. At least one of the two selected leptons must be matched to a trigger object and have a $p_T > 25$ GeV.

[3] This affects runs 202660–203027 during data taking period B.

7. The reconstructed invariant dilepton mass must fall within 25 GeV of the Z boson pole mass.

Since the resonances studied in this analysis decay into one leptonically and one hadronically decaying boosted Z boson, the sensitivity to high p_{T} lepton or jet pairs with a small separation angle must be optimised. The two jets often merge into a single reconstructed jet for very large resonance masses above ~ 1 TeV. From kinematics, the following relation can be deduced

$$m^2 = p_{\mathrm{T}}^2 \Delta R^2 z(1-z) \tag{9.1}$$

where m and p_{T} are the mass and transverse momentum of the parent particle and z the momentum fraction carried by one decay particle. As a rule of thumb, if the momentum is roughly evenly shared between the two decay particles then $z \sim 1/2$ and the separation between the two decay particles can be approximated as

$$\Delta R \sim \frac{2m}{p_{\mathrm{T}}}. \tag{9.2}$$

To cover a wide range of resonance masses, two selection categories are used to separately deal with resolved and merged jets from the Z boson decay. The former is used for graviton masses in the [300, 1000] GeV range and the latter for masses in the [1000, 2000] GeV range.

The exact selection cuts that define each signal region are determined by optimising the signal sensitivity. The selection cuts are determined by applying cuts on kinematic variables in signal (S) and background (B) MC samples. The choice of the cut value is made initially by minimising the distance in the signal efficiency (SE) versus background rejection (BR) plane between the point for a given cut and the (1,1) point. Once the optimal cut value is found, the final discriminating variable is examined to determine how the shape is biased and the values of S/B and $S/\sqrt{B}$ are calculated as a function of signal mass and optimised. In this analysis, the discriminating variables are the four-body invariant mass of the lepton pair and the leading jet pair, $m_{\ell\ell jj}$, or the three-body invariant mass of the lepton pair and the leading jet, $m_{\ell\ell J}$. The first step, for the resolved and merged selections, is to optimise the transverse momentum cut of the lepton pair, $p_{\mathrm{T}}^{\ell\ell}$, according to SE versus BR after all the preselection cuts have been applied. For the resolved region, different variables like the p_{T}^{jj}, $\cos\theta^*$, $\Delta\phi_{\ell\ell,\mathrm{j}_2}$ and $\Delta\phi_{jj}$ distributions[4] are then examined and the optimal variables are determined by comparing the S/B and $S/\sqrt{B}$ ratios within a $\pm 1\sigma$ window of the signal mass in the $m_{\ell\ell jj}$ distribution. For the merged region, cuts on the transverse momentum of the leading jet, p_{T}^{J}, and the mass of the leading jet, m_J, are optimised in that order by checking the SE versus BR for different cut values after all previous cuts have already been applied. From these studies, the following cuts for the signal region are chosen.

- **Resolved signal region**: $p_{\mathrm{T}}^{\ell\ell} > 50$ GeV, $\Delta\phi_{jj} < 1.6$, $65 < m_{jj} < 115$ GeV.

[4] The first variable is the transverse momentum of the two leading jets.The θ^* variable is defined in the rest frame of the $\ell\ell jj$ system as the angle between the direction of the dilepton system and the direction of the $\ell\ell jj$ system boosted from the lab frame to its rest frame. The $\Delta\phi_{\ell\ell,\mathrm{j}_2}$ variable is the azimuthal opening angle between the dilepton system and the second leading jet. The $\Delta\phi_{jj}$ variable is the dijet azimuthal opening angle. Both $\Delta\phi$ variables are measured in the lab frame.

- **Merged signal region**: $p_{\mathrm{T}}^{\ell\ell} > 200$ GeV, $p_{\mathrm{T}}^{J} > 200$ GeV, $m_J > 40$ GeV.

Figure 9.5 shows the SE versus BR for different $p_{\mathrm{T}}^{\ell\ell}$ cut values and for different graviton mass points in the resolved region as well as the S/B and $S/\sqrt{B}$ values as a function of graviton mass as the different cuts for the resolved selection are applied. Figure 9.6 shows the SE versus BR for different p_{T}^{J} and m_J cut values at different graviton mass points in the merged region. These figures are for the electron channel, only small differences are found in the muon channel. The overall sensitivity is summarised in figure 9.7 where the S/B and $S/\sqrt{B}$ values for the resolved and merged selections as a function of graviton mass in the electron and muon channels are shown.

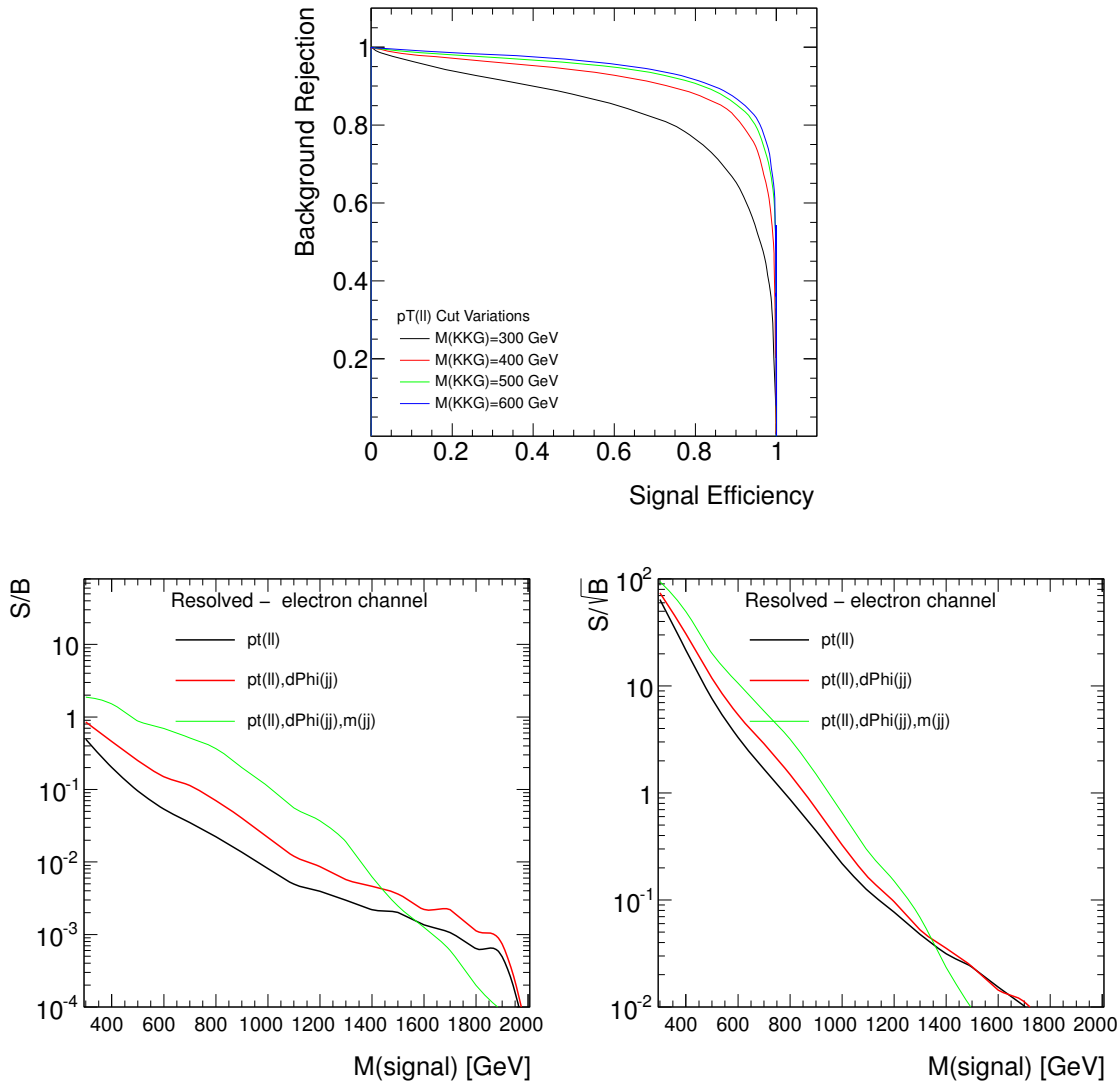

Figure 9.5: SE versus BR for different $p_{\mathrm{T}}^{\ell\ell}$ cut values (top). S/B (bottom left) and $S/\sqrt{B}$ (bottom right) values in the resolved signal region.

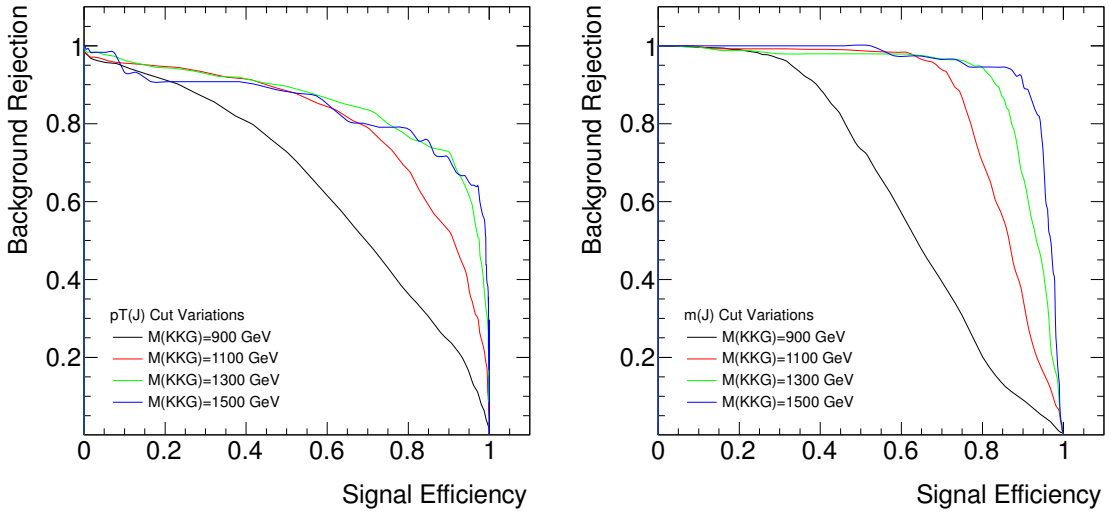

Figure 9.6: SE versus BR for different p_{T}^{J} (left) and m_J (right) cut values.

After applying the two selections separately, the $m_{\ell\ell jj}$ and $m_{\ell\ell J}$ invariant mass distributions are probed in the resolved and merged regimes, respectively. Figure 9.8 shows the mass dependent resolution of the $m_{\ell\ell jj}$ and $m_{\ell\ell J}$ distributions in the resolved and merged regions. The experimental resolution is mainly determined by the jet and lepton energy resolutions and is well modelled by a single Gaussian distribution in the peak region. The mass resolution is slightly worse for the muon than for the electron channel at high mass values and grows with mass, as is expected due to the degrading muon momentum resolution at higher p_{T}.

Figure 9.9 shows the signal acceptance, which is the fraction of signal events remaining after all selection cuts, as a function of the graviton mass. For masses below ∼700 GeV, the majority of events contain at least two jets but for higher masses the jets are starting to merge due to the boost of the parent. This means that when the hadronically decaying Z boson p_{T} is large enough, the ΔR separation between the quark and the antiquark is less than 0.4 and a single merged jet is reconstructed. An additional jet can be found due to ISR or FSR but, in that case, the dijet mass does not usually fall within the required range. The decrease in acceptance for the merged region above ∼1800 GeV is mainly due to the lepton isolation requirements. As with the jets, the leptons are produced close to each other and the energy from one lepton starts leaking into the 0.2 isolation cone of the second lepton which therefore fails the isolation requirement.

Control regions are defined to test the level of agreement between the data and background predictions before the data is surveyed in the signal region. The background estimation is validated in control regions that contain a negligible amount of signal and are ideally dominated by a single background, in this case Z+jets production. Two control regions are chosen to determine the normalisation and check the differential distributions of the selected kinematic variables. The control regions only differ from the signal region in that the dijet or single jet mass requirements are reversed.

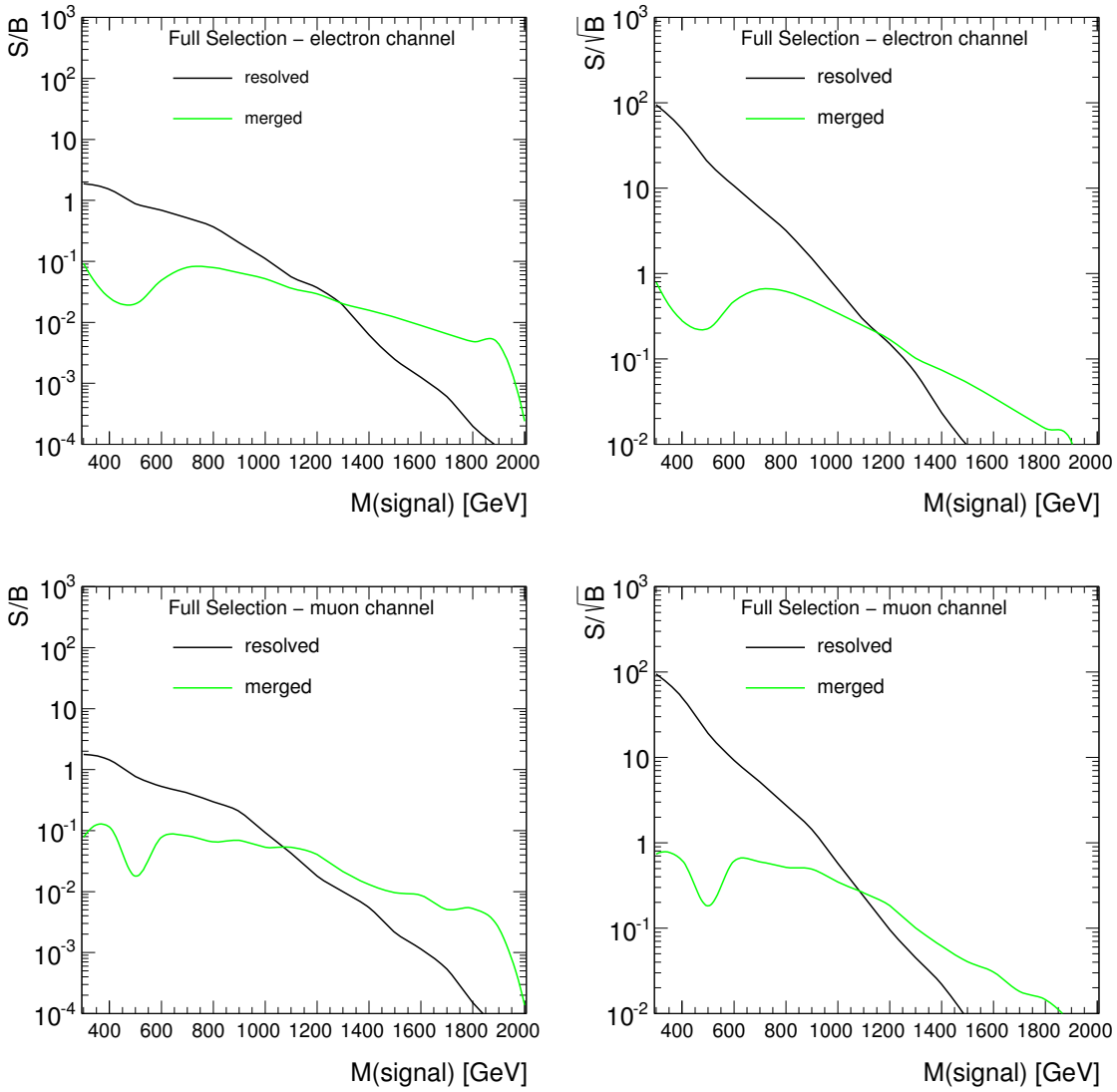

Figure 9.7: S/B (left) and $S/\sqrt{B}$ (right) values for the electron (top) and muon (bottom) channels in the resolved and merged signal regions.

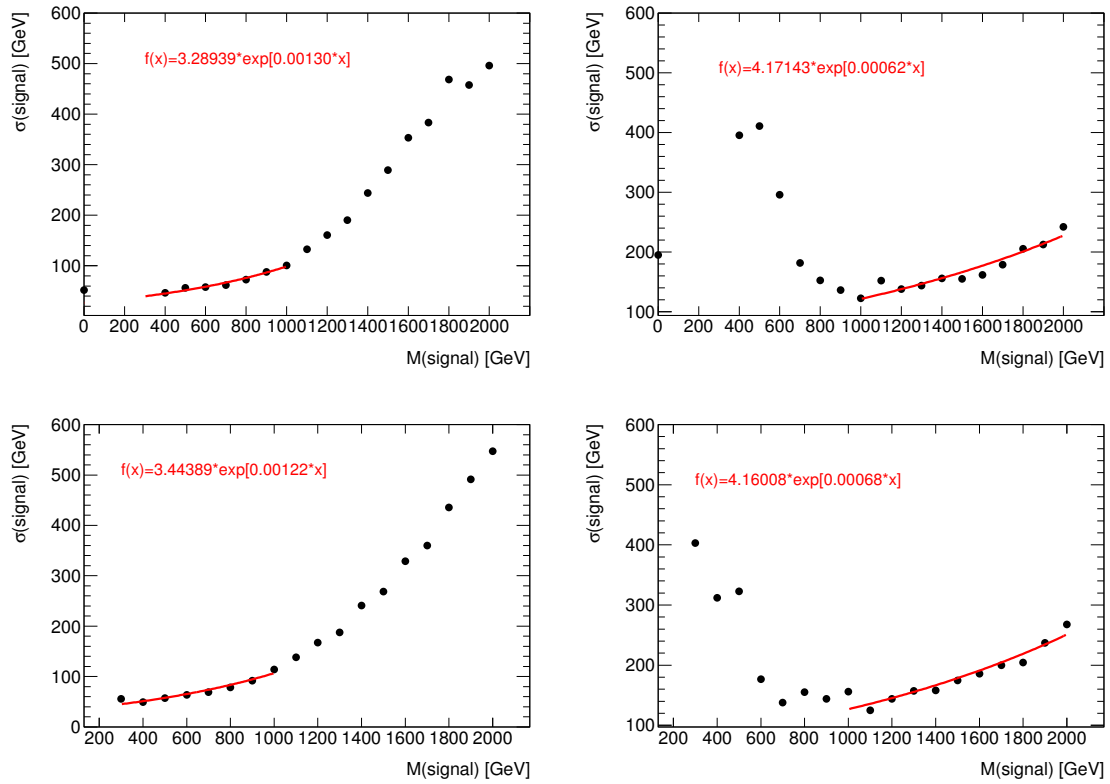

Figure 9.8: Reconstructed signal resolution as a function of G^* mass for the resolved (left) and merged (right) selection in the electron (top) and muon (bottom) channel.

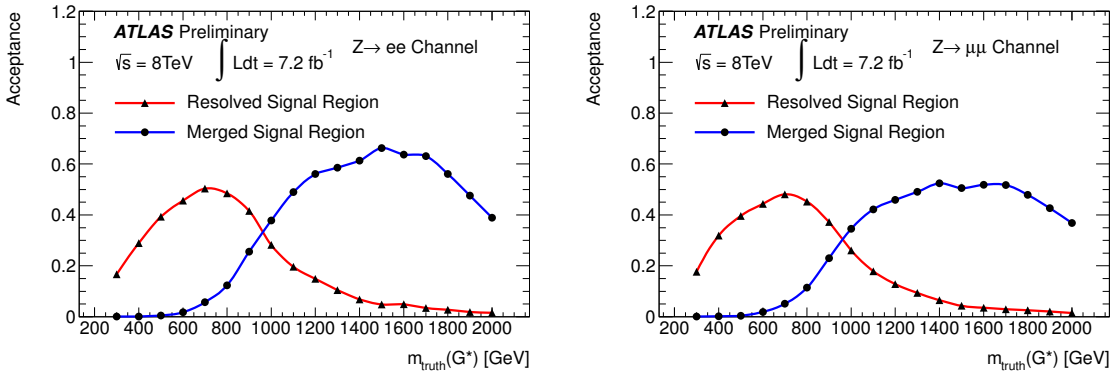

Figure 9.9: Signal acceptance as a function of G^* mass for the electron (left) and muon (right) channels for the resolved and merged selections.

- **Resolved control region**: $p_{\mathrm{T}}^{\ell\ell} > 50$ GeV, $\Delta\phi_{jj} < 1.6$, $m_{jj} \leq 65$ GeV or $m_{jj} \geq 115$ GeV.
- **Merged control region**: $p_{\mathrm{T}}^{\ell\ell} > 200$ GeV, $p_{\mathrm{T}}^{J} > 200$ GeV, $m_J < 40$ GeV.

9.7 Background Estimation

The background estimation method in the signal region is data-driven and will be described in section 9.9. However, before the signal region can be unblinded[5], the agreement between data and MC is checked in the control regions. The main background in this analysis is Z boson production in association with jets. Smaller backgrounds, on the order of a few percent, come from $t\bar{t}$ as well as WW, ZZ and WZ diboson production. A very small contribution comes from W+jets and QCD multijet events. All these backgrounds are estimated using MC simulation except for the latter which is estimated using a data-driven method described below. The generators used to simulate each category of background events and the cross sections of each process used for normalisation are listed in section 9.3.

As was seen in the previous section, the overall S/B ratio is strongly dependent on the graviton mass. The dominating background, by far, is Z+jets with about an 89% (97%) contribution estimated from MC in the resolved (merged) region. The top and diboson background expectations from MC are about 3% ($< 1\%$) and 8% (3%) in the resolved (merged) region, respectively. The W+jets background becomes negligibly small once the dilepton invariant mass cut is applied.

The QCD multijet background estimation relies on a combination of data-driven and MC estimates. The multijet background shape is obtained from the data and the non-QCD background from simulation. A loose control sample is selected as follows. In the electron channel, electrons which fail the medium++ quality requirement but pass all other cuts are selected whereas in the muon channel, muons which fail the isolation and impact parameter cuts but pass all other cuts are selected. The normalisation of the multijet background is determined by a maximum likelihood fit to the $m_{\ell\ell}$ spectrum between 40 GeV and 200 GeV. The fit uses a multijet template, obtained from the loose control sample, and non-QCD MC background templates, obtained by applying the standard selection cuts. Figure 9.10 shows the fit to the $m_{\ell\ell}$ distributions before applying the 66 GeV$< m_{\ell\ell} <$116 GeV cut. The multijet background within $|m_{\ell\ell} - m_Z| < 25$ GeV is found to be less than 1% for both channels.

Figure 9.11 shows a selection of control plots of the cut variables. The p_{T} distribution of the dilepton system is shown after the preselection cuts which includes the $\pm$25 GeV $m_{\ell\ell}$ window cut. The $\Delta\phi$ and mass distributions of the two leading jets are used for the resolved region. The p_{T} and mass cuts on the leading jets are used for the merged region. The distributions are shown after applying the selection cuts in the order listed above but without making the cut on the represented variable. The MC prediction is found to reproduce the data well. The systematic uncertainty is dominated by the jet energy scale uncertainty which will be discussed in section 9.8.

The $m_{\ell\ell jj}$ and $m_{\ell\ell J}$ distributions for data and MC background predictions in the resolved and merged control regions are shown in the top row of figure 9.12. The overall MC

[5]Unblinding refers to the procedure of not looking at the data in the signal region before the complete analysis procedure is fixed.

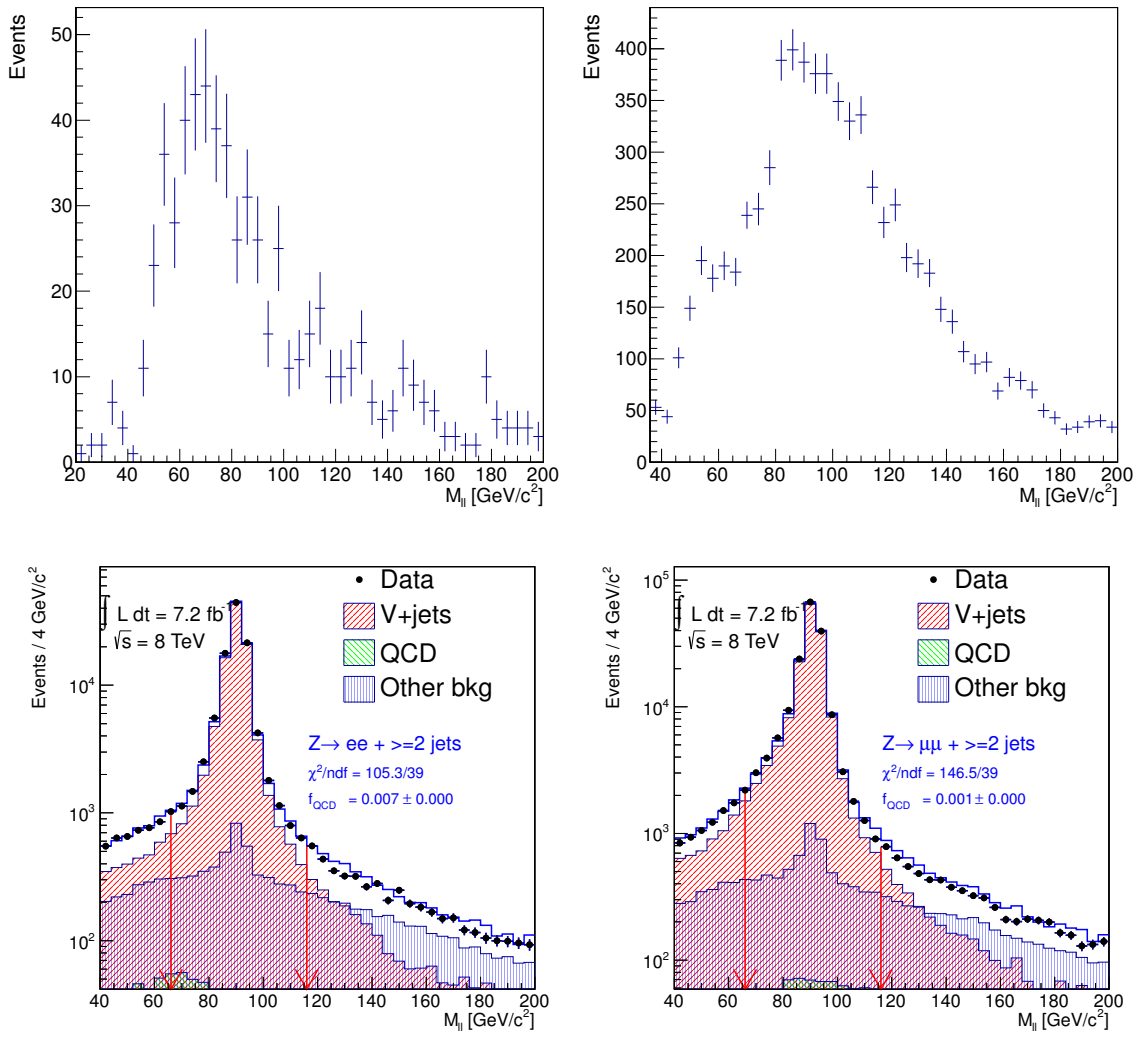

Figure 9.10: m_{ee} (left) and $m_{\mu\mu}$ (right) distributions fitted with multijet and non-QCD background templates. The top row shows the data-driven multijet templates and the bottom row shows the likelihood fit to data to obtain the multijet normalisation. The total background is shown by the empty blue histograms.

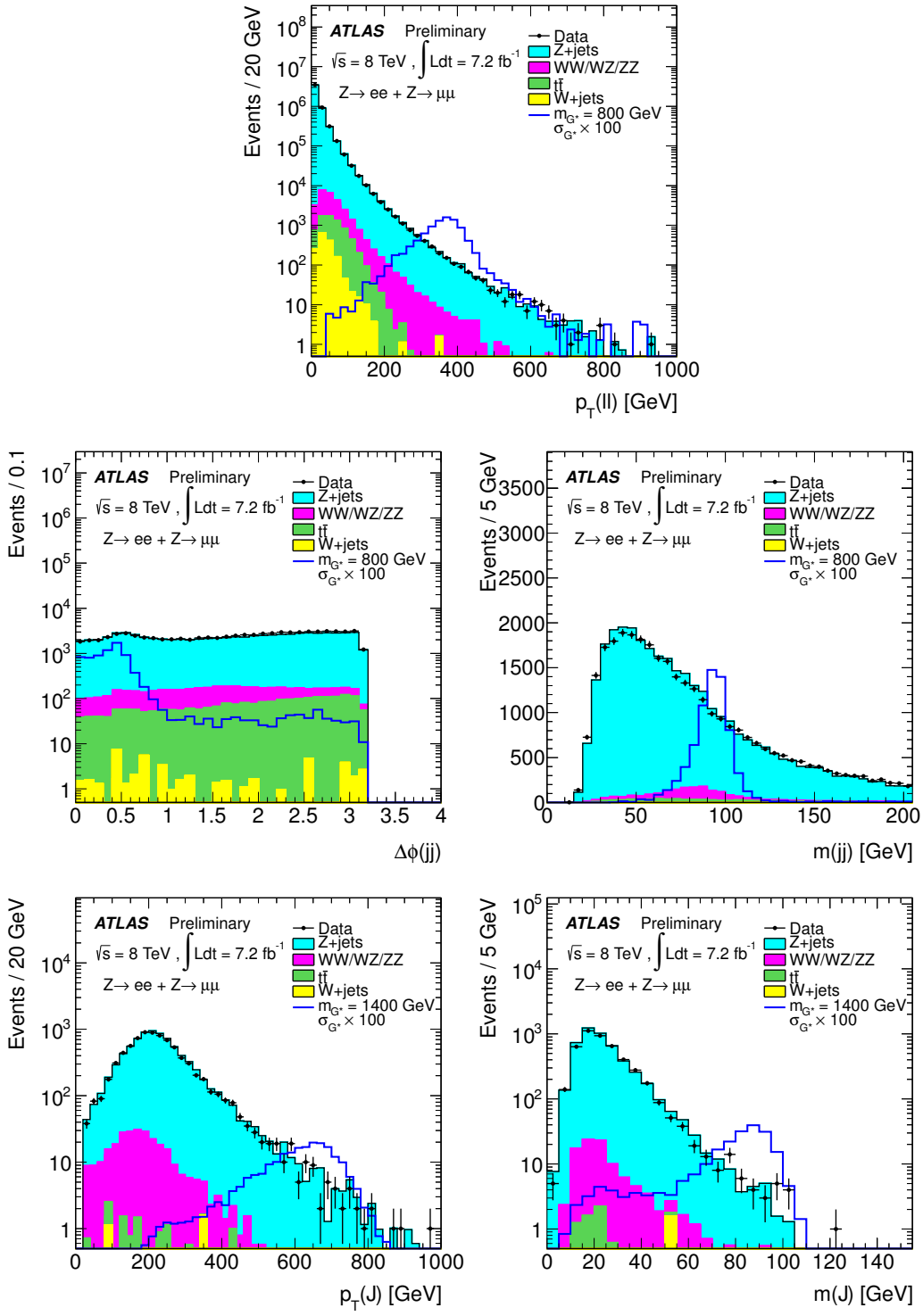

Figure 9.11: Data and MC comparison of the dilepton p_{T} (top), dijet $\Delta\phi$ (middle left), dijet invariant mass (middle right), leading jet p_{T} (bottom left) and leading jet invariant mass (bottom right) distributions.

background description agrees well with the data in these regions. Once the control region check is completed, the data in the signal region can be unblinded. The result is shown in the bottom row of figure 9.12. In the resolved (merged) signal region, a MC signal scaled up by a factor of 10^2 with a mass of 800 GeV (1400 GeV) is overlaid.

9.8 Systematic Uncertainties

In this section, systematic uncertainties on the signal acceptance are described. The different sources are luminosity, trigger, lepton reconstruction, jet energy scale and resolution, jet mass scale and resolution as well as theoretical PDF and ISR/FSR uncertainties.

9.8.1 Electrons and Muons

Uncertainties on the electron reconstruction and identification efficiencies, electron energy scale and resolution, muon reconstruction efficiency and muon momentum scale and resolution are estimated in the same way as described in section 8.9. The effect this has on the $m_{\ell\ell jj}$ and $m_{\ell\ell J}$ distributions and the signal acceptance is summarised in table 9.9.

9.8.2 Jets

Systematic uncertainties due to the jet energy scale (JES) and jet energy resolution (JER) are obtained from reconstructed jet response MC studies which are validated with in-situ data techniques [147]. The JES systematic uncertainty is derived using previous measurements of the 2010 JES uncertainty in the central region and the 2011 JES uncertainty taking into account pile-up, uniformity of the calorimeter response and special event topologies with close-by jets. The 2010 JES uncertainty is determined from the jet response in MC samples with different hadronic shower models or detector material conditions and from MC comparison to in-situ test-beam data. The pile-up correction is applied by default in the JES calibration to the $N_{\mathrm{PV}} = 1$ and $\mu = 0$ reference point. The JES uncertainty is applied simultaneously to all selected jets. The JER systematic uncertainty is determined from a combination of two different in-situ techniques: the dijet balance method and the bi-sector method, which are found to agree within 2% [212]. The signal acceptance uncertainty varies between 1 and 5% due to the JES uncertainty depending on the resonance mass[6], while the effect of the JER uncertainty is generally less than 1%. The mean and RMS of the $m_{\ell\ell jj}$ and $m_{\ell\ell j}$ signal peaks vary within 1-2% and 1-3% ($< 1\%$ and 1-2%) due to the JES (JER) uncertainty, respectively.

In the merged region, a cut on the leading jet mass is made and so a separate systematic uncertainty must be assigned to the jet mass as it contains additional information on the distribution of the jet constituents in the calorimeter. The jet mass scale (JMS) uncertainty is evaluated by data/MC comparisons of the jet mass measured in the calorimeter and the ID. The latter makes use of track jets, which will be explained below. The jet mass resolution (JMR) uncertainty is determined by comparing MC samples from different generators and simulation conditions. The methods are now described in detail.

[6] The variation becoming larger for smaller resonance masses.

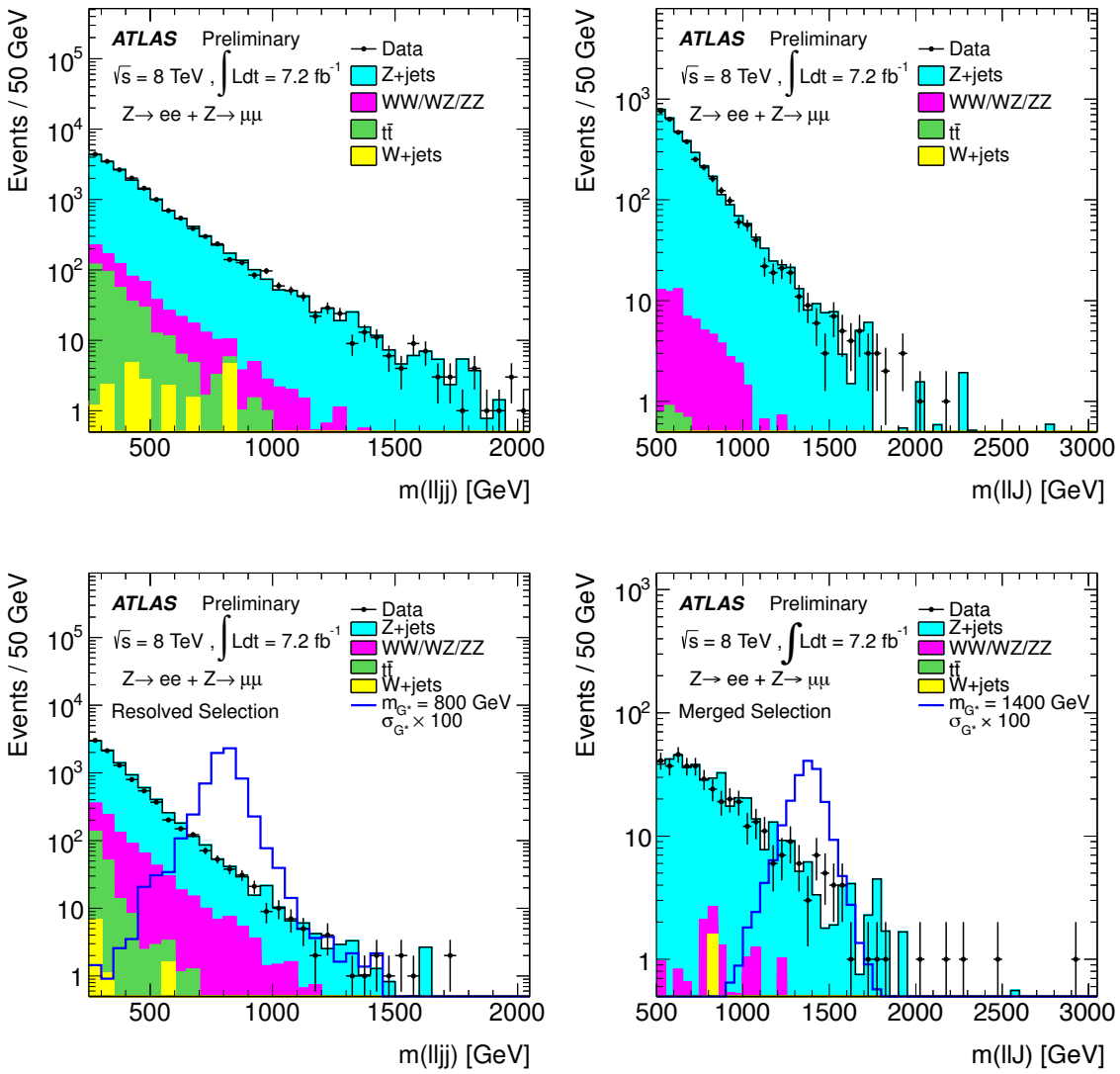

Figure 9.12: Data and MC comparison of the reconstructed $m_{\ell\ell jj}$ and $m_{\ell\ell J}$ distributions in the resolved (left) and merged (right) control (top) and signal (bottom) regions for the combined electron and muon channels.

The JMS uncertainty study uses 5.8 fb^{-1} of 8 TeV data and inclusive jet samples simulated with Pythia and the CT10 PDF set[7]. The study uses anti-k_T $R = 0.4$ EM+JES calibrated jets reconstructed as described in section 7.5. Track jets are reconstructed by running the jet algorithm on tracks reconstructed from the primary vertex. The data are collected with four single jet triggers listed in table 9.7. Double-counting is avoided by using $>$ 99% efficient, non-overlapping p_T ranges for each trigger which are also listed in table 9.7 [213]. Events must contain at least one primary vertex with at least five associated tracks, no "looser

Trigger	jet p_T range [GeV]
EF_j145_a4tchad	$185 \leq p_T < 240$
EF_j180_a4tchad	$240 \leq p_T < 300$
EF_j220_a4tchad	$300 \leq p_T < 480$
EF_j360_a4tchad	$p_T \geq 480$

Table 9.7: Trigger chains and jet p_T ranges used for the JMS uncertainty study.

bad" jets and at least two jets with $|\text{JVF}| > 0.5$. Tracks used for track jet reconstruction must have a p_T larger than 500 MeV, $|\eta| < 2.5$ and at least one (six) hits in the pixel (SCT) detector. The transverse and longitudinal impact parameters of the tracks must satisfy $|d_0| < 1.5$ mm and $|z_0 \sin\theta| < 1.5$ mm, respectively. The track jets are required to have $p_T > 10$ GeV and must be composed of at least two tracks. A match between calorimeter and track jets is then searched for within $\Delta R = 0.4$. Figure 9.13 (9.14) shows the calorimeter to track jet mass ratio as a function of calorimeter jet p_T (mass) in bins of calorimeter jet mass (p_T) for $R = 0.4$ EM+JES jets. The bottom panel shows the double data to MC ratio which is stable within 15% across the considered jet p_T and mass ranges except at very high p_T or mass values where statistical fluctuations dominate. A flat 15% JMS uncertainty is used and propagated as a $\pm 1\sigma$ shift to the final $m_{\ell\ell J}$ spectrum. The effect on the signal acceptance in the merged region is 1-5%.

The JMR uncertainty was previously studied in 7 TeV MC studies comparing the JMR of a nominal Pythia dijet sample with the MRST LO* PDF set to the following inclusive dijet samples with different event generators and detector material modelling

- Pythia with extra global dead material,
- POWHEG + Pythia,
- Herwig++ with ATLAS MC11 AUET2 LO** tune and MRST LO* PDF set,
- Pythia with Perugia 2011 tune.

The JMR is obtained from the standard deviation of a Gaussian fit to the calorimeter to track jet mass ratio. Figure 9.15 shows the JMR as a function of truth jet p_T (mass) in bins of truth jet mass (p_T) for EM+JES calibrated $R = 0.4$ anti-k_T jets. The overall JMR variation relative to the nominal sample is typically less than 10% for the p_T and mass ranges relevant in this

[7] The MCID numbers for these samples are 147912-147917.

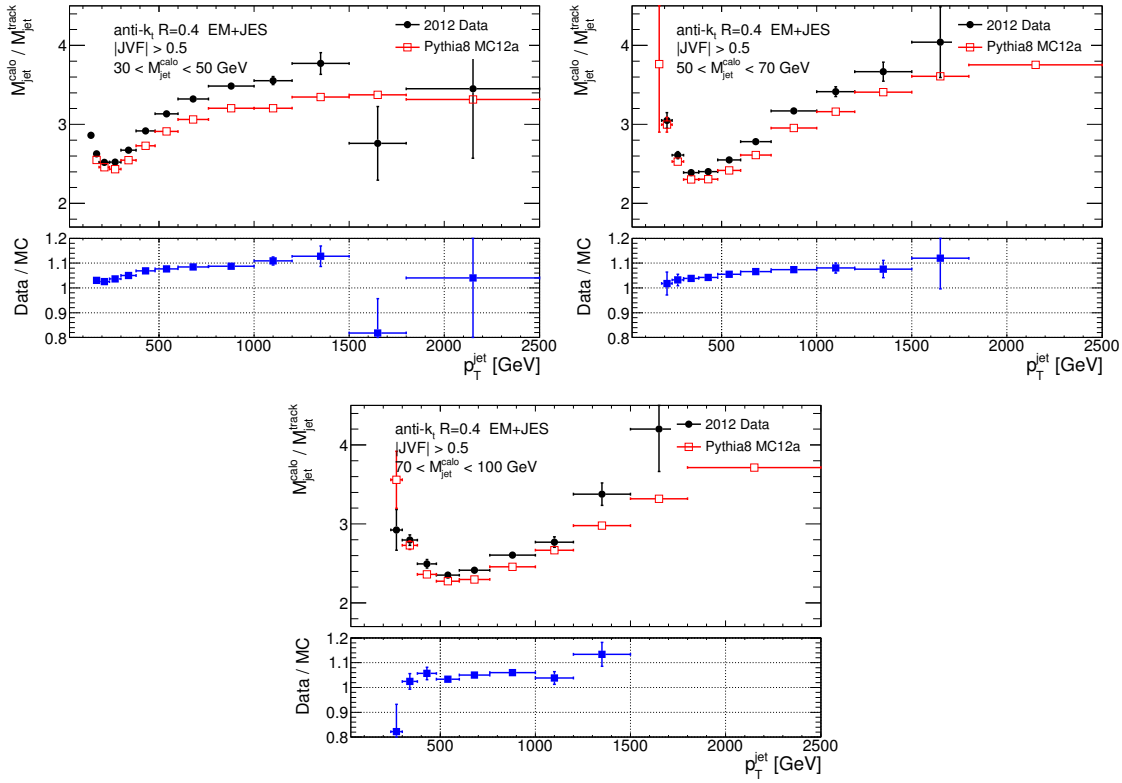

Figure 9.13: Data/MC comparison for the calorimeter to track jet mass ratio as a function of calorimeter jet p_{T} for $R = 0.4$ anti-k_{T} EM+JES calibrated jets in bins of calorimeter jet mass for 30-50 GeV (top right), 50-70 GeV (top right) and 70-100 GeV (bottom).

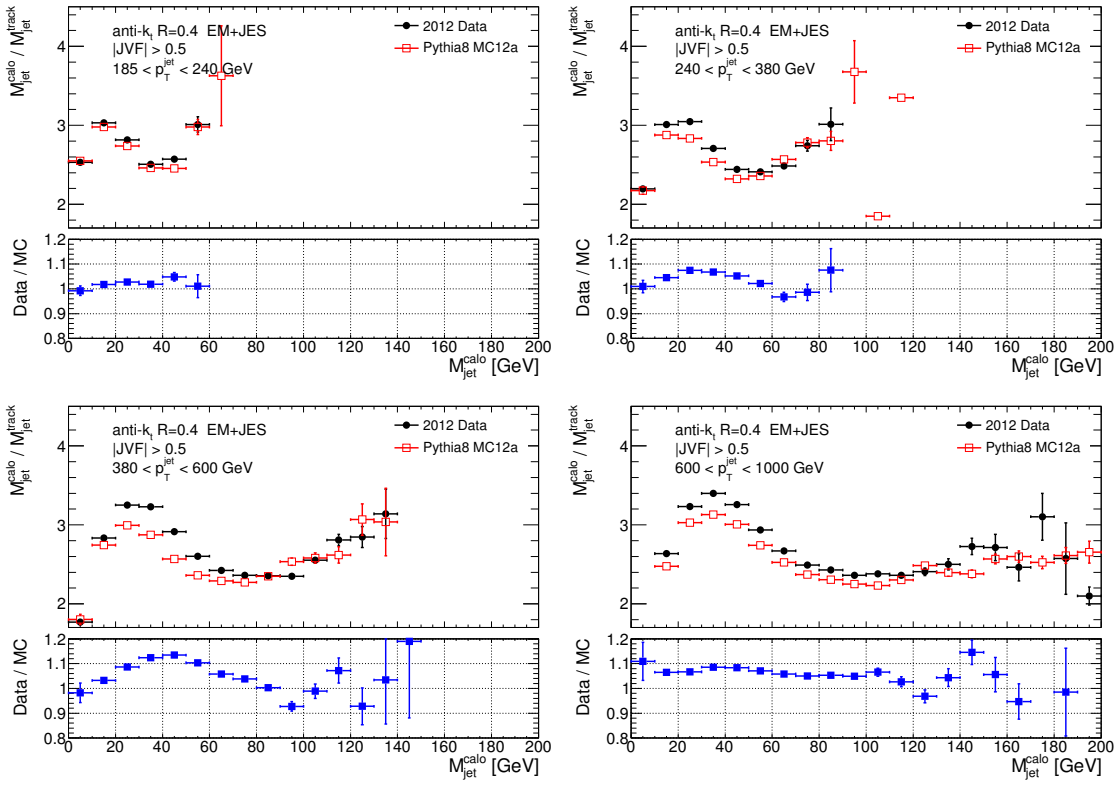

Figure 9.14: Data/MC comparison for the calorimeter to track jet mass ratio as a function of calorimeter jet mass for $R = 0.4$ anti-k_T EM+JES calibrated jets in bins of calorimeter jet p_T for 185-240 GeV (top left), 240-380 GeV (top right), 380-600 GeV (bottom left) and 600-1000 GeV (bottom right).

analysis. A more conservative 20% JMR uncertainty is used in this analysis and propagated to the $m_{\ell\ell J}$ distribution as these checks have not been repeated for 8 TeV MC samples. The overall effect on the signal acceptance is less than 1%.

9.8.3 Theoretical

Systematic uncertainties on the signal acceptance related to PDF sets are evaluated using the same method as described in section 8.9.4 but using the CTEQ6L1 and MSTW2008lo68cl sets, respectively. The systematic PDF uncertainty is found to only mildly depend on the graviton signal mass and is averaged to 2% for the resolved and merged regions.

A systematic uncertainty on the signal acceptance needs to be added to account for ISR and FSR which can produce additional jets. This can change the jet multiplicity and other kinematic distributions and potentially lead to the wrong jet being associated to the Z boson decay. The effect is checked by producing signal samples with varied ISR/FSR parameter settings in Pythia and measuring the relative signal acceptance variation. The nominal ISR/FSR parameters are varied so as to simultaneously increase or decrease the amount of ISR and FSR. Table 9.8 shows the relevant Pythia parameters and the values used in each sample. The largest relative acceptance variation is found to be about 10% for the graviton masses between 200 and 1500 GeV. No significant difference is seen between the resolved and merged selections. A flat 10% uncertainty is assigned to all signal mass samples used in this analysis.

Parameter	PARP(67)	PARP(64)	PARP(72)	PARJ(82)
Nominal	4.0	1.0	0.192	1.0
ISR/FSR up	6.0	0.25	0.384	0.5
ISR/FSR down	0.5	4.0	0.096	2.0

Table 9.8: ISR/FSR parameter settings used in Pythia.

9.8.4 Summary

Systematic uncertainties on the background estimation in the signal region will be described in the next section. Systematic uncertainties on the signal acceptance are taken into account for the sensitivity and limit calculations. The relative uncertainties from the different sources are summarised in table 9.9. The overall uncertainty on the signal acceptance is approximately 11-15% over the 300-2000 GeV mass range.

9.9 Limit Extraction Procedure

The data in the signal region now needs to be surveyed for any signs of presence of a graviton resonance in the invariant mass spectra. This is done using the BumpHunter [214], a model-independent, frequentist hypothesis test which is sensitive to local data excesses and

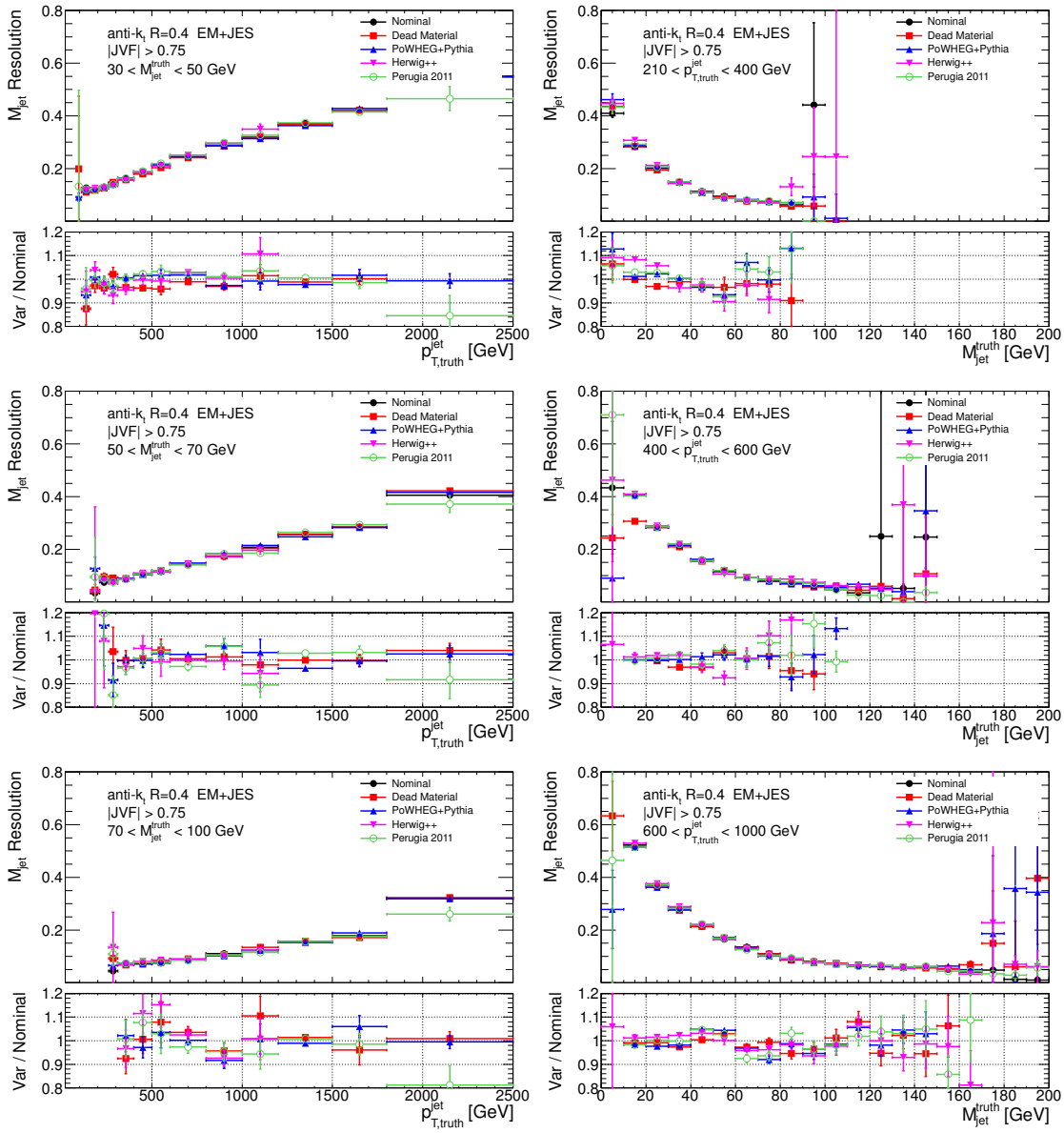

Figure 9.15: Calorimeter JMR as a function of truth jet p_{T} (left) and mass (right) for $R = 0.4$ anti-k_{T} jets calibrated with EM+JES scheme in bins of truth jet mass (p_{T}) for 30-50 GeV (210-400 GeV) (top), 50-70 GeV (400-600 GeV) (middle) and 70-100 GeV (600-1000 GeV) (bottom). The bottom panel shows the JMR ratio for various MC samples to the nominal PYTHIA sample.

Source	Resolved	Merged
Trigger	1%	1%
e reconstruction efficiency	2%	2%
e identification efficiency	2%	2%
e energy scale & resolution	1%	1%
μ reconstruction efficiency	$< 1\%$	$< 1\%$
μ p_{T} scale & resolution	$< 1\%$	$< 1\%$
Jet energy scale	$1 - 5\%$	$\sim 1\%$
Jet energy resolution	$< 1\%$	$1 - 2\%$
Jet mass scale	/	$1 - 5\%$
Jet mass resolution	/	$< 1\%$
PDF	2%	2%
ISR/FSR	10%	10%
Luminosity	3.6%	3.6%

Table 9.9: Summary of all relative signal acceptance uncertainties (%) in the resolved and merged regions.

which takes into account the look-elsewhere effect[8]. In particular, the level of agreement of the data with a smooth background hypothesis fit to the observed $m_{\ell\ell jj}$ and $m_{\ell\ell J}$ distributions is tested in the resolved and merged channels, respectively.

The exact functional form chosen to describe a smooth background hypothesis against which the data are tested has been used in several previous analyses [215–218] and is given by

$$f(m; p_{0,1,2,3}) = p_0 \frac{(1-x)^{p_1}}{x^{p_2+p_3 \ln(x)}}, \tag{9.3}$$

where $x = m_{\ell\ell jj}/\sqrt{s}$ or $m_{\ell\ell J}/\sqrt{s}$ and p_i $(i = 0, 1, 2, 3)$ are four free parameters fitted to the data. The fit is performed separately for the resolved and merged signal regions using the sum of electron and muon channels. The binning of the distributions is chosen to reflect the reconstructed width of the graviton signal, which was shown in figure 9.8. The $(1-x)^{p_1}$ term is added to enforce $f(m = \sqrt{s}) = 0$, which is the edge of available kinematic phase space.

An anti-bias mechanism is put in place to make sure that the background fit does not absorb a significant signal, if present, thereby biasing the background shape. An initial χ^2 fit is first performed over the whole spectrum. If the p-value[9] of this fit has a probability of less than 1%, then the fit is redone multiple times while iteratively removing various mass windows from the fit until the sidebands are fitted well. The mass windows are chosen such that they are consistent with the width of the signal for which the search is performed. If a p-value of at least 0.01 cannot be achieved, the window which maximises the χ^2 probability is excluded, even if the latter is less than 1%. This is then taken as the background expectation.

[8] This is equivalent to saying that the BumpHunter looks for an excess at different resonance mass points without any prior bias.

[9] The probability that the background would fluctuate to give at least one excess at least as significant as the most significant excess observed in data in any of the considered mass windows.

It should be noted that this procedure was not needed in the initial fit to the actual data used in this analysis.

The left column of figure 9.16 shows that the function is capable of fitting the SM MC background prediction. The systematic uncertainty on the background estimation is estimated using pseudo-experiments in which the nominal fit to the $m_{\ell\ell jj}$ or $m_{\ell\ell J}$ distributions is randomly Poisson fluctuated in each bin. The resulting distribution is then re-fit using equation 9.3 and the corresponding log-likelihood is calculated. The uncertainty from these pseudo-experiments, shown in the right column of figure 9.16, is maximally 5% in the considered region of the $m_{\ell\ell jj}$ distribution and can vary from 10-40% across the considered region of the $m_{\ell\ell J}$ distribution.

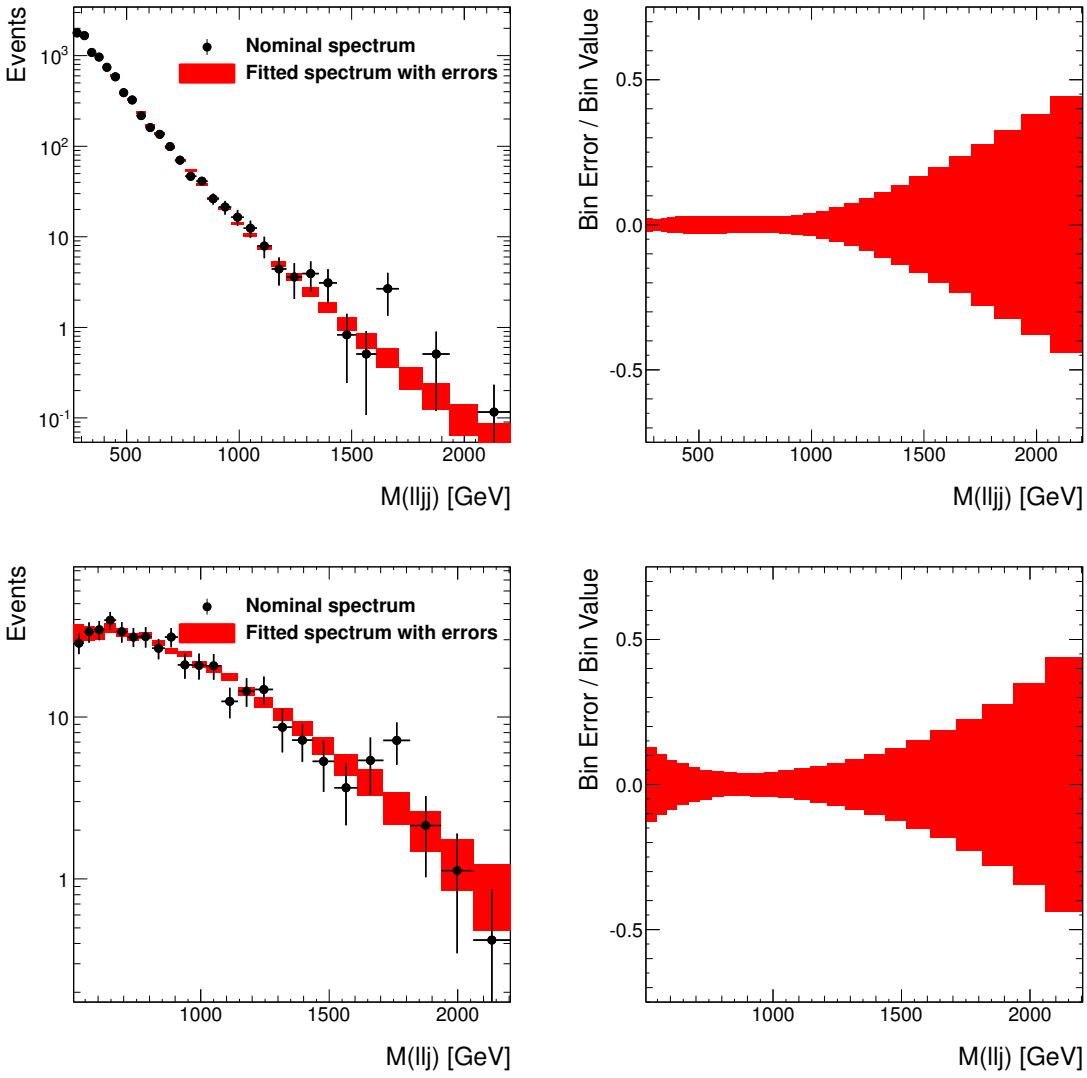

Figure 9.16: Fit to MC background prediction for the combined electron and muon channels with the estimated systematic uncertainty (left) and associated relative estimated systematic uncertainties (right) for the resolved (top) and merged (bottom) regions.

If no signal is found, limits are set on the production rate of a range of graviton masses, assuming the signal would be added to the background estimation described in the previous step. Upper limits are derived based on Bayes' theorem. Signal templates at the various graviton mass points are used and express the expected number of signal events after full event selection. Each template is normalised to a total area s, where s is the unknown parameter of interest on which the limit is set, in this case the cross section. The upper limit at a 95% credibility level (C.L.) on s is the 95% quantile of $p(s|\mathbf{D})$, where $\mathbf{D}$ is the data. In other words, the value x for which

$$\int_{-\infty}^{x} p(s|\mathbf{D})\, \mathrm{d}s = 0.95. \tag{9.4}$$

The prior is assumed to be flat for $s \geq 0$ and null for $s < 0$. The latter expresses the assumption that the graviton cross section is not negative. This ensures that the posterior will always be null at $s < 0$ and the upper limit on s is bound to be positive. This prevents the Bayesian limits from excluding the no-signal hypothesis due to a downward fluctuation of the data. The method is parameterised by three Gaussian nuisance parameters. One nuisance parameter for the signal shape and normalisation changes, respectively, as discussed in section 9.8 and one for the background fit. The latter shifts the background in all bins coherently by equal fractions of the standard deviation[10] corresponding to each bin.

The result from the main background estimation and limit setting procedure, shown in figure 9.19, is cross-checked using the RooStats [219] package, which uses a binned maximum-likelihood fit. The fit is performed to $m_{\ell\ell jj}$ and $m_{\ell\ell J}$ MC histogram templates obtained for the combination of the mutually exclusive[11] resolved and merged regions in the combined electron and muon channels. For each fit, signal, Z+jets, top (all from MC) and QCD multijet backgrounds components are included. The fit ranges from 300-2000 GeV in bins of 50 GeV. Nuisance parameters include a 20% systematic uncertainty on the background normalisation with a shape uncertainty taken from varying the JES by $\pm 1\sigma$ and a conservative 30% systematic uncertainty on the signal normalisation. The RooStats result is shown in figure 9.17, which can be compared to figure 9.19.

9.10 Results

The data and fitted background distributions for the final $m_{\ell\ell jj}$ and $m_{\ell\ell J}$ invariant mass spectra, after all resolved and merged signal region selection cuts have been applied, are shown in figure 9.18. The BumpHunter algorithm test for the presence of a spin-2 bulk RS graviton resonance returns no signal feature and the data are consistent with a smoothly falling background distribution. This can be seen from the local deviation of the data from the background expectation shown in the bottom panels of figure 9.18 and taking into account statistical uncertainties only.

[10] These are estimated by Poisson fluctuating the observed data and fitting many different resulting pseudo-spectra so that the standard deviation of each bin can be recorded.

[11] Here, if an event is found in the merged selection, it is vetoed in the resolved selection.

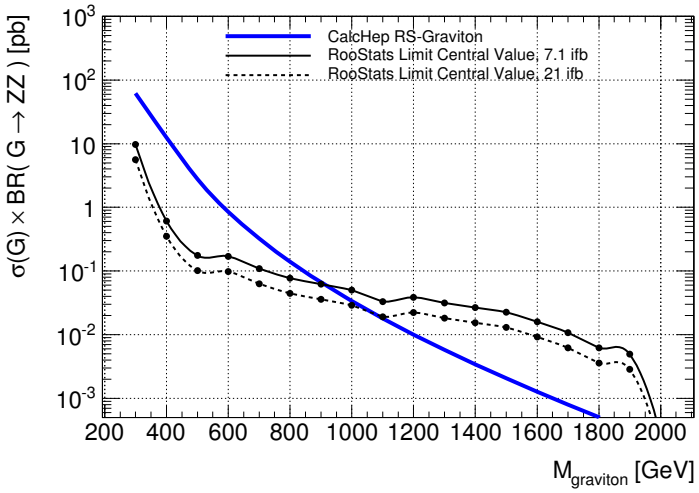

Figure 9.17: Cross-check of limits using RooStats.

Since no significant signal is observed, the result is interpreted within the context of the previously mentioned benchmark model to set Bayesian limits on $\sigma(pp \to G^*) \times \mathrm{BR}(\mathrm{G}^* \to \mathrm{ZZ})$ as described in section 9.9. The limits for the resolved and merged signal selections are combined by taking the resolved selection for masses below 1000 GeV and the merged selection above, based on the better expected limit in each mass region and assuming that m_{G^*} can be reconstructed through $m_{\ell\ell jj}$ or $m_{\ell\ell J}$, respectively. The observed and expected 95% C.L. upper limits, calculated for signal mass points between 300 GeV and 2 TeV, are listed in table 9.10 and shown as a smooth interpolation between discrete mass points in figure 9.19. The LO theoretical prediction for the bulk RS model is overlaid in the latter. The inner and outer bands on the expected limit represent $\pm 1\sigma$ and $\pm 2\sigma$ variations, respectively. The limits can be translated into observed and expected 95% C.L. lower limits on the bulk RS Graviton mass, assuming a coupling $\kappa/\bar{m}_{\mathrm{Planck}} = 1.0$, of 850 and 870 GeV, respectively.

Figure 9.20 shows an event display of a representative candidate event recorded in the merged muon channel. The value of the reconstructed three-body invariant mass is $m_{\mu\mu J} = 2.9$ TeV.

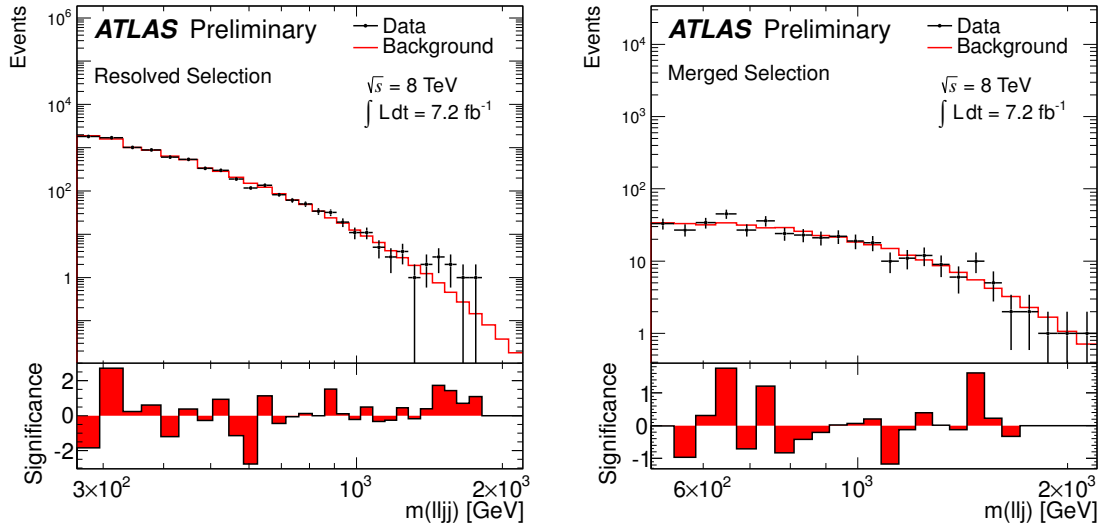

Figure 9.18: The reconstructed $m_{\ell\ell jj}$ and $m_{\ell\ell J}$ distributions in the resolved (left) and merged (right) signal regions for the combined electron and muon channels. The data and the smoothly falling background fit are shown.

m_{G^*} [GeV]	Observed limit [pb]	Expected limit [pb]
300	1.860	1.353
400	0.338	0.498
500	0.238	0.272
600	0.075	0.168
700	0.085	0.112
800	0.088	0.086
900	0.098	0.080
1000	0.088	0.092
1100	0.044	0.063
1200	0.039	0.049
1300	0.041	0.042
1400	0.041	0.037
1500	0.042	0.032
1600	0.030	0.028
1700	0.021	0.025
1800	0.019	0.024
1900	0.020	0.025
2000	0.022	0.027

Table 9.10: Observed and expected 95% C.L. upper limits on $\sigma(pp \to G^*) \times \mathrm{BR}(G^* \to ZZ)$ for the bulk RS graviton with a coupling of $\kappa/\bar{m}_{\mathrm{Planck}} = 1.0$.

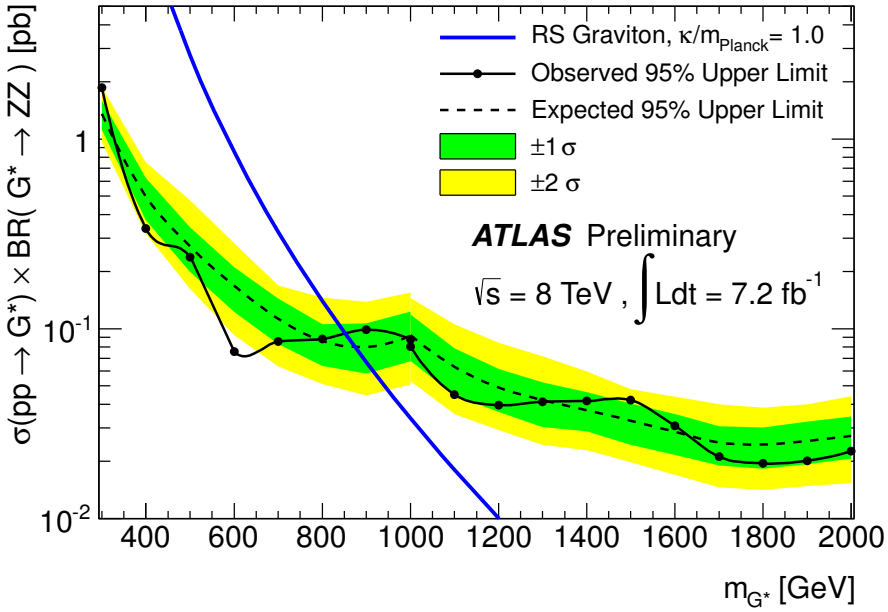

Figure 9.19: Observed and expected 95% C.L. upper limits on $\sigma(pp \to G^*) \times \mathrm{BR}(G^* \to ZZ)$ for the bulk RS graviton with a coupling of $\kappa/\bar{m}_{\mathrm{Planck}} = 1.0$.

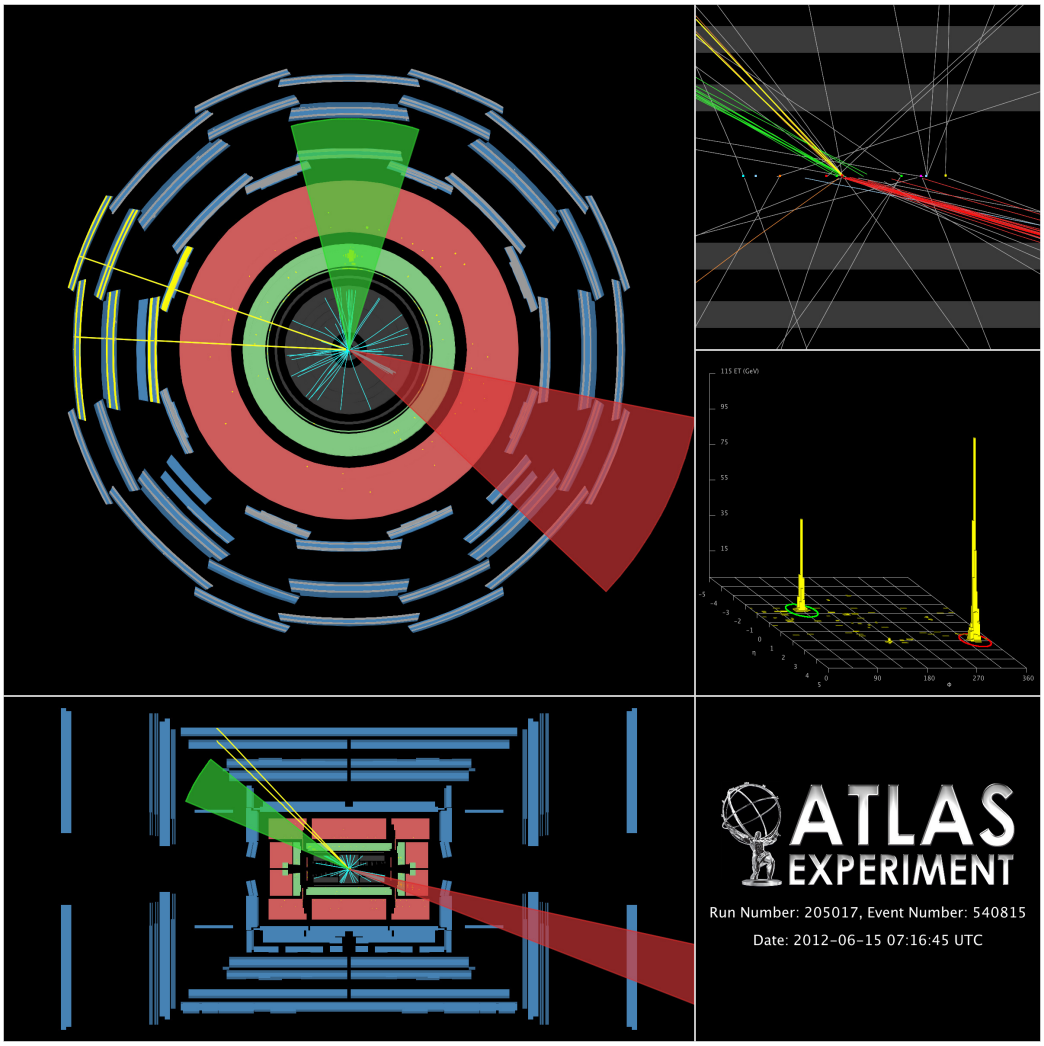

Figure 9.20: Event display of a high-mass candidate event from the merged muon channel. The two muons are shown in yellow and the leading jet as a red cone. It should be noted that the leading jet in this event, shown as the larger cone, is reconstructed in the end cap of the hadronic calorimeter and therefore the energy deposits are not visible in the top left (x,y) view but can be seen in the bottom left and middle right views.

Chapter 10

Conclusion

In this thesis, diboson production has been discussed from three different angles. A phenomenological study of anomalous triple gauge boson couplings for diboson production, a measurement of $W^{\pm}Z$ production and a search for heavy resonances decaying into a pair of Z bosons have been presented. The two experimental results use proton-proton collision data produced at centre of mass energies of $\sqrt{s} = 7$ TeV and $\sqrt{s} = 8$ TeV, respectively, collected with the ATLAS detector at the LHC.

The underlying structure of anomalous triple gauge boson couplings for charged vertices within an effective Lagrangian framework has been studied and their leading order implementation into the Herwig++ event generator has been described. One-loop corrections for massive diboson production in the presence of aTGCs have been calculated and the $\mathcal{O}(\alpha_s)$ realization using the POWHEG method, based on the SM case [82], has been outlined. The impact of aTGC parameters on the production cross section and several kinematic variables for proton-proton collisions at LHC energies have been studied. It has been shown that aTGCs become important in the same phase space regions as next-to-leading order QCD corrections. It is therefore vital to include these corrections to get a precise test for aTGCs. An alternative implementation within the `POWHEG BOX` framework has since become available [84].

A measurement of $W^{\pm}Z$ production has been published using a dataset of 4.6 fb^{-1} produced at $\sqrt{s} = 7$ TeV [151]. Fiducial and total $W^{\pm}Z$ production cross sections have been measured using $W^{\pm}Z$ candidate events with fully leptonic final states containing at least three leptons, electrons or muons, and large missing transverse momentum. A total of 317 $W^{\pm}Z$ candidate events are observed while 68 ± 10 background events are expected. The fiducial[1] and total $W^{\pm}Z$ production cross sections are measured to be

$$\sigma_{WZ}^{\text{fid}} = 92^{+7}_{-6}(\text{stat}) \pm 4(\text{syst}) \pm 2(\text{lumi}) \text{ fb}$$

and

$$\sigma_{WZ}^{\text{tot}} = 19.0^{+1.4}_{-1.3}(\text{stat}) \pm 0.9(\text{syst}) \pm 0.4(\text{lumi}) \text{ pb}$$

respectively. For the first time using LHC data, normalised differential fiducial cross sections are measured, using an iterative Bayesian unfolding technique, as a function of p_{T}^{Z} and m_{WZ}.

[1] The cuts for the fiducial phase space are defined in section 8.11.1.

The measurements are dominated by statistical uncertainties and are in agreement with NLO SM predictions. Limits on anomalous triple gauge couplings are extracted, with and without a form factor, in one and two dimensions using the observed p_{T}^{Z} spectrum. The 95% confidence intervals without a form factor are determined to be

$$\begin{aligned} \Delta g_1^Z &\in [-0.057, 0.093], \\ \Delta\kappa^Z &\in [-0.37, 0.57], \\ \lambda^Z &\in [-0.046, 0.047]. \end{aligned}$$

The limits supersede an earlier ATLAS measurement [92] and represent the most constraining result to date using the $W^{\pm}Z \to \ell^{\pm}\nu\ell^{+}\ell^{-}$ channel only.

A second measurement has been presented that searches for resonant ZZ diboson production in the dilepton, electron or muon, plus one or two jet decay channels and uses 7.2 fb^{-1} of $\sqrt{s} = 8$ TeV data [196]. The signal sensitivity is optimised by exploiting resolved and merged topologies. No features indicating a new resonance are observed in the four-body $m_{\ell\ell jj}$ or three-body $m_{\ell\ell J}$ data distributions. Upper limits at the 95% C.L. are set, using a Bayesian technique, for the bulk Randall-Sundrum graviton model with a coupling parameter equal to $\kappa/\bar{m}_{\mathrm{Planck}} = 1.0$. The cross section limits on $\sigma(pp \to G^*) \times \mathrm{BR}(G^* \to ZZ)$ range from 1.86 pb to 22 fb for graviton masses of 300 GeV to 2.0 TeV, respectively. These limits are translated into 95% C.L. observed and expected lower graviton mass limits of 850 GeV and 870 GeV, respectively.

Looking forward, both of the experimental analyses presented here will benefit greatly from increased centre of mass energies at the LHC. An ATLAS measurement of the $W^{\pm}Z$ production cross section at $\sqrt{s} = 8$ TeV has already been performed using 12.8 fb^{-1} of data and is now dominated by systematic uncertainties [220]. As the diboson cross section is proportional to the square of aTGC parameters, the statistical sensitivity for aTGC limits will only improve as $\sqrt[4]{\mathcal{L}}$. The more important factor for higher sensitivity will be the increase in centre of mass energy and a precision down to $\mathcal{O}(10^{-3})$ is foreseen for $\sqrt{s} = 14$ TeV [62]. More stringent limits are expected using $\ell\nu jj$ final states due to the higher branching ratio and mixing of $W^{+}W^{-}$ and $W^{\pm}Z$ contributions, which will increase the sensitivity to $\Delta\kappa^Z$. The graviton search allows to readily test further benchmark models, such as Technicolor, extended Higgs sectors or extra vector boson models, and serves as a basis for future studies involving jet substructure and boosted techniques that can help discover possible new resonances at so far unexplored energies.

Bibliography

[1] ATLAS Collaboration, G. Aad et al., *Observation of a new particle in the search for the Standard Model Higgs boson with the ATLAS detector at the LHC*, Phys.Lett. **B716** (2012) 1–29, arXiv:1207.7214 [hep-ex].

[2] CMS Collaboration, S. Chatrchyan et al., *Observation of a new boson at a mass of 125 GeV with the CMS experiment at the LHC*, Phys.Lett. **B716** (2012) 30–61, arXiv:1207.7235 [hep-ex].

[3] D. Griffiths, *Introduction to Elementary Particles*. Wiley-VCH, 2004.

[4] J. Chadwick, *Possible Existence of a Neutron*, Nature **129** (Feb, 1932) 312. http://www.nature.com/nature/journal/v129/n3252/pdf/129312a0.pdf.

[5] A. H. Compton, *A Quantum Theory of the Scattering of X-rays by Light Elements*, Phys. Rev. **21** (May, 1923) 483–502. http://link.aps.org/doi/10.1103/PhysRev.21.483.

[6] C. M. G. Lattes, H. Muirhead, G. P. S. Occhialini and C. F. Powell, *Processes Involving Charged Mesons*, Nature **159** (May, 1947) 694–697. http://www.nature.com/nature/journal/v159/n4047/abs/159694a0.html.

[7] P. A. M. Dirac, *Quantised Singularities in the Electromagnetic Field*, Proceedings of the Royal Society of London. Series A **133** (1931) no. 821, 60–72. http://rspa.royalsocietypublishing.org/content/133/821/60.short.

[8] C. D. Anderson, *Early Work on the Positron and Muon*, American Journal of Physics **29** (1961) no. 12, 825–830. http://link.aip.org/link/?AJP/29/825/1.

[9] C. D. Anderson, *The Positive Electron*, Phys. Rev. **43** (Mar, 1933) 491–494. http://link.aps.org/doi/10.1103/PhysRev.43.491.

[10] O. Chamberlain, E. Segrè, C. Wiegand, and T. Ypsilantis, *Observation of Antiprotons*, Phys. Rev. **100** (Nov, 1955) 947–950. http://link.aps.org/doi/10.1103/PhysRev.100.947.

[11] B. Cork, G. R. Lambertson, O. Piccioni, and W. A. Wenzel, *Antineutrons Produced from Antiprotons in Charge-Exchange Collisions*, Phys. Rev. **104** (Nov, 1956) 1193–1197. http://link.aps.org/doi/10.1103/PhysRev.104.1193.

[12] C. L. Cowan, F. Reines, F. B. Harrison, H. W. Kruse, and A. D. McGuire, *Detection of the Free Neutrino: a Confirmation*, Science **124** (1956) no. 3212, 103–104. http://www.sciencemag.org/content/124/3212/103.short.

[13] G. D. Rochester, C. C. Butler, *Evidence for the Existence of New Unstable Elementary Particles*, Nature **160** (1947) 855–857.

[14] F. Halzen and A. D. Martin, *Quarks & Leptons: An Introductory Course in Modern Particle Physics*. John Wiley & Sons, Inc., 1984.

[15] O. W. Greenberg, *Spin and Unitary-Spin Independence in a Paraquark Model of Baryons and Mesons*, Phys. Rev. Lett. **13** (Nov, 1964) 598–602. http://link.aps.org/doi/10.1103/PhysRevLett.13.598.

[16] R. K. Ellis, W. J. Stirling and B. R. Webber, *QCD and Collider Physics*. Cambridge University Press, 2003.

[17] J. J. Aubert et al., *Experimental Observation of a Heavy Particle J*, Phys. Rev. Lett. **33** (Dec, 1974) 1404–1406. http://link.aps.org/doi/10.1103/PhysRevLett.33.1404.

[18] J. E. Augustin et al., *Discovery of a Narrow Resonance in e^+e^- Annihilation*, Phys. Rev. Lett. **33** (Dec, 1974) 1406–1408. http://link.aps.org/doi/10.1103/PhysRevLett.33.1406.

[19] B. J. Bjørken and S. L. Glashow, *Elementary particles and SU(4)*, Physics Letters **11** (Aug, 1964) 255–257.

[20] S. L. Glashow, J. Iliopoulos, and L. Maiani, *Weak Interactions with Lepton-Hadron Symmetry*, Phys. Rev. D **2** (Oct, 1970) 1285–1292. http://link.aps.org/doi/10.1103/PhysRevD.2.1285.

[21] M. L. Perl et al., *Evidence for Anomalous Lepton Production in e^+e^- Annihilation*, Phys. Rev. Lett. **35** (Dec, 1975) 1489–1492. http://link.aps.org/doi/10.1103/PhysRevLett.35.1489.

[22] J. A. Appel et al., *Observation of a Dimuon Resonance at 9.5 GeV in 400-GeV Proton-Nucleus Collisions*, Phys. Rev. Lett. **39** (Aug, 1977) 252–255. http://link.aps.org/doi/10.1103/PhysRevLett.39.252.

[23] CDF Collaboration, F. Abe et al., *Observation of Top Quark Production in $p\bar{p}$ Collisions with the Collider Detector at Fermilab*, Phys. Rev. Lett. **74** (Apr, 1995) 2626–2631. http://link.aps.org/doi/10.1103/PhysRevLett.74.2626.

[24] D0 Collaboration, S. Abachi and others., *Search for High Mass Top Quark Production in $p\bar{p}$ Collisions at $\sqrt{s} = 1.8$ TeV*, Phys. Rev. Lett. **74** (Mar, 1995) 2422–2426. http://link.aps.org/doi/10.1103/PhysRevLett.74.2422.

[25] P. W. Higgs, *Broken Symmetries and the Masses of Gauge Bosons*, Phys. Rev. Lett. **13** (Oct, 1964) 508–509. http://link.aps.org/doi/10.1103/PhysRevLett.13.508.

[26] F. Englert and R. Brout, *Broken Symmetry and the Mass of Gauge Vector Mesons*, Phys. Rev. Lett. **13** (Aug, 1964) 321–323. http://link.aps.org/doi/10.1103/PhysRevLett.13.321.

[27] G. S. Guralnik, C. R. Hagen, and T. W. B. Kibble, *Global Conservation Laws and Massless Particles*, Phys. Rev. Lett. **13** (Nov, 1964) 585–587. http://link.aps.org/doi/10.1103/PhysRevLett.13.585.

[28] S. L. Glashow, *Partial-symmetries of weak interactions*, Nuclear Physics **22** (1961) no. 4, 579 – 588. http://www.sciencedirect.com/science/article/pii/0029558261904692.

[29] A. Salam and J. C. Ward, *Electromagnetic and weak interactions*, Physics Letters **13** (Nov, 1964) 168–171.

[30] S. Weinberg, *A Model of Leptons*, Phys. Rev. Lett. **19** (Nov, 1967) 1264–1266. http://link.aps.org/doi/10.1103/PhysRevLett.19.1264.

[31] G. Arnison et al., *Experimental observation of isolated large transverse energy electrons with associated missing energy at s=540 GeV*, Physics Letters B **122** (1983) no. 1, 103 – 116. http://www.sciencedirect.com/science/article/pii/0370269383911772.

[32] J. Beringer et al. (Particle Data Group), *The Review of Particle Physics*, Phys. Rev. D **86** (2012) 010001.

[33] CDF Collaboration, D0 Collaboration, T. Aaltonen et al., *Combination of the top-quark mass measurements from the Tevatron collider*, Phys.Rev. **D86** (2012) 092003, arXiv:1207.1069 [hep-ex].

[34] E. Otten and C. Weinheimer, *Neutrino mass limit from tritium beta decay*, Rept.Prog.Phys. **71** (2008) 086201, arXiv:0909.2104 [hep-ex].

[35] M. E. Peskin and D. V. Schroeder, *An Introduction to Quantum Field Theory*. Westview Press, 1995.

[36] A. Martin, W. Stirling, R. Thorne, and G. Watt, *Parton distributions for the LHC*, Eur.Phys.J. **C63** (2009) 189–285, arXiv:0901.0002 [hep-ph].

[37] G. Gounaris and C. G. Papadopoulos, *Studying trilinear gauge couplings at Next Linear Collider*, Eur.Phys.J. **C2** (1998) 365–372, arXiv:9612378 [hep-ph].

[38] A. Denner, S. Heinemeyer, I. Puljak, D. Rebuzzi, and M. Spira, *Standard Model Higgs-Boson Branching Ratios with Uncertainties*, Eur.Phys.J. **C71** (2011) 1753, arXiv:1107.5909 [hep-ph].

[39] J. F. Gunion, S. Dawson, H. E. Haber, and G. L. Kane, *The Higgs hunter's guide*. Frontiers in Physics. Westview, Boulder, CO, 1990.

[40] E. Asakawa and S. Kanemura, *The vertex and single charged Higgs boson production via WZ fusion at the Large Hadron Collider*, Physics Letters B **626** (2005) no. 14, 111 – 119. http://www.sciencedirect.com/science/article/pii/S0370269305011482.

[41] M. S. Chanowitz and W. B. Kilgore, *W^+Z and $W^+\gamma^*$ backgrounds to strong W^+W^+ scattering at the LHC*, Phys.Lett. **B347** (1995) 387–393, arXiv:hep-ph/9412275 [hep-ph].

[42] J. Butterworth, B. Cox, and J. R. Forshaw, *WW scattering at the CERN LHC*, Phys.Rev. **D65** (2002) 096014, arXiv:hep-ph/0201098 [hep-ph].

[43] H. Baer, M. Drees, F. Paige, P. Quintana, and X. Tata, *Trilepton signal for supersymmetry at the Fermilab Tevatron revisited*, Phys.Rev. **D61** (2000) 095007, arXiv:hep-ph/9906233 [hep-ph].

[44] K. Lane and E. Eichten, *Two-scale technicolor*, Physics Letters B **222** (1989) no. 2, 274 – 280. http://www.sciencedirect.com/science/article/pii/0370269389912653.

[45] J. C. Pati and A. Salam, *Lepton number as the fourth "color"*, Phys. Rev. D **10** (Jul, 1974) 275–289. http://link.aps.org/doi/10.1103/PhysRevD.10.275.

[46] K. Agashe, H. Davoudiasl, G. Perez, and A. Soni, *Warped Gravitons at the LHC and Beyond*, Phys.Rev. **D76** (2007) 036006, arXiv:hep-ph/0701186 [hep-ph].

[47] J. Ellison and J. Wudka, *Study of trilinear gauge boson couplings at the Tevatron collider*, Ann.Rev.Nucl.Part.Sci. **48** (1998) 33–80, arXiv:hep-ph/9804322 [hep-ph].

[48] ATLAS Collaboration, G. Aad et al., *Measurement of ZZ production in pp collisions at $\sqrt{s} = 7$ TeV and limits on anomalous ZZZ and $ZZ\gamma$ couplings with the ATLAS detector*, arXiv:1211.6096 [hep-ex].

[49] O. Eboli, M. Gonzalez-Garcia, and S. Lietti, *Bosonic quartic couplings at CERN LHC*, Phys.Rev. **D69** (2004) 095005, arXiv:hep-ph/0310141 [hep-ph].

[50] S. Godfrey, *Quartic gauge boson couplings*, arXiv:hep-ph/9505252 [hep-ph].

[51] P. Bell, *Quartic Gauge Couplings and the Radiation Zero in $pp \to \ell^\pm \nu\gamma\gamma$ events at the LHC*, Eur.Phys.J. **C64** (2009) 25–33, arXiv:0907.5299 [hep-ph].

[52] M. K. Gaillard, P. D. Grannis, and F. J. Sciulli, *The Standard model of particle physics*, Rev.Mod.Phys. **71** (1999) S96–S111, arXiv:hep-ph/9812285 [hep-ph].

[53] S. Weinberg, *What is quantum field theory, and what did we think it is?*, arXiv:hep-th/9702027 [hep-th].

[54] K. Hagiwara, R. Peccei, D. Zeppenfeld, and K. Hikasa, *Probing the weak boson sector in $e^+e^- \to W^+W^-$*, Nuclear Physics B **282** (1987) no. 0, 253 – 307. http://www.sciencedirect.com/science/article/pii/0550321387906857.

[55] Z. Ajaltouni et al., *Triple gauge boson couplings*, arXiv:hep-ph/9601233 [hep-ph].

[56] W. J. Marciano and A. Queijeiro, *Bound on the W-boson electric dipole moment*, Phys. Rev. D **33** (Jun, 1986) 3449–3452. http://link.aps.org/doi/10.1103/PhysRevD.33.3449.

[57] D. Zeppenfeld, *Low-energy constraints and anomalous triple gauge boson couplings*, arXiv:hep-ph/9307333 [hep-ph].

[58] L. J. Dixon, Z. Kunszt, and A. Signer, *Vector boson pair production in hadronic collisions at order α_s : Lepton correlations and anomalous couplings*, Phys.Rev. **D60** (1999) 114037, arXiv:hep-ph/9907305 [hep-ph].

[59] D0 Collaboration, V. Abazov et al., *Measurement of the WW production cross section with dilepton final states in $p\bar{p}$ collisions at $\sqrt{s} = 1.96$ TeV and limits on anomalous trilinear gauge couplings*, Phys.Rev.Lett. **103** (2009) 191801, arXiv:0904.0673 [hep-ex].

[60] ATLAS Collaboration, G. Aad et al., *Expected Performance of the ATLAS Experiment - Detector, Trigger and Physics*, arXiv:0901.0512 [hep-ex].

[61] D. Zeppenfeld and S. Willenbrock, *Probing the three-vector-boson vertex at hadron colliders*, Phys. Rev. D **37** (Apr, 1988) 1775–1786. http://link.aps.org/doi/10.1103/PhysRevD.37.1775.

[62] H. Aihara et al., *Anomalous gauge boson interactions*, arXiv:hep-ph/9503425 [hep-ph].

[63] CDF Collaboration, T. Aaltonen et al., *Measurement of the W^+W^- Production Cross Section and Search for Anomalous $WW\gamma$ and WWZ Couplings in $p\bar{p}$ Collisions at $\sqrt{s} = 1.96$ TeV*, Phys.Rev.Lett. **104** (2010) 201801, arXiv:0912.4500 [hep-ex].

[64] U. Baur, T. Han, and J. Ohnemus, *WZ production at hadron colliders: Effects of nonstandard WWZ couplings and QCD corrections*, Phys.Rev. **D51** (1995) 3381–3407, arXiv:hep-ph/9410266 [hep-ph].

[65] G. Bella, *Weighting Di-Boson Monte Carlo Events in Hadron Colliders*, arXiv:0803.3307 [hep-ph].

[66] J. Polchinski, *Effective field theory and the Fermi surface*, arXiv:hep-th/9210046 [hep-th].

[67] Working Group on Electroweak precision measurements at the LHC. https://indico.cern.ch/conferenceDisplay.py?confId=145744.

[68] Working Group on Electroweak precision measurements at the LHC. http://indico.cern.ch/conferenceDisplay.py?confId=178469.

[69] E. Accomando and A. Kaiser, *Electroweak corrections and anomalous triple gauge-boson couplings in W^+W^- and $W^\pm Z$ production at the LHC*, Phys.Rev. **D73** (2006) 093006, arXiv:hep-ph/0511088 [hep-ph].

[70] U. Baur, T. Han, and J. Ohnemus, *Amplitude zeros in $W^\pm Z$ production*, Phys.Rev.Lett. **72** (1994) 3941–3944, arXiv:hep-ph/9403248 [hep-ph].

[71] J. M. Campbell, R. K. Ellis, and C. Williams, *Vector boson pair production at the LHC*, JHEP **1107** (2011) 018, arXiv:1105.0020 [hep-ph].

[72] W. Hollik et al., *Electroweak physics*, Acta Phys.Polon. **B35** (2004) 2533–2555, arXiv:hep-ph/0501246 [hep-ph].

[73] A. Bierweiler, T. Kasprzik, and J. H. Kühn, *Electroweak accuracy in V-pair production at the LHC*, arXiv:1208.3404 [hep-ph].

[74] R. W. Brown, D. Sahdev, and K. O. Mikaelian, *$W^\pm Z^0$ and $W^\pm\gamma$ pair production in νe, pp, and $p\bar{p}$ collisions*, Phys. Rev. D **20** (Sep, 1979) 1164–1174. http://link.aps.org/doi/10.1103/PhysRevD.20.1164.

[75] U. Baur, E. Glover, and J. van der Bij, *Hadronic production of electroweak vector boson pairs at large transverse momentum*, Nuclear Physics B **318** (1989) no. 1, 106 – 136. http://www.sciencedirect.com/science/article/pii/0550321389900497.

[76] J. Ohnemus, *Order-α_s calculation of hadronic $W^\pm Z$ production*, Phys. Rev. D **44** (Dec, 1991) 3477–3489. http://link.aps.org/doi/10.1103/PhysRevD.44.3477.

[77] S. Frixione, P. Nason, and G. Ridolfi, *Strong corrections to WZ production at hadron colliders*, Nuclear Physics B **383** (1992) no. 12, 3 – 44. http://www.sciencedirect.com/science/article/pii/0550321392906682.

[78] L. J. Dixon, Z. Kunszt, and A. Signer, *Helicity amplitudes for $\mathcal{O}(\alpha_s)$ production of W^+W^-, $W^\pm Z$, ZZ, $W^\pm\gamma$, or $Z\gamma$ pairs at hadron colliders*, Nucl.Phys. **B531** (1998) 3–23, arXiv:hep-ph/9803250 [hep-ph].

[79] J. M. Campbell and R. K. Ellis, *An Update on vector boson pair production at hadron colliders*, Phys.Rev. **D60** (1999) 113006, arXiv:hep-ph/9905386 [hep-ph].

[80] S. Frixione, F. Stoeckli, P. Torrielli, B. R. Webber, and C. D. White, *The MC@NLO 4.0 Event Generator*, arXiv:1010.0819 [hep-ph].

[81] P. Nason, *A New method for combining NLO QCD with shower Monte Carlo algorithms*, JHEP **0411** (2004) 040, arXiv:hep-ph/0409146 [hep-ph].

[82] K. Hamilton, *A positive-weight next-to-leading order simulation of weak boson pair production*, JHEP **1101** (2011) 009, arXiv:1009.5391 [hep-ph].

[83] S. Gieseke, D. Grellscheid, K. Hamilton, A. Papaefstathiou, S. Plätzer, et al., *Herwig++ 2.5 Release Note*, arXiv:1102.1672 [hep-ph].

[84] T. Melia, P. Nason, R. Rontsch, and G. Zanderighi, *W^+W^-, WZ and ZZ production in the POWHEG BOX*, J. High Energy Phys. **1111** (2011) 078, arXiv:1107.5051 [hep-ph].

[85] CDF Collaboration, T. Aaltonen et al., *Measurement of the WZ Cross Section and Triple Gauge Couplings in $p\bar{p}$ Collisions at $\sqrt{s} = 1.96$ TeV*, Phys.Rev. **D86** (2012) 031104, arXiv:1202.6629 [hep-ex].

[86] D0 Collaboration, V. M. Abazov et al., *Measurement of the $WZ \to \ell\nu\ell\ell$ cross section and limits on anomalous triple gauge couplings in $p\bar{p}$ collisions at $\sqrt{s} = 1.96$ TeV*, Phys.Lett. **B695** (2011) 67–73, arXiv:1006.0761 [hep-ex].

[87] D0 Collaboration, V. M. Abazov et al., *Limits on anomalous trilinear gauge boson couplings from WW, WZ and $W\gamma$ production in $p\bar{p}$ collisions at $\sqrt{s} = 1.96$ TeV*, Phys.Lett. **B718** (2012) 451–459, arXiv:1208.5458 [hep-ex].

[88] The LEP Collaborations ALEPH, DELPHI, L3, OPAL, and the LEP TGC Working Group, *A Combination of Results on Charged Triple Gauge Boson Couplings Measured by the LEP Experiments*, (2005) . http://lepewwg.web.cern.ch/LEPEWWG/lepww/tgc/.

[89] CMS Collaboration, *Measurement of the WW, WZ and ZZ cross sections at CMS*, CMS-PAS-EWK-11-010, CERN, Geneva, 2011.

[90] CMS Collaboration, S. Chatrchyan et al., *Measurement of W^+W^- Production and Search for the Higgs Boson in pp Collisions at $\sqrt{s} = 7$ TeV*, Phys.Lett. **B699** (2011) 25–47, arXiv:1102.5429 [hep-ex].

[91] CMS Collaboration, S. Chatrchyan et al., *Measurement of the sum of WW and WZ production with W+dijet events in pp collisions at $\sqrt{s} = 7$ TeV*, Eur. Phys. J. C **73** (2013) 2283, arXiv:1210.7544 [hep-ex].

[92] ATLAS Collaboration, G. Aad et al., *Measurement of the WZ production cross section and limits on anomalous triple gauge couplings in proton-proton collisions at $\sqrt{s} = 7$ TeV with the ATLAS detector*, Phys.Lett. **B709** (2012) 341–357, arXiv:1111.5570 [hep-ex].

[93] M. Bähr, S. Gieseke, M. Gigg, D. Grellscheid, K. Hamilton, et al., *Herwig++ Physics and Manual*, Eur.Phys.J. **C58** (2008) 639–707, arXiv:0803.0883 [hep-ph].

[94] L. Lönnblad, *ThePEG, Pythia7, Herwig++ and Ariadne*, Nuclear Instruments and Methods in Physics Research Section A: Accelerators, Spectrometers, Detectors and Associated Equipment **559** (2006) no. 1, 246 – 248. http://www.sciencedirect.com/science/article/pii/S0168900205022783.

[95] M. Bähr, S. Gieseke, and M. H. Seymour, *Simulation of multiple partonic interactions in Herwig++*, JHEP **0807** (2008) 076, arXiv:0803.3633 [hep-ph].

[96] B. R. Webber, *A QCD model for jet fragmentation including soft gluon interference*, Nuclear Physics B **238** (1984) no. 3, 492 – 528. http://www.sciencedirect.com/science/article/pii/055032138490333X.

[97] HepMC, *A C++ Event Record for Monte Carlo Generators*, http://lcgapp.cern.ch/project/simu/HepMC/download/.

[98] The ROOT team, *The ROOT Users Guide*, http://root.cern.ch/drupal.

[99] H. Murayama, I. Watanabe, and K. Hagiwara, *HELAS : HELicity amplitude subroutines for feynman diagram evaluations*. National Laboratory for High Physics, Ibaraki-ken, Japan, 1992.

[100] P. Nason and G. Ridolfi, *A Positive-weight next-to-leading-order Monte Carlo for Z pair hadroproduction*, JHEP **0608** (2006) 077, arXiv:hep-ph/0606275 [hep-ph].

[101] P. Nason, *MINT: A Computer program for adaptive Monte Carlo integration and generation of unweighted distributions*, arXiv:0709.2085 [hep-ph].

[102] B. Mele, P. Nason, and G. Ridolfi, *QCD radiative corrections to Z boson pair production in hadronic collisions*, Nuclear Physics B **357** (1991) no. 2 - 3, 409 – 438. http://www.sciencedirect.com/science/article/pii/055032139190475D.

[103] S. Frixione, *A next-to-leading order calculation of the cross section for the production of W+W pairs in hadronic collisions*, Nuclear Physics B **410** (1993) no. 2, 280 – 324. http://www.sciencedirect.com/science/article/pii/055032139390435R.

[104] K. Hamilton. Private communication.

[105] Wolfram Research, Inc., *Mathematica Edition: Version 7.0*. 2008.

[106] Topdrawer. http://www.rcnp.osaka-u.ac.jp/~okamura/ftp/pub/index.php?dir=topdrawer/.

[107] A. Jacholkowska, J. Kalinowski, and Z. Was, *Library of SM and anomalous WWγ couplings for the $e^+e^- \to f\bar{f}n\gamma$ Monte Carlo programs*, Comput.Phys.Commun. **124** (2000) 238–242, arXiv:hep-ph/9905225 [hep-ph].

[108] M. Cacciari, G. P. Salam, and G. Soyez, *FastJet User Manual*, Eur.Phys.J. **C72** (2012) 1896, arXiv:1111.6097 [hep-ph].

[109] S. Alioli, P. Nason, C. Oleari, and E. Re, *NLO Higgs boson production via gluon fusion matched with shower in POWHEG*, JHEP **0904** (2009) 002, arXiv:0812.0578 [hep-ph].

[110] ATLAS Collaboration, *ATLAS detector and physics performance: Technical Design Report, 1*, CERN-LHCC-99-014, CERN, Geneva, 1999.

[111] ATLAS Collaboration, *ATLAS detector and physics performance: Technical Design Report, 2*, CERN-LHCC-99-015, CERN, Geneva, 1999.

[112] ATLAS Collaboration, *The ATLAS Experiment at the CERN Large Hadron Collider*, JINST **3** (2008) S08003.

[113] CMS Collaboration, *CMS Physics Technical Design Report Volume I : Detector Performance and Software*, CERN-LHCC-2006-001, CERN, Geneva, 2006.

[114] CMS Collaboration, *The CMS Experiment at the CERN LHC*, JINST **3** (2008) S08004.

[115] LHCb Collaboration, *LHCb technical proposal*, CERN-LHCC-98-04, CERN, Geneva, 1998.

[116] LHCb Collaboration, *The LHCb Detector at the LHC*, JINST **3** (2008) S08005.

[117] ALICE Collaboration, *The ALICE experiment at the CERN LHC*, JINST **3** (2008) S08002.

[118] O. Brüning et al., *LHC Design Report Volume I The LHC Main Ring*, CERN-2004-003-V1, CERN, Geneva, 2004.

[119] O. Brüning et al., *LHC Design Report Volume II The LHC Infrastructure and General Services*, CERN-2004-003-V2, CERN, Geneva, 2004.

[120] M. Benedikt et al., *LHC Design Report Volume III The LHC Injector Chain*, CERN-2004-003-V3, CERN, Geneva, 2004.

[121] L. Evans and P. Bryant, *LHC machine*, JINST **3** (2008) S08001.

[122] C. Lefevre, *LHC: the guide*, 2008.

[123] R. Scrivens et al., *Overview of the status and developments on primary ion sources at CERN*, CERN-ATS-2011-172, Sep, 2011.

[124] ATLAS Data Summary, *2012 Records*, `https://atlas.web.cern.ch/Atlas/GROUPS/DATAPREPARATION/DataSummary/2012/records.html`.

[125] F. Hügging, *The ATLAS Pixel Detector*, IEEE Transactions on Nuclear Science **53** (June, 2006) 1732–1736, `arXiv:physics/0412138`.

[126] ATLAS Collaboration, G. Aad et al., *Luminosity Determination in pp Collisions at $\sqrt{s} = 7$ TeV Using the ATLAS Detector at the LHC*, Eur.Phys.J. **C71** (2011) 1630, `arXiv:1101.2185 [hep-ex]`.

[127] ATLAS Collaboration, *Updated Luminosity Determination in pp Collisions at $\sqrt{s} = 7$ TeV using the ATLAS Detector*, ATLAS-CONF-2011-011, CERN, Geneva, Mar, 2011.

[128] ATLAS Collaboration, *Luminosity Determination in pp Collisions at $\sqrt{s} = 7$ TeV using the ATLAS Detector in 2011*, ATLAS-CONF-2011-116, CERN, Geneva, Aug, 2011.

[129] ATLAS Collaboration, *Improved Luminosity Determination in pp Collisions at $\sqrt{s} = 7$ TeV using the ATLAS Detector at the LHC*, ATLAS-CONF-2012-080, CERN, Geneva, Jul, 2011.

[130] S. Agostinelli et al., *Geant4 – a simulation toolkit*, Nuclear Instruments and Methods in Physics Research Section A: Accelerators, Spectrometers, Detectors and Associated Equipment **506** (2003) no. 3, 250 – 303. http://www.sciencedirect.com/science/article/pii/S0168900203013688.

[131] J. Boudreau et al., *ATLAS detector simulation: status and outlook*, ATL-SOFT-PUB-2005-004. CERN-ATL-SOFT-PUB-2005-004. ATL-COM-SOFT-2005-008, CERN, Geneva, Dec, 2005.

[132] P. F. Åkesson et al., *ATLAS Tracking Event Data Model*, ATL-SOFT-PUB-2006-004. ATL-COM-SOFT-2006-005. CERN-ATL-COM-SOFT-2006-005, CERN, Geneva, Jul, 2006.

[133] T. G. Cornelissen et al., *Updates of the ATLAS Tracking Event Data Model (Release 13)*, ATL-SOFT-PUB-2007-003. ATL-COM-SOFT-2007-008, CERN, Geneva, Jun, 2007.

[134] T. Cornelissen et al., *Concepts, Design and Implementation of the ATLAS New Tracking (NEWT)*, ATL-SOFT-PUB-2007-007. ATL-COM-SOFT-2007-002, CERN, Geneva, Mar, 2007.

[135] ATLAS Collaboration, *Performance of primary vertex reconstruction in proton-proton collisions at $\sqrt{s}$ =7 TeV in the ATLAS experiment*, ATLAS-CONF-2010-069, CERN, Geneva, Jul, 2010.

[136] ATLAS Collaboration, *Performance of the ATLAS Inner Detector Track and Vertex Reconstruction in the High Pile-Up LHC Environment*, ATLAS-CONF-2012-042, CERN, Geneva, Mar, 2012.

[137] F. Meloni, A. Milov, S. Pagan-Griso, K. Prokofiev, and A. Wildauer, *Vertexing Performance Data vs MC comparison for LPCC*, ATL-COM-PHYS-2011-1312, CERN, Geneva, Sep, 2011.

[138] S. Pagan Griso, K. Prokofiev, A. Andreazza, K. Grimm, E. Guido, F. Meloni, M. Rudolph, A. Salzburger, and A. Wildauer, *Vertex reconstruction plots : Collision performance plots for approval*, ATL-COM-PHYS-2012-561, CERN, Geneva, May, 2012.

[139] W. Lampl, S. Laplace, D. Lelas, P. Loch, H. Ma, S. Menke, S. Rajagopalan, D. Rousseau, S. Snyder, and G. Unal, *Calorimeter Clustering Algorithms: Description and Performance*, ATL-LARG-PUB-2008-002. ATL-COM-LARG-2008-003, CERN, Geneva, Apr, 2008.

[140] ATLAS Collaboration, *Electron and photon reconstruction and identification in ATLAS: expected performance at high energy and results at 900 GeV*, ATLAS-CONF-2010-005, CERN, Geneva, Jun, 2010.

[141] `https://twiki.cern.ch/twiki/bin/viewauth/AtlasProtected/TechnicalitiesForMedium1`.

[142] D. Adams et al., *Track reconstruction in the ATLAS Muon Spectrometer with MOORE 007*, ATL-SOFT-2003-007, CERN, Geneva, May, 2003.

[143] S. Hassani, L. Chevalier, E. Lanon, J.-F. Laporte, R. Nicolaidou, and A. Ouraou, *A muon identification and combined reconstruction procedure for the ATLAS detector at the LHC using the (MUONBOY, STACO, MuTag) reconstruction packages*, Nuclear Instruments and Methods in Physics Research Section A: Accelerators, Spectrometers, Detectors and Associated Equipment **572** (2007) no. 1, 77 – 79. `http://www.sciencedirect.com/science/article/pii/S0168900206019863`.

[144] R. Nicolaidou, L. Chevalier, S. Hassani, J. F. Laporte, E. L. Menedeu, and A. Ouraou, *Muon identification procedure for the ATLAS detector at the LHC using Muonboy reconstruction package and tests of its performance using cosmic rays and single beam data*, Journal of Physics: Conference Series **219** (2010) no. 3, 032052. `http://stacks.iop.org/1742-6596/219/i=3/a=032052`.

[145] `https://twiki.cern.ch/twiki/bin/viewauth/AtlasProtected/QualityDefinitionStaco`.

[146] S. Tarem, Z. Tarem, N. Panikashvili, and O. Belkind, *MuGirl - Muon identification in ATLAS from the inside out*, Nuclear Science Symposium Conference Record, IEEE **1** (2007) 617–621.

[147] ATLAS Collaboration, G. Aad et al., *Jet energy measurement with the ATLAS detector in proton-proton collisions at* $\sqrt{s} = 7$ *TeV*, `arXiv:1112.6426 [hep-ex]`.

[148] M. Cacciari, G. P. Salam, and G. Soyez, *The anti-k_t jet clustering algorithm*, JHEP **0804** (2008) 063, `arXiv:0802.1189 [hep-ph]`.

[149] ATLAS Collaboration, G. Aad et al., *Performance of Missing Transverse Momentum Reconstruction in Proton-Proton Collisions at 7 TeV with ATLAS*, Eur.Phys.J. **C72** (2012) 1844, `arXiv:1108.5602 [hep-ex]`.

[150] ATLAS Collaboration, *Performance of Missing Transverse Momentum Reconstruction in ATLAS with 2011 Proton-Proton Collisions at* $\sqrt{s} = 7$ *TeV*, ATLAS-CONF-2012-101, CERN, Geneva, Jul, 2012.

[151] ATLAS Collaboration, G. Aad et al., *Measurement of $W^{\pm}Z$ production in proton-proton collisions at* $\sqrt{s} = 7$ *TeV with the ATLAS detector*, Eur.Phys.J. **C72** (2012) 2173, `arXiv:1208.1390 [hep-ex]`.

[152] `http://atlasdqm.web.cern.ch/atlasdqm/grlgen/`.

[153] https://atlas-datasummary.cern.ch/lumicalc.

[154] ATLAS Collaboration, *Athena Computing Framework ATLAS Internal Webpage*, https://twiki.cern.ch/twiki/bin/viewauth/Atlas/AthenaFramework.

[155] G. Corcella, I. Knowles, G. Marchesini, S. Moretti, K. Odagiri, et al., *HERWIG 6.5: An Event generator for hadron emission reactions with interfering gluons (including supersymmetric processes)*, JHEP **0101** (2001) 010, arXiv:hep-ph/0011363 [hep-ph].

[156] S. Jadach, Z. Was, R. Decker, and J. Kühn, *The τ decay library TAUOLA, Version 2.4*, Comput. Phys. Commun. **76** (1993) 361.

[157] P. Golonka and Z. Was, *PHOTOS Monte Carlo: A Precision tool for QED corrections in Z and W decays*, Eur.Phys.J. **C45** (2006) 97–107, arXiv:hep-ph/0506026 [hep-ph].

[158] M. L. Mangano, F. Piccinini, A. Polosa, M. Moretti, and R. Pittau, *ALPGEN, a Generator for Hard Multiparton Processes in Hadronic Collisions*, JHEP **07** (2003) 001, arXiv:hep-ph/0206293.

[159] J. Alwall, P. Demin, S. de Visscher, R. Frederix, M. Herquet, et al., *MadGraph/MadEvent v4: The New Web Generation*, JHEP **0709** (2007) 028, arXiv:0706.2334 [hep-ph].

[160] https://twiki.cern.ch/twiki/bin/viewauth/AtlasProtected/PythiaB.

[161] T. Gleisberg, S. Höche, F. Krauss, M. Schönherr, S. Schumann, et al., *Event generation with SHERPA 1.1*, JHEP **0902** (2009) 007, arXiv:0811.4622 [hep-ph].

[162] J. Butterworth, E. Dobson, U. Klein, B. Mellado Garcia, T. Nunnemann, J. Qian, D. Rebuzzi, R. Tanaka, *Single Boson and Diboson Production Cross Sections in pp Collisions at $\sqrt{s} = 7$ TeV*, ATL-COM-PHYS-2010-695, CERN, Geneva, 2010.

[163] ATLAS Collaboration, *Performance of the ATLAS muon trigger in 2011*, ATLAS-CONF-2012-099, CERN, Geneva, Jul, 2012.

[164] https://twiki.cern.ch/twiki/bin/viewauth/Atlas/TrigMuonEfficiency.

[165] https://twiki.cern.ch/twiki/bin/viewauth/AtlasProtected/MCPAnalysisGuidelinesRel17MC11a.

[166] ATLAS Collaboration, *Muon reconstruction efficiency in reprocessed 2010 LHC proton-proton collision data recorded with the ATLAS detector*, ATLAS-CONF-2011-063, CERN, Geneva, Apr, 2011.

[167] ATLAS Collaboration, *Combined Muon Performance Public Results*, https://twiki.cern.ch/twiki/bin/view/AtlasPublic/MuonPerformancePublicPlots.

[168] ATLAS Collaboration, *Muon Momentum Resolution in First Pass Reconstruction of pp Collision Data Recorded by ATLAS in 2010*, ATLAS-CONF-2011-046, CERN, Geneva, Mar, 2011.

[169] `https://twiki.cern.ch/twiki/bin/viewauth/AtlasProtected/IsoIPSF`.

[170] ATLAS Collaboration, G. Aad et al., *Electron performance measurements with the ATLAS detector using the 2010 LHC proton-proton collision data*, Eur.Phys.J. **C72** (2012) 1909, `arXiv:1110.3174 [hep-ex]`.

[171] T. Serre and J. Maurer, *Electron identification efficiency dependence on pile-up*, ATL-COM-PHYS-2012-260, CERN, Geneva, Mar, 2012.

[172] A. Ahmad and M. Boonekamp, *Calibrated $Z \to e^+e^-$ invariant mass with 2011 data*, ATL-COM-PHYS-2011-1637, CERN, Geneva, Nov, 2011.

[173] ATLAS Collaboration, *Reconstruction and Calibration of Missing Transverse Energy and Performance in Z and W events in ATLAS Proton-Proton Collisions at 7 TeV*, ATLAS-CONF-2011-080, CERN, Geneva, Jun, 2011.

[174] `https://twiki.cern.ch/twiki/bin/view/AtlasProtected/HowToCleanJets`.

[175] `https://twiki.cern.ch/twiki/bin/viewauth/AtlasProtected/ElectronGamma`.

[176] ATLAS Collaboration, G. Aad et al., *Measurement of the top quark-pair production cross section with ATLAS in pp collisions at $\sqrt{s} = 7$ TeV*, Eur.Phys.J. **C71** (2011) 1577, `arXiv:1012.1792 [hep-ex]`.

[177] J. Nielsen, *W/Z+Jet Cross Section Measurements at the Large Hadron Collider*, Prog. High Energy Phys. **3** (Jun, 2009) 68. 5 p.

[178] ATLAS Collaboration, M. Groll, *Associated Production of Weak Bosons at the LHC with the ATLAS Detector*, J. Phys. Conf. Ser. **171** (2009) 012086.

[179] H.-L. Lai, M. Guzzi, J. Huston, Z. Li, P. M. Nadolsky, J. Pumplin, and C.-P. Yuan, *New parton distributions for collider physics*, Phys. Rev. D **82** (Oct, 2010) 074024. `http://link.aps.org/doi/10.1103/PhysRevD.82.074024`.

[180] F. James, *MINUIT - Function Minimization and Error Analysis*. CERN Program Library entry D506, Geneva, 1998.

[181] J. Neyman, *Outline of a Theory of Statistical Estimation Based on the Classical Theory of Probability*, Royal Society of London Philosophical Transactions Series A **236** (Aug, 1937) 333–380.

[182] G. J. Feldman and R. D. Cousins, *Unified approach to the classical statistical analysis of small signals*, Phys. Rev. D **57** (Apr, 1998) 3873–3889. `http://link.aps.org/doi/10.1103/PhysRevD.57.3873`.

[183] http://indico.cern.ch/getFile.py/access?contribId=1&resId=0&materialId=slides&confId=160815.

[184] G. Cowan, K. Cranmer, E. Gross, and O. Vitells, *Asymptotic formulae for likelihood-based tests of new physics*, Eur. Phys. J. **C 71** (2011) 1554, arXiv:1007.1727 [hep-ph].

[185] G. D'Agostini, *Improved iterative Bayesian unfolding*, ArXiv e-prints (Oct, 2010) , arXiv:1010.0632 [physics.data-an].

[186] V. Blobel, *An Unfolding method for high-energy physics experiments*, arXiv:hep-ex/0208022 [hep-ex].

[187] A. Hocker and V. Kartvelishvili, *SVD approach to data unfolding*, Nucl.Instrum.Meth. **A372** (1996) 469–481, arXiv:hep-ph/9509307 [hep-ph].

[188] B. Malaescu, *An iterative, dynamically stabilized method of data unfolding*, ArXiv e-prints (July, 2009) , arXiv:0907.3791 [physics.data-an].

[189] L. Randall and R. Sundrum, *Large Mass Hierarchy from a Small Extra Dimension*, Phys. Rev. Lett. **83** (Oct, 1999) 3370–3373. http://link.aps.org/doi/10.1103/PhysRevLett.83.3370.

[190] L. Randall and R. Sundrum, *An Alternative to Compactification*, Phys. Rev. Lett. **83** (Dec, 1999) 4690–4693. http://link.aps.org/doi/10.1103/PhysRevLett.83.4690.

[191] H. Davoudiasl, J. Hewett, and T. Rizzo, *Experimental probes of localized gravity: On and off the wall*, Phys.Rev. **D63** (2001) 075004, arXiv:hep-ph/0006041 [hep-ph].

[192] J. Ellis, *The superstring: theory of everything, or of nothing?*, Nature **323** (Oct, 1986) 595–598. http://dx.doi.org/10.1038/323595a0.

[193] E. Eichten and K. Lane, *Low-scale technicolor at the Tevatron and LHC*, Phys.Lett. **B669** (2008) 235–238, arXiv:0706.2339 [hep-ph].

[194] S. Catterall, L. Del Debbio, J. Giedt, and L. Keegan, *Monte Carlo renormalization group minimal walking technicolor*, Phys. Rev. D **85** (May, 2012) 094501. http://link.aps.org/doi/10.1103/PhysRevD.85.094501.

[195] J. Andersen, O. Antipin, G. Azuelos, L. Del Debbio, E. Del Nobile, et al., *Discovering Technicolor*, Eur.Phys.J.Plus **126** (2011) 81, arXiv:1104.1255 [hep-ph].

[196] ATLAS Collaboration, *Search for resonant ZZ production in the $ZZ \to \ell\ell q\bar{q}$ channel with the ATLAS detector using 7.2 fb^{-1} of $\sqrt{s} = 8$ TeV p-p collision data*, ATLAS-CONF-2012-150, CERN, Geneva, Nov, 2012.

[197] D0 Collaboration, V. M. Abazov et al., *Search for resonant WW and WZ production in $p\bar{p}$ collisions at $\sqrt{s} = 1.96$ TeV*, Phys.Rev.Lett. **107** (2011) 011801, arXiv:1011.6278 [hep-ex].

[198] CDF Collaboration, T. Aaltonen et al., *Search for WW and WZ resonances decaying to electron, missing E_T, and two jets in $p\bar{p}$ collisions at $\sqrt{s} = 1.96$ TeV*, Phys.Rev.Lett. **104** (2010) 241801, arXiv:1004.4946 [hep-ex].

[199] CDF Collaboration, T. Aaltonen et al., *Search for $X \to ZZ$ with 3 fb^{-1} and Forward Tracking*, http://www-cdf.fnal.gov/physics/exotic/r2a/20081120.ZZ_resonance/public.html.

[200] CMS Collaboration, S. Chatrchyan et al., *Search for a narrow spin-2 resonance decaying to a pair of Z vector bosons in the semileptonic final state*, Phys.Lett. **B718** (2013) 1208–1228, arXiv:1209.3807 [hep-ex].

[201] CMS Collaboration, *Search for exotic resonances decaying into $V + Z$ using final states with a jet and a lepton pair*, CMS-PAS-EXO-11-081, CERN, Geneva, 2012.

[202] ATLAS Collaboration, G. Aad et al., *Search for new particles decaying to ZZ using final states with leptons and jets with the ATLAS detector in $\sqrt{s} = 7$ Tev proton-proton collisions*, Phys.Lett. **B712** (2012) 331–350, arXiv:1203.0718 [hep-ex].

[203] ATLAS Collaboration, G. Aad et al., *Search for new phenomena in the $WW \to \ell\nu\ell'\nu'$ final state in pp collisions at $\sqrt{s} = 7$ TeV with the ATLAS detector*, Phys.Lett. **B718** (2013) 860–878, arXiv:1208.2880 [hep-ex].

[204] https://twiki.cern.ch/twiki/bin/viewauth/Atlas/AtlfastII.

[205] A. Pukhov, *CalcHEP 2.3: MSSM, structure functions, event generation, batchs, and generation of matrix elements for other packages*, arXiv:hep-ph/0412191 [hep-ph].

[206] J. Pumplin, D. Stump, J. Huston, H. Lai, P. M. Nadolsky, et al., *New generation of parton distributions with uncertainties from global QCD analysis*, JHEP **0207** (2002) 012, arXiv:hep-ph/0201195 [hep-ph].

[207] T. Sjöstrand, S. Mrenna, and P. Z. Skands, *A Brief Introduction to PYTHIA 8.1*, Comput.Phys.Commun. **178** (2008) 852–867, arXiv:0710.3820 [hep-ph].

[208] J. M. Butterworth, J. R. Forshaw, and M. H. Seymour, *Multiparton interactions in photoproduction at HERA*, Z.Phys. **C72** (1996) 637–646, arXiv:hep-ph/9601371 [hep-ph].

[209] S. Frixione and B. R. Webber, *Matching NLO QCD computations and parton shower simulations*, JHEP **0206** (2002) 029, arXiv:hep-ph/0204244 [hep-ph].

[210] https://twiki.cern.ch/twiki/bin/viewauth/AtlasProtected/InDetTrackingPerformanceGuidelines.

[211] https://twiki.cern.ch/twiki/bin/view/AtlasPublic/EgammaTriggerPublicResults.

[212] G. Romeo, A. Schwartzman, R. Piegaia, T. Carli, and R. Teuscher, *Jet Energy Resolution from In-situ Techniques with the ATLAS Detector Using Proton-Proton Collisions at a Center of Mass Energy $\sqrt{s} = 7$ TeV*, ATL-COM-PHYS-2011-240, CERN, Geneva, Mar, 2011.

[213] `https://twiki.cern.ch/twiki/bin/viewauth/AtlasProtected/JetStudies2012#2012_jet_trigger_efficiencies`.

[214] G. Choudalakis, *On hypothesis testing, trials factor, hypertests and the BumpHunter*, ArXiv e-prints (Jan, 2011) , `arXiv:1101.0390 [physics.data-an]`.

[215] ATLAS Collaboration, G. Aad et al., *Search for New Physics in the Dijet Mass Distribution using 1 fb^{-1} of pp Collision Data at $\sqrt{s} = 7$ TeV collected by the ATLAS Detector*, Phys.Lett. **B708** (2012) 37–54, `arXiv:1108.6311 [hep-ex]`.

[216] CMS Collaboration, S. Chatrchyan et al., *Search for Resonances in the Dijet Mass Spectrum from 7 TeV pp Collisions at CMS*, Phys.Lett. **B704** (2011) 123–142, `arXiv:1107.4771 [hep-ex]`.

[217] ATLAS Collaboration, G. Aad et al., *Search for production of resonant states in the photon-jet mass distribution using pp collisions at $\sqrt{s} = 7$ TeV collected by the ATLAS detector*, Phys.Rev.Lett. **108** (2012) 211802, `arXiv:1112.3580 [hep-ex]`.

[218] CMS Collaboration, *Search for New Physics in the Paired Dijet Mass Spectrum*, CMS-PAS-EXO-11-016, CERN, Geneva, 2012.

[219] K. Cranmer, G. Lewis, L. Moneta, A. Shibata, and W. Verkerke, *HistFactory: A tool for creating statistical models for use with RooFit and RooStats*, CERN-OPEN-2012-016, New York U., New York, Jan, 2012.

[220] ATLAS Collaboration, *A Measurement of WZ Production in Proton-Proton Collisions at $\sqrt{s} = 8$ TeV with the ATLAS Detector*, ATLAS-CONF-2013-021, CERN, Geneva, Mar, 2013.